7-1-2002

Tectonic development of Proterozoic structures and their influence on Laramide and Miocene deformation, north Virgin Moutains, SE Nevada and NW Arizona

Mark Cameron Quigley

TECTONIC DEVELOPMENT OF PROTEROZOIC STRUCTURES AND THEIR INFLUENCE ON LARAMIDE AND MIOCENE DEFORMATION, NORTH VIRGIN MOUNTAINS, SE NEVADA AND NW ARIZONA

BY

MARK CAMERON QUIGLEY

HON B.SC. GEOLOGY, UNIVERSITY OF TORONTO, 1999

THESIS

Submitted in Partial Fulfillment of the
Requirements for the Degree of

Master of Science
Earth and Planetary Sciences

The University of New Mexico
Albuquerque, New Mexico

July 2002

Mark Cameron Quigley
Candidate

Earth and Planetary Sciences
Department

This thesis is approved, and it is acceptable in quality and form for publication on microfilm:

Approved by the Thesis Committee:

Karl E Karlstrom, Chairperson

Jane Selverstone

Adam Bowdon

Accepted:

Dean, Graduate School

Date

Dedication

To my brother, Jeff, my parents, Alan
and Marylysbeth, and my late grandfather,
Basil, who inspired all those around him
to seek an understanding of natural things

Acknowledgments

I'd like to thank Karl Karlstrom for his inspiration, tireless work ethic, and gentle guidance throughout the project. His enthusiasm and flexibility as a supervisor beveled the troughs inherently present in graduate studies. Co-authors Simon Hook (NASA), Matt Heizler (New Mexico Tech), and Shari Kelley (New Mexico Tech) provided comments on the manuscript and contributed to the technical sections on MASTER imagery, Ar-Ar thermochronology, and apatite fission-track, respectively. Their help in producing these manuscripts was invaluable. Jane Selverstone and Adrian Brearley provided helpful comments as committee members. Mike Spilde (UNM), Nelia Dunbar (New Mexico Tech), Mike Williams (UMass) and Mike Jercinovic (UMASS) helped with U/Pb monazite analyses and provided data for the project. Sam Bowring (M.I.T) conducted U/Pb analyses on apatite and zircon that will appear in the Proterozoic chapter once it is submitted for publication.

The UNM Tectonic Studies Group (Colin Shaw, Annie McCoy, Mike Timmons, Micah Jessup, Amanda Tyson, Toti Larson, Kurt Steffan, Jamie Barnes) contributed their thoughts on various aspects of the project, and provided a broad spectrum of geologic interests to feed from. Thanks to the Faculty and graduate students at UNM. Thanks to Elizabeth Langenburg, Amanda Tyson, and Jason Ray for their energy and interest as field assistants, and to Jason for his B.A. thesis on the Cabin Canyon shear zone. Thanks to the University of New Mexico, the Department of Earth and Planetary Sciences, NASA, and the Geological Society of America for partially funding my research.

Thanks to the eclectic group of friends and housemates I have gathered during my time at UNM. Your patience, support, and social and academic diversity are appreciated. Special thanks to my family Alan, Maryliz, and Jeff Quigley, and to my friends from Canada, for providing geographically distant support that seemed so close. It is in the dew of unconditional friendship that the heart finds its morning, and is refreshed.

TECTONIC DEVELOPMENT OF PROTEROZOIC STRUCTURES AND THEIR INFLUENCE ON LARAMIDE AND MIOCENE DEFORMATION, NORTH VIRGIN MOUNTAINS, SE NEVADA AND NW ARIZONA

BY

MARK CAMERON QUIGLEY

ABSTRACT OF THESIS

Submitted in Partial Fulfillment of the
Requirements for the Degree of

Master of Science
Earth and Planetary Sciences

The University of New Mexico
Albuquerque, New Mexico

July 2002

TECTONIC DEVELOPMENT OF PROTEROZOIC STRUCTURES AND THEIR INFLUENCE ON LARAMIDE AND MIOCENE DEFORMATION, NORTH VIRGIN MOUNTAINS, SE NEVADA AND NW ARIZONA

Mark Cameron Quigley

Hon. B.Sc. Geology, University of Toronto, 1999

M.S. Earth and Planetary Sciences, University of New Mexico, 2002

ABSTRACT OF THESIS

The northeast-trending Virgin Mountain anticline (VMA) of the North Virgin Mountains straddles the boundary between the unextended Colorado Plateau and the highly extended crust of the central Basin and Range province. The anticline is 50 km long and 8 km wide, is doubly-plunging, and has overturned Paleozoic beds on both limbs. The crystalline core of the VMA is composed of Paleoproterozoic supracrustal and intrusive rocks that record four tectonic events from circa 1740 Ma to 1550 Ma (D_1-D_4) characterized by distinct structural fabrics and associated metamorphic assemblages and microstructures. The most prominent Proterozoic structure is the Virgin Mountains shear zone (VMSZ), which was initially defined as a crustal weak zone during D_1 northeast-southwest contraction and may represent an important crustal suture, as it contains "exotic lithologies" commonly associated with ophiolites. A clockwise-rotating strain field during progressive east-west (D_2) and northwest-southeast (D_3) contractional events resulted in the prominent northeast-strike of this zone. Late Paleoproterozoic, east-west contraction across this zone (D_4) resulted in a complex array of linked, dextral

transpressive shear zones which partitioned strain into strike-slip, pure-shear, reverse, and normal sense deformation zones. Deformation within the VMSZ continued to 1600 and 1550 Ma based on syn-tectonic monazite rim ages that are associated with sub 500°C (greenschist facies) metamorphic assemblages and textures, and sub 500°C deformational microstructures. Development of these highly fissile shear zones later controlled the geometry of Laramide and Miocene brittle deformation.

The Proterozoic basement in the core of the VMA now resides at elevations of more than 2 km above sea level, roughly 2.5 km higher than the elevation of basement in the adjacent Colorado Plateau. The northeast trend and vertical uplift of the anticline is a result of Miocene east-west extensional deformation superimposed on the pre-existing northeast- and north-trending structural grains created during Paleoproterozoic (D_2, D_3, D_4) and Laramide contractional tectonic events. Outward-verging monoclinal reverse faults similar in style to Laramide-aged faults in the Colorado Plateau are present on the east and west limbs of the VMA, and we propose that much of the vertical uplift of the anticline occurred during this time. The geometry of Miocene deformation was both strongly partitioned and directed by these pre-existing structures, and also manifest as steeply dipping conjugate normal faults in the Mesozoic and Paleozoic section that soled into basal detachments in the Cambrian Bright Angel shale and at the Great Unconformity. Apatite-fission track (AFT) dates range from 21.7 ± 2.3 Ma directly below the Cambrian – Precambrian unconformity to 14.0 ± 2.5 Ma in the core of the VMA, and indicate that the anticline was unroofed in Miocene time. Short AFT lengths (<13μm) with large standard deviations (>2.5) from the 22-20 Ma AFT ages suggest that Proterozoic rocks of the VMA cooled slowly through the AFT partial annealing zone at

22-20 Ma, prior to extension, while longer AFTs suggest rapid cooling and syn-extensional exhumation from 16-14 Ma. We interpret the former ages to represent pre-extensional erosional cooling of a regionally elevated terrain, contrary to most models which assume a peneplain pre-extensional surface. Our model is consistent with geophysical, sedimentological, and tectonic studies of the region.

MODIS/ASTER Airborne Simulator (MASTER) remote sensing data were acquired over the VMA in order to evaluate the utility of the data for geological mapping in a structurally complex area. These data proved invaluable in producing more than 60 km^2 of new geologic mapping by the first author, and recognizing many of the key structures which led to our Proterozoic, Laramide, and Miocene tectonic interpretations.

TABLE OF CONTENTS

LIST OF FIGURES

PLATE (in back pocket)

LIST OF TABLES

Chapter 1:

Preface and introduction to the North Virgin Mountains

This thesis presents my thoughts and efforts as the first author of three distinct chapters, resulting from collaboration with Prof. Karl Karlstrom (UNM), Dr. Simon J. Hook (NASA), Prof. Shari Kelley (NM Tech) and Prof. Matt Heizler (NM Tech). These chapters will be submitted to refereed journals upon final completion of this thesis.

The thesis incorporates results of the detailed structural mapping, MASTER remote sensing image interpretation and regional mapping, metamorphic and microstructural petrology, sedimentology, U/Pb geochronology, Ar-Ar thermochronology and apatite fission-track thermochronometry, used in developing integrative models of the Proterozoic, Laramide, and Miocene tectonic evolution of the North Virgin Mountains in SE Nevada and NW Arizona (Figure 1-1). Prior to this study, more than 50% of the Proterozoic core of the Virgin Mountain anticline remained unmapped, little (if any) reliable geochronology existed, and no model for the Proterozoic tectonic evolution of this region existed. To fill these voids, the first author produced a complete geologic map of the North Virgin Mountains (see Plate 1), sampled for geochronology, and developed a tectonic model for the long-lived Paleoproterozoic tectonic history of this area. Despite numerous attempts, no model existed to explain the genesis of the Virgin Mountain anticline in the context of all available geologic and geophysical data, another contribution of this thesis. The uplift and exhumation history of the Virgin Mountain anticline is, for the first time, quantified, on the basis of reconstructive cross-

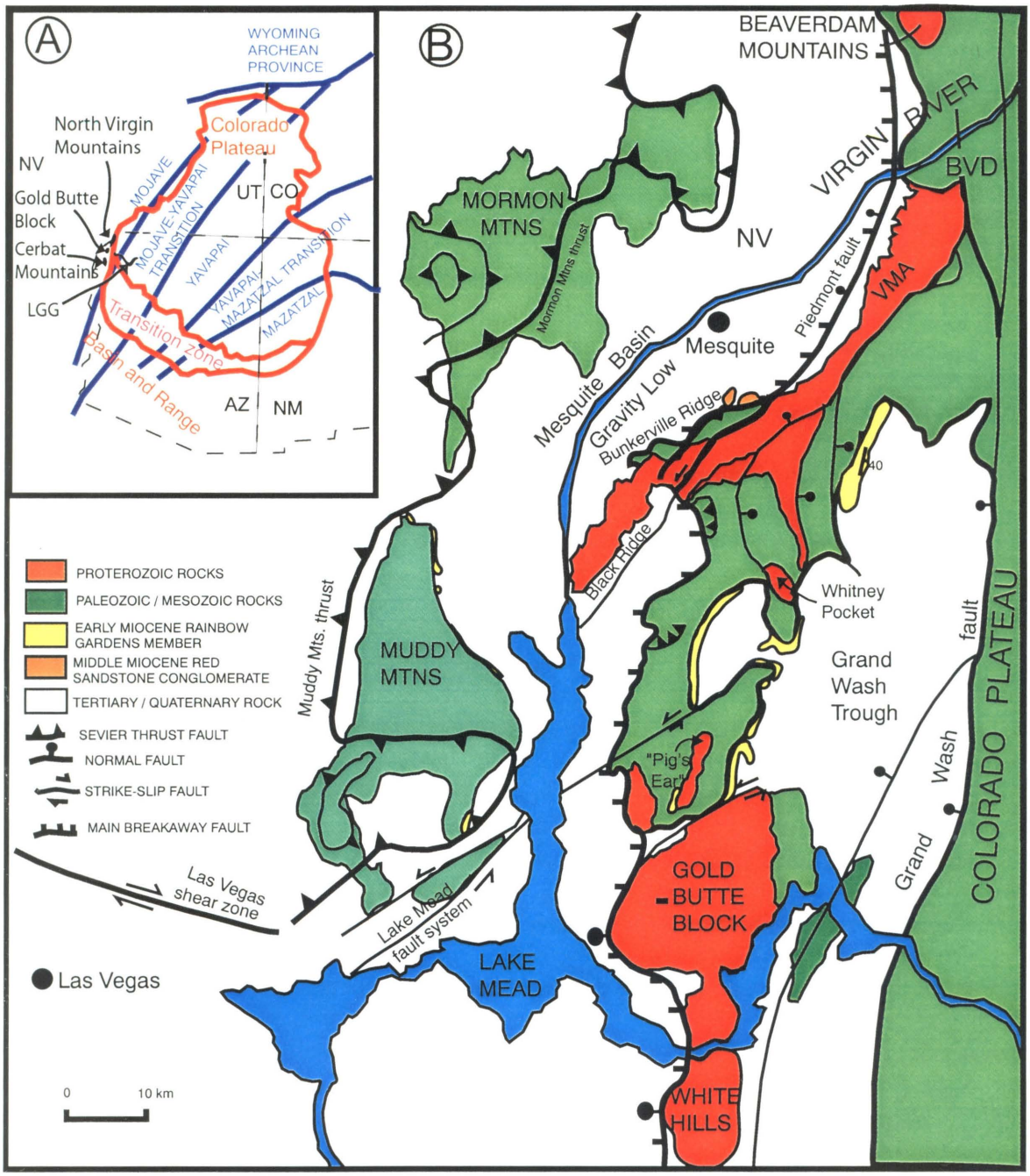

Figure 1-1) : A) Location of the North Virgin Mountains (NVM) relative to major Proterozoic outcroppings (Gold Butte Block, Cerbat Mountains, and the Lower Granite Gorge of the Grand Canyon (LGG), Proterozoic crustal provinces (Mojave, Yavapai, Mazatzal) and major geomorphic features (Colorado Plateau, Basin and Range). B) The basement-cored structure of the NVM reflects its anticlinal geometry (Virgin Mountain Anticline, VMA), that formed between the eastern edge of the Sevier Thrust Belt and the western-most "Meriwhitica" Monocline ("MM", grey in A), and between the Colorado Plateau and Basin and Range Provinces, created during middle Miocene extension (A, in red, and B).

sections by the first author, and an apatite fission-track study conducted by the first author and Shari Kelley.

The three chapters, although written as separate manuscripts, are bound by the unifying hypothesis that basement fabrics creating during the Paleoproterozoic significantly affected the geometry of Laramide contraction and Miocene extension, and thus the current geometric expression of the Virgin Mountain anticline.

Chapter two, entitled "Paleoproterozoic tectonic history of North Virgin Mountains, southeast Nevada and northwest Arizona: Genesis and evolution of a long-lived transpressional deformation zone" includes the main results of over six months of fieldwork by the first author traversing roughly 80 km^2 of Proterozoic basement in the North Virgin Mountains and region, including side trips to Proterozoic rocks exposed in the Gold Butte Block (Figure 1-1) and the Grand Canyon. Detailed work on these Proterozoic rocks resulted in: 1) production of 1:8,000, 1:12,000 and 1:24,000 scale maps of tectonically significant areas; 2) development of progressive model of D_1 through D_4 deformation events and associated metamorphism; 3) identification of a major crustal weak zone (the Virgin Mountain shear zone), which may represent an accretionary crustal suture that was repeatedly reactivated through time; 4) documentation of dextral transpressive strains within this shear zone, and preliminary U/Pb dating of its movement history; and 5) a model for the Proterozoic thermal evolution of the North Virgin Mountains based on Ar-Ar thermochronology.

Chapter three, entitled: "Influence of Proterozoic and Laramide structures on Miocene extension and genesis of the Virgin Mountain anticline, southeast Nevada and northwest Arizona: Constraints from structural and apatite fission-track analysis"

includes; 1) the main results of an apatite fission-track study of the Miocene exhumational history of the Virgin Mountain anticline (VMA); 2) documentation of basement-flanking Laramide monoclines and reconstruction of the pre-extensional structure of VMA; 3) documentation of a regional detachment at the Great Unconformity and in the Bright Angel shale, which developed during early Miocene extension; 4) documentation of an unroofing sequence in syn-extensional Miocene conglomerates, and implications for timing of exhumation of the VMA; and 5) development of time-sectioned pre-extensional, syn-extensional, and post-extensional cross-sections / tectonic models which integrate geophysical, sedimentological, structural, and thermochronological data.

Chapter four, entitled: "The use of MASTER remote sensing imagery for detailed structural and tectonic studies: A case study from the North Virgin Mountains" is a shorter, more technical chapter describing the principles and roles of MASTER images in the production of geologic maps of the North Virgin Mountains, both during field mapping and "office mapping" in the laboratories at the University of New Mexico. The importance of integrating MASTER images into traditional geologic mapping techniques (i.e. air photo interpretation, field work) are emphasized, and sample images and interpretations are presented. Moreover, the use of MASTER images for detailed structural and sedimentologic studies are emphasized.

Chapter 2:

Paleoproterozoic tectonic history of North Virgin Mountains, southeast Nevada and northwest Arizona: Genesis and evolution of a long-lived transpressional deformation zone

Mark Quigley and Karl Karlstrom, Department of Earth and Planetary Sciences, University of New Mexico

Matt Heizler, New Mexico Institute of Technology

1. Abstract

Structural and geochronological studies of the North Virgin Mountains of southeast Nevada and northwest Arizona place new constraints on the Paleoproterozoic tectonic evolution of this region, and identify a major crustal weak zone that was repeatedly reactivated through time. Structural fabrics were created during a clockwise rotating contractional strain field from circa 1740 to 1640 Ma. D_1 is characterized by a northwest-striking, moderately northeast-dipping foliation (S_1) that is axial planar to cryptically defined, macroscopic F_1 nappe folds of unknown vergence, and is associated with upper amphibolite to granulite facies metamorphism. D_2 is characterized by intense steepening, refolding, and transposition of S_1 foliations during east-west contraction, resulting in a north-striking subvertical foliation (S_2). D_3 is characterized by progressive rotation and localized overprinting of S_2 during northwest-southeast contraction and northwest-side-up thrusting, resulting in a northeast-striking foliation (S_3). Both D_2 and D_3 were associated with upper amphibolite facies metamorphism, and the transition from D_2 to D_3 was synchronous with intense granitic magmatism and partial melting, and indicated by the north to northeast-strike of granitic bodies and syn-magmatic and syn-

melting D_3 structures. D_3 appears to represent a deformation continuum through upper amphibolite to lower amphibolite facies metamorphic conditions, as indicated from a variety of metamorphic textures and assemblages associated with consistent kinematics along the major, northeast-striking Virgin Mountains shear zone (VMSZ). This deformation zone was reactivated during D_4 east-west contraction, resulting in complexly partitioned, dextral transpressive shearing associated with upper greenschist facies metamorphism.

Although currently expressed as a northeast-striking, composite S_3 / S_4 high strain zone, the VMSZ initiated as a crustal weak zone during D_1 continental assembly, marked by the interleaving of "exotic lithologies" including pillow basalt, calc-amphibolite gneiss, chert, marble, and ultramafic rock slivers. These lithologies may represent components of ophiolitic fragments along a widely distributed Mojave-Yavapai province boundary. Deformation within the VMSZ during D_2 (ca. 1700 Ma) progressed to increasingly partitioned deformation as the crust cooled, a likely product of collisional exhumation. Hornblende ^{40}Ar / ^{39}Ar dates suggest NVM crust cooled through ~525°C between 1640 and 1660 Ma. Deformation within the VMSZ continued to 1600 and 1550 Ma based on syn-tectonic monazite rim ages that are associated with sub 500°C (greenschist facies) metamorphic assemblages and textures, and sub 500°C deformational microstructures. Deformation thus continued longer here than in other areas of the southwestern United States, reaffirming the tectonic significance of the VMSZ as a substantially weak intracontinental deformation zone. U-Pb apatite dates of 1420 Ma and ^{40}Ar / ^{39}Ar biotite dates indicate that crust was ca. 450°C in the Mesoproterozoic and

while it is possible that the shear zone was reactivated then, no geochronologic data was found to support this.

2. Introduction

The period between 1780 and 1650 Ma was one of major crustal growth in North America, as juvenile oceanic island arcs, marginal basins, and fragments of older crust were accreted to Archean cratons (Karlstrom and Bowring, 1988, 1993; Hoffman, 1988; Condie, 1983). Isotopic and geochronologic data define three Paleoprotoerozoic crustal provinces in the southwestern United States; the Mazatzal, Yavapai, and Mojave (Karlstrom and Bowring, 1993). The Mojave province is characterized by enriched Nd and Pb isotopic signatures (Bennett and DePaolo, 1987), pre-1800 Ma crustal components from Pb isotopes and geochronology (Chamberlain and Bowring, 1990; Wooden and Miller, 1990; Wooden and Dewitt, 1991), up to 2600 Ma SHRIMP ages on inherited and detrital zircons (Wooden and Miller, 1990), and generally upper amphibolite to granulite facies metamorphism (Thomas et al., 1988; Fryxell et al., 1991; Duebendorfer et al., 2001). Conversely, the Yavapai and Mazatzal provinces are characterized by juvenile (at 1750 Ma) Nd and Pb isotopic signatures, little or no pre-1800 Ma material (Bennett and DePaolo, 1987; Wooden and Dewitt, 1991), and greenschist to amphibolite facies metamorphism (Williams, 1991). Juvenile terranes of the Yavapai province may have been assembled together and with the Mojave province before their final amalgamation to the Wyoming craton at 1780-1750 Ma (Jones et al.,

1996; Deubendorfer et al., 2001; Jessup et al., in prep), and later addition of the Mazatzal province at 1.65 Ga.

A period of relative structural quiescence in the southwest United States (1600-1500 Ma) was followed by intense bimodal magmatism, metamorphism, and partitioned contractional deformation during circa 1400 Ma tectonism (e.g. Nyman et al., 1994; Shaw et al., 2001; McCoy et al., 2002). Localized deformation during this time spanned distances of up to 1000 kilometers from any proposed accretionary margin, predominately reactivating older crustal weak zones. Karlstrom et al. (2001) proposed that long-lived contractional deformation affected southern North America from 1800 Ma (the Yavapai orogeny) to 1000 Ma (the Grenville orogeny) along a Cordilleran-type orogenic system that extended from Australia to Baltica. If so, inboard effects of contractional deformation may have been felt in the southwest United States for up to 800 m.y. (Karlstrom et al., 2001; Timmons et al., 2001). What the Mojave province was initially accreted to remains enigmatic, as the western margin of the Mojave was rifted away during the Neoproterozoic rifting of Rodinia. The favored AUSWUS reconstruction (Karlstrom et al., 1999) places Australia in this position, thus studying key areas of the Mojave province, such as the North Virgin Mountains, are important for understanding possible Australian connections. The apparent lack of 1600-1500 Ma tectonism as documented for the southwest United States, as mentioned above, is intriguing, given the pronounced tectonism of this age along possible extensions of this orogenic belt (i.e. Betts and Gilles, 2000). Unraveling the geologic history of Proterozoic rocks in the southwest United States thus involves understanding the genesis and evolution of crustal weak zones through time.

In the southwestern United States, considerable effort has been made to identify distinct terrane boundaries, sutures, and/or major structures within the Yavapai and Mojave provinces (Bennett and DePaolo, 1987; Wooden et al., 1988; Karlstrom and Bowring, 1988, 1993; Karlstrom and Humphries, 1998). Recent work confirms that sutures are identifiable using combined geological and seismic studies (Tyson et al., in press), and that many zones identified in the subsurface are associated with "tectonic mélange" along high-strain zones at the surface, including probable ophiolitic fragments such as pillow basalts, marbles, cherts and ultramafic rocks (i.e., Cavosie, unpublished M.S. thesis; Cavosie and Selverstone, in press; Karlstrom et al., in press). Furthermore, regionally documented orthogonal contraction directions (Albin and Karlstrom, 1991; Deubendorfer et al., 2001; Jessup et al., in prep; this study) complicate the geometry of these zones and make interpretations of their initial geometry and vergence difficult. Once established, however, these crustal weak zones are often episodically reactivated during further crustal accretion and/or later tectonic events, and represent excellent locations to study the inboard effects and partitioning of continental deformation (i.e, Shaw et al., 2001; McCoy et al., 2002; this study).

Transpression is a common feature of both plate margins and of reactivated weak zones, and takes place along most of presently active convergent plate margins. Strain complexities recorded by finite strain markers within these zones are often compounded by the lack of a temporal context for when these structures developed. Combining structural and microstructural analysis, metamorphic petrology, and ^{40}Ar / ^{39}Ar thermochronometry with an evolving U-Pb monazite geochronology technique represents the best integrative method in resolving the spatial versus temporal strain partitioning

complexities that may develop in a zone of recurrent reactivation, such as that within the North Virgin Mountains. Thus, this study addresses fundamental problems in structural geology: What are the roles of crustal weak zones during peak continental deformation and progressive deformation at shallower crustal levels? How is deformation spatially and temporally partitioned throughout transpressional zones? How can the observed fabrics in natural shear zones be used to meaningfully characterize bulk finite strains and reconstruct tectonic evolution?

In order to address these problems, we consider the genesis and complex tectonic history of the transpressional Virgin Mountains shear zone (VMSZ) in the North Virgin Mountains, in the context of local, regional, and continental scale tectonics.

3. North Virgin Mountains

The North Virgin Mountains (NVM) are a northeast-trending, basement-cored anticline that straddles the Basin and Range-Colorado Plateau along the Nevada-Arizona border, roughly 130 kilometers northeast of Las Vegas, Nevada (Figure 1-1). The Paleoproterozoic (~1700 Ma) rocks that make up the core of the anticline are part of the Mojave crustal province, which extends as far east as a boundary in central Arizona (Wooden and DeWitt, 1991) and the Upper Granite Gorge of the Grand Canyon (Ilg et al., 1996). This polydeformed metamorphic terrane had a long Proterozoic history which ended with deposition of late Precambrian-Cambrian miogeoclinal strata on exhumed middle crustal basement rocks during breakup of Rodinia. Present exposures are due to rapid exhumation during middle Miocene extension, when Proterozoic fabrics were

brittely reactivated by normal and strike-slip faults (Quigley et al., 2001). Despite intense deformation within the Phanerozoic rocks that flank the range, detailed mapping of the Proterozoic basement foliations and correlation with unextended basement in the Colorado Plateau suggests minimal reorientation and / or tilting of the Proterozoic core of the VMA during Miocene extension. Thus, Proterozoic foliation orientations can be used to meaningfully characterize Proterozoic strain fields. Relative to basement blocks shown in Figure 1-1, the NVM differs from the Gold Butte block, in which Proterozoic basement has been strongly east-tilted (Fryxell et al., 1992), but is similar to the two small blocks north of the Gold Butte fault and at Whitney Pocket.

Significant tectonic boundaries lie in the vicinity of the North Virgin Mountains, including: 1) the proposed Mojave –Yavapai Proterozoic province boundary to the east (Inset to Fig. 1-1; Karlstrom and Bowring, 1988); 2) the edge of the Cordilleran miogeocline, which developed during Neoproterozoic breakup of the supercontinent Rodinia; 3) the eastern edge of low-angle Sevier thin-skinned thrusting (Figure 1-1; Axen et al., 1990); 4) the western limit of Laramide high-angle reverse faulting typically found within in the Colorado Plateau (Huntoon, 1990); and 5) the breakaway zone for the Basin and Range-Colorado Plateau transition (Fig. 1; Wernicke and Axen, 1988). In spite of the tectonic significance of this region, many areas remain incompletely mapped. Previous work in the Proterozoic rocks was conducted by Beal (1965), who mapped and classified roughly 50 percent of the exposed NVM rocks at 1:24,000 scale, and later by Williams et al. (1997) and Beard (1993), who refined Beal's mapping in the central NVM. Our work, which involved mapping at scales of 1:24,000 and 1:12,000, structural, metamorphic, and microstructural analysis, geochronology, and thermochronometry, is

the first comprehensive geological investigation of the Proterozoic rocks of the NVM, and yields the first interpretation of the Paleoproterozoic tectonic history of this region. Mapping was greatly aided by use of MASTER images which helped delineate basement rocks and fabrics (Quigley et al., in prep).

Supracrustal rocks

Supracrustal rocks comprise over 70 percent of the exposed Paleoproterozoic rocks within the NVM (Plate 1). Mineralogical descriptions of these rocks primarily follow the work of Beal (1965), but genetic names are herein assigned in order to help characterize the tectonic context of the units. Metasedimentary gneiss and schist make up roughly 60 percent of the NVM, and range in composition from pelitic (meta-mudstones) to psammitic (meta-arenites and wackes). Amphibolite gneiss (10 percent) is half composed of metabasaltic rocks, which locally preserve flattened pillow structures (Figure 2-1c) and are interlayered within metasedimentary rocks, and half of diorite and gabbroic intrusive rocks, which are commonly associated with granodioritic plutons where they are present as xenoliths and dikes (see below). Ultramafic rocks consist primarily of hornblendites and pyroxenites, and are usually present as small (2-10 meter wide) pods within metasedimentary or metaigneous rocks. A localized belt of "exotic lithologies", consisting of an intimate mixture of ultramafic rocks, diopside marble, metachert, pelite, and calc-amphibolite or calc-silicate gneiss (Figure 2-1), is present along the spine of the NVM, and is interpreted as a tectonic mélange characterized by tectonically juxtaposed units.

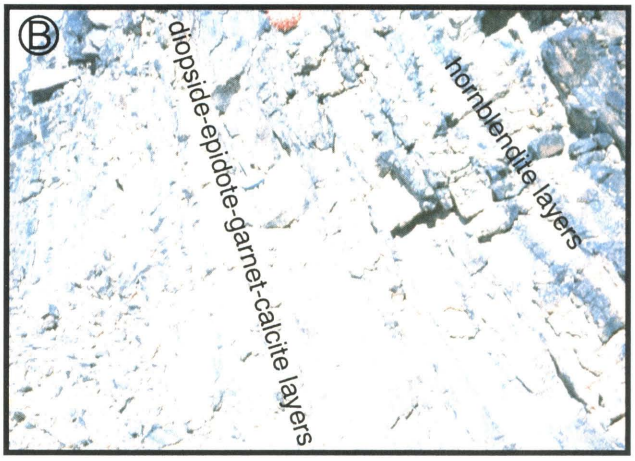

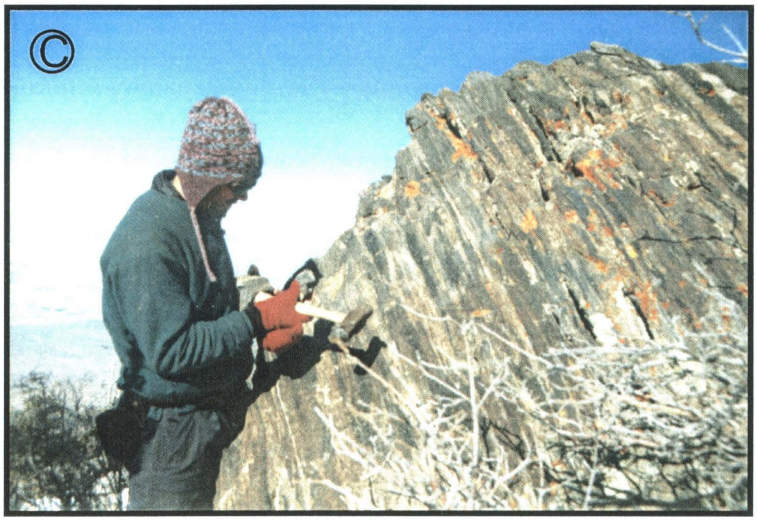

Figure 2-1:
(A) Interlayered marble, ultramafic, and chert domains forming a "tectonic melange" at the contact between grandiorite gneiss and grt-sil-bt metasedimentary gneiss in the South Spur segment of the VMSZ. This northeast-trending belt also includes interlayered calc-silicate, ultramafic and hornblendite gneiss in the Black Ridge segment (B), and variably deformed pillow basalt and calc-silicate gneiss in the Mount Bangs segment (C).
Boudinaged, discontinuous belts of these "exotic litholiges", ranging in thickness from 100m to less than 1m, are interpreted as a tectonic melange, and may mark the location of a Paleoproterozoic suture or obducted accretionary wedge formed during accretion of island arcs to the Mojave crustal province. At the very least, these units represent a zone of dramatic crustal juxtaposition, as deep crustal ultramafic rocks are intimately interlayered with metasedimentary rocks originally deposited at the earth's surface. The gneiss at the southern end of Black Ridge consists of hornblendite layers, ultramafic fragments, and diopside-epidote-garnet-calcite layers of similar texture and composition to the marble layers observed at (A), and yields a U/Pb zircon age of 1700 Ma.

Intrusive rocks

Intrusive rocks comprise less than 30 percent of the exposed Paleoproterozoic lithologies within the NVM, and are divided into granodiorite gneiss (13%), monzogranite gneiss (8%), leucopegmatite dikes (5%), and gabbroic, amphibolitic, and dioritic dikes and xenoliths (3%; Plate 1). Granodiorite dikes and plutons are strongly foliated and occur as NE-elongated bodies up to two kilometers wide, consisting of medium- to coarse-grained, locally K-feldspar or quartz phyric compositions with dramatic compositional variability. The granodioritic composition grades into quartz monzonite, granitic, diorite and gabbro compositions, is commonly associated with "salt and pepper" amphibolite gneiss, and contains abundant screens and xenoliths of gabbro, diorite, pyroxenite, amphibolite, and hornblendite. Co-mingling textures with mafic rocks are abundant, where amphibolitic and gabbroic rocks are present both as crosscutting dikes and dismembered xenoliths. These associations suggest that the granodiorite may represent an intermediate part of a differentiated and mingled arc plutonic complex, similar to those seen in the Grand Canyon and elsewhere in the Southwest (e.g., Ilg et al., 1996).

Monzogranite gneiss commonly outcrops as bright-red colored plutons and dikes up to one kilometer wide, which grade from coarse-grained, biotite-hornblende bearing K-feldspar rich granite and syenogranite to quartz phyric and peraluminous leucogranite, quartz monzonite, and aplite. Microcline augen textures and/or strong lineations are developed locally, mylonitic foliations are abundant, and pseudotachlyte bands are locally seen. Granite bodies predominantly occur as northeast-striking dikes and sills that

intrude granodiorite and supracrustal gneisses, most commonly at lithologic contacts, and locally contain large panels of amphibolite and granodiorite gneiss.

Leucopegmatite dikes are generally northeast striking, commonly isoclinally folded, and internally massive to mylonitized, and crosscut all lithologies present in the NVM. Two phases appear to be present, a white, peraluminous phase and a pink phase, however, crosscutting relationships between the two are not observed.

4. Structural geology and metamorphism

Regional Structural Geology and Metamorphism

Although this is the first structural and metamorphic study of the North Virgin Mountains, detailed structural studies of the region include the Granite Gorges of the Grand Canyon (Ilg et al., 1996; Karlstrom et al., in press) and the Cerbat Mountains (Duebendorfer et al., 2001). In these regions, S_1 fabrics are shallowly dipping and interpreted to have formed during bedding sub-parallel thrusting and tectonic burial to depths of 20-25 km (Duebendorfer et al., 2001). Strongly developed regional S_2 fabrics are subvertical, strongly reorient and overprint S_1, and strike to the northeast. Regional lower-temperature S_3 fabrics commonly reactivate the northeast-trending S_2 foliations, and are often associated with the circa 1400 Ma pluton-enhanced deformation event. Present foliation patterns in the NVM are dominated by northeast-striking subvertical fabrics that have overprinted earlier north-striking and northwest-striking fabrics, a

pattern similar to the regional fabrics described from nearby locations in the Grand Canyon and Arizona Transition Zone.

Metamorphic studies and GASP barometry from the Grand Canyon (Karlstrom and Williams, in press; Ilg et al., 1996, Williams unpublished data) and Cerbat Mountains (Duebendorfer et al., 2001) suggest clockwise looping P-T paths, with peak temperatures determined from metamorphic assemblages reaching above 700°C, and peak pressures of 5-6 kilobars. Karlstrom and Williams (in press) suggest that peak temperatures were attained during D_2, facilitated by voluminous plutonism and synchronous with NW-SE contraction. Dubendorfer et al. (2001) suggest that peak metamorphic conditions were attained during D_1 NE-SW contraction, and that nearly isothermal decompression occurred during D_2. GASP thermobarometry from the Gold Butte Block indicates pressures of 5-6 kilobars and ~ 3 kbar (Fryxell et al., 1992), interpreted to record different depths in the tilted Miocene Gold Butte block. Karlstrom et al., (in prep) suspect that they trap different parts of the looping Proterozoic P-T path instead.

At least four generations of structures and fabrics are present in the NVM, distinguishable by overprinting, fabric style and associated microstructures, relationships with intrusive rocks, and textural relationships with metamorphic minerals and porphyroblasts. Correlating fabric generations from place to place in order to evaluate the far-field stresses that generated the fabric is difficult for several reasons: 1) Polyphase deformation resulted in foliation reactivation often without strong development of a new fabric; 2) Significant deformation partitioning took place between weak versus strong lithologies such that strain heterogeneity can reflect either/both temporal and spatial partitioning; 3) Miocene extension may have locally reoriented Proterozoic fabrics

through tilting, folding, and faulting. The first topic is addressed through interpreting microstructural and metamorphic textures; in most Proterozoic rocks within the VMA, lower-temperature fabrics reactivate or overprint higher-temperature fabrics, and varying degrees of retrogression are present. Shear sense and fabric orientations were therefore correlated with the metamorphic and/or microstructural grade of the fabric to establish its timing relationship within the evolution from higher to lower temperature deformation in the region. The second topic is addressed by integrating structural analysis with U/Pb monazite dating, in an attempt to quantify timing of deformation. The final topic was found not to be a large concern; analysis of the Miocene deformation (Quigley et al., in prep) suggests that Proterozoic core of the VMA, at a regional scale, remained a relatively intact (autochtonous) block during Phanerozoic tectonism. Brittle deformation in the basement was localized along high-angle faults, and Phanerozoic brittle-folding, tilting, and reorientation of Proterozoic foliations, while locally present, did not reorient Proterozoic fabrics substantially.

Characterization of Structural Domains

We have divided the basement outcrops into three different structural domains (Figure 2-2, Figure 2-3), distinct from one another in the style and metamorphic grade of structures preserved and the intensity of D_1 through D_4 fabrics. The domains are: 1) south of the VMSZ (Domain I), where D_1/D_2 features are preserved; 2) north of the VMSZ (Domain II), where D_2 structures are similar to Domain I, and 3) and the VMSZ itself, where northeast-striking D_3 (high temperature) and D_4 (lower temperature) shear zones

Figure 2-2: Foliation trajectory and kinematic analysis map of the North Virgin Mountains, including structural domains and their boundaries. Kinematics associated with strongly partitioned D3 and D4 deformation within the Virgin Mountain shear zone (Domain III) shown in red: U=up, D=down, arrows = strike-slip movement. See text for details of structural domains.

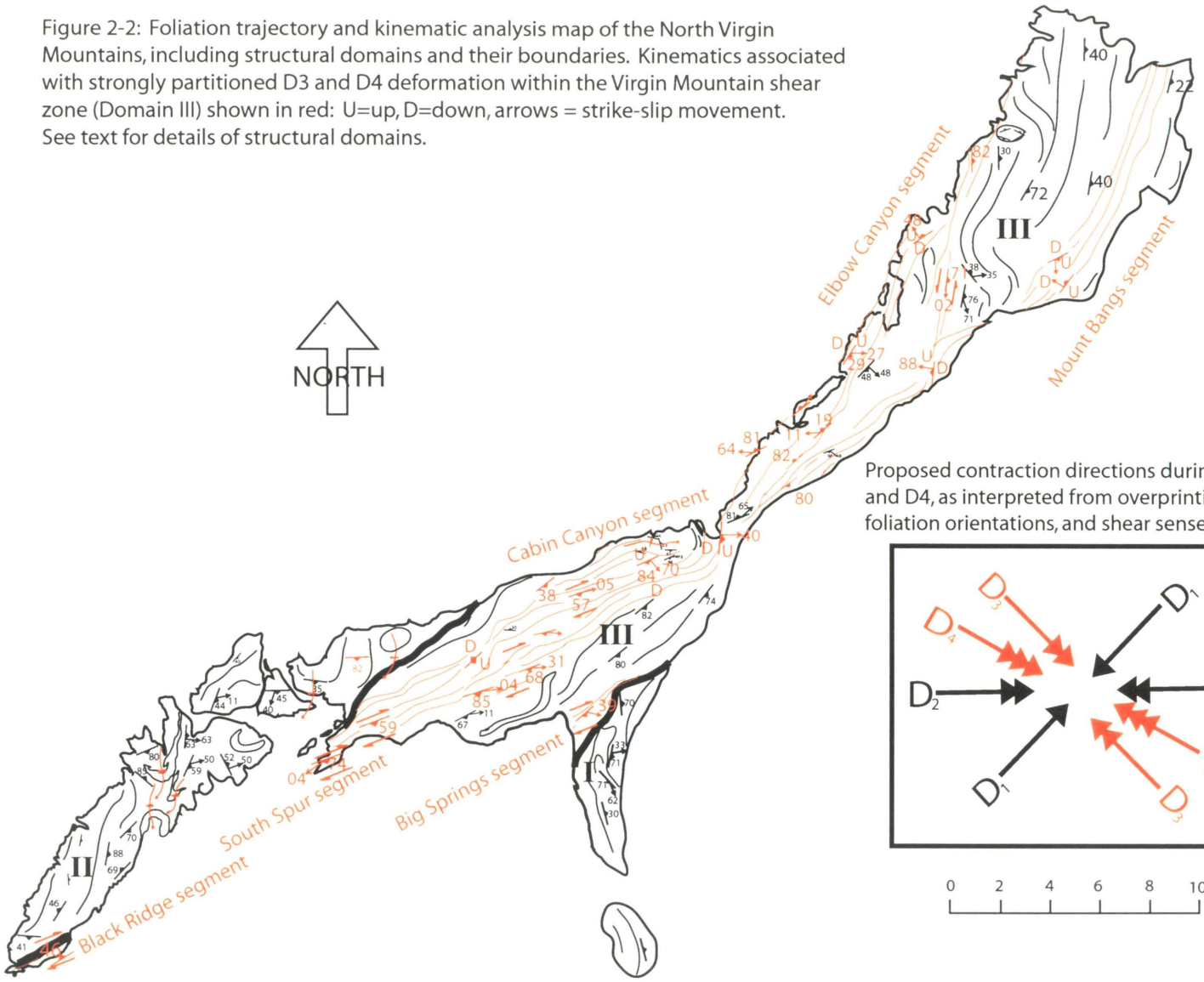

Proposed contraction directions during D1, D2, D3, and D4, as interpreted from overprinting relationships, foliation orientations, and shear sense indicators

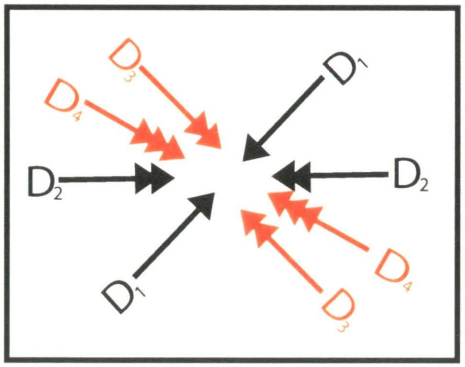

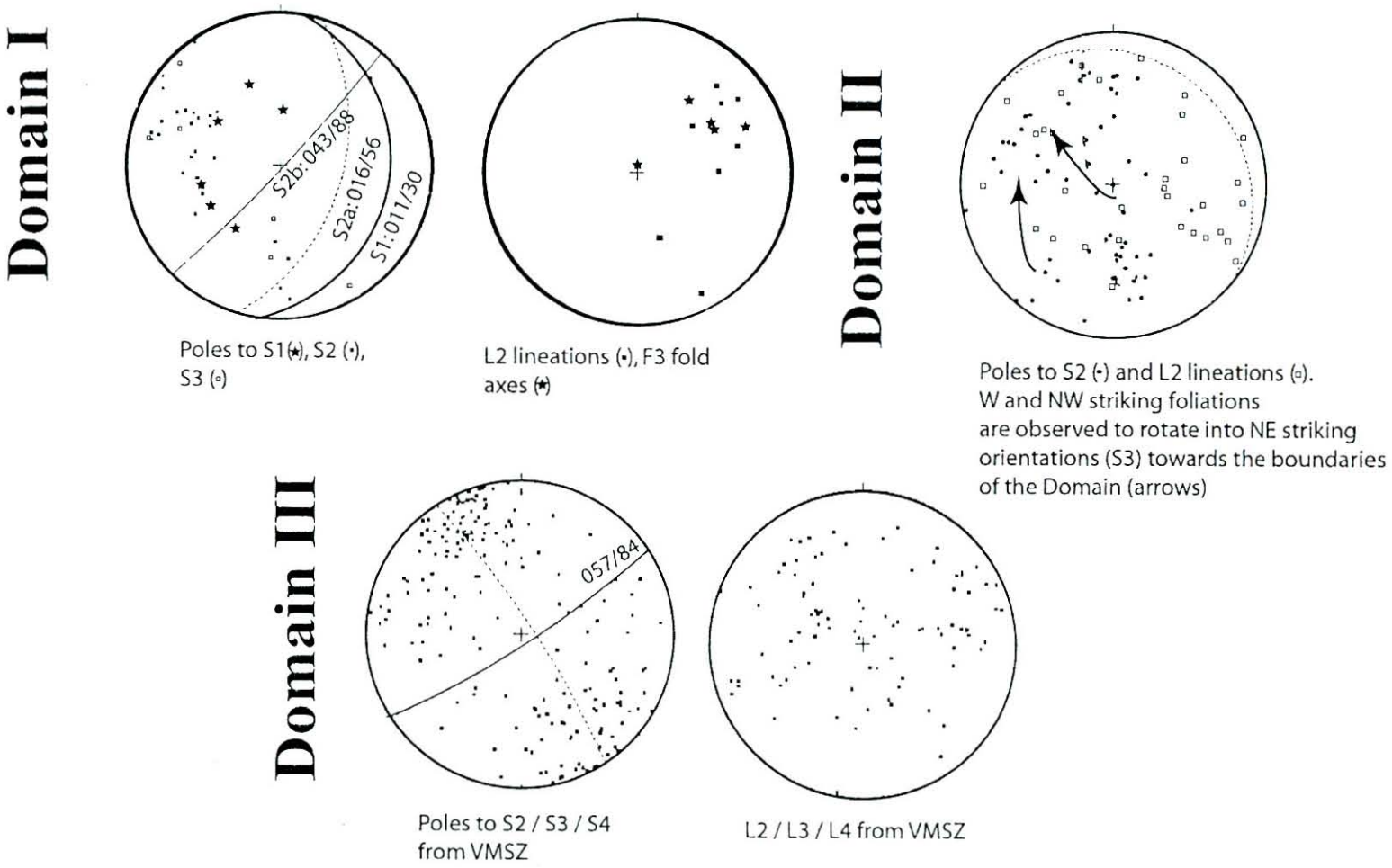

Figure 2-3: Equal area projection stereonets of poles-to-foliations, lineations, and fold axes from the North VIrgin Mountains. Structural domains as classified in text, see Figure 2-2. See text for details

dominate the structure of the VMA and helped control all subsequent deformations (Domain III). As an overview, deformational events produced: S_1 = low-angle foliation preserved only locally; S_2 = north-striking subvertical fabric (early syn-plutonic); S_3 = northeast-striking high temperature (syn-plutonic) subvertical fabric; S_4 = northeast-striking lower temperature mylonitic fabric.

Structural domain I: Deformation south of the VMSZ

The Big Springs area, roughly four kilometers south of the VMSZ domain boundary, preserves excellent overprinting relationships between S_1, S_2, and S_3 fabrics within a package of pelitic and semi-pelitic schists. D_3 and D_4 strains are significantly lower in this domain than those within the VMSZ, making it possible to discern the early fabric generations. S_1 is preserved as shallowly-dipping micaceous foliations in outcrop, and evident as biotite-muscovite trails in porphyroblasts and low D_2 strain areas in thin section, often at a high angle to the S_2 matrix foliation (Figure 2-4). Matrix foliation (S_2) is characterized by compositional layering (cryptic S_0) and gneissic foliation, with layer-parallel leucocratic domains (Figure 2-4). The compositional layering is interpreted as both bedding (S_0) and S_2 (a composite fabric), as it parallels lithologic contacts between pelitic and semi-pelitic schists, and is internally defined by a strong foliation characteristic of S_2. Measured S_1 foliations dip moderately to the east (Figure 2-3A, starred) and are folded about the same northeast-striking F_3 axis as the more steeply dipping S_2 foliations (Figure 2-3A, closed boxes). F_2 folds are generally subvertical and isoclinal, and have a strong axial planar cleavage (S_2, Figure 2-5). While the original

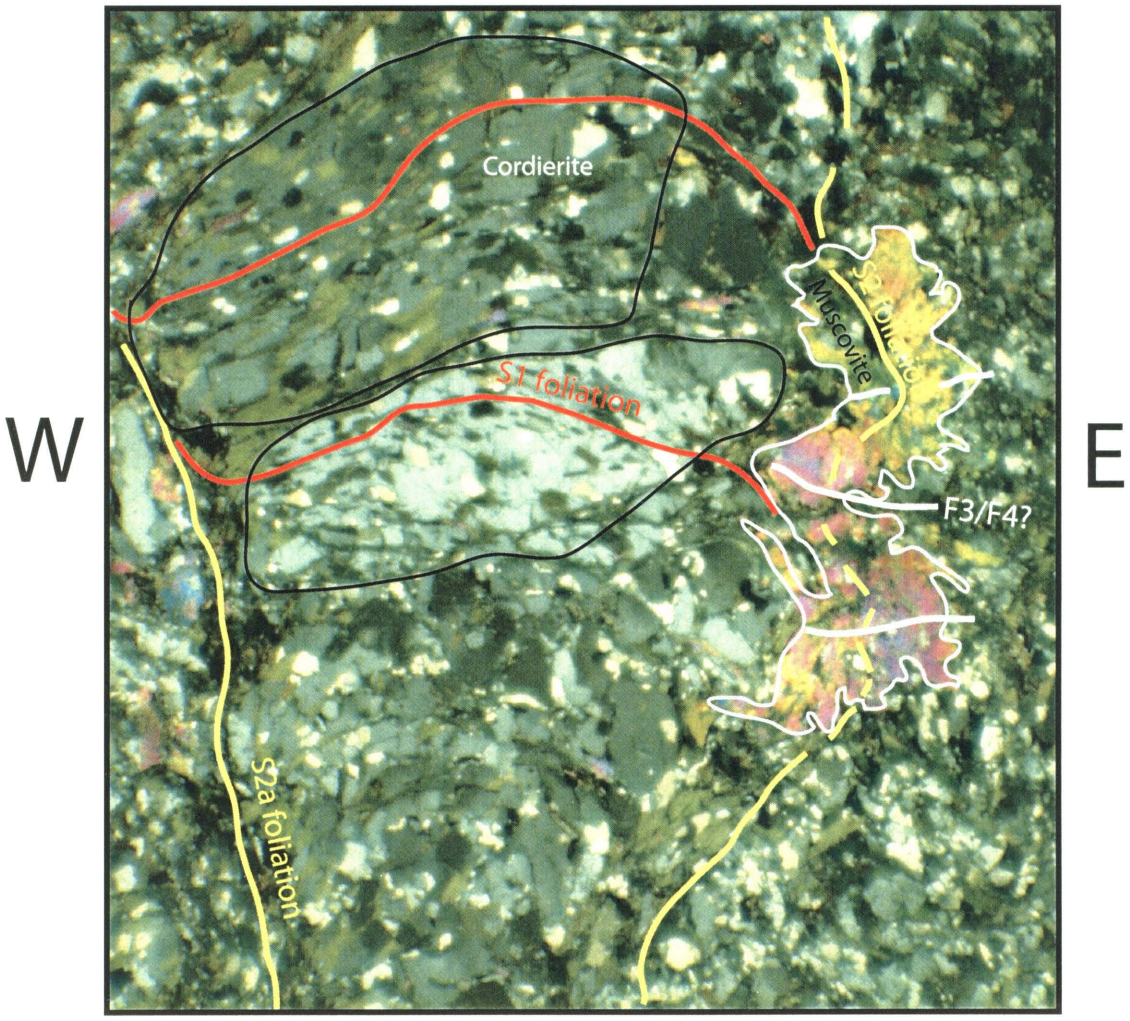

Figure 2-4: Orthogonal S1 (red) and S2 foliations (yellow) in the Big Spring area (Domain I). S1 foliation is defined by aligned biotite and elongate quartz crystals within corderite porphyroblasts; it undulates throughout the Big Springs area, dipping moderately at high angles to the compositional layering / S2 composite fabric. The high angle or orthogonal relationship between bedding contacts and S1 in the schists suggests that the S1 in this area formed in the hinge region of large-scale D1 nappe folds (see text). S2 formed parallel to compositional layering, and strongly folded and reoriented S1into a N-S, subvertical orientation outside of porphyroblasts. Early development of S2a was accompanied by cordierite growth, as gentle folds of the S1 fabric are overgrown by these porphyroblasts, and coarse muscovites which overgrow sillimanite in the schists (see Figure 2-5, text) and commonly parallel S2a. S2 is intensely developed in Domain I. Finally, low temperature deformation, as determined from quartz microstructures, metamorphic textures and assemblages, commonly reactivates the S2 foliation resulting in shear bands and folding and kinking of muscovite (see figure). Timing of this deformation is unconstrained, but transitional Regime 1-Regime 2 quartz microstructures (Hirth and Tullis) and undulatory extinction in feldspars and muscovites suggest upper greenschist facies deformational conditions, suggesting late syn-D3, or D4 development. Figure 2.5 cm wide.

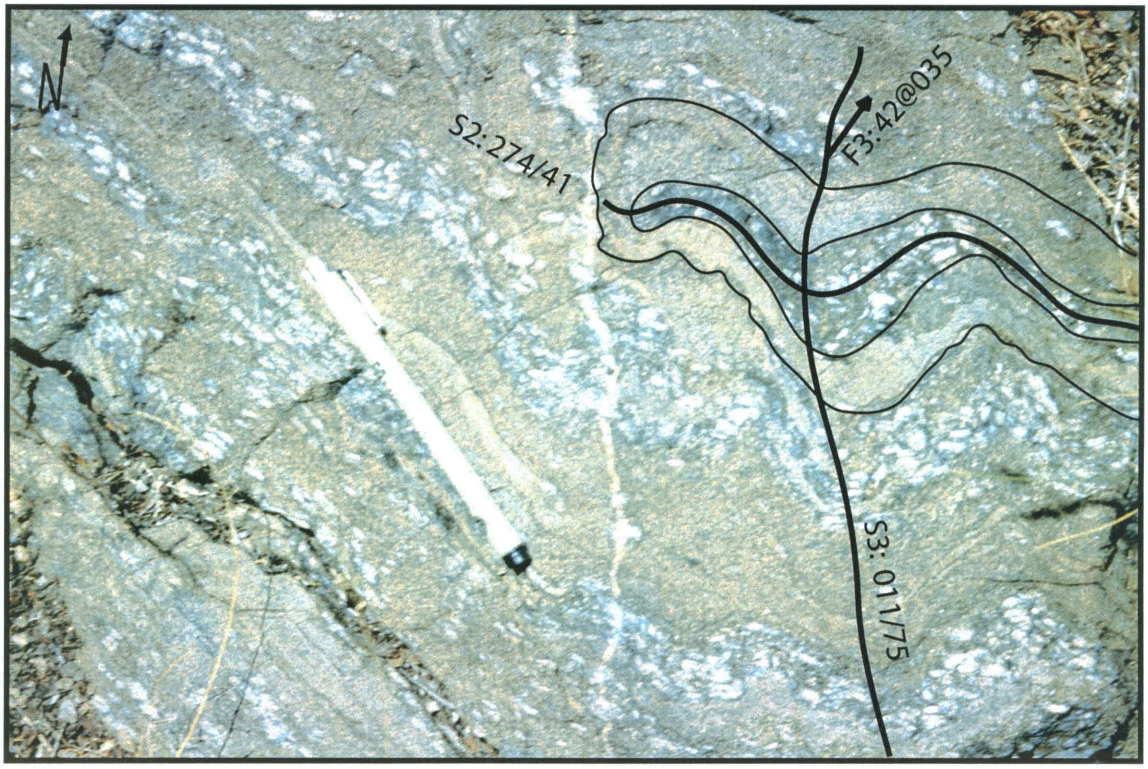

Figure 2-5: F2 isoclinal folds in semi-pelitic "pod-rock" sillimanite schist refolded by F3 closed folds, Big Springs Canyon (Domain I). Orthogonal relationships between S2 and S3 are developed only in the NE-trending hinge regions of F3 folds. Elsewhere, S2 is progressively reactivated and reoriented from a dominant NS orientation into the NE-trend charactertistic of the VMSZ (Domain II). Where parallel, F2 and F3 folds are distinguishable in that the former have axial planes locally defined by alignment of quartz-muscovite-sillimanite "pods", while the latter fold and deform these pods. NE-trending F3 folds formed in Domain I as a far-field response to NW-SE D3 contraction and NW-side-up thrusting in the VMSZ (Domain II). Leucopegmatite dikes and veins ranging from 10 meters to 5 millimeters in width parallel S3 throughout all domains, visible here as the thin pegmatite vein parallel to S3 and orthogonal to S2.

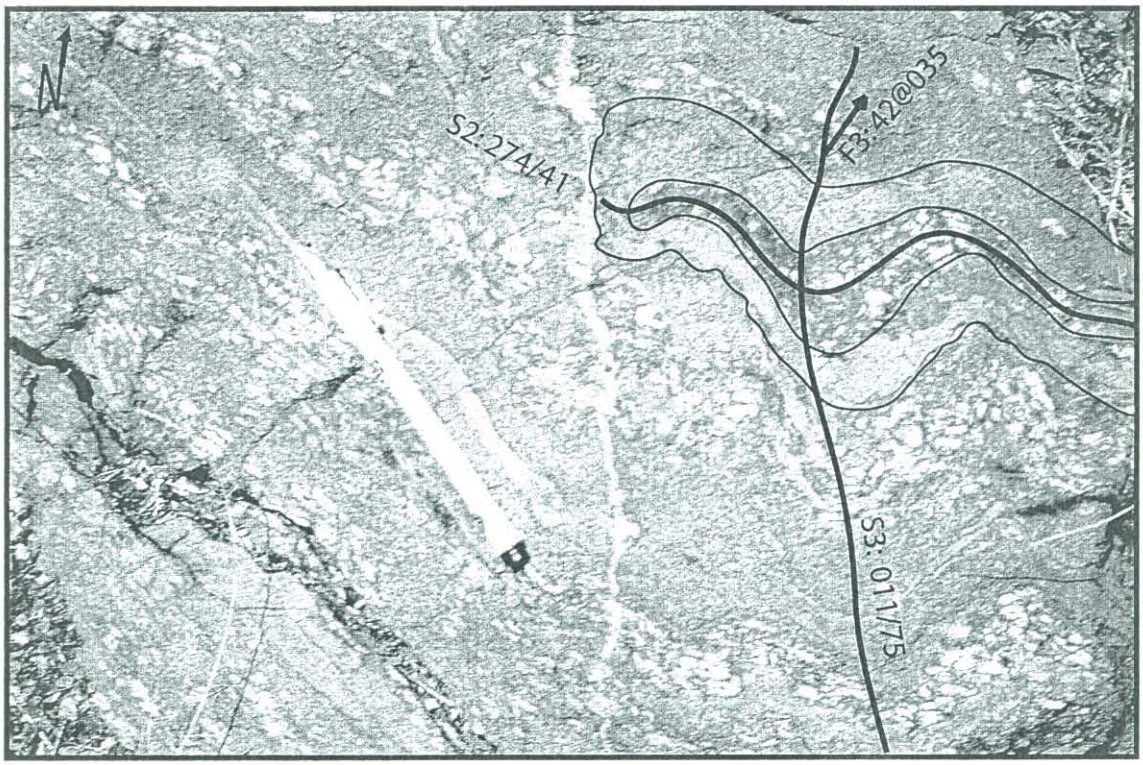

Figure 2-5: F2 isoclinal folds in semi-pelitic "pod-rock" sillimanite schist refolded by F3 closed folds, Big Springs Canyon (Domain I). Orthogonal relationships between S2 and S3 are developed only in the NE-trending hinge regions of F3 folds. Elsewhere, S2 is progressively reactivated and reoriented from a dominant NS orientation into the NE-trend charactertistic of the VMSZ (Domain II). Where parallel, F2 and F3 folds are distinguishable in that the former have axial planes locally defined by alignment of quartz-muscovite-sillimanite "pods", while the latter fold and deform these pods. NE-trending F3 folds formed in Domain I as a far-field response to NW-SE D3 contraction and NW-side-up thrusting in the VMSZ (Domain II). Leucopegmatite dikes and veins ranging from 10 meters to 5 millimeters in width parallel S3 throughout all domains, visible here as the thin pegmatite vein parallel to S3 and orthogonal to S2.

orientation of S_1 is unknown in the VMA, studies elsewhere in the region have documented WNW-strikes and shallow dips to the north and south in low strain zones within the region (Albin and Karlstrom, 1991; Duebendorfer et al., 2001; and others). Generation of the S_1 fabric is attributed to bedding sub-parallel, SW-vergent thrusting and nappe development in the Cerbat Mountains to the south (Duebendorfer et al., 2001). In the Big Springs area, where S_1 is orthogonal to compositional layering, it is interpreted as the axial planar fabric formed within the hinge region of an S_1 nappe, which is consequently refolded during E-W D_2 contraction. This is compatible with models for complex crustal assembly along NW-trending, possibly arcuate subduction systems proposed by Jessup et al. (in prep).

The N-S-striking S_2 has an average orientation of 016/56° and is folded and transposed into NE and ENE orientations (S_3) to the west and north (Figure 2-2, 2-3). Development of strong ENE-plunging lineations (L_3, Figure 2-3A) is interpreted to be due to progressive F_3 folding of S_2 into large antiforms and synforms. The hinge regions of map-scale S_3 folds preserve orthogonal relationships between F_2 isoclines and tight F_3 folds, with an average orientation 043/88° (Figure 2-5). More commonly, S_2 and S_3 are superposed and associated with boudinaged and variably folded leucopegmatites and melt-filled tension gashes, suggesting that emplacement of leucopegmatites was synchronous with late-D_2, early- D_3 deformation, a relationship observed throughout the VMA. Where parallel, F_2 are distinguished from F_3 in that the former have axial planes defined by leucocratic "pods", and the latter fold these pods (Figure 2-5). Thus, we interpret D_2 and D_3 to be part of a progressive deformation involving a clockwise rotating contractional strain field from E-W to NW-SE (Figure 2-2, inset).

NE-striking foliations in Domain I have locally been reactivated at lower temperature by dextral-reverse D_4 mylonitic shear zones. It is unclear whether the steeply-plunging lineation recorded within the Big Springs segment of the VMSZ records the D_4 movement direction or is associated with D_3. This segment marks the southern boundary of the VMSZ, and S_1 through S_4 fabrics are completely transposed. Evidence for lower-temperature deformation is also present outside of the Big Springs segment, as determined from microstructural analysis (i.e., "kinked" micas, Figure 2-4).

Domain I: Metamorphism and microstructures

The pelitic schists and gneisses in Domain I contain the best record of the first metamorphic event and associated tectonic fabric, due to their relatively "sheltered" structural-thermal position away from D_3 high-strain zones and intrusions, which essentially obliterate any evidence of M_1 to the north. Pelitic rocks contain the mineral assemblage K-feldspar + biotite + muscovite + fibrolitic sillimanite + plagioclase + quartz + cordierite + garnet + tourmaline, indicating metamorphism to upper-amphibolite facies. Textural relations suggest that the M_1 mineral assemblage is composed of fibrolitic sillimanite + K-feldspar + muscovite + quartz + biotite, because these minerals define the S_1 foliation as inclusion trails in D_2 porphyroblasts (Figure 2-4). Fibrolite-biotite intergrowths are common and strongly folded, and muscovite and biotite are fine-grained. The M_2 mineral assemblage is composed of cordierite + muscovite + quartz + biotite + K-feldspar + tourmaline ± garnet. Cordierite porphyroblasts overgrow M_1 mineral assemblages and preserve the orthogonal relationships between S_1 and S_2 at this

location (Figure 2-4). The prograde reaction: biotite + sillimanite + quartz → cordierite + K-feldspar + H_2O (Deer et al., 1992) appears to have been the cordierite-forming reaction. Muscovite is coarse-grained and texturally diagnostic from M_1 muscovites in that it contains folded fibrolite and biotite inclusion trails and wormy (symplectitic) intergrowths of quartz (Figure 2-6). These coarse muscovites are interpreted to have grown late-syn D_2 and early D_3 as they are partially aligned in the S_2 foliation but locally overgrow folded S_1 and S_2 (Fig 2-6). In other sections, coarse muscovites are axial planar to NE-trending F_3 folds of S_2, suggesting synchronous growth with rotation of the N-trending S_2 into the NE-trending orientation of S_3. The reverse second-sillimanite isograd retrograde reaction (H_2O + sil + kspar → musc + qtz) appears to have been important in this region during late D_2 early D_3, as these large muscovites are intergrown with quartz and commonly overgrow the sillimanite-biotite fabrics. K-feldspar is present in very small amounts in isolated domains of these rocks, suggesting that it may have been the limiting reactant during the aforementioned reaction.

Lower temperature microstructures, including kinking of the coarse muscovite and development of undulatory extinction within quartz grains, suggest that some deformation oblique to S_2 occurred below amphibolite facies conditions characteristic of M_2 / M_3 (Figure 2-6). This is confirmed by localized retrogression of biotite rims to chlorite, a reaction determined elsewhere to be synchronous with M_3 and lower-temperature deformation within the VMSZ.

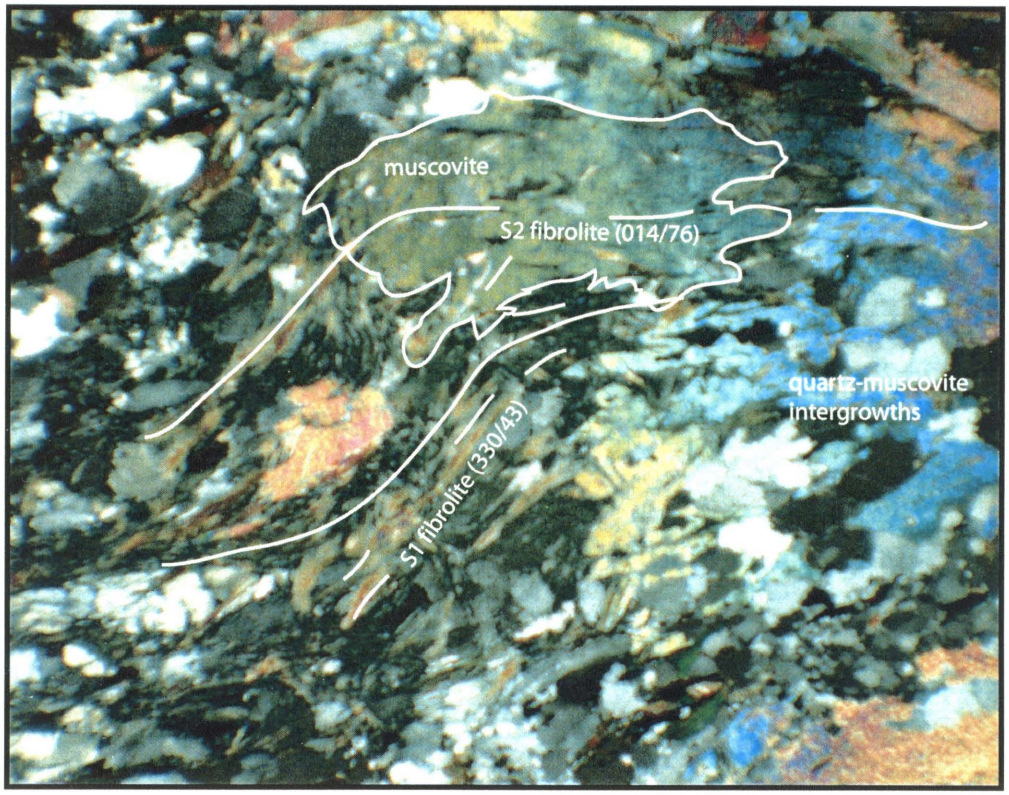

Figure 2-6: Textural evidence constraining metamorphic conditions of S1 and S2 foliation development. Fibrolite grew during S1 and was reoriented and overgrown by muscovite during development of S2. Absence of coexisting K-feldspar and muscovite, and wormy quartz-muscovite intergrowth textures suggest that this structural transition occurred as the second-sillimanite isograd was crossed during retrograde metamorphism, invoking the reaction fibrolite + K-feldspar + water --> muscovite + quartz. Figure 1.5 cm wide

Structural domain II: Deformation north of the VMSZ

The Black Ridge and Government Springs areas, which compose the structural domain north and west of the VMSZ, are similar to the Big Springs area in that they are characterized by S_2 fabrics that are variably folded and reoriented into S_3 orientations. S_1 is not observed here due to intensity of S_2. Unlike Domain I, the intensity of D_3 deformation in this domain has significantly reoriented the N-S S_2 into ENE-WSW to NES_3 orientation (Figure 2-3B). We interpret the stereonet (Figure 2-3B) to describe this progressive rotation of moderately dipping, N to NW striking S_2's into NE- and E-striking orientations. We interpret the lineation data, although complex, to represent the similar clockwise rotation of NW-plunging L_2's into NE- and E- plunging L_3 orientations (Figure 2-3B). The plunge of L_3's is broadly consistent with L_3 and F_3 fold axes plunges mapped in Domain I (Figure 2-3).

Complex folding is revealed in NE Black Ridge, where steeply-dipping foliations and lithologic contacts are folded about N to NNW-trending axial traces (Figure 2-3). The planar outcrop pattern is suggestive of a Ramsay-type 2 superposed fold interference pattern, where a gently inclined axial plane is refolded by a highly oblique fold with a steep axial plane, yielding a "mushroom" outcrop pattern (Ramsay and Huber, 1987). In the axial planar region, despite poor development of an axial planar foliation, fold axes are intensely developed and associated pencil structures in metasedimentary schists yield length:width aspect ratios up to 60:1. These folds are in turn refolded into NE-trending orientations towards higher strain domains, where they are associated with lower-amphibolite facies axial planar fabrics (see *Metamorphism and microstructures*). The

general map pattern of these folds is suggested as representing the progressive refolding of an initially shallow-dipping F_1 nappe fold during rotating E-W (D_2) to NW-SE contraction (D_3). Significant ENE-WSW shortening synchronous with dextral transpressive slip along the VMSZ may have tightened this fold during D_3, and dextrally drag-folded the axial plane into the NE-orientation present (Figure 2-2, see Plate 1). Although we believe this to be the best interpretation, other possibilities exist given the complex deformation history of this region.

In close proximity to the boundary with the VMSZ domain, NW-side-up shear bands and drag folds are present orthogonal to S_3 planes and parallel to lineations. These structures formed during D_3 NW-side-up, NE-SW contraction along the VMSZ, and progressive rotation and transposition of S_2 by S_3.

A NE-striking D_4 dextral strike-slip shear zone is present within monzogranite gneiss in the Government Spring area. In the far southwest corner of the NVM, the Black Ridge segment of the VMSZ marks the SW boundary of Domain II (Figure 2-2). The Hen Spring fault, a Miocene left-lateral fault of unknown separation, marks the E boundary see Figure 3-2).

Domain II: Metamorphism and microstructures

Pelitic rocks within Domain II contain the assemblage garnet + biotite + sillimanite + K-feldspar + plagioclase + quartz. Notably, the muscovite and cordierite abundant in the rocks south of the VMSZ are either absent or present in very low amounts, suggesting that metamorphic conditions within these pelites were not favorable

to cordierite or muscovite growth. These pelitic gneisses are commonly migmatitic where in close proximity to monzogranite bodies, and are cut by numerous granitic and pegmatitic dikes. While these injection migmitites are common, evidence of anatectic migmitization (leucosome / melanosome pairs) is also present. Sillimanite is abundant as fine-grained fibrolitic mats intergrown with biotite, and large (up to 4mm) euhedral crystals. Locally, coarse sillimanite crystals are orthogonal to S_3/S_4, suggesting that the sillimanite probably grew during M_2 peak metamorphism but may have continued growing during early M_3. Coarse sillimanites are folded and mechanically reoriented parallel to S_3, and smaller sillimanite needles are isoclinally folded within this fabric, interpreted to represent sillimanite deformation within its stability field. Recalling that M_3 in Domain I was marked by a retrograde transition from the sillimanite + K-feldspar + H_2O field to the muscovite + quartz field (the reverse *second sillimanite isograd*), and assuming that Domain I and Domain II pelitic schists have similar bulk compositions, the distinction between Domain I D_3 structures, which developed during sillimanite *instability*, and Domain II D_3 structures, which developed during sillimanite *stability* and localized sillimanite growth, is an important one. Coupled with the observation that Domain II pelites are commonly migmatized and Domain I pelites are not, we suggest that Domain II represents hotter (and probably deeper) crust during D_3, and that NW-side-up thrusting within the VMSZ associated with D_3 bought these domains into juxtaposition at a similar crustal level. Furthermore, the abundance of pegmatites in Domain II relative to Domain I may have kept the local crustal temperature high during this deformation and prohibited retrograde metamorphism as Domain II rose to shallower crustal levels (see *Paleoproterozoic tectonic history...*).

The granodiorite gneiss north of the Domain III greenschist facies mylonites in Black Ridge (see below) is tightly folded and displays a strong axial planar fabric defined by a mylonitic foliation (Fig. 2-7). Garnets within this rock, which contain lobate, high-temperature quartz intergrowths, appear to have been stable under mylonitic deformation conditions, as no signs of alteration are present. Quartz deformed under Regime 2 climb-accommodated dislocation creep deformation conditions, forming core and mantle structures (Hirth and Tullis, 1992), whereas feldspars deformed under Regime 1 recrystallization-accommodated dislocation creep deformation conditions (Hirth and Tullis, 1992). These metamorphic and microstructural observations suggest that folding and development of the "higher temperature" mylonitic fabric (which is characteristic of the late D_3 event) occurred between ~500 and 650°C. This represents continuing deformation during crustal evolution to shallower depths.

Structural domain III: Introduction to transpressional modeling

In order to properly describe deformation within the VMSZ, we must first review the concept of transpression. Transpression, as defined by Harland (1971), refers to the synchronous transcurrent and shortening deformation caused by oblique convergence across a high strain zone (shear zone). Sanderson and Marchini (1984) were the first to describe the kinematics of such a deformation by considering constant-volume homogeneous deformation in a vertical shear zone that was laterally confined with a fixed basal surface but free top surface. This avoids the lateral "space problem" by disallowing horizontal extrusion while allowing for frictionless vertical extrusion during

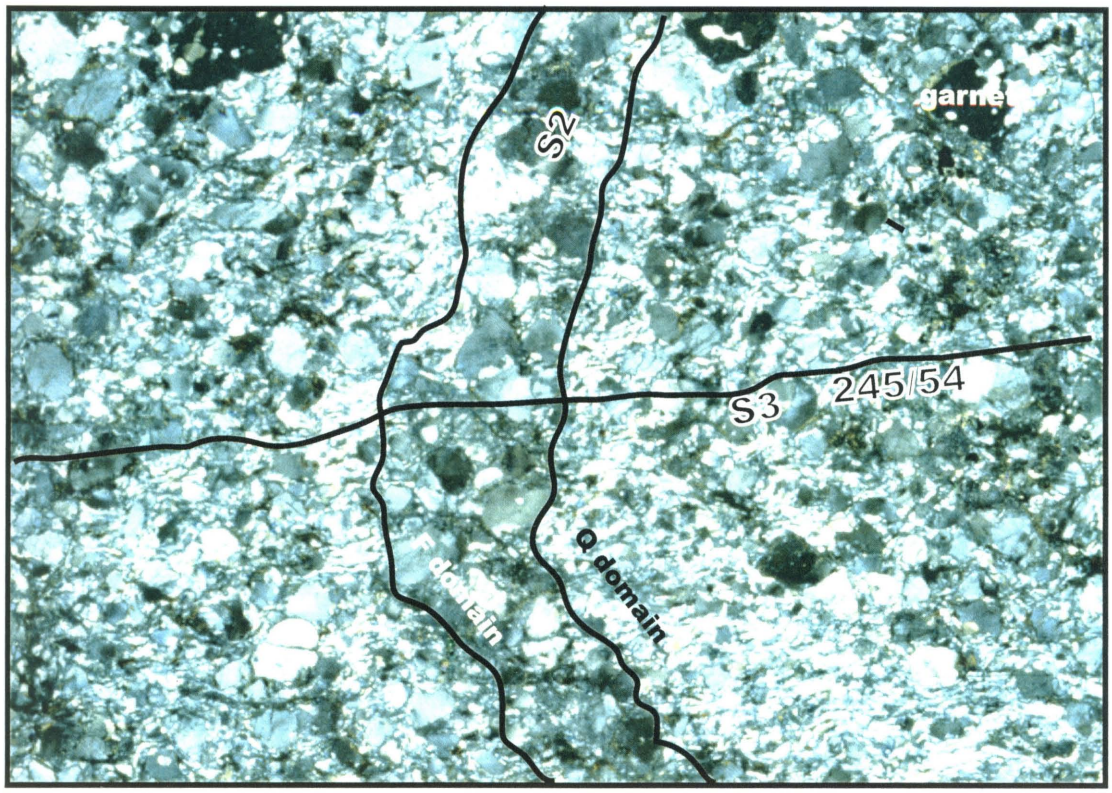

Figure 2-7: Folding of S2 and development of S3 axial planar mylonitic foliation within granodiorite gneiss, north of the Black Ridge segment, Domain II. Originally north-south striking S2a is characterized by the strong foliation and compositional layering, which formed during upper amphibolite facies metamorphism and deformation (D2). Q domains are quartz dominated, F domains are feldspar dominated. Garnets contain lobate, unstrained quartz inclusions, remnants of the high temperature garnet growth. The NE-striking S3 axial planar foliation formed synchronous with folding of S2, and is characterized by Regime 2 climb-accommodated dislocation creep microstructures in Q domains (core-mantle textures) and Regime 1 recrystallization-accommodated dislocation creep microstructures in F domains (coarse feldspars separated by fine-grained high strain domains). Together with unretrogressed garnet textures, and recognizing the caveats in the interpretation (strain rate, fluid availability), the temperature of D3 deformation is bracketed between 500 and 600 °C, consistent with the late D3 interpretations in Elbow Canyon.

deformation. Robin and Cruden (1994) questioned why vertically frictionless zones would be laterally confined, and created a model allowing no slip in any direction at the zone boundaries, resulting in a heterogeneous deformation across the zone ("confined" transpression). Their continuum mechanics approach to transpressional modeling yielded heterogeneous strain patterns despite the mechanical isotropy of the deformation zone, with vertical "bulging" in the center of the zone, and vorticity vectors (i.e., shear sense indicators) commonly non-parallel to any of the principal directions of instantaneous or finite strain. Foliation orientations are subvertical and more oblique to the zone boundaries in the center of the zone (larger simple-shear strain), and less steep but more parallel to the zone boundaries at the edge of the zone (larger pure-shear strain). Stretching lineations are steeper towards the center of the zone (increased vertical extrusion), and inclined towards the edges of the zone. These results suggest that, even in a mechanically isotropic material, transpressive strain is strongly heterogeneous, commonly triaxial, and dependent on the pure shear / simple shear strain ratio.

Jones and Tanner (1995) discussed how the presence of pre-existing lithological, rheological, and/or structural weaknesses partition transpressional strain in a deformation zone. They confirmed that complex structural styles can occur in deformational models that have well defined and relatively uncomplicated boundary conditions if these anisotropies exist. Simple-shear deformation zones may act concurrently with pure-shear zones to accommodate overall transpressional deformation. Jones and Tanner (1995) interpreted this as evidence that fault systems can result from localized stress orientations and mechanical anisotropy, and need not reflect regional stress regimes. Jones et al. (1997) allowed for unconfined boundary slip in their model, refining the Sanderson and

Marchini (1984) model to permit vertical slip at the basal surface and "lateral extrusion" on the model edges (stretching in the horizontal direction causing the deformation zone to lengthen relative to the undeformed zone margins). Tikoff and Greene (1997) addressed the behavior of stretching lineations in transpressional zones using field examples and kinematic modeling of shear zones from the Sierra Nevada batholith. As noted previously, modeling of some transpressional deformations indicates that the long axis of the finite strain ellipsoid, and thus the finite stretching lineation, is vertical whereas the bulk deformation involves a significant component of strike-slip (Sanderson and Marchini, 1984; Robin and Cruden, 1994). This is increasingly recognized in nature, where asymmetric shear sense indicators are observed on faces orthogonal to the stretching lineation, and are not present on faces parallel to lineation (Robin and Cruden, 1994). Tikoff and Greene (1997) argued that wrench-dominated transpression (i.e., angle of convergence less than 20° from the shear plane) results in development of initially subhorizontal stretching lineations, and later development of vertical lineations during progressive deformation. The conclusion is that the orientation of the lineation in transpressional shear zones may not necessarily correlate with the transport direction, and may reflect strain partitioning, along-strike variations in finite strain, and/or the amount of finite strain recorded during different parts of a progressive deformation.

Bell (1981) and Hudleston (1999) presented the concept of shear zone linkage, and discussed how problems of strain compatibility (i.e., strain "space problems") may be resolved if individual shear zones are linked together in an appropriate fashion. This appears to be quite applicable to many ductile shear zones, where a variety of seemingly

distinct kinematic histories for different segments may be part of a complexly partitioned, linked shear zone array.

There are several reasons why we think the VMSZ has a transpressional history. The VMSZ clearly anastomoses along its strike length, consisting predominantly of northeast-striking segments linked by north-striking and east-striking curved segments. North-striking bends in the VMSZ (see Figure 2-2, Domain III, 1 kilometer east of the Cabin Canyon segment) contain reverse and normal sense kinematics depending on their structural positions and linkage with major northeast-striking strike-slip zones, and are interpreted to represent restraining and releasing bends, respectively. Within the northeast-striking zones, parallel pure shear-, simple shear-, and general shear–dominated shear zones with similar microstructural and metamorphic characteristics suggests complexly partitioned transpressional deformation. The challenge is to quantify observations that these shear zones were deforming synchronously.

Structural domain III: Deformation and shear sense within the VMSZ

The VMSZ domain is characterized by a NE-striking, subvertical $S_2/S_3/S_4$ composite foliation (Figure 2-3C) that follows the axis of the VMA, from the SW edge of Black Ridge to the NE corner of the Mount Bangs area (Figure 2-2). Isoclinal folds with steep axial planes plunge moderately to the NE and SW, and lineations are variable between down-dip and strike-slip orientations (Figure 2-3C). Similar to Domains I and II, structural data is explained by progressive rotation of the NS-trending S_2 into a steep NE-trending orientation (S_3), synchronous with NW-side-up transpressional thrusting and

NW-SE contraction (D_3). Evidence of the high-temperature conditions of D_3 thrusting includes melt-filled shear bands (Figure 2-8A) and syn-intrusion folding of leucopegmatites (Figure 2-8B). Later dextral-transpressional contraction (D_4) reactivated and steepened this structure, with interconnecting anastomosing shear zones permeating throughout this zone of weakness. The VMSZ correspondingly records evidence of later, lower-temperature deformation (S_4) superimposed on higher-temperature deformational fabrics (S_2, S_3, Figure 2-8). Evidence for the D_1 event is preserved only as cryptic inclusion trails within garnet porphyroclasts, with any evidence for S_1 in the matrix completely obliterated by $S_2 - S_4$. The reactivation of the S_2 foliation during progressive transpressional deformation from deep (D_3) to shallow (D_4) crustal levels resulted in the complex finite strain pattern mapped throughout this domain. Structures yielding consistent shear sense commonly display different microstructural and metamorphic "grades", suggesting that the kinematics within the VMSZ were evolved slowly during crustal cooling and probable shallowing of crustal levels. D_2 structures include isoclinal folds in migmatitic layers. D_3 structures include isoclinal to tight folds of leucopegmatite dikes, refolded isoclines, sheath folds, NW-side up shear bands (Figure 2-8A) and asymmetric melt pods (Figure 2-8B), steeply plunging lineations, and L-tectonite mylonites. D_4 structures include dextral strike-slip zones with spectacular structural asymmetry and strong lineations, oblate (flattening) domains with conjugate shear bands and weakly developed vertical stretching lineations, steeply lineated L>>S prolate (stretching) domains with poor asymmetry, and obliquely lineated reverse and normal sense tectonites with excellent asymmetry. Although D_4 strain is most intense along pre-

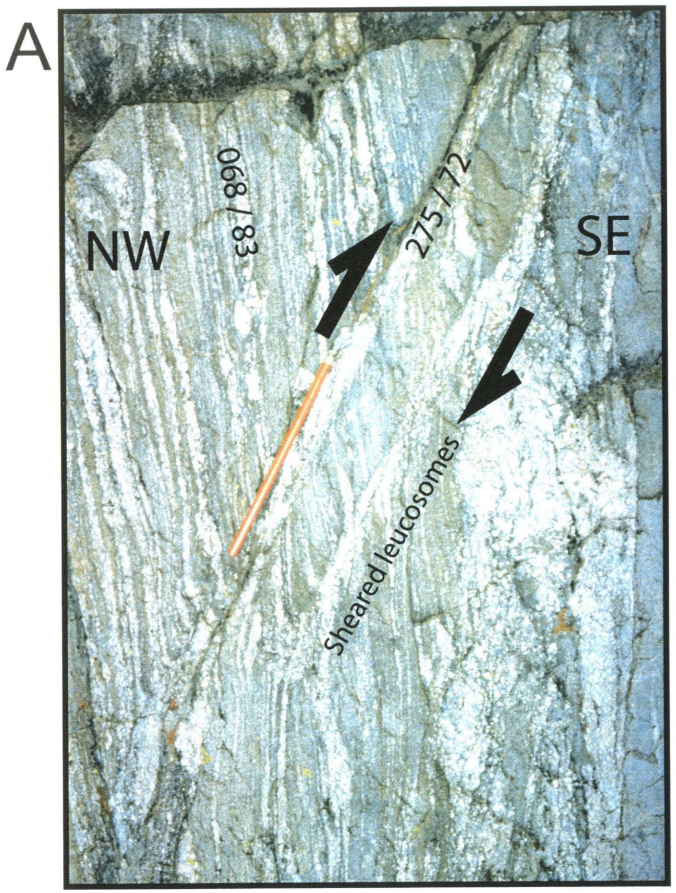

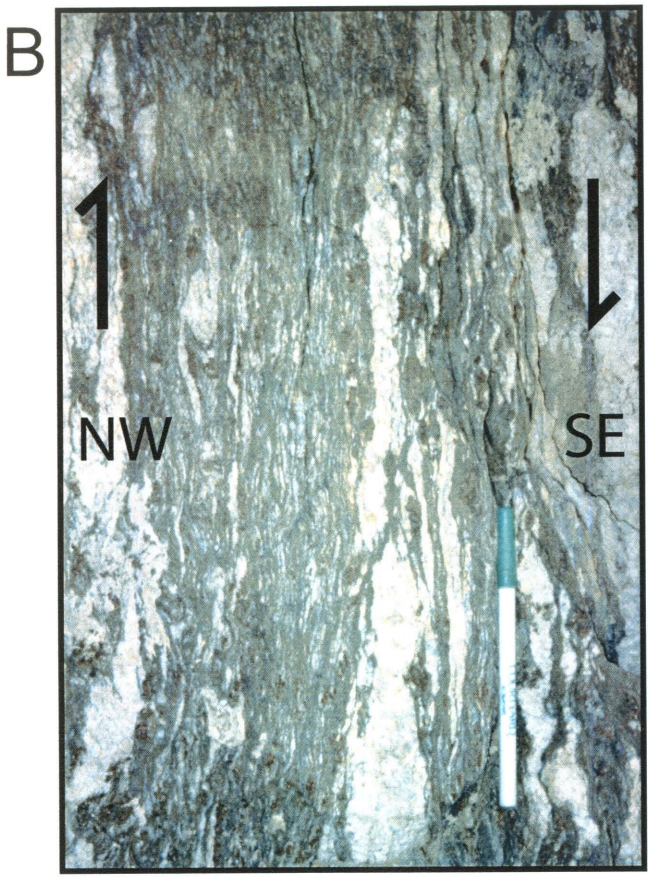

FIgure 2-8A: Melt-filled shear bands in granodiorite gneiss, north boundary of the Cabin Canyon segment, VMSZ. Drag-folded leucosomes bleed into shear bands and indicate NW-side-up shear sense, suggesting deformation was synchronous with intrusion of leucosomes, and under high temperature (upper amphibolite) conditions. Geologic relationships suggest that this deformation resulted in the reorientation of north-striking S2 into northeast-striking S3.

Figure 2-8B: NW-side-up drag folds of boudinaged pegmatites within subvertical, NE-striking, garnet-sillimanite paragneiss in the VMSZ. Bleeding of folded leucosomes into coarser pegmatites suggests syn-magmatic deformational conditions, confirmed by microstructural analysis. This deformation resulted in reorientation of the north-striking S2 fabric into the northeast-striking S3 orientation during NW-side-up transpressional contraction.

existing NE-trending lithologic and structural heterogeneities, 90 percent of the Proterozoic rocks within the VMSZ domain have been strongly overprinted by this event.

The VMSZ domain is subdivided into segments along its length, each of which was studied extensively and contains distinct structural patterns and differing degrees of fabric intensity and overprinting, as discussed below. Overall, the story presented here is that of E-W general shear involving shortening and dextral shear on the pre-existing NE trending high strain zone.

Cabin Canyon Segment

The Cabin Canyon segment (Figure 2-3, Figure 2-9) provides the best evidence for partitioned dextral-transpressive deformation in the VMSZ. Detailed mapping reveals strain patterns indicative of transpressional deformation; simple-shear dominated, dextral strike-slip domains with subhorizontal lineations are flanked by pure-shear dominated, weakly to non-lineated domains with flattened, prolate feldspar porphyroclasts and conjugate shear bands, and steeply plunging LS mylonites with reverse sense kinematics.

The narrow (~15m max) dextral strike-slip ultramylonite zones contain a variety of shear sense indicators on faces paralleling the lineation, including sigma and delta porphyroclasts (Figure 2-9, 2-10), antithetic bookshelf-type structures, asymmetric myrmekite fabrics in K-feldspars, C-S fabrics, and shear bands. The subhorizontal lineation developed in these zones thus appears to represent the movement direction.

Pure-shear domains contain mylonitic, conjugate shear planes at roughly 30° from the mylonitic foliation on vertical rock faces (inset to Figure 2-9). Foliation planes

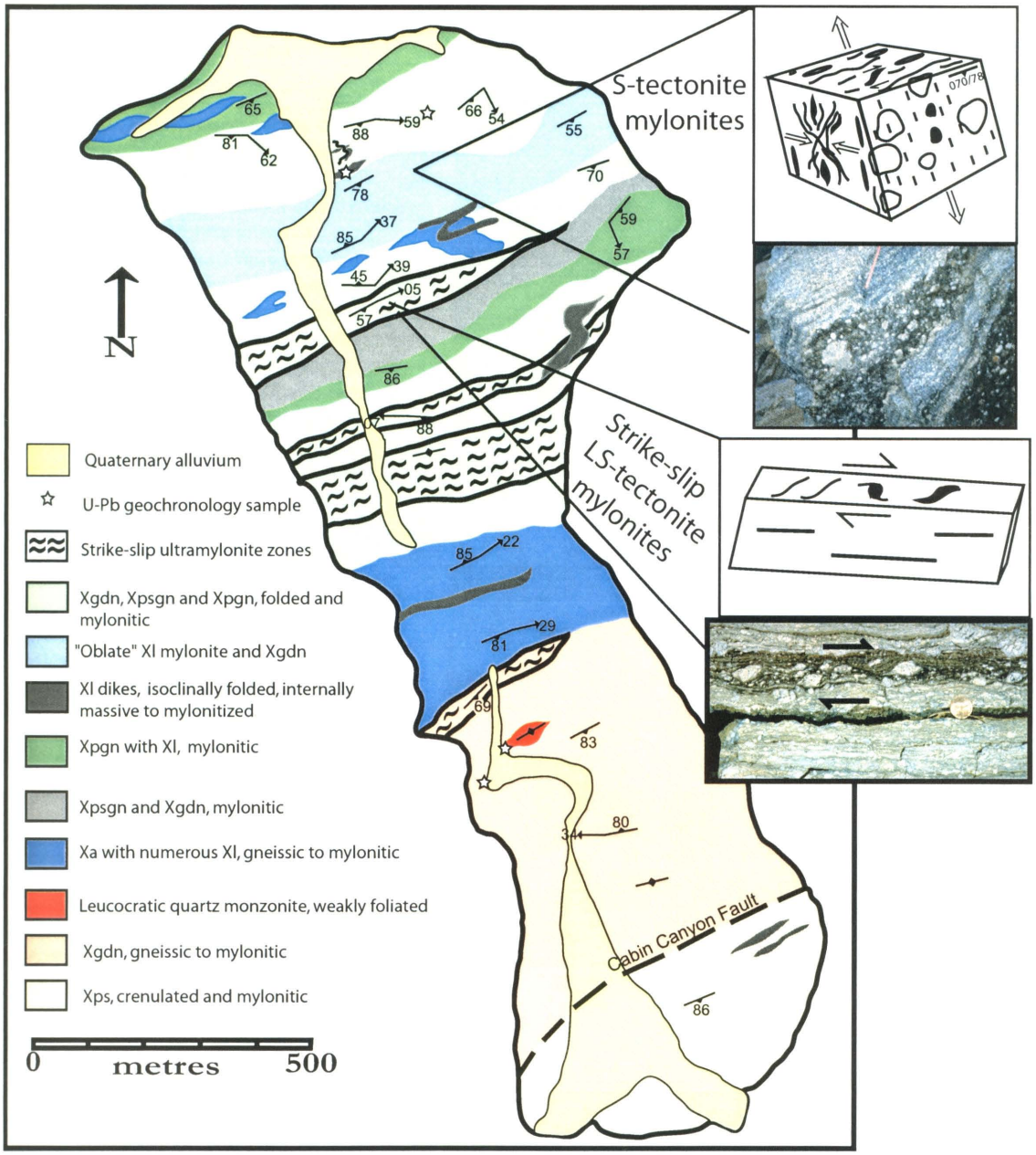

Figure 2-9: Geology of the Cabin Canyon segment of the VMSZ. Lithologic abbreviations (i.e. Xps) defined in Plate 1: *Geologic Map of the North Virgin Mts*. Dextral strike-slip deformation within LS-tectonite zones occurred synchronously with pure-shear deformation and foliation - orthogonal shortening in S-tectonite zones. Analysis of metamorphic textures and assemblages and microstructures associated with mylonitization are consistent within the S and LS domains. This dramatic strain partitioning is observed throughout the VMSZ, where thrust sense, normal sense, dextral-oblique sense, sinstral strike-slip sense, and dextral strike-slip zones operated synchronously to accommodate heterogeneous dextral transpressional strain during D4. Inset of the S-tectonite mylonites displays "pancaked" K-feldspar porphyroclasts on mylonitic foliation (XY) planes that are strongly deformed on XZ and YZ planes orthogonal to the foliation. Weak lineations on the XY plane and conjugate shear bands on the YZ plane indicate vertical stretching and horizontal shortening associated with mylonitization, while localized dextral shear sense indicators on the XZ plane suggest some component of rotational deformation. Inset of the LS-tectonites display strong horizontal lineations on foliation planes and abundant dextral shear sense indicators orthogonal to foliation, suggesting deformation was dominated by strongly rotational simple shear strains.

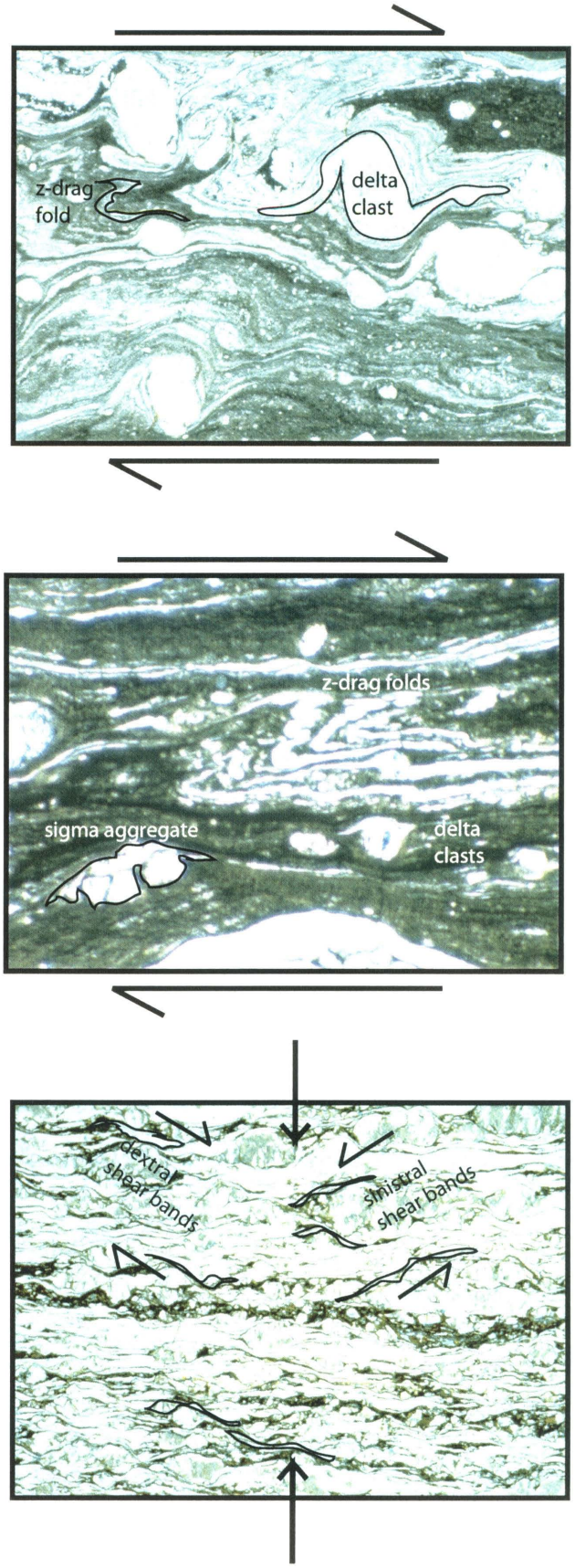

Figure 2-10: Photomicrographs of shear sense indicators within the Cabin Canyon segment of the VMSZ. Sections A) and B), cut parallel to the strong horizontal lineation, commonly reveal beautifully asymmetric shear sense indicators consistent with dextral strike-slip movement along these NE-trending, steeply-dipping ultramylonite zones. These include rotated K-feldspar porphyroclasts with dextral delta-type asymmetry, dextral z-drag folds, and dextrally sheared sigma aggregates and porphyroclasts. Highly asymmetric indicators are present throughout this "strike-slip LS-tectonite mylonite" zone (Figure 2-9).
Section C, cut parallel to the weak down-dip lineation in the "S-tectonite mylonite" zone, reveals conjugate dextral and sinistral shear bands and sigma-type porphyroclasts at angles 30-40 degrees from the NE-striking foliation. These structures formed during shortening across the pre-existing foliation under mylonitic conditions.
Metamorphic observations, including retrogression of garnet porphyroclasts to biotite and chlorite, as well as microstructural evidence, suggest that deformation in A,B, and C took place under similar thermal conditions. Differences in grainsize are interpreted to represent the differences in lithology. This suggests that mylonitic deformation within the Cabin Canyon segment was synchronously partitioned into dextral strike-slip domains A), B) and pure-shear, foliation perpendicular shortening domains C) during overall dextral transpressive deformation. While we favor this hypothesis, another possibility is that the dextral strike-slip domains reflect later dextral shearing unrelated to the NW-SE shortening strains recorded in C). Width of sections A and B is 5mm, section C is 10mm.

contain large (>12cm) "pancake-like" K-feldspar porphyroclasts (Figure 2-9), likely derived via the mechanical dismemberment of leucopegmatite dikes during deformation. The same crystals appear as highly flattened leucosomes on faces perpendicular to the mylonitic foliation, resulting in aspect ratios of roughly 30:30:1. The combination of these oblate flattening strains, conjugate shear bands recording vertical extension parallel to the foliation planes (Figure 2-10), and development of a weak, vertical stretching lineation suggest that shortening in these domains was accommodated by intense vertical "extrusion", similar to that first predicted by the Sanderson and Marchini (1984) transpression model. While grain-sizes are coarser in these domains relative to the ultramylonitic strike-slip domains, the microstructures and metamorphic reactions are suggestive of similar tectonic conditions. The strike-slip domains are thus inferred to have recorded more intense finite strains than the oblate domains, as opposed to recording a different deformation event. Further evidence of increased strain in the strike-slip mylonites is that obliquely plunging fold axes in the wallrocks have been rotated into parallelism with the lineation in the strike-slip domains.

Interpreting the kinematics in the strongly lineated, obliquely plunging domains is more complicated. Although oblique-dextral deformation predominates, sinistral-oblique N-side-up indicators are observed in some of the northern locations. Shear sense indicators such as shear bands and sigma porphyroclasts are associated with lower temperature microstructures (relative to the peak metamorphic microstructures associated with the steeply oblique-sense indicators) and are commonly observed on faces non-parallel to the strong stretching lineation. The apparent conflict between opposing senses of shear is reconciled with the interpretation of early, high-temperature NW-side up

thrusting (D_3) and development of the stretching lineation, overprinted by the upper greenschist facies dextral transpressive deformation (D_4), with some sinistral faults operating during D_4 shortening to accommodate space problems, structural anisotropies, and heterogeneous transpression. The steeply plunging lineation is interpreted to be the result of the earlier event based on 1) the differing character between it and the strike-slip and vertical lineations observed in the simple shear and pure shear dominated domains, respectively, 2) the obliquity of lower temperature shear sense indicators to this lineation, and 3) apparent overprinting and reorientation of this lineation proximal to the strike-slip domains.

To the east of Cabin Canyon in Lime Kiln Canyon, the mylonitic foliation is strongly folded and displays a combination of N and NE-trending dextral-oblique strike slip segments and N-trending, W-side-up reverse segments (Figure 2-2). Because of the thrust sense indicators here and parasitic mylonitic folds that appear to be the same metamorphic grade as the shear zone, this is interpreted as a partitioned, syn-mylonitic renstraining bend in the Cabin Canyon segment rather than a post-mylonite fold of the zone.

Elbow Canyon Segment

The Elbow Canyon segment (Figure 2-2 and 2-11) is characterized by two types of mylonitic deformation; L-tectonite D_3 mylonites with localized NW-side-up shear sense, and a thin (3m) D_4 mylonite zone with sinistral E-side-up shear sense.

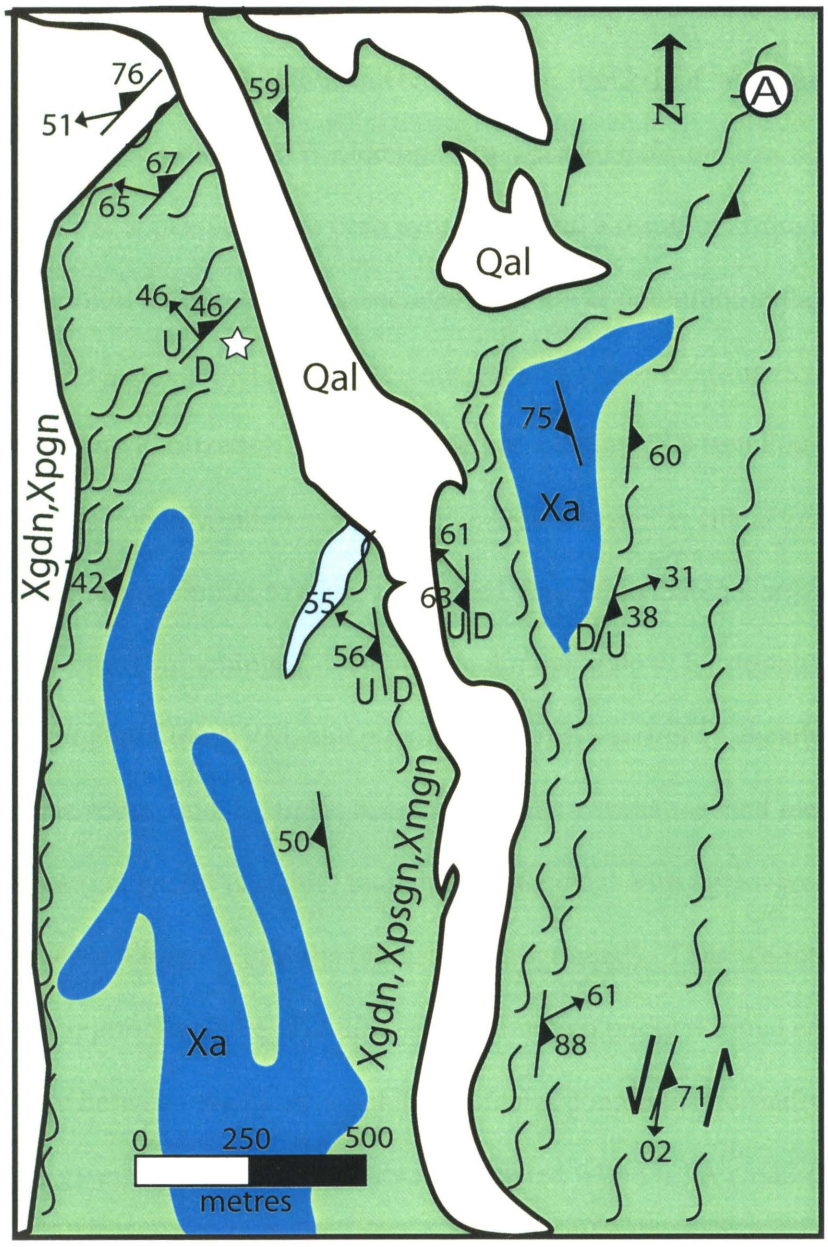

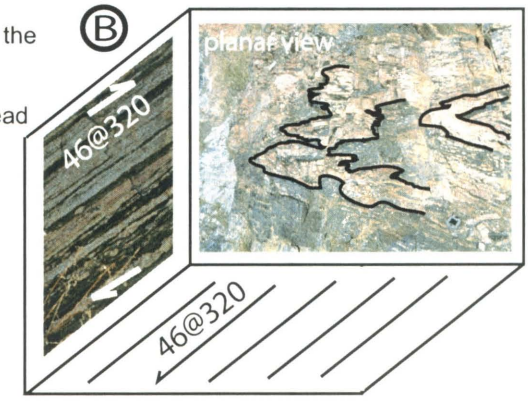

Figure 2-11: A) Geology of the Elbow Canyon segment of the VMSZ. B) Three-dimensional view of the strongly prolate strains associated with NW-side-up mylonites (location of B is starred in A). The mylonites are classified as D3 instead of D4 (see text for details). Planar view shows complexly folded compositional layering, defined by granitic and pegmatitic dikes cross-cutting pelitic schist. The fabric as seen on this face is not mylonitic. Side view shows strongly developed mylonitic fabric defining fold axes of folds seen on planar view surface. This fabric is also seen on the botttom surface, suggesting that mylonitic overprinting of the higher temperature foliation was strongly constrictional, generating a mylonitic L-tectonite.

The D_3 L-tectonite mylonites display an intense vertical stretching lineation at ~ 48 → 320° (Figure 2-11B) with localized evidence (bookshelf structures, sigma K-feldspar porphyroclasts) for NW-side up (thrust-sense) deformation, although much of the deformation appears to have been symmetric and a result of strongly prolate coaxial strain. Mylonitic deformation is associated with lower amphibolite facies microstructures, and garnet and hornblende remained stable during mylonitization. Although this mylonitization reactivates the pre-existing, NE-trending, high-temperature S_3, we classify mylonitization as progressive D_3 because it is characterized by: 1) NW-side-up kinematics, similar to those associated with D_3 in Cabin Canyon (Figure 2-8A); 2) Intense vertical stretching (L-tectonite) of similar style to L_3 stretching lineations mapped throughout the NVM, and parallel to the fold axis of F_3 sheath folds mapped 20 meters to the south; and 3) Higher temperature microstructures and metamorphic assemblages (i.e. garnet is stable) than those associated with upper-greenschist facies D_4 mylonites withi similar protoliths (garnet is retrogressed). Thus we interpret this mylonite to represent active NW-side-up deformation under thermal conditions intermediate between the upper amphibolite facies conditions normally associated with D_3, and the greenschist facies conditions associated with D_4. A small D_4 shear zone with left-lateral, E-side up sigma porphyroclasts wraps around amphibolite boudins to the south of the L-tectonite mylonites. This is interpreted as an accommodation zone enclosing the more competent amphibolite unit, resulting from the combination of heterogeneous mylonitic deformation and rheologic anisotropy, and does not reflect the regional strains associated with D_4.

Mount Bangs Segment

A transect across the Mount Bangs segment (Figure 2-2, 2-12) reveals the best example of compositionally partitioned deformation in the VMSZ. The presence of rheologically "strong" amphibolitic gneisses and ultramafic rocks contrasts with the thickest exposed package of rheologically "weak" calcitic marbles and leucopegmatites. Kinematic analysis reveals NW-side-down (normal) deformation in a leucopegmatite dike and associated pelitic wallrock, NW-side down (reverse) kinematics in pelitic schists and granitic gneisses to the northwest, and NW-side-up dextral-reverse kinematics in the calcitic marble unit to the north.

The marked rheological anisotropy resulted in the significant strain heterogeneity observed throughout the transect. Ductile deformation is most pronounced around the edges of boundinaged mafic and ultramafic packages, which range from strongly to weakly foliated but show little evidence for internal deformation associated with the ductile deformation. While little evidence of their 3-dimensional geometry is observed, significant metamorphism, boudinage and internal deformation of these mafic units likely occurred during higher temperature deformation (D_3), with the mylonitic deformation event (D_4) significantly less penetrative. Conversely, the diopside-bearing marble units and associated ultramafic clasts ("tectonic mélange") experienced penetrative ductile shearing and complex folding during the D_4 event. Although the folds are somewhat chaotic, when interpreted in conjunction with rotated feldspar and ultramafic sigma clasts, deformation is described as dextral oblique.

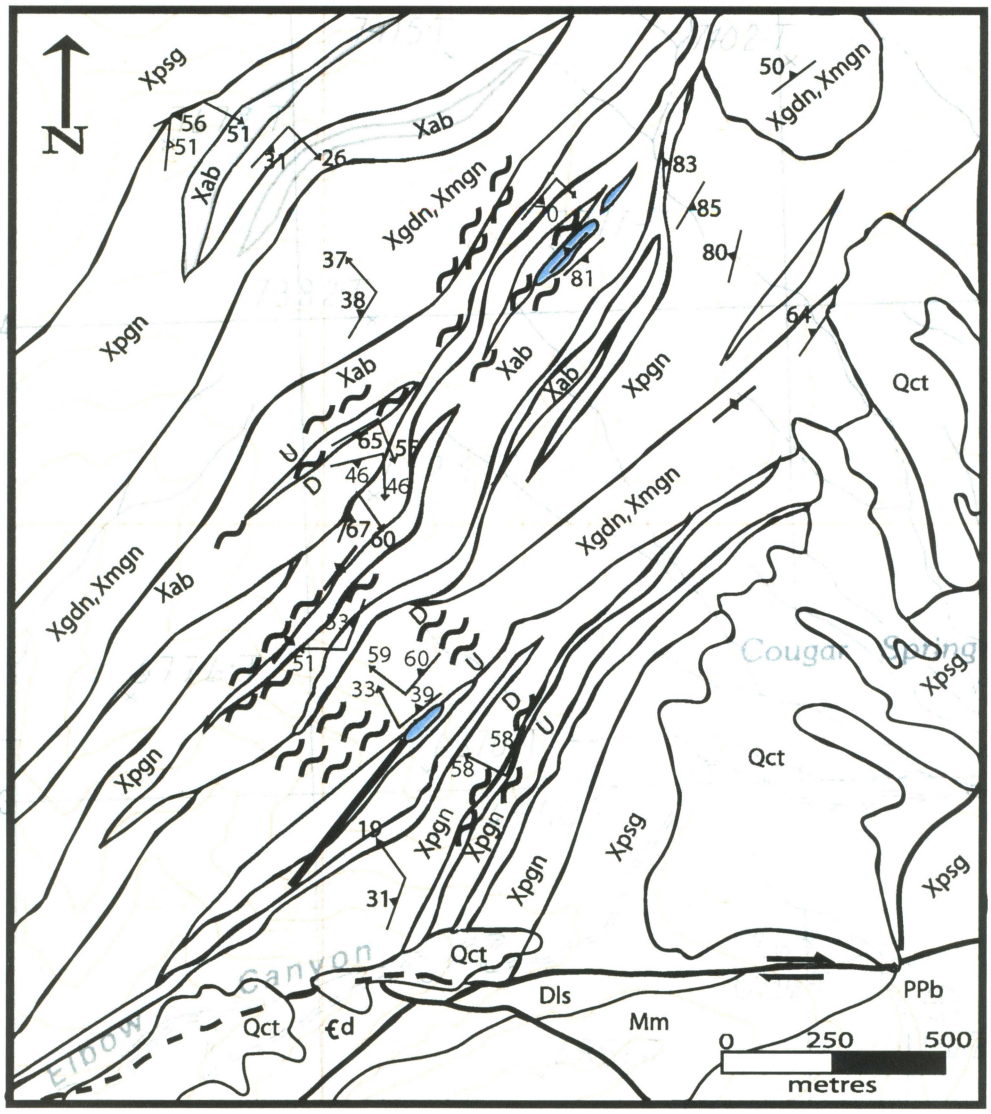

Phanerozoic

- Qct — Colluvium and terrace gravels (Pleistocene)
- PPb — Bird Spring Formation (Lower Permian and Pennsylvanian)
- Mm — Monte Cristo Limestone (Mississippian)
- Dls — Limestone (Devonian)
- €d — Dolomite (Upper Cambrian)

Paleoproterozoic

- Leucopegmatite dikes, isoclinally folded and boudinaged, internally massive to mylonitic
- Xmgn — Monzogranite and quartz monzonite gneiss
- Xgdn — Granodiorite to granitic orthogneiss
- Xab — Amphibolite and calc-amphibolite gneiss
- Xpgn — Pelitic and semi-pelitic gneiss and schist
- Xpsg — Psammitic gneiss and orthogneiss
- Diopside-bearing fragmental marbles, ultramafic pods, calc-amphibolite and amphibolite gneiss
- D_3 mylonite, with kinematic analysis (Up, Down)

Figure 2-12: Geology of the Mount Bangs segment of the VMSZ (Domain III). D4 mylonite zones reactivate the NE-trending S3 fabric. A belt of exotic lithologies, including 2 pyroxene ultramafic rocks interlayered with granitic and metasedimentary rocks suggest, at least, dramatic juxtaposition of distinct crustal domains, with the possibility, at most, that ophiolitic segments were obducted in the early tectonic history of the NVM.

South Spur Segment

Although it is poorly exposed due to intense Miocene and possibly Laramide brittle reactivation, the South Spur segment contains mylonites throughout its strike length. The best exposures of mylonites occur within vertical, NE-trending, sheared leucopegmatite dikes, which preserve spectacular SE-side up shear sense indicators including sigma and delta K-feldspar porphyroclasts, antithetic bookshelf fractures and shear bands.

Black Ridge Segment

The Black Ridge segment contains abundant, NE-trending, greenschist facies D_4 ductile shear zones partitioned within the variety of quartzofeldspathic units that occur in that area. Similar to other segments, strain is best developed around the edges of competent ultramafic boudins, although localized shear zones away from these rheologic contrasts exist. Where developed, lineations are subhorizontal and dextral kinematic indicators are prevalent. Wall rock lineations are commonly vertical, and show some evidence that they have rotated into shallower orientations as they approach the shear zone, similar to the relationships observed in Cabin Canyon.

Summary of Kinematic analysis (Figure 2-3)

Kinematic analysis of the VMSZ suggests that D_3 structures include steeply oblique to down-dip lineations and NW-side-up shear sense indicators, and D_4 structures

include dextral-strike-slip indicators and subhorizontal lineations. NW- and SE-side up reverse and normal sense indicators with moderately to steeply plunging lineations, and pure shear indicators with subvertical lineations are also part of the D_4 displacement field. These complexities arise due to variations in shear zone orientation and geometry, rheologic heterogeneities, and arguably, timing of deformation. Seemingly incompatible structures can be easily created during heterogeneously partitioned dextral transpressive deformation, and are correlated based on metamorphic conditions and deformation microstructures.

Domain III: Metamorphism and microstructures within the VMSZ

Metamorphic assemblages and textures preserved within the VMSZ rocks are highly variable, due to the variety of lithologies present, the varying rheologic and chemical competencies of these lithologies, and the heterogeneous nature of deformation and metamorphism throughout this zone. Although some lithologies preserve higher temperature deformational textures, the overprinting of high temperature fabrics by lower temperature mylonites are the dominant microstructures throughout the VMSZ.

In general, rocks with oblique sense lineations or strong prolate (L-tectonite) strains are characterized by lower amphibolite facies metamorphic textures and assemblages, and microstructures suggestive of deformation temperatures between 500-650°C, depending on strain rate (Hirth and Tullis, 1992). These mylonites are found in Elbow Canyon, and along the Domain II-Domain III boundary in Black Ridge, described previously. Rocks with vertical or horizontal lineations and highly prolate (S-tectonite)

or asymmetric (simple-shear dominated) strains, in general, are characterized by greenschist facies textures and assemblages and microstructures suggestive of deformation temperatures between 350-450°C (Hirth and Tullis, 1992). These mylonites are found throughout the VMSZ, but most notably in the Black Ridge, South Spur, and Cabin Canyon segments.

Pelitic rocks within the VMSZ contain the assemblage garnet + biotite + sillimanite + K-feldspar + plagioclase + quartz. Similar to Domain II, the muscovite and cordierite abundant in Domain I are either absent or present in very low amounts, suggesting that metamorphic conditions (absence of muscovite) and possibly bulk rock compositions (absence of cordierite) within these pelites were not favorable to growth of these minerals. Garnet porphyroclasts contain coarse, elongate quartz inclusions with locally present polygonal grain boundaries, interpreted as high-temperature quartz growth during late D_1 or D_2, as quartz inclusion trails are oblique to the dominant S_3/S_4 matrix foliation. Timing of garnet growth relative to fabric development thus appears to be synchronous with cordierite growth in the pelites to the south. Sillimanite occurs both as fine-grained fibrolite mats intergrown with biotite, as observed to the south, but more dominantly as large (up to 4mm) euhedral crystals that predominantly lie within the S_3/S_4 plane. Evidence for retrograde D_4 greenschist-facies reactions within the pelitic rocks is present and usually associated with the abundant lower-temperature strain domains present throughout these rocks. Garnet is replaced by biotite along internal fractures, and K-feldspar is commonly retrogressed to sericite. Sillimanite is locally boudinaged within S_4 and replaced by chlorite in boudin necks. Although garnet, sillimanite, feldspar and biotite display predominantly brittle microstructures, quartz domains often show evidence

for subgrain rotation and climb-accommodated dislocation creep, and are thus the best domains to examine for shear sense.

Mafic rocks within the VMSZ contain a variety of assemblages and are variably retrogressed, although most remained competent "lumps" during D_4 and thus preserve higher-temperature assemblages and textures. An amphibolite pod from the Cabin Canyon segment contains the assemblage hornblende + plagioclase + garnet + biotite + opaques. Matrix hornblende is visibly zoned with hornblenditic cores and actinolitic rims where conjugate fractures intersect the rock. Tiny hornblende-actinolite grain aggregates have formed along these conjugates. Garnet is retrogressed to biotite along grain edges and in pressure shadows where fractures permeate. Hornblende + garnet + plagioclase + opaques are intergrown and probably grew during peak metamorphism (M_2), and greenschist facies retrogression of garnet to biotite and hornblende to actinolite was a result of late M_3 or M_4, which was minimal in this rock due to its relatively chemical and rheologic competency during D_4 metamorphism and deformation.

Conspicuously layered ultramafic and calc-silicate rocks crop out within the Black Ridge, Mount Bangs, and South Spur segments of the VMSZ (Figure 2-2). These ultramafic pods contain the assemblage clinopyroxene + garnet + quartz + calcite + hornblende + plagioclase + epidote + zoisite + sericite, and are interlayered with amphibolites, pelitic schists, marbles, and possibly cherts. Diopside is coarse grained, zoned, and interlocks with andradite garnet and calcite. Wormy symplectic intergrowths of plagioclase and epidote are present, a texture suggestive of upper amphibolite to granulite conditions (Selverstone, person. commun). Hornblende layers are coarse grained and interlocking. Quartz fills in grain boundaries and veins, and is interpreted to

be secondary. Few signs of retrogression of the peak metamorphic assemblage are present, although lower temperature microstructures within the quartz veins are abundant.

An ultramafic pod within the Mount Bangs segment contains the assemblage clinopyroxene + orthopyroxene + hercynite, indicative of metamorphism to the granulite facies. Orthopyroxene has been intensely pseudomorphed by serpentine + brucite, with highly altered relict cores the only remaining evidence of this mineral. Clinopyroxene is coarse grained and euhedral. Although the granulite facies metamorphic assemblage and texture is well preserved, retrogression of pyroxene to serpentine and brucite represents a greenschist facies reaction that probably occurred during D_4. Ultramafic rocks within the Cabin Canyon segment contain the granulite assemblage orthopyroxene + hornblende + biotite + plagioclase ± clinopyroxene and are coarse grained, interlocking, and unretrogressed.

Granitic, granodioritic, and psammitic rocks contain the assemblage quartz + plagioclase + K-feldspar + biotite ± muscovite ± garnet ± epidote ± hornblende ± actinolite. These assemblages are strongly deformable under lower amphibolite and greenschist facies deformation conditions due to the structural incompetence of quartz and feldspar relative to mafic minerals, and thus rarely preserve the high temperature microstructures present within the pelitic and ultramafic rocks. Without exception, all granitic rocks within the VMSZ show some degree of lower temperature deformation, and most are strongly mylonitic. Quartz microstructures indicate deformation occurred predominantly by subgrain rotation and climb-accommodated dislocation creep, whereas feldspars deformed by internal kinking and development of mechanical twins, brittle fracturing, and recrystallization-accommodated dislocation creep, together suggestive of

lower amphibolite to greenschist deformation conditions (350-500°C, Hirth and Tullis, 1992). Garnet has been retrogressed and locally pseudomorphed by plagioclase + epidote +/- actinolite, resulting in a "disaggregation" of originally euhedral garnet porphyroclasts during progressive strain. Hornblende has broken down to form actinolite. The microstructures and metamorphic relations thus suggest that deformation and metamorphism occurred under upper greenschist facies conditions. Garnets are completely pseudomorphed by chlorite in the mylonitic matrix, but retain their chemical and structural characteristics where they were harboured within K-feldspar porphyroclasts (Figure 2-13), a key textural relationship tying the mylonitic deformation in the matrix to retrograde upper-greenschist facies metamorphism, "Matrix" pseudeomorphed garnets display fine-grained chlorite tails indicative of dextral shear sense, and are internally cut by dextral shear bands. These observations suggest that retrogression of the garnets was, at least in part, intimately linked with D_4 dextral deformation in the VMSZ.

5. Geochronology

U/Pb monazite dating of the VMSZ

In situ electron microprobe dating of monazite grains in VMSZ mylonitic rocks was done by the first author at the New Mexico Institute of Technology under the supervision of Dr. Nelia Dunbar, and by Dr. Mike Williams and Dr. Mike Jercinovic at the University of Massachusetts. Monazites were located in thin section by conducting

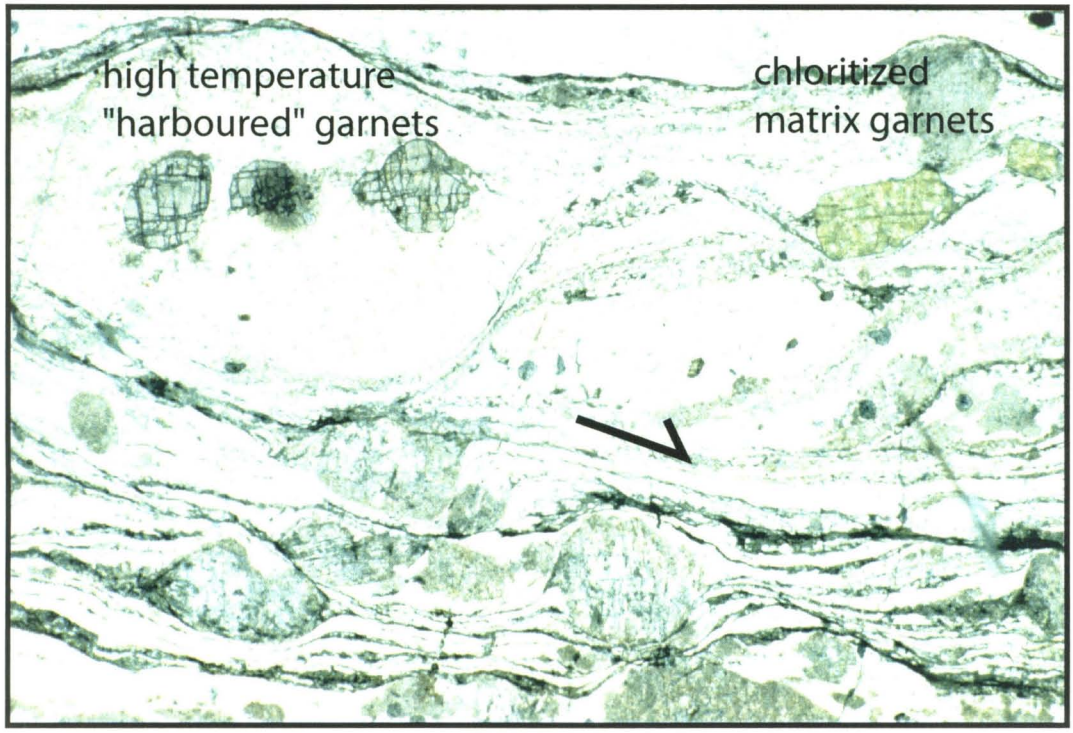

Figure 2-13 Coeval upper-greenschist facies metamorphism and dextral strike-slip deformation in the Black Ridge segment, as determined by the complete retrogression of garnet porphyroclasts to chlorite within the mylonitic matrix and associated chloritic dextral shear tails. Garnets within K-feldspar porphyroclasts are chemically and structurally "shielded" from this deformation and associated metamorphic fluids and are thus preserved. Any interaction of these garnets with matrix fluids has resulted in retrogression, visible as the chloritic tails on the right edge of the K-spar porphyroclast. Abundant shear bands, S-C fabrics, and sigma porphyroclasts give dextral shear sense. Scale 3cm wide.

automated back-scatter electron scans for Ce and EDS point analyses on the JEOL 5800LV scanning electron microscope at the University of New Mexico. X-ray maps and spot analyses of U, Th, Pb, and Y were conducted for selected monazite grains using the Cameca SX100 electron at the NM Tech and the Cameca SX50 at UMass. This method is still evolving, and new techniques are currently being used for calculating background matrix values (Williams pers. comm., 2002).

Monazite can grow as a primary mineral from a melt, a hydrothermal mineral during fluid flux, or a metamorphic mineral during thermal/deformation events (Williams et al., 1999). In order to place time constraints on deformational events, monazite growth must be correlative with development of a tectonic fabric. Monazite commonly grows as a rim on an older core (Williams et al., 1999), with rims growing preferentially in the direction of infinitesimal elongation during strain. Thus zoned, syndeformational monazites were targeted for analysis.

Preliminary U-Pb monazite ages from mylonitic rocks in the Elbow Canyon segment of the VMSZ yield age clusters in at least three distinct intervals, correlative with multiple growth patterns and chemical U-Th-Pb zoning visible in backscatter images and compositional maps of the grains (Figure 2-14, Table 2-1). Earliest growth occurred circa 1695 Ma, determined from core analyses of zoned monazites and consistent with the zircon ages described above. This growth appears to be associated with the regional upper amphibolite M_2 or M_3 metamorphism and granitic plutonism. Progressive monazite growth intervals are recorded at 1600 and 1550 Ma, with peaks also recorded at 1670, 1650, 1630, and 1500 Ma. Monazite growth rims are structurally asymmetric, and commonly elongated parallel to the composite high-temperature S_2 / S_3 and lower-

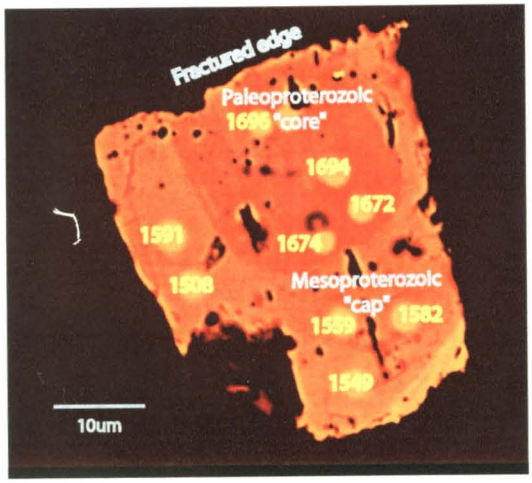

SEM "Black-body" Back-Scatter Image of monazite Q295a

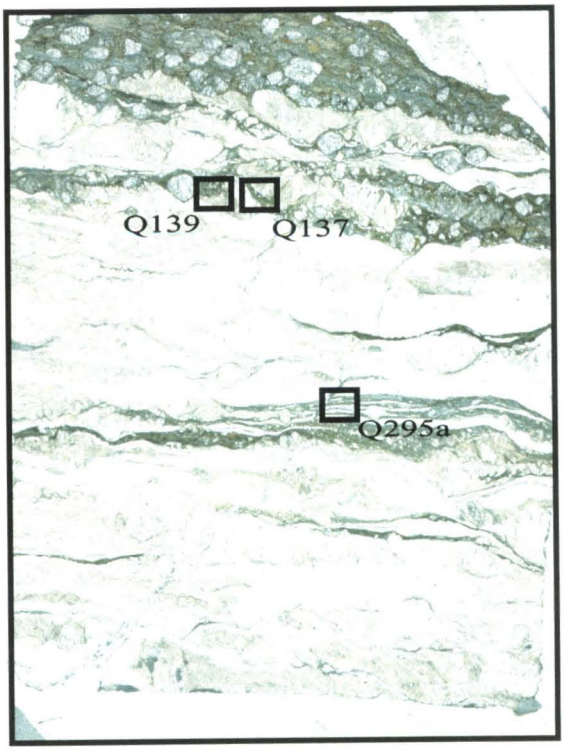

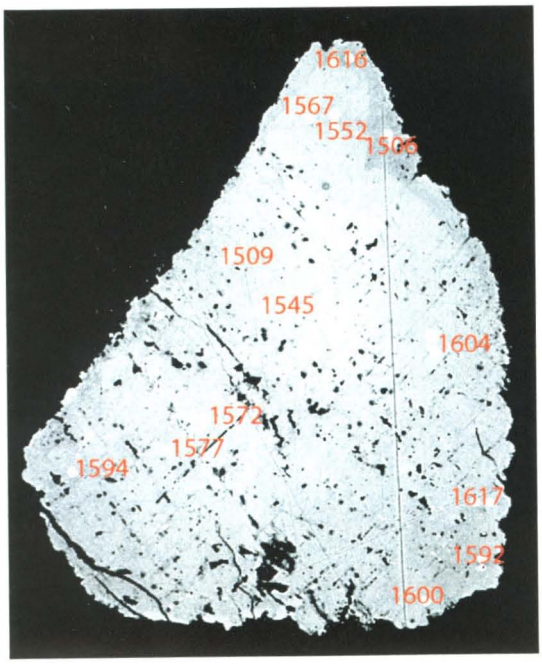

Monazite 137 Relected light photograph: 150 X 150 um

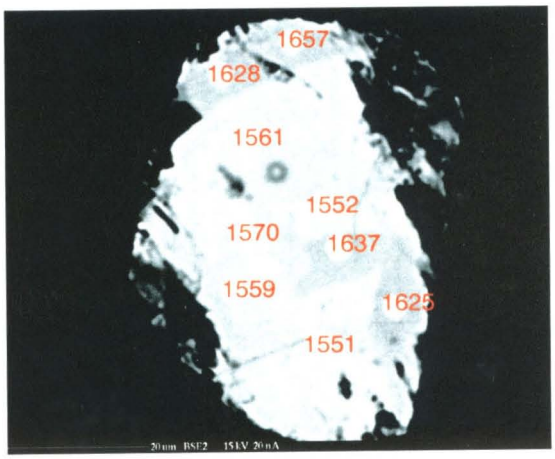

Monazite 139

Figure 2-14: U-Pb monazite spot-analysis ages from the L>>S mylonites in the Elbow Canyon segment. See text and Table 2-2 for details.

Table 2-1: Y,Th,U,Pb point analyses from monazite grains

Decay Constants	
Th232	4.95E-11
U238	1.55E-10
U235	9.85E-10

	Analysis (ppm)				Calc	Individual Age Terms (n=3)					
Anal #	Y	Th	U	Pb	Pb cor	Pb	232	238	235	Age (a)	Age (Ma)
137-1	2.3351	3.7883	1.0907	0.581	0.57679682	0.57684223	0.282847337	0.266931508	0.027063385	1616000000	1616
137-2	2.5304	3.6627	1.3826	0.6013	0.59674528	0.596586755	0.254152919	0.312550788	0.029883048	1506000000	1506
137-3	1.5072	6.7768	0.6639	0.6584	0.65568704	0.655610654	0.485160961	0.155240093	0.015209599	1552000000	1552
137-4	1.3398	6.8828	0.5992	0.655	0.65258836	0.653324133	0.497699168	0.141636716	0.013988249	1567000000	1567
137-5	1.3204	6.9555	0.6074	0.6367	0.63432328	0.634430567	0.483636449	0.137615728	0.013178389	1509000000	1509
137-6	1.2975	7.0127	0.5963	0.6542	0.6518645	0.651964287	0.499697301	0.138725921	0.013541065	1545000000	1545
137-7	2.1219	7.0966	1.0076	0.7989	0.79508058	0.794921816	0.525763419	0.244525827	0.02463257	1604000000	1604
137-8	2.4144	4.0586	1.2178	0.6362	0.63185408	0.631724201	0.303223975	0.298245737	0.030254489	1617000000	1617
137-9	2.2857	3.4646	1.3212	0.6106	0.60648574	0.606586249	0.255515622	0.319051061	0.032019566	1597000000	1597
137-10	1.915	4.8184	1.4059	0.702	0.698553	0.730477839	0.356053242	0.340225088	0.034199508	1600000000	1600
137-11	1.7835	7.7568	0.8359	0.7838	0.7805897	0.780692815	0.562758863	0.198297454	0.019636498	1572000000	1572
137-12	1.8821	7.414	0.8532	0.7661	0.76271222	0.762962836	0.539667078	0.203127188	0.02016857	1577000000	1577
137-13	2.4768	4.9814	1.2605	0.7054	0.70094176	0.700844745	0.366662506	0.303747476	0.030434763	1594000000	1594
295a-1	0.4683	3.5144	0.825	0.5119	0.51105706	0.511114505	0.275601021	0.212990284	0.0225232	1694000000	1694
295a-2	0.9443	1.4007	0.18	0.1631	0.16140026	0.161437905	0.109978806	0.046533005	0.004926094	1696000000	1696
295a-3	0.7231	2.686	0.5696	0.3475	0.34619842	0.346287279	0.196416993	0.136287509	0.013582778	1584000000	1584
295a-4	1.9218	3.8613	1.168	0.631	0.62754076	0.627701385	0.299079924	0.297500606	0.031120855	1674000000	1674
295a-5	1.8604	3.7885	0.8335	0.5306	0.52725128	0.52724234	0.29307585	0.212012354	0.022154136	1672000000	1672
295a-6	1.3756	7.0808	0.6322	0.6898	0.68732392	0.687399248	0.520171564	0.152020091	0.015207594	1591000000	1591
295a-7	1.1672	7.6194	0.4363	0.6586	0.65649904	0.656144736	0.544388566	0.101798424	0.009957746	1549000000	1549
295a-8	1.6188	7.8693	0.7693	0.7798	0.77688616	0.776803216	0.574696663	0.183807401	0.018299151	1582000000	1582
295a-9	1.5854	7.9201	0.7223	0.7591	0.75624628	0.75611591	0.56966882	0.169753394	0.016693696	1559000000	1559
295a-10	1.4636	7.9097	0.5934	0.6996	0.69696552	0.696808705	0.54960655	0.134343896	0.012858259	1508000000	1508
295b-1	1.4259	8.1567	0.6797	0.7644	0.76183338	0.761611435	0.586295722	0.159626292	0.015689421	1558000000	1558
295b-2	1.5238	8.0543	0.7117	0.7517	0.74895716	0.74880961	0.568903125	0.164007922	0.015898564	1532000000	1532
139-1	2.5251	1.7398	1.4356	0.5367	0.53215482	0.532246809	0.133332143	0.361450094	0.037464572	1657000000	1657

Table 2-1(continued): Y,Th,U,Pb point analyses from monazite grains											
	Analysis (ppm)				Calc		Individual Age Terms (n=3)				
Anal #	Y	Th	U	Pb	Pb cor	Pb	232	238	235	Age (a)	Age (Ma)
139-2	2.3647	1.7495	1.5989	0.5707	0.56644354	0.566492295	0.131633198	0.394593526	0.040265571	1628000000	1628
139-3	1.4716	7.3554	0.6534	0.7016	0.69895112	0.698678638	0.529756924	0.153782474	0.01513924	1561000000	1561
139-4	1.9972	4.6229	0.9417	0.6112	0.60760504	0.60766802	0.349831011	0.23385755	0.023979459	1637000000	1637
139-6	2.5365	1.7776	1.4379	0.5283	0.5237343	0.523688713	0.133490947	0.35412046	0.036077307	1625000000	1625
139-7	1.6796	7.6146	0.7409	0.7377	0.73467672	0.73484712	0.544775375	0.173119454	0.016952292	1551000000	1551
139-8	1.5816	6.8152	0.7275	0.6808	0.67795312	0.677986072	0.490196707	0.170975487	0.016813878	1559000000	1559
139-9	1.6253	7.7589	0.7116	0.75	0.74707446	0.747409836	0.562166858	0.168568247	0.01667473	1570000000	1570
139-10	1.0946	6.9713	0.5313	0.6373	0.63532972	0.635491466	0.499085499	0.124234164	0.012171803	1552000000	1552

temperature S_4 foliation. At present, we interpret the ages determined from monazite analyses to record distinct monazite growth intervals that post-date 1,680 Ma during D_3 and D_4 tectonism.

We recognize the alternate possibility: that the dates may be suspect, as the microprobe dating method is relatively new and under development (Williams, person. commun.). However, we note that diffusional Pb loss from monazites is believed to be negligible below its 700 + degree closure temperature. Also, the boundaries between compositional domains are sharp and the cores of the grains give ages expected for the Yavapai orogeny (1700-1690 Ma), similar to the Grand Canyon samples (Karlstrom et al., in press). If partial dissolution were the explanation for the daughter loss, we would expect textural evidence for this type of process, which is not evident. Admittedly, new work suggests that choice of background from which peaks are calculated is a critical step that can result in miscalculation of dates (Williams, person. commun.), so we entertain the possibility that the 1600-1500 Ma dates may be too young. Preliminary 1690-1670 Ma dates from the Cabin Canyon shear zone may confirm this hypothesis.

If the dates are robust, the VMSZ provides evidence of recurrent mobilization of a partitioned, inboard crustal weak zone over a time interval of tectonic convergence of several hundred million years (1.7-1.5 Ga). Monazite structural asymmetry, and evidence that the growth of other metamorphic minerals was synchronous with the D_3 deformation, suggests that these dates may in fact be representative of the long-lived, complex history of the VMSZ. Monazite rim dates of 1,600 and 1,550 Ma, while preliminary and requiring further analysis, may record deformation during a time-period where much of the rest of the southwestern U.S. was tectonically stable. Detailed

structural and geochronological studies of mylonitic shear zones comparable to the VMSZ have not, to our knowledge, been conducted in the Proterozoic exposures of the Mojave crustal province west of the VMSZ. Further work may help confine the nature and pervasiveness of this event.

U-Pb dating of apatite

Apatites were dated using the U-Pb apatite-feldspar method (see Chamberlain and Bowring, 2001) by Sam Bowring (MIT). Samples were collected from Black Ridge and from Whitney Pocket (Figure 2-15). Dates were 1446, 1424, 1423, and 1410 Ma. These are interpreted to record cooling of these rocks through about 450°C at this time, and confirm that the Proterozoic crust was hot during the circa 1400 Ma event. While these dates lend support for the idea that the D_4 event may have been at 1420 Ma, this is not supported by the monazite dates. Alternatively, we suggest that the circa 1400 Ma event may have involved crustal heating to ca. 450°C, but with little deformation in the immediate area, consistent with the structural and metamorphic evidence for rapidly exhuming continual deformation, and the monazite dates. We note the apparent lack of deformation within the ~1400 Ma Gold Butte granite (Volbroth, 1962), roughly 50 kilometers to the south of the North Virgin Mountains.

39Ar/40Ar thermochronometry

Several amphiboles (5), micas (9) and K-feldspars (9) were dated by the $^{40}Ar/^{39}Ar$ age spectrum technique. Analytical data and details of the methods, and apparent ages for

the micas and amphiboles, are summarized in Appendix A. Sample locations appear in Figure 2-15. Composite age spectra diagrams are given in Figures 2-16, 2-17, 2-18 for the amphiboles, micas and K-feldspars, respectively. The results exhibit variable complexity, but in most cases an apparent weighted mean age (referred to as a plateau age) is reported for each sample (see Figures 2-16 to 2-18, Summary). In nearly all cases, the MSWD determined for the plateau ages are very high and indicated scatter in apparent ages well above that accommodated by analytical uncertainty. The use of the term plateau age here does not imply concordance of the steps used to calculate the age, rather it is designated as the age that may best correspond to the time of closure of a given mineral.

Amphiboles:

Amphiboles have assigned ages ranging from 1524 to 1668 Ma with 4 of the 5 samples falling between 1630 to 1668 Ma (Appendix A, Summary). Amphibole age spectra complexities are mainly related to either excess argon (e.g. Q81) or contamination by a relatively high K, low argon retentivity, phase (e.g. Q60B, Q90A). In the case of Q81, the total gas age is ~2050 Ma and initial steps are older than 9 Ga, clearly indicating an excess argon component. Samples with a high K contaminant are generally recognized by an inverse relationship between age and K/Ca value. Because amphiboles and their younger fine-grained contaminating phases do not degas identically in the laboratory, the age spectrum complexity can be understood in terms of which phase is dominating the gas release. In the case of Q60B, approximately 90% of the spectrum exhibits the relationship of young apparent age correlating with high apparent K/Ca. Coupling these

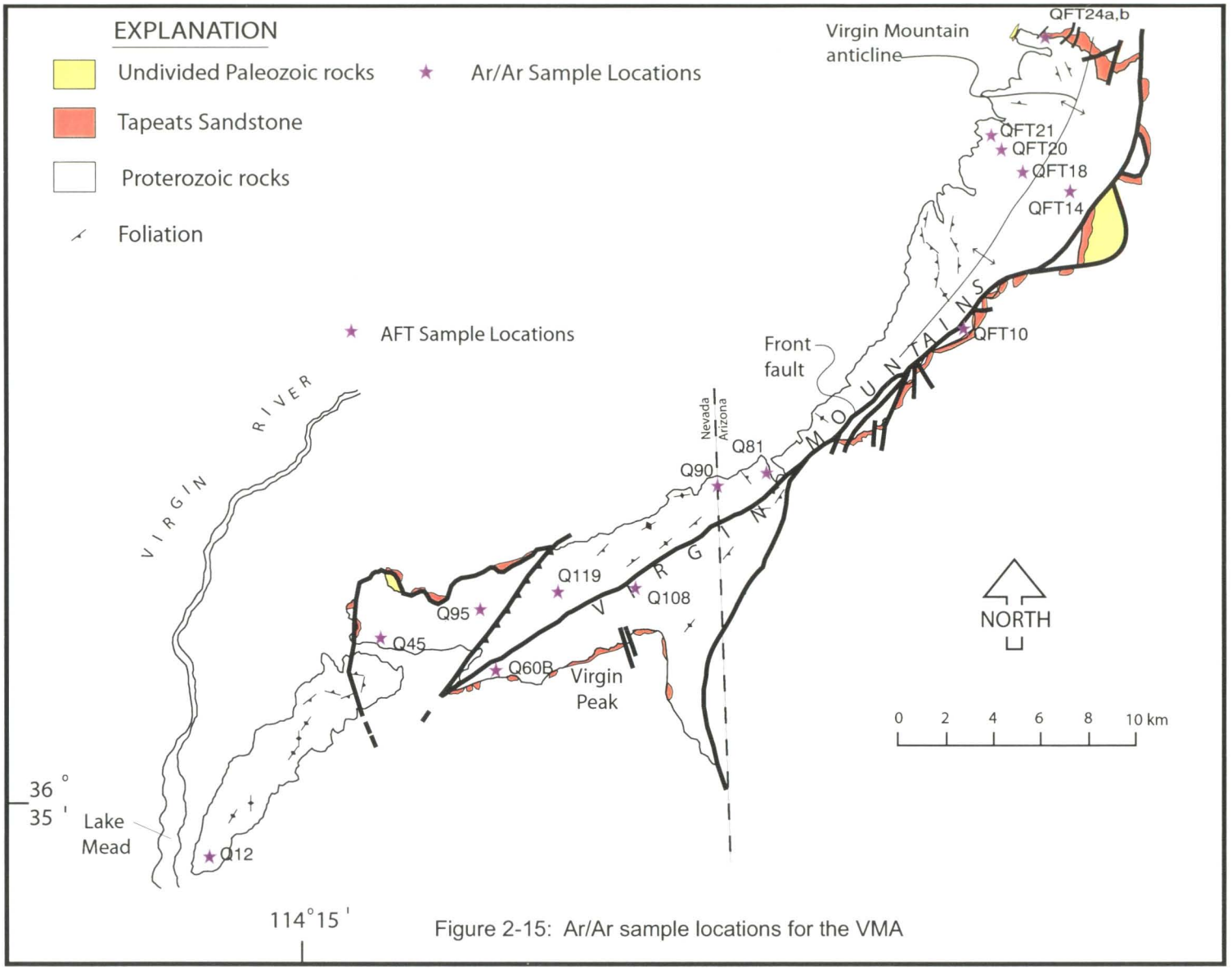

Figure 2-15: Ar/Ar sample locations for the VMA

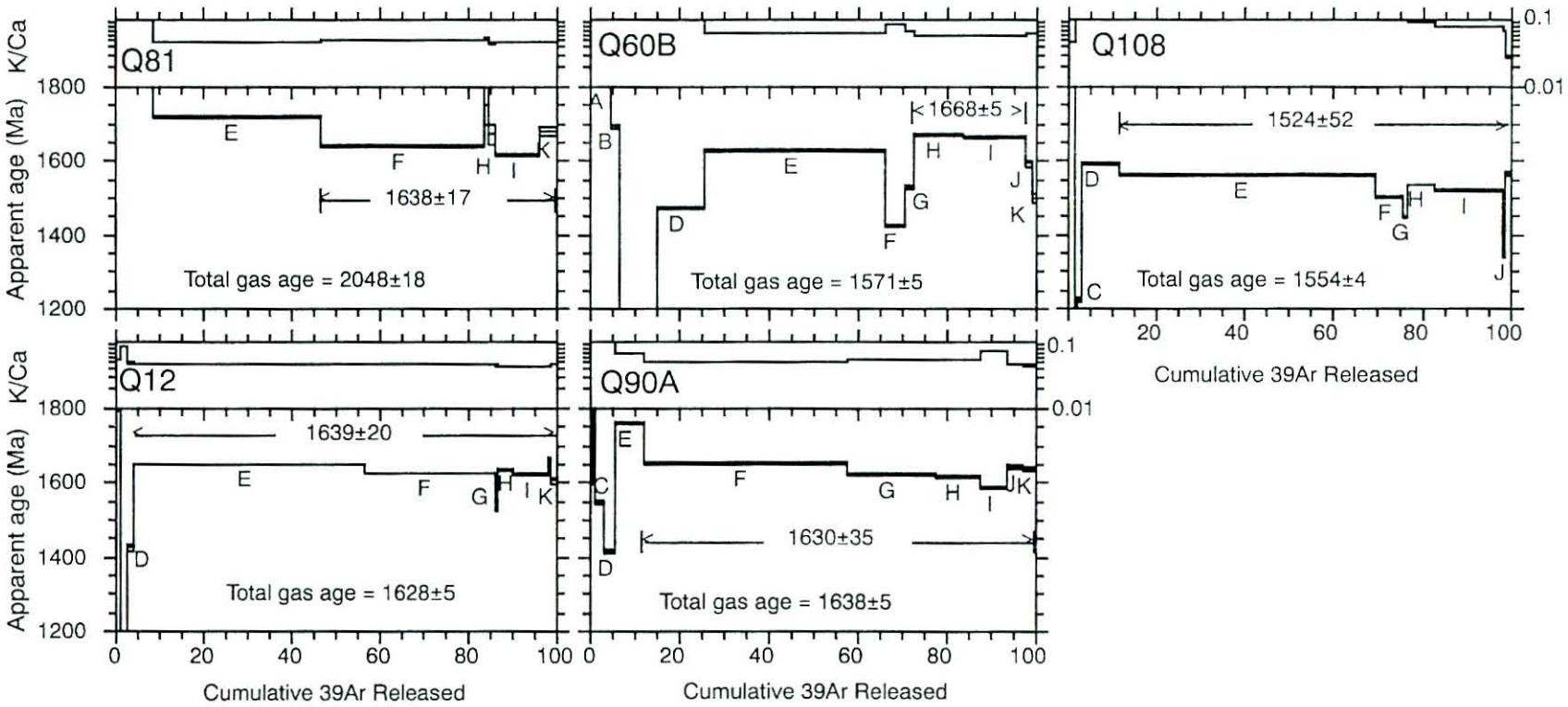

Figure 2-16. Hornblende age spectrum and K/Ca diagrams from the North Virgin Mountains. Sample locations appear in Figure 2-15

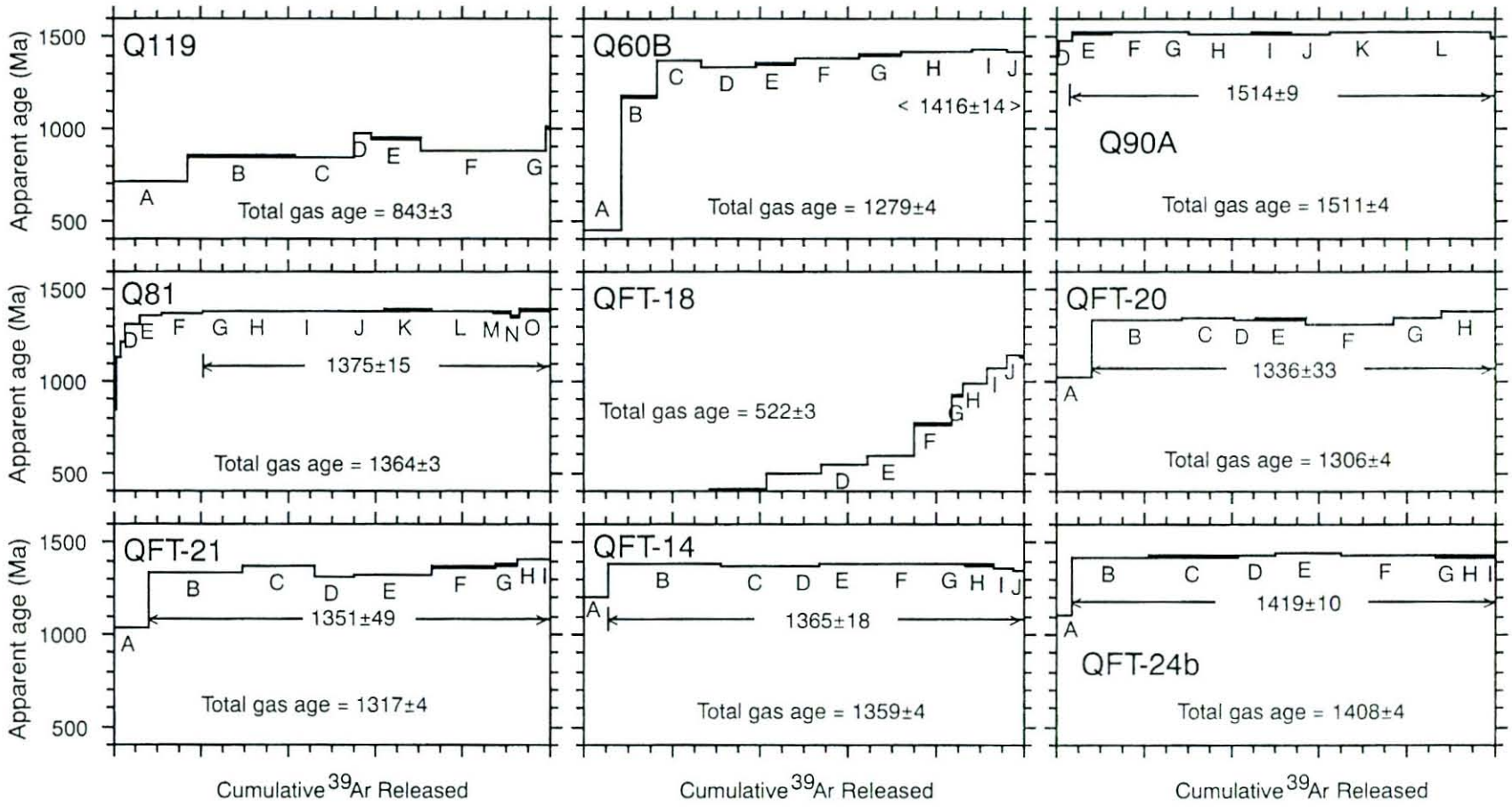

Figure 2-17: Biotite Ar / Ar analyses from the North Virgin Mountains. Station locations appear in Figure 2-15

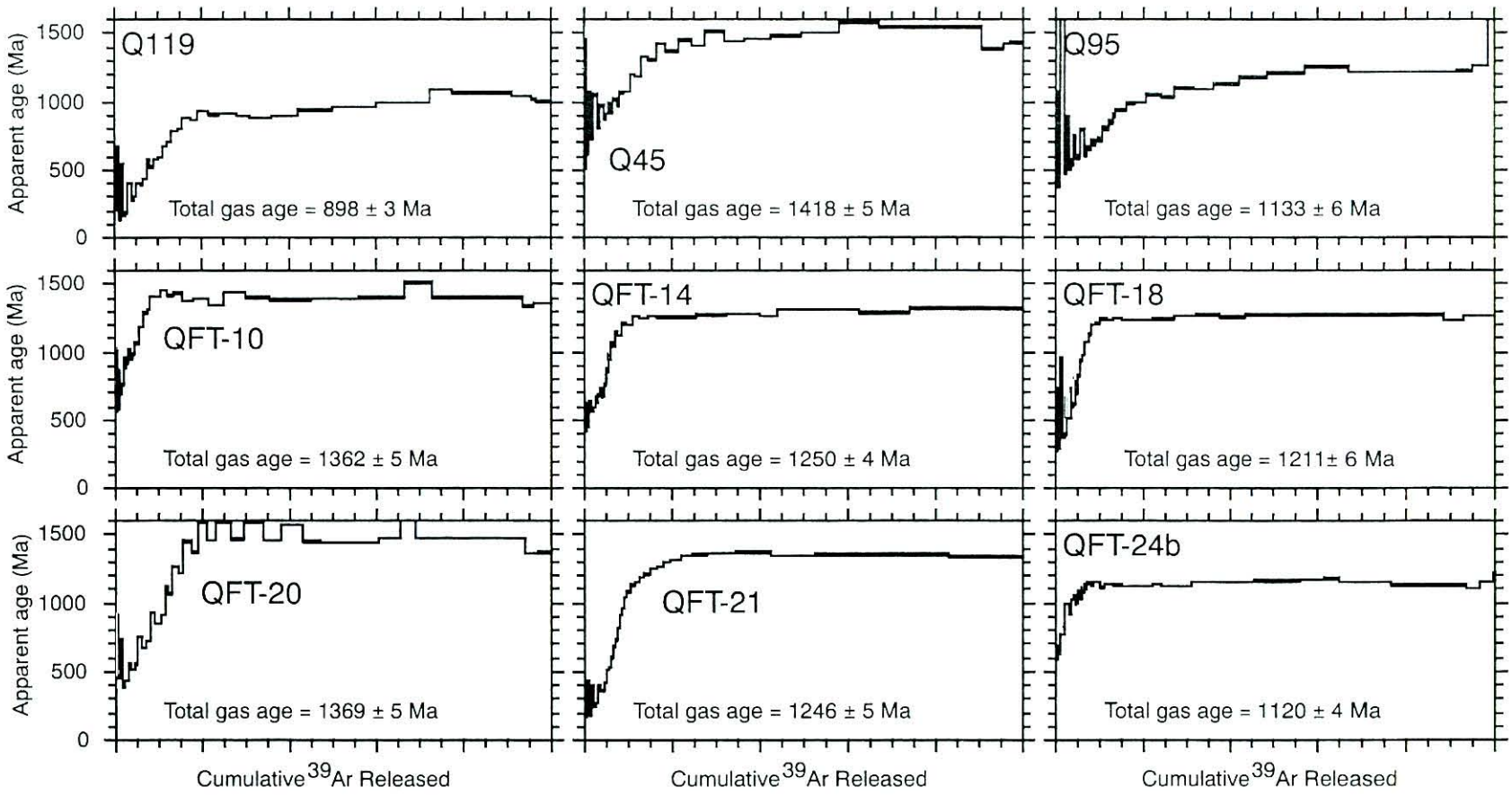

Figure 2-18: K-feldspar Ar-Ar spectra for the North Virgin Mountains

consequences to the amphibole age spectra with more subtle effects associated with ^{39}Ar recoil and argon loss (associated with complex geological histories) makes high precision interpretation of the amphibole spectra impossible. For instance, the 1524±52 Ma apparent age assigned to Q108 is anomalous relative to the other samples, however its age spectrum alone does not indicate any more complexity than the other samples. It is suggested that this sample has undergone partial argon loss following initial closure to argon diffusion (i.e. Shaw, 2001 unpublished PhD thesis) related to either alteration or reheating. Overall this sample does have high K/Ca and high bulk K_2O compared to the other samples and may indicate that it is pervasively contaminated with another less retentive phase.

The 4 amphiboles with apparent ages ranging from ~1630 to 1670 Ma are interpreted as recording the approximate time of argon closure. Based on various studies summarized in McDougall and Harrison (1999), the amphibole ages probably correspond to a temperature of ca. 500°C, consistent with structural and metamorphic observations, and preliminary U/Pb monazite ages, which suggest peak metamorphism (~700°C) and deformation occurred prior to 1700 Ma, and deformation through 1700-1600 Ma was marked by retrograde metamorphism and progressively lower temperature microstructures suggesting an amphibolite (>500°C) to greenschist (<500°C) facies thermal path.

Micas:

Like the amphiboles, the micas are variably complex (Figure 2-17, Appendix A). The biotite complexity is probably best explained by non-uniform internal age distributions resulting from extended periods near the mica bulk closure temperature and

argon loss associated with alteration. Many biotites show evidence for retrogression to chlorite, confirming the influence of the latter. Six of the 8 biotite samples have assigned ages of 1336 to 1514 Ma, whereas two samples are anomalously young (Q119, QFT-18) and are not assigned a plateau age. The highly disturbed and anomalously young QFT-18 sample is recognizably chloritized and has an apparent K_2O of only ~2%. Q119 also has overall low K (~6%) with most steps in the age spectrum ranging from 800 to 1000 Ma. The final low K biotite, Q60B, reveals apparent ages climbing to nearly 1420 Ma, and therefore low bulk K_2O does not necessarily always correlate to low apparent age. Biotite sample Q90A has an overall flat spectrum, but its age of 1514 Ma is much older than all the other biotites. A single muscovite (Q81) from the study area was analyzed and it reveals a fairly flat spectrum with an assigned age of 1375 Ma.

Considering the relatively small study area, there is substantial spread in the biotite apparent ages. There does not appear to be a systematic variation in biotite age relative to map pattern, therefore the wide range in apparent ages are thought to be related to variations in argon retentivity and local thermal history. Except for sample Q90A, the mica data are consistent with the interpretation that the region was above the nominal closure temperature (350°C) for micas and the complexity of individual spectra is probably related to partial argon loss related to the relatively high post 1.4 Ga temperatures, suggested previously by the U/Pb apatite data (pg 2-52), and by the K-feldspar data discussed below.

K-feldspars:

K-feldspar age spectra are characterized by significant age gradients that reflect the complex thermal history of the region. Several samples have initial ages younger than

525 Ma and therefore represent Cretaceous or Tertiary exhumation of basement that was above 150°C following deposition of the Tapeats Sandstone in the Cambrian. Samples nearest the Tapeats unconformity do not reveal ages younger than the Tapeats, despite their Miocene (15-10 Ma) apatite fission-track ages (Figure 3-5, Chapter 3), which approximate cooling through 110°C during that time interval. This suggests long residence (greater than 1100 m.y.) of this crust at temperatures between 250°C and 110°C.

In general, samples that reveal the most post 500 Ma argon loss also yield the youngest high-temperature age spectrum steps. This observation is consistent with deeper Precambrian paleodepths being exhumed during the Cretaceous and/or the Tertiary. Excess argon contaminating the initial apparent ages coupled with overall small degrees of Phanerozoic argon loss make it impossible to distinguish between exhumation in the Cretaceous versus the Tertiary (see Chapter 3).

Multiple diffusion domain thermal history modeling results for the K-feldspars are summarized in Figure 2-18, although several important details are not rigorously dealt with here. The models indicate temperatures passing between 250 to 350°C at about 1400 Ma, with some samples being above 300°C as late as ca. 1100 Ma (QFT-24b). Sample Q119 appears to record high temperatures as late as ca. 900 Ma and may explain the overall young biotite from this sample. However, this sample was found to be highly altered to sericite and therefore its utility as a reliable thermochronometer is suspect. The K-feldspar cooling histories recorded by these samples are similar to many others from throughout the Southwest USA and will be the subject of additional study that is not directly related to the high-temperature history of the NVM.

6. Paleoproterozoic tectonic evolution of the North Virgin Mountains

In the North Virgin Mountains, cryptic D_1 structures record northeast-southwest shortening and associated large nappe folds of unknown vergence. S_1 fabrics are associated with upper-amphibolite to granulite facies metamorphic textures and assemblages. Northwest-striking D_1 fabrics have also been documented in the Granite Gorges of the Grand Canyon (Ilg et al., 1996), the Cerbat Mountains (Duebendorfer et al., 2001), and the Grand Wash Cliffs (Albin and Karlstrom, 1991), all of which are within the eastern Mojave province. This northwest-trending D_1 fabric is also present in the Yavapai province in central Arizona (Karlstrom, 1988). Although the nature of the contact between these two provinces is still poorly understood, the similarity in D_1 fabrics across the boundary zone, and the ubiquitous high-temperature metamorphism associated with D_1 in the Mojave, suggests that S_1 may record evidence of Mojave – Yavapai crustal assembly and the suturing of these terrains between ca. 1740 and 1720 Ma (Duebendorfer et al., 2001).

The earliest deformations remain incompletely understood, but we speculate that the "exotic lithology" belt in the NVM may represent obducted pieces of a subducted oceanic lithosphere or slices of arc crust in an intraplate deformation zone. Distinguishing between these hypotheses is difficult and must be done geochemically (i.e. Karlstrom and Seaman, 2001). In either case, the juxtaposition of deep crustal rocks (ultramafic rocks) with quiet marine sedimentary rocks (cherts and pelites) and metabasalts (pillow lavas) represent dramatic vertical transport along these deformation

zones. The current NE-strike of these bodies does not necessarily confirm that they were emplaced during D_3, although this event was certainly characterized by intense vertical transport, given the abundance of L-tectonitized intrusions, juxtaposition of differing crustal levels across the VMSZ, and stretching structures such as strong lineations and sheath folds. Scattered ultramafic bodies south and north of the VMSZ may represent remnants of a severely dismembered suture zone that formed during D_1. Given the structural complexities created during orthogonal orogenesis, establishing the timing at which these ultramafic rocks were emplaced is difficult.

The D_2 event resulted in the formation of north-striking, subvertical fabrics that mostly obliterated the record of D_1 deformation. This was followed by the rotation and reactivation of S_2 into the northeast-striking S_3 orientation during D_3, synchronous with northwest-side-up thrusting along the VMSZ and intense granitic magmatism, probably a result of decompression melting in this region. While this event is best viewed as a progressive change in the strain field from E-W to NW-SE contraction, most lithologic contacts in the NVM (Domain III) strike to the northeast, confirming the intensity of NW-SE contractional strains associated with D_3. In the Lower Granite Gorge of the Grand Canyon, and elsewhere in the Yavapai province, Karlstrom and Bowring (1993) suggested that it is the northeast-striking S_2 foliation that records the amalgamation of the Mojave and Yavapai provinces at ca. 1700-1680 Ma with the rest of Laurentia. Jessup et al. (in prep) have provided an intriguing model whereby an arcuate subduction system (analogous to the Banda arc) collided with the Archean Wyoming province from 1.75-1.70 Ga, resulting in earlier NW-striking foliations, clockwise rotation of the strain field from NW to NE, and welding of terranes to Laurentia by 1.69 Ga. The similiarity in style

and chronology of structural overprinting in the North Virgin Mountains area may record similar continued progressive deformation in SW Laurentia.

The cessation of major granitic magmatism and consequent cooling of NVM crust was marked by the intrusion of leucopegmatite dikes, which locally cross-cut the higher temperature fabrics, and by progressively partitioned deformation, which continued to record northwest-side-up shearing under lowering temperature conditions (lower-amphibolite facies in Elbow Canyon). This D_3 event thus records a thermal continuum from penetrative upper amphibolite facies deformation to partitioned, ductile, lower amphibolite deformation conditions during NW-SE crustal contraction and associated crustal exhumation.

This NE-striking zone was reactivated during D_4 east-west contraction, resulting in complexly partitioned deformation consistent with various models of transpression. Inhomogeneous strains were partitioned into dextral strike-slip domains, "vertically extruding" pure shear domains, normal-sense "accommodational" domains, and reverse-sense contractional domains. These strain complexities arose more from pre-existing structural and rheologic anisotropies and inevitable infinitesimal strain heterogeneities (i.e. Robin and Cruden, 1994) than from changing far-field stresses, as metamorphic assemblages and textures, microstructures, and preliminary U/Pb monazite ages suggest that deformation within these zones was synchronous and related to WNW-ESE contraction and dextral transpression. The transition from D_3 to D_4 was marked by retrograde metamorphic reactions and formation of lower temperature microstructures indicative of upper greenschist facies deformation conditions, and rotation of vertically

dominated strain markers (lineations) into subhorizontal orientations (i.e. Cabin Canyon segment).

7. Implications for supercontinent Rodinia reconstructions

In reconstructing Precambrian plate configurations, where stratigraphic records are often absent, determining tectonic "fingerprints" of different Precambrian terrains may offer the best method to correlating crustal blocks that may once have been joined. The rifted western margin of Laurentia (including the Mojave province) formed during the Neoproterozoic breakup of the supercontinent Rodinia. The search for the rifted crust that once formed the continuation of the Mojave orogenic belt has led to controversial reconstructions juxtaposing Antarctica (SWEAT, Moores, 1991), Australia (AUSWUS, Karlstrom et al., 1999), Siberia (Sears and Price, 2000), and south China (Li et al., 1995) Proterozoic terranes with this rifted margin.

Preliminary 1600-1550 U/Pb monazite ages from the NVM are unusual for the southwestern United States. Other areas of 1600-1500 Ma deformation are known from eastern Australia (Betts and Giles, 2000), which may have been close to the Mojave province as proposed by the AUSWUS reconstruction (Karlstrom et al., 1999). Obviously, more detailed structural, metamorphic, and zircon and monazite geochronologic studies of the Mojave Province, such as this one, as well as further integrative studies of possible rifted counterparts, are required to resolve this issue.

9. Summary and conclusions (see Figure 2-19)

1. The heterogeneous metamorphic suite in the North Virgin Mountains of the eastern Mojave Province includes juxtaposed pillow basalt, marble, chert, calc-amphibolite gneiss, and ultramafic rock slivers. This tectonic mélange of "exotic lithologies" may represent ophiolitic fragments within an accretionary complex that was obducted during D_1 or early D_2 continental assembly and strongly deformed during D_3. This rheologically weak "suture zone", deemed the Virgin Mountain shear zone, was repeatedly reactivated during tectonic evolution of the NVM in response to the compressional stresses created during intracontinental orogenesis.

2. Four deformational events have been recognized in the North Virgin Mountains. D_1 is characterized by a northwest-striking, moderately northeast-dipping foliation that is axial planar to cryptically defined, macroscopic D_1 nappe folds of unknown vergence. D_2 is marked by intense steepening, refolding, and transposition of S_1 fabrics during E-W contraction. D_3 is marked by a rotation and transposition of S_1 and S_2 fabrics into a NE-striking, sub-vertical orientation during NW-SE contraction and NW-side-up thrusting. D_4 complexly reactivated the NE-striking S_3 foliation during E-W contraction, resulting in complexly-partitioned, dextral tranpressive strains

3. Hornblende Ar-Ar ages suggest NVM crust cooled through ~500°C between 1670 and 1630 Ma. Deformation within the VMSZ was still ongoing at this time, based on 1600 and 1550 Ma syn-tectonic monazite rim ages, sub 500°C (greenschist facies) metamorphic assemblages and textures, and sub 500°C greenschist facies microstructural estimates from mylonitic rocks. Deformation during this time period has not been

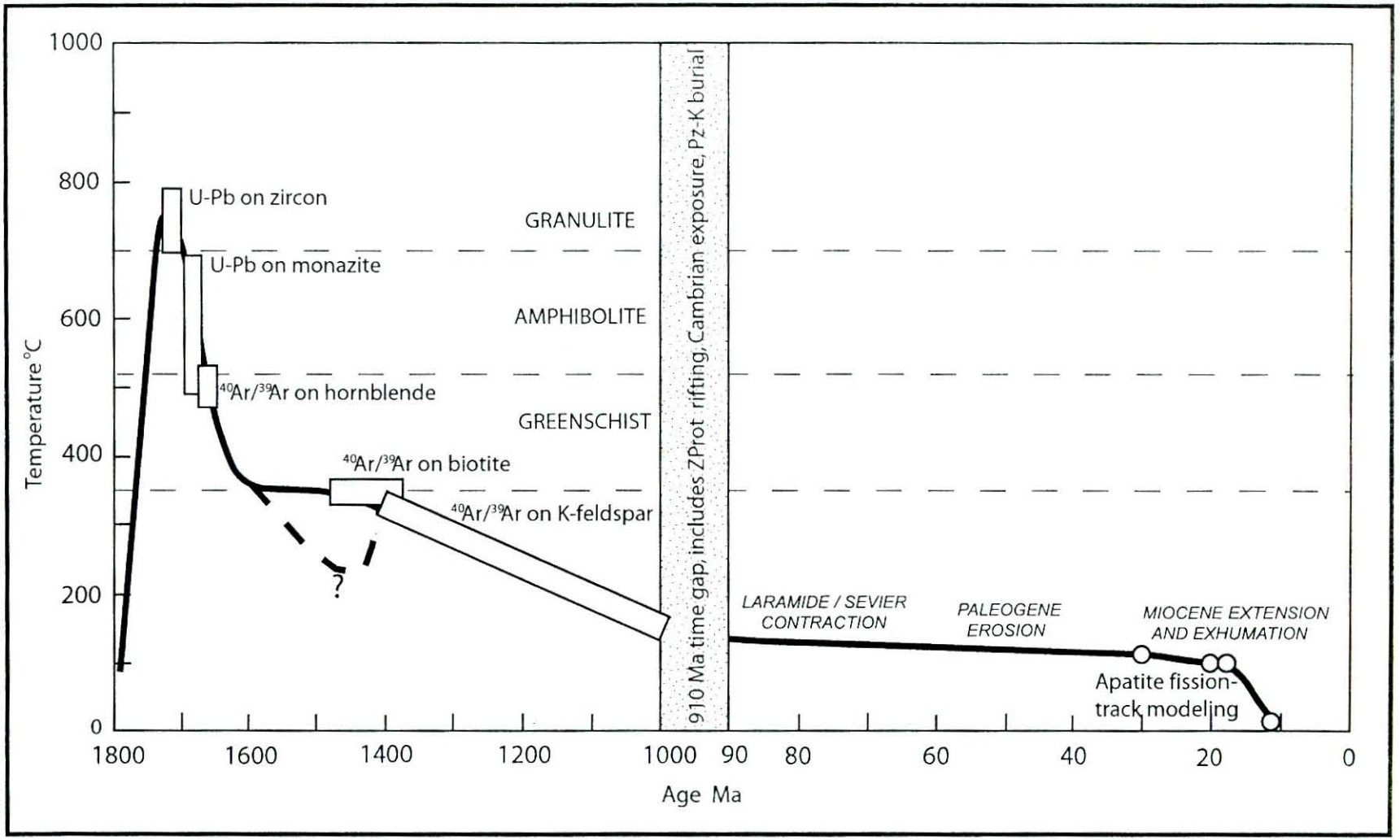

Figure 2-19: Generalized tectonothermal history of the North Virgin Mountains

previously documented in the southwestern United States, reaffirming the tectonic significance of the VMSZ as a substantially weak intracontinental deformation zone which may have accommodated far-field contractional deformation, generated at a continental margin more than 1000 kilometers to the east.

4. NVM crust cooled through 450°C at 1420 Ma and through 300-350°C by 1400 Ma, based on highly variable biotite Ar-Ar ages. Ar-Ar plateau ages up to 1515 Ma and 1545 Ma in biotite and K-feldspar respectively, suggest that the NVM crust may have cooled through 250°C in the early Mesoproterozoic, before localized reheating at 1.42 Ga. Younger ages are either a result of localized circa 1400 Ma heating, as observed throughout the southwestern United States, or complexities in Ar-Ar systematics. At present, we do not have evidence that deformation took place during circa 1400 Ma regional tectonism, despite the similarity in appearance of the VMSZ with circa 1400 Ma shear zones in the southwestern United States.

Chapter 3:

Influence of Proterozoic and Laramide structures on Miocene development of the Virgin Mountain anticline, southeast Nevada and northwest Arizona: Constraints from structural and apatite fission-track analysis

Mark Quigley and Karl Karlstrom, Department of Earth and Planetary Sciences, University of New Mexico

Shari Kelley, New Mexico Institute of Technology

1. Abstract

The northeast-trending Virgin Mountain anticline (VMA) of the North Virgin Mountains straddles the boundary between the unextended Colorado Plateau and the highly extended crust of the central Basin and Range province. The anticline is 50 km long and 2-8 km wide, is doubly-plunging, and is locally flanked by overturned Paleozoic strata on both limbs. The Proterozoic basement in the core of the VMA now resides at elevations of more than 2 km above sea level, roughly 2.5 km higher than the elevation of basement in the adjacent Colorado Plateau. The complex geometry of Miocene deformation and the high structural elevation of basement in this region was greatly simplified by Wernicke and Axen (1988), who interpreted the VMA as a short-wavelength, isostatically uplifted footwall resulting from top-to-the-west normal faulting. More detailed examinations of the VMA resulted in models invoking north-south shortening accompanying extension (Anderson and Barnhard, 1993), "tectonic rafting" or lower-middle crustal flow (Anderson et al., 1994; Langenheim et al., 2001), and/or large-offset strike-slip faulting (Beard, 1996; Campagna and Aydin 1994; Duebendorfer et al., 1998). The relative importance of Miocene isostatic versus tectonic forces remains

Chapter 3

Influence of Proterozoic and Laramide structures on Miocene development of the Virgin Mountain anticline, southeast Nevada and northwest Arizona: Constraints from structural and apatite fission-track analysis

Mark Quigley and Karl Karlstrom, Department of Earth and Planetary Sciences, University of New Mexico

Shari Kelley, New Mexico Institute of Technology

1. Abstract

The northeast-trending Virgin Mountain anticline (VMA) of the North Virgin Mountains straddles the boundary between the unextended Colorado Plateau and the highly extended crust of the central Basin and Range province. The anticline is 50 km long and 2-8 km wide, is doubly-plunging, and is locally flanked by overturned Paleozoic strata on both limbs. The Proterozoic basement in the core of the VMA now resides at elevations of more than 2 km above sea level, roughly 2.5 km higher than the elevation of basement in the adjacent Colorado Plateau. The complex geometry of Miocene deformation and the high structural elevation of basement in this region was greatly simplified by Wernicke and Axen (1988), who interpreted the VMA as a short-wavelength, isostatically uplifted footwall resulting from top-to-the-west normal faulting. More detailed examinations of the VMA resulted in models invoking north-south shortening accompanying extension (Anderson and Barnhard, 1993), "tectonic rafting" or lower-middle crustal flow (Anderson et al., 1994; Langenheim et al., 2001), and/or large-offset strike-slip faulting (Beard, 1996; Campagna and Aydin 1994; Duebendorfer et al., 1998). The relative importance of Miocene isostatic versus tectonic forces remains unconstrained, but we add the interpretation that geometry of Miocene structures was strongly influenced by pre-existing northeast- and north-trending structural grains created during Paleoproterozoic and Laramide tectonic events. Proterozoic influence is shown by the parallelism of all fault-bounded margins of the anticline with basement foliation and ductile shear zones. Laramide ancestry is suggested by outward-verging monoclinal reverse faults and associated flexures similar in style to Laramide-aged structures in the Colorado Plateau. The location and orientation of these structures are consistent with the regional systematic spacing and orientation of Laramide structures in the less extended Colorado Plateau to the east. Our structural studies suggest that Miocene extension (18-10 Ma) initiated through formation of steeply dipping normal faults in the Mesozoic and Paleozoic section that soled into basal detachments in the Cambrian Bright Angel shale and at the Great Unconformity, resulting in tectonic transport of allochthonous Phanerozoic sections over para-autochthonous Proterozoic basement. Similar fault geometries are observed throughout the South Virgin Mountains 50-80 km to the south, confirming the importance of low angle detachment faults during crustal extension in this region. Apatite-fission track (AFT) dates range from 21.7 ± 2.3 Ma directly below the Cambrian – Precambrian unconformity to 14.0 ± 2.5 Ma in the core of the VMA, indicating two distinct stages of exhumation and cooling. 21-19 Ma samples contain short AFT lengths (<13 μm) with large standard deviations (>2.5 μm), suggesting longer residence in the AFT partial annealing zone during 21-19 Ma slow erosional (pre-extensional) exhumation of a regionally elevated terrain (similar to Grand Canyon). 18-14 Ma samples contain longer AFT lengths (13-14 μm) with small standard deviations (<2 μm), suggesting rapid cooling through the AFT partial annealing zone at 18-14 Ma, and/or large-offset strike-slip faulting (Beard, 1996; Campagna and Aydin 1994; Duebendorfer et al., 1998). The relative importance of Miocene isostatic versus tectonic forces remains

interpreted to mark the onset of regional extension and associated rapid exhumation. Subaerial exposure of Proterozoic rocks of the Virgin Mountain anticline occurred at 16-10 Ma, as recorded in syn-extensional conglomerates of the Thumb Member of the Horse Spring Formation (Beard, 1996) and the Red Sandstone unit (Bohannon, 1984). Further transpressional deformation resulted in localized overturning of these sediments on the west flank of the VMA. Quaternary faulting along the west limb of the VMA continues to reactivate Proterozoic mylonite zones.

2. Introduction and regional setting

Detailed geologic mapping in the Lake Mead region of southeast Nevada and northwest Arizona (Longwell et al, 1965; Beal, 1965; Moore, 1976; Seager, 1972; Hintze, 1986; Wernicke and Axen, 1988; Anderson and Barnhard, 1993; Beard, 1993, 1996; Billingsley, 1995; Billingsley and Bohannon, 1995; Bohannon, 1991; Bohannon and Lucchitta, 1991; Williams et al., 1997, Quigley et al., 2001) delineated the sharp east-west structural transition from the essentially unextended Colorado Plateau to highly extended crust of the Basin and Range (up to several hundred percent extension; Wernicke et al, 1988). The boundary is locally sharp and defined by the Virgin-Beaver Dam breakway zone (VBBZ; Wernicke and Axen, 1988) and the Grand Wash fault (Figure 3-1). This boundary seems to have developed along the zone that was the hingeline for the Paleozoic Cordilleran miogeocline and the eastern extent of the thin-skinned Cretaceous Sevier thrust belt (Axen et al., 1990). This zone has apparently

remained weak since late Proterozoic crustal thinning related to rifting of Rodinia (Karlstrom and Humphreys, 1998).

The Colorado Plateau east of the VBBZ consists of a basement of Proterozoic high-grade gneiss and granitoids, non-conformably overlain by a roughly 2 kilometer thick, gently northeast tilted (<5 degrees) Paleozoic section and 1-2 km thick Mesozoic section. The Plateau was less affected by Mesozoic shortening and Miocene extension than the Basin and Range region, although monoclines and fault reactivation of Proterozoic high-angle faults in the basement (i.e. Timmons et al., 2001) record modest basement shortening and extension. Of importance to this study, areas to the west and south of the present-day Colorado Plateau were elevated relative to the Plateau in the late Mesozoic, resulting in southwest-directed deposition of Eocene "rim gravels" onto the Plateau. High topography to the south (Mogollon highlands) resulted in southward erosional beveling of the Phanerozoic section, and high topography to the west was a product of the Sevier thrust belt. We argue that both of these paleogeographic features influenced the structural and thermal architecture of the Virgin Mountain Anticline (VMA), the basement-cored, doubly plunging anticline targeted in this study. Unextended Colorado Plateau to the immediate west offers a template of what the VMA region may have looked like prior to Miocene deformation. The Plateau is segmented by curvaceous, north-striking, steeply dipping, basement-penetrating faults with systematic spacing of roughly five kilometers (Figure 3-1). These faults formed as normal faults mainly during Proterozoic inception of the Cordilleran miogeocline, were inverted to form reverse faults and monoclines in response to Late Cretaceous contraction (some preserve vertical offsets ranging from 100 to 500 meters), and were reactivated again

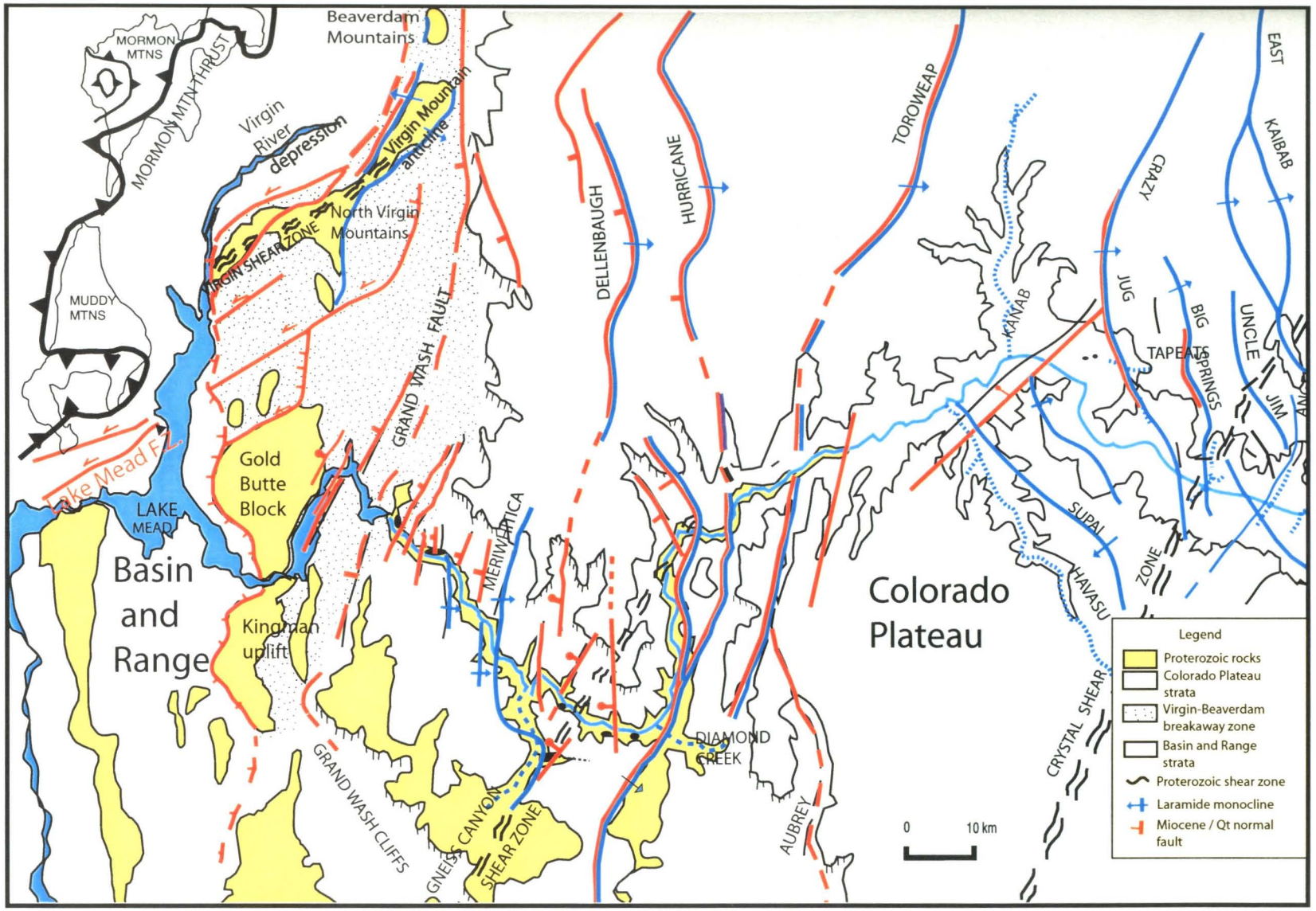

Figure 3-1: Geographic / tectonic position of the VMA of the North Virgin Mountains, between the Colorado Plateau and Basin and Range, and between Laramide monoclines and the eastern Sevier thrust belt.

during Miocene crustal extension (Huntoon, 1990; Timmons et al., 2001; Karlstrom et al., 1998). Some, like the Hurricane fault have remained active into the Quaternary (Stewart and Taylor, 1996). The Hurricane fault is one of a family of structures that had important Laramide slip (based on apatite fission track data, Naesser et al., 1989), before inversion by Miocene normal faulting (Figure 3-1), and we infer that the faults bounding the VMA may have had a similar history.

The Basin and Range west of the VBBZ consists of extensional allochthons of east-tilted Paleozoic through Miocene strata and a fault geometry that consists of complexly linked listric normal and steeply-dipping strike-slip faults. Miocene deformation strongly overprints the Late Jurassic to Cretaceous, thin-skinned Sevier thrust belt (Burchfiel et al, 1974), which broadly overlapped with the development of Late Cretaceous Laramide contraction faults (Dorr et al., 1977). Easternmost Sevier thrusts (the Mormon Mountains thrust, Axen at al., 1990; the Muddy Mountains thrust, Bohannon, 1983) propagated as far east as the present edge of the Colorado Plateau. Thus, the VBBZ, including the North Virgin Mountains, was in the zone of transition between thin-skinned Sevier and thick-skinned Laramide contractional deformation, just as it now is a zone of transition between extensional allochthons of the Basin and Range province that have been translated tens of kilometers to the west, and modest displacement high-angle normal faults of the Colorado Plateau.

Structural geometries vary greatly along the Colorado Plateau- Basin and Range boundary, and this variation is important in unraveling the history of the boundary zone. The Lake Mead region is characterized by dramatic north-south (as well as east-west) undulations in vertical structural relief of the basement-cover contact, producing

topographically high "domes" cored by exhumed Proterozoic rocks. These domes reach peak elevations exceeding 2440 meters in the North Virgin Mountains at Mount Bangs, 2000 meters in the Beaverdam Mountains, and > 1600 meters in the South Virgin Mountains (Gold Butte block). The correlative Proterozoic-Cambrian unconformity reaches depths of 8000 meters below sea level in the Virgin River depression (Figure 3-1), one of the deepest basins in the Basin and Range (Bohannon et al, 1993), 800-900 meters below sea level in the Virgin River Gorge (see Figure 1-1), and 1200-1300 meters below sea level at the base of the Hurricane cliffs.

An east-west transect of the Cambrian - Precambrian unconformity from the east edge of the Colorado Plateau to the Virgin River depression reveals a vertical relief of roughly 10 kilometers in a lateral distance of less than 20 kilometers (Figure 3-1). A roughly north-south transect from the Beaverdam Mountains to the South Virgin Mountains reveals an estimated vertical relief of this surface of six kilometers. The origin of the pronounced basement-cored uplifts within the Lake Mead region is highly controversial, and has been the focus of structural (Moore, 1972; Wernicke and Axen, 1988; Anderson and Barnhard, 1993; Anderson et al., 1994; Campagna and Aydin, 1994; Duebendorfer et al, 1998; Brady et al, 2001; Karlstrom et al, 2001; Quigley et al, 2001; this study), sedimentological (Beard, 1996), and geophysical (Bohannon et al., 1993; Langenheim et al., 2001) studies. We suggest that these structures have a Mesozoic contractional ancestry that was accentuated during Miocene extension. We note similar N-S complexities in the frontal thrust structure and interaction of thin-skinned and thick-skinned shortening in Wind Rivers area (Dorr et al., 1977) and Montana thrust belt.

3. The Virgin Mountain anticline

The Virgin Mountain anticline (VMA) in the North Virgin Mountains (Figure 1-1, 3-1) is a NE trending, generally fault-bounded anticline cored by highly deformed, granulite to amphibolite-grade Paleoproterozoic basement rocks. Detailed study of Proterozoic rocks in the core of the VMA (Quigley et al., 2001; Quigley et al., in review) confirms that it is a relatively intact and unrotated crustal block, quite distinct from the largely rotated Proterozoic core of the Gold Butte Block to the south (Figure 3-1). Localized internal faulting separates three parts to the core of the anticline; the NE-striking Black Ridge segment, the ENE-striking Bunkerville Ridge / Cabin Canyon segment, and the NNE-striking Mount Bangs segment (Figure 3-2). While each segment has a slightly differing architecture, the general geometry of sparsely faulted basement flanked by intensely faulted and folded Phanerozoic rocks permits charcterization of the gross structure as an anticline. The VMA core is flanked by relatively flat-lying Phanerozoic rocks to the northeast (the Colorado Plateau), north-dipping Paleozoic rocks to the north, and complexly folded and faulted Phanerozoic rocks to the west (Basin and Range) and southeast (VBBZ), forming the doubly plunging, east-tilted structure. The east limb of the VMA, although faulted, is mostly intact, consisting of moderately east-dipping Cambrian through early Miocene sedimentary rocks separated by erosional disconformities. North-northeast striking Cambrian through Triassic strata obtain vertical dips against the Spoon / Front fault in the vicinity of Mount Bangs (Figure 3-2, 3-8). Phanerozoic rocks along the west limb are highly attenuated, and exposed only in the far northwest and in Bunkerville Ridge (Figure 3-2). In the far northwest, the lower

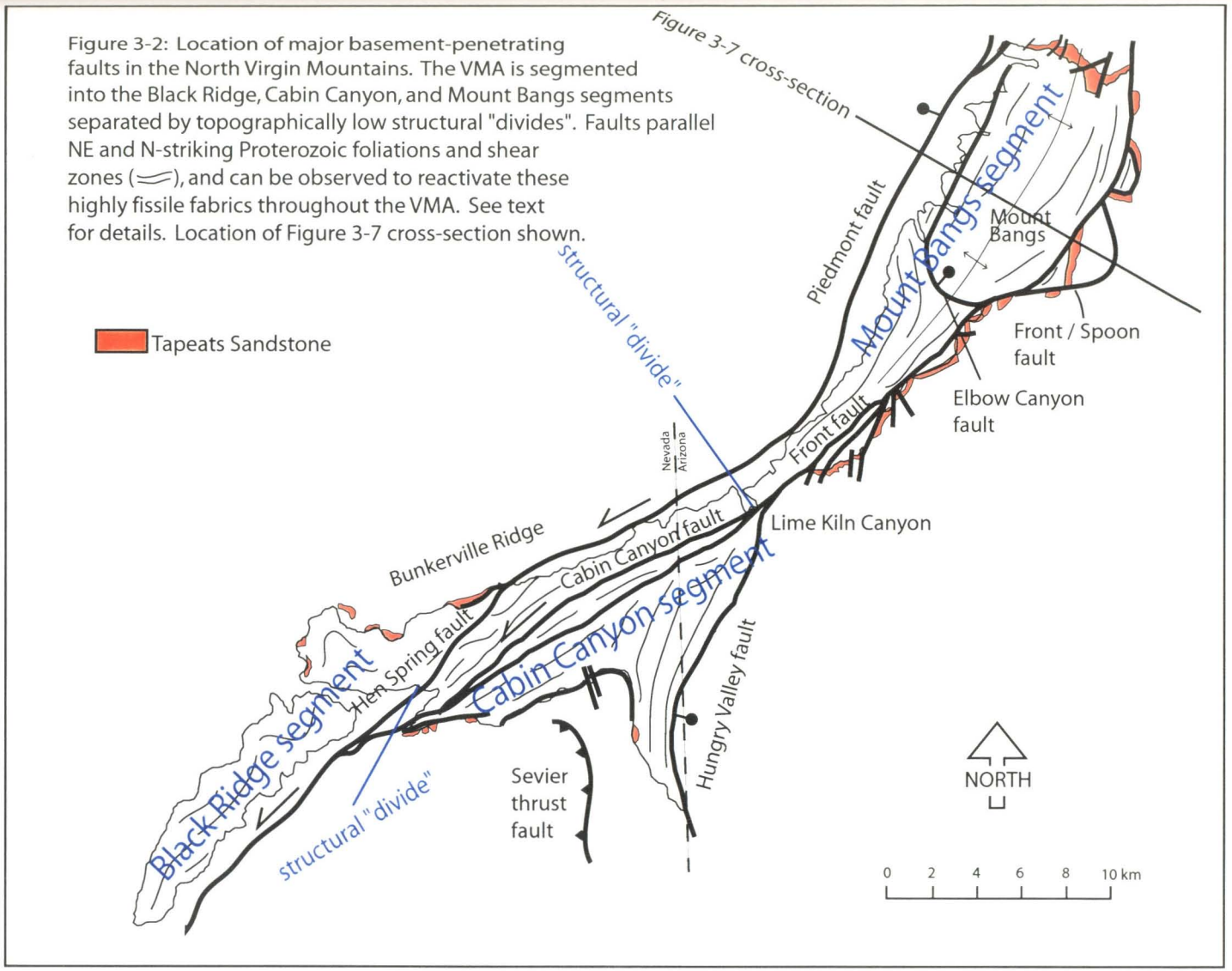

Figure 3-2: Location of major basement-penetrating faults in the North Virgin Mountains. The VMA is segmented into the Black Ridge, Cabin Canyon, and Mount Bangs segments separated by topographically low structural "divides". Faults parallel NE and N-striking Proterozoic foliations and shear zones (≈), and can be observed to reactivate these highly fissile fabrics throughout the VMA. See text for details. Location of Figure 3-7 cross-section shown.

Cambrian section is greatly thinned and overturned 50° to the east against Proterozoic rocks in a north-striking reverse fault relationship. Bunkerville Ridge is composed of east-northeast striking, subvertical to overturned late Paleozoic limestones, Mesozoic clastic rocks, and Miocene conglomerates, angularly overlain to the north by Pliocene and Quaternary alluvial strata of the Virgin River depression. Between these two areas, the western edge of the VMA is sharply defined by the steeply west-dipping, listric Piedmont fault (Figure 1-1, 3-2), which separates footwall Proterozoic rocks from the late Miocene-Pliocene Muddy Creek Formation, vertically offsetting the Proterozoic-Cambrian unconformity by roughly 8 kilometers (Bohannon at al., 1993). It is likely that the steeply NW tilted cover rocks exposed in the far northwest and Bunkerville Ridege are buried beneath the Muddy Creek Formation along this transect.

The position, orientation and geometry of this anticline are enigmatic. The VMA straddles the Colorado Plateau-Basin and Range boundary, with its northeast end essentially on the Colorado Plateau (although elevated) and its western end well into the Basin and Range province (Figure 3-1). The orientation of the VMA is clockwise to that expected for east-west shortening related to Mesozoic contraction, and has neither the orientation nor geometry expected for structures associated with roughly east-west Miocene extensional deformation (extension towards 260° in Lake Mead area, Anderson et al., 1994; west-northwest extension in the South Virgin Mountains, Brady, 2001). We propose that this orientation was strongly influenced by the orientation and geometry of older structures. The contractional nature of the VMA (folding and overturning of beds on its limbs and vertical uplift of basement rocks) is anomalous relative to the styles of extensional structures seen in the Basin and Range. VMA uplift-bounding reverse faults

strike and dip parallel to Miocene normal faults, leading early workers to propose that uplifts such as the VMA and Beaverdam Mountains were a product of Late Cretaceous contraction (Beal, 1965; Moore, 1972; Hintze, 1986), subsequently modified during Miocene extension. The presence of moderately east-tilted early Miocene sedimentary rocks disconformably overlying tilted Cretaceous strata on the east flank of the VMA (Wernicke and Axen, 1988; Figure 1-1, Plate 1), coupled with regional studies of fault systems and Miocene stratigraphy (i.e. Beard, 1996; Brady, 2001), basement apatite fission-tracks which yield middle Miocene ages (Fitzgerald, 1991), compressional-style folds and faults in Neogene strata (Bohannon, 1983) and geophysical studies of the Virgin River depression (Bohannon et al, 1993; Langenheim et al., 2001) led to the interpretation that basement uplifts such as the VMA were entirely Miocene in age, and that the pre-Miocene basement-cover contact in the region was "continuous and undeformed" (i.e. Langenheim et al., 2001). Reverse movements on north and northeast-striking faults and development of the dramatic structural relief of the VMA were interpreted as 1) footwall isostatic response to tectonic denudation (Wernicke and Axen, 1988); 2) structural culminations of the north-south shortening and three-dimensional strain complexities accompanying extension (Anderson and Barnhard, 1993); 3) linked strike-slip faulting and normal fault systems (Campagna and Aydin, 1994; Beard, 1996; Duebendorfer et al., 1998); or 4) upper crustal responses to heterogeneous middle or lower crustal flow (Kruse et al., 1991; Anderson et al, 1994; Bohannon et al, 2001). None of these studies considered the role pre-extensional structures played in determining the location, orientation, and geometry of structures such as the VMA. Furthermore, these recent studies have focused on explaining the complex structure of the

VMA solely as a result of a Miocene extension, neglecting the possibility of a Laramide contractional ancestry to this structure.

4. Reactivation of Proterozoic fabrics

Highly fissile metamorphic foliations in the Proterozoic basement rocks coring the VMA ubiquitously strike parallel to the VMA margins, suggesting a key linkage between these older fabrics and the genesis of the anticline. Structural mapping of the Proterozoic rocks revealed a complex history of Paleoproterozoic tectonism, resulting in north and northeast-striking, mostly steep foliations and lithologic contacts, and northeast-striking steeply dipping shear zones (Quigley et al, 2002, Figure 3-2). With few exceptions (Elbow Canyon fault, Hen Spring fault; Figure 3-2), the Phanerozoic reverse, normal, and strike-slip faults that cut the VMA core strongly reactivate these Paleoproterozoic foliations and lithologic contacts. Thus, Phanerozoic brittle deformation was partially controlled by the partitioning of far-field strains into weak zones within the Proterozoic crust.

The most notable of these structures is the northeast-striking Cabin Canyon fault, which brittlely reactivates the Paleoproterozoic Virgin Mountain shear zone throughout its strike length before merging with the Front Fault at Lime Kiln Canyon to the east and the Hen Spring fault to the west (Figure 3-2). Despite a paucity of kinematic indicators (i.e. slickenlines, offsets) the Cabin Canyon-Front fault has been interpreted as a Miocene strike-slip fault with 10-15 kilometers of left-lateral offset (Campagna and Aydin, 1994, Williams et al., 1997), based on piercing points within Proterozoic rocks. Detailed

mapping of these Proterozoic rocks (Quigley et al, 2002), however, reveals lithologic heterogeneity within the Proterozoic basement that precludes an accurate estimation of basement offset. Although left-lateral movement is conceivable, given demonstrated left-lateral displacement in faults of similar orientation to the south (Beard, 1996), offsets along this and other basement-penetrating faults are largely unconstrained due to the lack of viable piercing points.

The Front fault reactivates a ductile shear zone at the contact between granitic and metasedimentary gneiss east of Lime Kiln Canyon (Figure 3-2). The Hen Spring fault reactivates the Proterozoic foliation at the southeastern edge of Bunkerville Ridge, where it separates Paleozoic rocks from the basement. To the southwest, it cuts Proterozoic lithologic contacts, one of the few basement-penetrating faults in the VMA to do so (Figure 3-2).

The Piedmont fault and associated strands follow the strike of the north-northeast striking Virgin Mountain shear zone along the western margin of the VMA, and reactivate strongly developed foliation planes along the range front (Figure 3-2). Locally, reactivated segments of the Piedmont fault cut Quaternary fans, confirming that Proterozoic foliations continued to influenced fault orientations and geometries after the most intense period of crustal extension. On the west limb of the VMA in the vicinity of Mt Bangs, a segment of the Piedmont fault preserves reverse sense offset, suggestive of an earlier contractional history.

The basement-penetrating, Miocene extensional faults that segment the Colorado Plateau east of the VMA have had long histories of recurrent activity, with well documented Mesoproterozoic, Neoproterozoic, and Laramide movements that commonly

reactivated Paleoproterozoic basement foliations (i.e., Huntoon, 1990, Karlstrom et al, 1998; Timmons et al, 2001). We note that the major, basement-penetrating extensional faults bounding the VMA (Piedmont fault, Front fault, Hungry Valley fault; Figure 3-2) have similar geometries and parallelism with Proterozoic foliations, and thus infer that these faults probably had histories similar to those within the Colorado Plateau. Earlier movements along these faults undoubtably rendered them susceptible to reactivation during Miocene deformation, despite highly variable orientations with respective to the extension direction.

5. Laramide and Sevier contractional structures

Beal (1965), Moore (1972), and Beard (1993) mapped north- and northeast-trending thrust faults that cut Paleozoic and Mesozoic rocks in the North Virgin and Beaverdam Mountains. These faults, which were consequently folded and / or cross cut by normal or strike-slip faults (Beal, 1965; Moore, 1972), are interpreted to represent frontal thrusts of the Sevier belt, with lesser displacements than the proposed main frontal thrust exposed in the Mormon and Muddy Mountains to the west (Figure 3-1). In pre-extensional reconstructions (i.e., Axen et al., 1990; Duebendorfer et al, 1998) the Mormon and Muddy Mountains are juxtaposed with the Beaverdam and North Virgin Mountains, respectively, juxtaposing frontal Sevier thrust faults with the VMA region. Basement-penetrating, high-angle reverse faults are also present. In cross-sections of the VMA (Moore, 1972; Bohannon and Lucchitta, 1991), Paleozoic and Mesozoic rocks are upturned vertically against the northeast-striking, west-dipping Front – Spoon and Lime

Kiln reverse faults (Figure 3-2, see Figure 3-5), a geometry reminiscent of the systematically-spaced, basement-penetrating Laramide reverse faults and associated outward-verging, monoclinal forced folds of Phanerozoic strata in the Colorado Plateau (i.e. Meriwhitica, Hurricane monoclines). New mapping in the northwest corner of the VMA reveals a similar fault geometry, where tectonically thinned lower Cambrian Tapeats sandstone is overturned 46 degrees to the east and juxtaposed with Proterozoic basement along a north-striking, east-dipping reverse fault (Figure 3-3). The presence of "Sevier-style" thrust faults and "Laramide-style" reverse faults, the latter of which bound the Proterozoic core of the VMA to the east and west and strike orthogonal to the proposed extension direction, suggest that the pre-extensional Proterozoic-Cambrian surface was locally disrupted and elevated along paired monoclines bounding the initial VMA uplift (Figure 3-1). This uplift is supported by sedimentological studies of the pre-extensional Rainbow Garden Member (Beard, 1996) and is reasonable, given the tectonic position of the VMA between frontal thrusts of the Sevier belt and Laramide reverse faults of the Colorado Plateau. Projection of the systematic spacing interval of Laramide faults within the Colorado Plateau (Figure 3-1) would place reverse faults within the VMA, where these basement-penetrating faults of similar geometries and orientations exist.

6. Miocene structures

Many structural and tectonic studies in the Lake Mead region have focused on the geometry, timing, and kinematic significance of Miocene extensional faults, and we turn

Figure 3-3: Monoclinal west limb of the Virgin Mountain anticline, consisting of, from east (left) to west (right), 60 degrees west-dipping Muav Limestone, moderately west-dipping to sub-vertical Bright Angel Shale, sub-vertical to 46 degrees east-dipping-overturned Tapeats Sandstone, and Proterozoic gneiss. Similar geometries are commonly observed in Laramide-aged monoclines within the Colorado Plateau platformal sequences in the Grand Canyon, roughly 50 km to the east. The angularity in dip between the structurally competent Muav Limestone and Tapeats Sandstone is achieved through spectacular tectonic thinning and bedding "splaying" within the incompetent Bright Angel Shale. The inferred reverse fault that places Proterozoic gneiss at higher elevations than Muav Limestone in this area is interpreted to dip 46 degrees to the east, the dip of drag-folded Tapeats Sandstone at the Cambrian / Precambrian contact.

the reader to the following studies for a thorough treatment of these structures. Studies have centered on the significance of strike-slip faulting during crustal extension (Beard, 1996; Dubendorfer et al, 1998; Campagna and Aydin, 1994), the role of isostasy in generating basement uplifts (Wernicke and Axen, 1988), palinspastic reconstructions (i.e. Wernicke and Axen, 1988; Duebendorfer 1998), and the kinematic significance of low-angle normal faults (Wernicke 1984; Carpenter and Carpenter, 1988; Brady, 2000). The importance of strike-slip faulting and isostasy in generating the VMA uplift remains unconstrained, due to the lack of quantitative data supporting either of these processes (see *Tectonic Interpretation...*). Here we focus on low-angle normal faults mapped within the middle Cambrian Bright Angel shale and at the Great Unconformity (Figure 3-4), and present an alternative model for the structural evolution of the VMA in association with such faults. We interpret these extensional faults to have effectively decoupled the Proterozoic basement from the lower Cambrian section, and the lower Cambrian from the rest of the Phanerozoic section, and were consequently the major structures that exhumed the core of the VMA.

The contact between the Cambrian Tapeats sandstone and underlying Proterozoic rocks is, in many places, a zone of brittle detachment of allochthonous (translated and angular) blocks above autochthonous or paratochthonous basement (Figure 3-4). Similar relationships are observed between the Cambrian Muav limestone, the underlying Bright Angel shale, and the underlying Tapeats sandstone. In both cases, paratochtonous and allochthonous hanging wall fault blocks override sub-horizontal normal faults, which sole from steep dips within the Paleozoic section into basal detachment faults within the rheologically weak Bright Angel shale and near the Great Unconformity (Figure 3-4), the

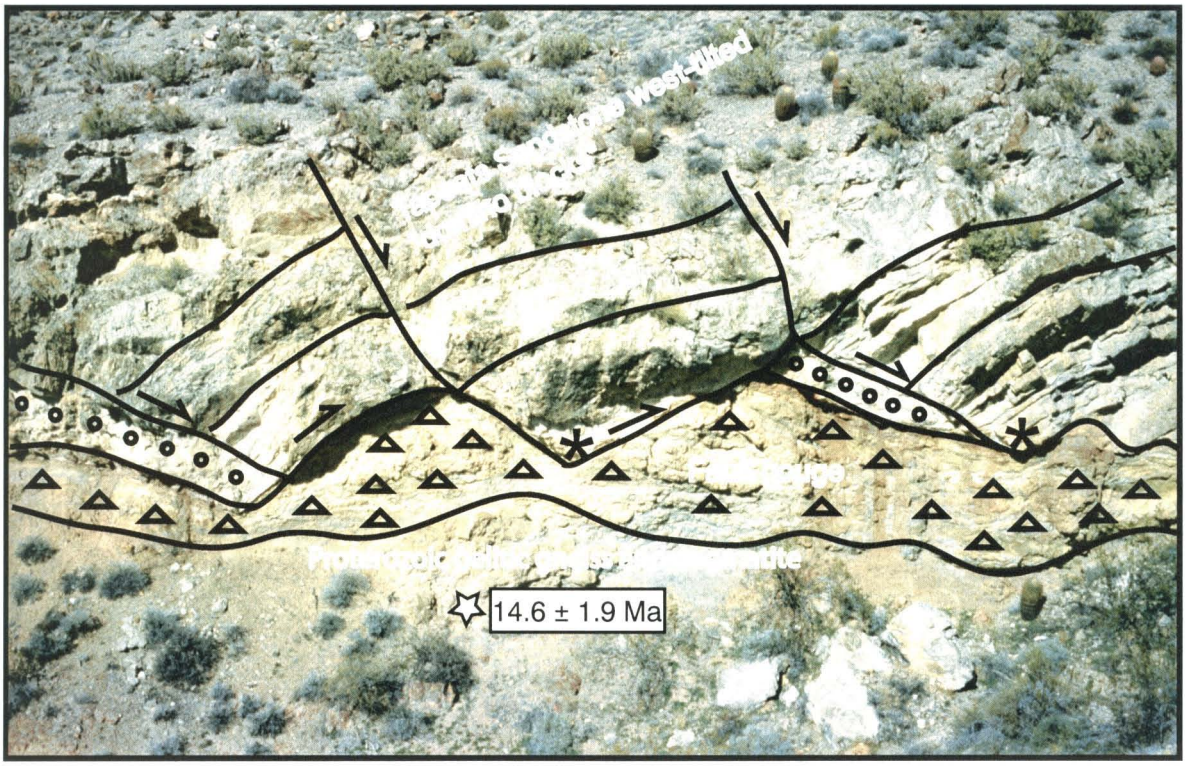

Figure 3-4: "Rosetta stone" outcrop of normal faults soling into a subhorizontal detachment fault, effectively decoupling basement from cover. This outcrop provides an analogue for the proposed regional detachment system as observed within the VMA and in the South Virgin Mountains (Karlstrom et al., in prep.) Allochtonous, west-tilted "domino blocks" of Tapeats sandstone overide para-autochtonous, sub-horizontal Tapeats cataclasite zones (open circles), fault gouge at the Great Unconformity (open triangles), and Proterozoic pelitic gneiss and pegmatite. The domino blocks are separated by moderately east dipping normal faults that sole out into a flat-lying detachment fault near or at the Great Unconformity, and do not appear to penetrate deeply into the Proterozoic rocks, although it is likely that some component of Proterozoic crust was removed during faulting. The allochtonous blocks dip roughly 50 degrees towards 335°, and also contain evidence of fault slip along bedding planes. The Tapeats cataclasite zones appear to have glided basally along, or close to the Great Unconformity during top to the SE movement along this detachment fault. This suggests that the detachment fault initiated and moved at low angles. The ultra-fine grained fault gauge is composed of low-grade alteration minerals (clays) and contains numerous conjugate normal faults and shear bands related to semi-ductile SE-NW extensional faulting. The Proterozoic rocks below it are partially altered and yield an apatite fission-track age of 14.6 Ma. The proposed extension direction is 120°, roughly perpendicular to the trend of "fault block corners" (*). See text for details.

latter of which represents a fundamental strength change from basally weak, vertically strong Tapeats strata to basally strong, vertically weak Proterozoic foliations. At their base, these faults are not unlike ramp-flat decollements, except they record crustal extension and translation of hanging walls along low angle (2-10°) fault planes, thought to be theoretically unfavorable for slip (*Anderson theory*, Anderson, 1944). Consequently, the Bright Angel shale displays dramatic tectonic thinning and angular (>60°) internal bedding refractions between overlying and underlying more competent strata. Normal and antithetic-normal faults within the Muav limestone are commonly so deflected by the Bright Angel shale that the base of the Bright Angel shale / top of the Tapeats sandstone contact is undeformed. The best-exposed example of these detachment faults in the VMA is at the north end of the VMA, where the Proterozoic core and overlying strata commonly dip 10-20 degrees to the north orthogonal to the east-west striking Great Unconformity (Figure 3-4).

Based on our structural data, the following conclusions are drawn regarding low-angle faulting in the VMA: 1) extensional block faulting along low-angle detachment faults extensively decoupled Proterozoic basement from its Phanerozoic cover, and was associated with extension towards 120° (i.e. towards the adjacent, relatively stable Colorado Plateau); 2) this style of deformation was presumably early in the period of Miocene extension, as the detachment surface now arches over the VMA core and gently dips "uphill" (west) where normal fault blocks show top-to-the-east, normal displacements (Figure 3-4). We do not discount the possibility that movement on the basal detachment was synchronous with doming of this surface, however we favor the former interpretation, given our assertion that doming of this fault surface was related to

the more dramatic, top-to-the-west normal faulting and exhumation of the VMA; 3) that similar detachment fault geometries observed throughout the South Virgin Mountains 50-80 km to the south (Karlstrom et al, in prep) confirm the regional presence of low angle detachment faults, and suggest that these faults were significant in controlling the geometry of Miocene crustal extension.

Development of west-dipping listric normal faults east of the VMA (i.e. Spoon fault, West Branch fault, Grand Wash fault, see "*Tectonic evolution...*") resulted in the wholesale eastward tilting of Phanerozoic strata on the eastern limb of the VMA. We interpret the VMA core to have resided in the hanging wall to these faults and the footwall to the major faults to the immediate west of the uplift (i.e. Piedmont fault), and not have been significantly tilted during this extension. The Piedmont fault system is interpreted to have been the major fault in exhuming the core of the VMA, providing its geometry is as we have interpreted it in the cross-sectional reconstructions.

7. Apatite fission-track thermochronometry

Sampling strategy and results

Samples for apatite fission-track (AFT) thermochronometry were collected from the Proterozoic core of the VMA in Februrary 2001. Sample preparation was done by Kelley and Quigley at the New Mexico Institute of Technology, and fission tracks were counted and measured by Kelley. The method is outlined in Appendix B, and the results are shown in Figure 3-5 and Table 3-1.

TABLE 3-1. APATITE FISSION-TRACK DATA FOR NORTH VIRGIN MOUNTAINS, NEVADA AND ARIZONA

Sample Number	Rock Type	UTM Coordinates	Elevation (m)	Number of Grains Dated	ρ_s x 10^5 t/cm^2	ρ_i x 10^5 t/cm^2	ρ_d x 10^5 t/cm^2	Central Age (Ma) (±1 S.E.)	$P(\chi)^2$ (%)	Uranium Content (ppm)	Mean Track Length (µm) (± 1 S.E.)	Standard Deviation Track Length
QFT1	granodioite gneiss	11S 0741414 4045720		20	2.23 (286)	8.32 (5323)	1.148 (4609)	**14.7±1.1**	99	87	13.9 ± 0.4 (61)	1.7
QFT2	granitic gneiss	11S 0743400 4048286		20	0.92 (118)	3.18 (2035)	1.151 (4609)	**15.9 ± 1.6**	99	33	-	-
QFT3B	quartz diorite	11S 0749392 4054220		20	2.06 (264)	7.7 (4929)	1.159 (4609)	**14.8 ± 1.1**	99	80	13.6 ± 0.4 (125)	2.1
QFT4	mylonitic granite	11S 0748044 4056172		5	0.68 (12)	2.29 (202)	1.159 (4609)	**16.4 ± 4.9**	>99	24	-	-
QFT5	granite below Tapeats ss.	11S 0747195 4056460		20	0.9 (115)	2.29 (1466)	1.161 (4609)	**21.7 ± 2.3**	95	24	12.9 ± 0.6 (71)	2.6
QFT6	mylonite	11S 0761956 4061148		20	0.64 (68)	2.09 (1102)	1.169 (4609)	**17.2 ± 2.3**	98	21	-	-
QFT7	granodiorite	11s 0767184 4062385		20	0.22 (23)	0.64 (339)	1.169 (4609)	**18.9 ± 4.1**	95	7	12.7 ± 2.0 (14)	3.9
QFT8	granodiorite	11s 0766531 4059572		20	0.85 (110)	3.21 (2054)	1.175 (4609)	**15.0 ± 1.6**	>99	33	14.7 ± 0.6 (36)	1.9
QFT10	monzonite and granite	11S 0234848 4066588		20	0.63 (79)	1.76 (1101)	1.176 (4609)	**20.1 ± 2.5**	91	18	13.1 ± 0.7 (61)	2.7
QFT12	mylonite	12S 0239721 4074546		20	0.36 (46)	1.06 (676)	1.184 (4609)	**19.2 ± 3.1**	99	11	13.4 ± 0.8 (13)	1.4
QFT13	granitic gneiss	12S 0239193 4074497		13	0.68 (57)	2.71 (1127)	1.186 (4609)	**14.3 ± 2.0**	85	27	-	-
QFT14	leucogranite summit Mt. Bangs	12S 0245335 4075485		15	0.46 (34)	1.87 (688)	1.189 (4609)	**14.0 ± 2.5**	99	19	-	-
QFT17	psammite	12S 0244732 4045895		20	0.77 (99)	2.94 (1883)	1.205 (4609)	**15.1 ± 1.7**	82	29	14.0 ± 0.5 (56)	1.9
QFT19	psammite	12S 0243912 4075937		20	0.37 (37)	1.43 (708)	1.212 (4609)	**15.1 ± 2.6**	>99	14	13.7 ± 0.8 (19)	1.8
QFT20	granite	12S 0242728 4077259		20	0.82 (100)	2.80 (1700)	1.220 (4609)	**17.1 ± 1.9**	99	28	-	-
QFT22	mylonite	12S 0241076 4078220		20	0.50 (63)	1.75 (1104)	1.221 (4609)	**16.6 ± 2.3**	>99	17	13.8 ± 0.7 (33)	2

TABLE 3-1. APATITE FISSION-TRACK DATA FOR NORTH VIRGIN MOUNTAINS, NEVADA AND ARIZONA

Sample Number	Rock Type	UTM Coordinates	Elevation (m)	Number of Grains Dated	ρ_s x 10^5 t/cm^2	ρ_i x 10^5 t/cm^2	ρ_d x 10^5 t/cm^2	Central Age (Ma) (±1 S.E.)	$P(\chi)^2$ (%)	Uranium Content (ppm)	Mean Track Length (µm) (± 1 S.E.)	Standard Deviation Track Length
QFT23	biotite schist	12S 0243296 4083542		20	0.49 (61)	1.81 (1131)	1.167 (4609)	**15.0 ± 2.1**	>99	19	14.3 ± 1.5 (4)	1.5
QFT24A	fractured granite	12S 0244469 4083477		11	0.43 (29)	2.31 (776)	1.167 (4609)	**10.4 ± 2.0**	92	24	-	-
QFT24B	biotite gneiss	12S 0244469 4083477		20	0.66 (68)	2.53 (1296)	1.167 (4609)	**14.6 ± 1.9**	90	26	-	-

ρ_s - spontaneous track density ρ_i - induced track density (reported induced track density is twice the measured density)

Number in parenthesis is the number of tracks counted for ages and fluence calibration or the number of track measured for lengths.

ρ_d - track density in muscovite detector covering CN-6 (1.05 ppm); Reported value determined from interpolation of values for detectors covering standards at the top and bottom of the reactor packages (fluence gradient correction)

S.E. = standard error $P(\chi)^2$ = Chi-squared probability - = no data

$\lambda_f = 1.551 \times 10^{-10} yr^{-1}$, g=0.5 zeta = 4772 ± 340 for apatite

Mean track lengths not corrected for length bias (Laslett and others, 1982)

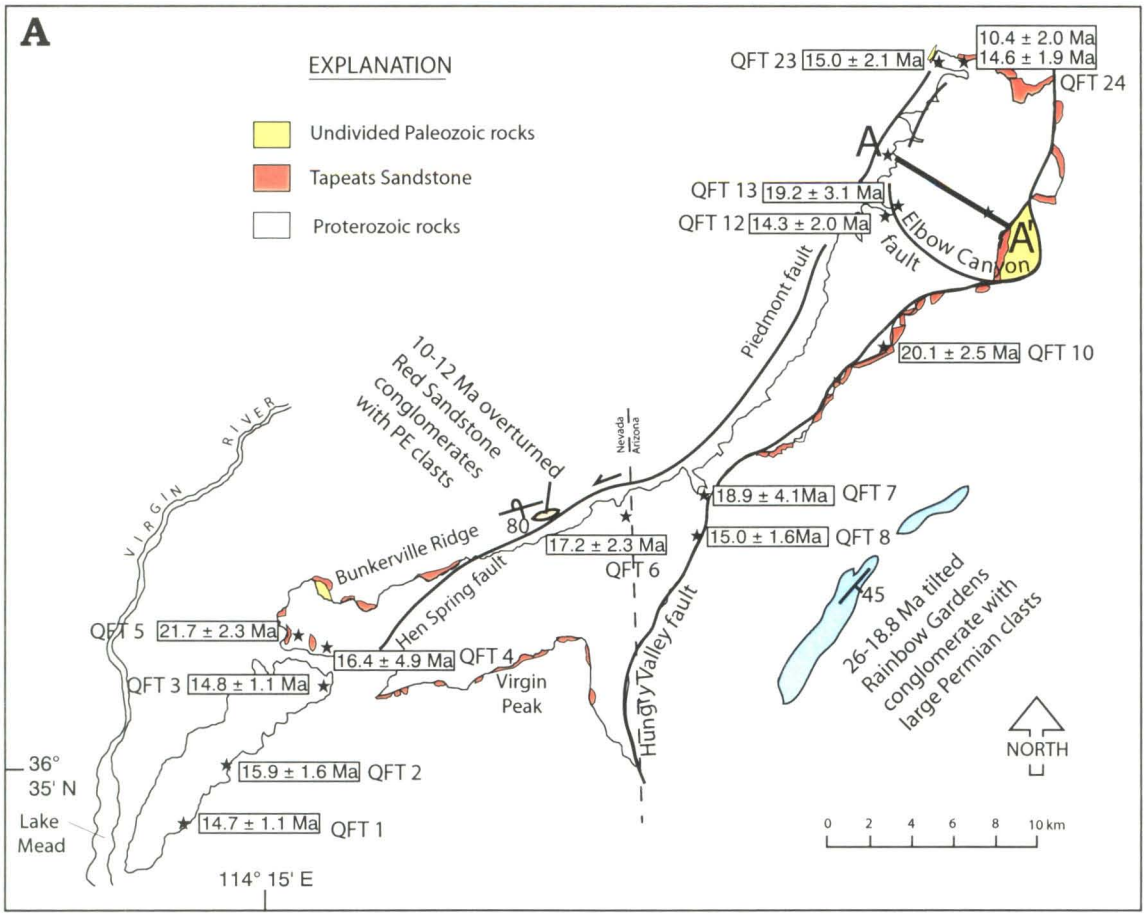

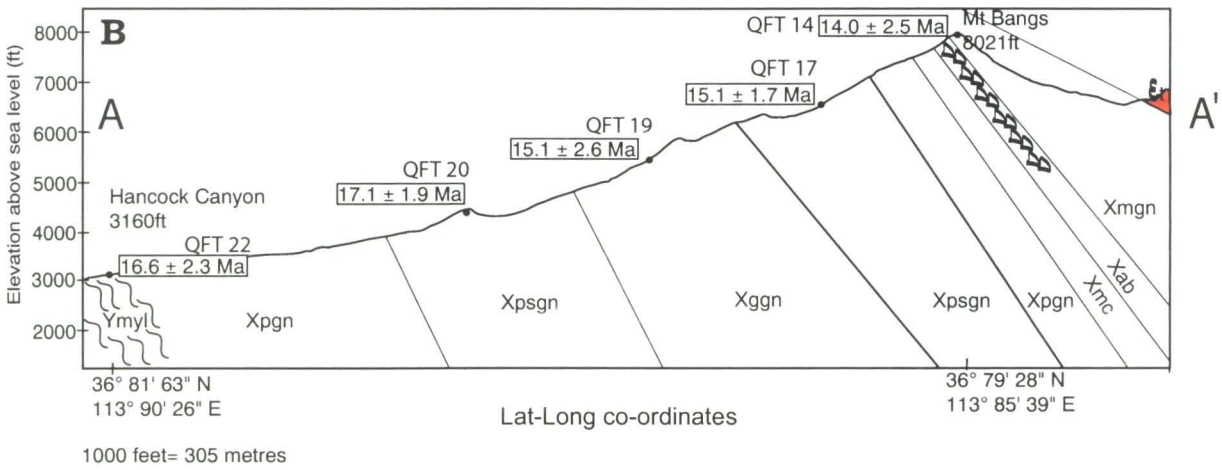

Figure 3-5: Apatite fission track data from the Virgin Mountain anticline, with important structural and sedimentary / tectonic features. Cross-section A-A shows results from the age-elevation traverse. See text for details and interpretation.

Samples QFT 1, QFT 2, QFT 3B, QFT 4, QFT 6, and QFT 7 were collected away from major structures in order to obtain spaced AFT coverage of the VMA (Figure 3-5). Ages range from 18.9 ± 4.1 Ma to 14.7 ± 1.1 Ma and appear to decrease from west to east, although exceptions exist (QFT 3B). Although we could consider these ages to be statistically equivalent, track lengths from the youngest samples (13.6 ± 0.4 μm, 13.9 ± 0.4 μm) are long relative to the track length from the oldest sample (12.9 ± 0.8 μm, Table 3-1), although the latter sample has only 14 confined tracks. Furthermore, 1.7-2.1 standard deviations of track length from the youngest samples are small relative to the older sample (3.9, Table 3-1). Samples QFT 5 and QFT 10 were collected 1 meter and roughly 400 meters below the Great Unconformity, respectively, where the overlying Tapeats Sandstone rests in depositional contact (autochthonous). The samples should represent the shallowest levels of Proterozoic crust in the VMA, and yield the oldest AFT ages; QFT 5 yields the oldest AFT age in the VMA (21.7 ± 2.3 Ma), and QFT 10 the second oldest (20.1 ± 2.5 Ma, Table 3-1).

Sample QFT 8 was collected from the Proterozoic footwall of the Hungry Valley fault in Lime Kiln Canyon (Figure 3-5) in order to estimate the amount of offset which may have occurred along this structure, similar to studies of Laramide faults by Kelley et al (2001) in the Grand Canyon. This sample could not prove or disprove Laramide movement on the Hungry Valley fault, as it was at temperatures above 110°C (AFT annealing zone, age = 0) until 15 Ma. Samples QFT 12 and QFT 13 were collected on either side of the Elbow Canyon fault (Figure 3-5A), in order to test Anderson and Barnhard's (1993) hypothesis that significant north tilting and offset of the basement culminations took place along this south-dipping fault. We expected to find the younger

AFT age on the north side of the fault (upthrown block), however, this turned out to be the older age. If the age difference reflects the earlier cooling of QFT 12, it may represent a slightly higher crustal level than QFT 13, and would suggest either post 14 Ma, north-side–down normal movement along a north-dipping fault, or reverse sense movement along a south-dipping fault. Given the right-lateral offset of Tapeats sandstone where the Elbow Canyon fault merges with the Front / Spoon fault (Figure 3-2, 3-5A), we believe the former to be true, contradictory to Anderson and Barnhard's (1993) interpretation of northward tilting of the north block relative to the south block across a south dipping normal fault, which would have resulted in exposure of deeper crustal levels north of the fault.

Samples QFT 14, QFT 17, QFT 19, QFT 20, and QFT 22 were collected along an age-elevation traverse from the peak of Mount Bangs (2442 meters) to the opening of Hancock Canyon (900 meters, Figure 3-5B), to determine if a fossil geotherm is present over a possible crustal depth of 1500 meters. AFT ages range from 14.0 ± 2.5 Ma at the peak of Mount Bangs to 17.1 ± 1.9 Ma, and do not record younging AFT age with decreasing elevation, as would be expected for a vertically deepening crustal profile (i.e. Naeser, 1979; Fitzgerald and Gleadow, 1990, and references therein, See *Discussion and Interpretation*).

Sample QFT 23 was collected 50 meters east of the monoclinal reverse fault in the northwest corner of the VMA, and similar to QFT 8, yields a 15 Ma age neither indicative nor disproving of Laramide movement on this fault. Samples QFT 24A and QFT 24B were collected from Proterozoic rocks 1 meter and 5 meters beneath the basal

detachment fault at the Great Unconformity (Figure 3-4, 3-5). QFT 24A was collected from strongly altered fault gouge, and yields an anomalously young age (Table 3-1). QFT 24B yields a young age (14.6 ± 1.9 Ma) given its position beneath the Great Unconformity. Since this boundary zone is heavily faulted and overlain by para-autochthonous and allochthonous Tapeats sandstone, and the top 2-3 meters of Proterozoic basement is heavily altered and consists of fault gouge, this young age is consistent with removal of some Proterozoic crust during initial detachment faulting and/or later deformation and exhumation (Figure 3-4).

Discussion and Interpretation

Apatite fission-track ages and track lengths from the VMA range from 22 Ma to 14 Ma and 12.7 μm to 14.7 μm (Table 3-1), indicating that VMA crust below the Great Unconformity cooled through ~110°C in the middle Miocene. Here we address and provide tectonic interpretations for four main trends in the data: 1) apparent southwestward younging of AFT ages from Cabin Canyon (QFT 6, Figure 3-5A) to Black Ridge (QFT 1, Figure 3-5A); 2) lack of a vertical age profile from the age-elevation traverse at Mount Bangs (Figure 3-5B); 3) shorter track lengths in 22-20 Ma samples relative to 14-17 Ma samples; and 4) regionally "young" (22-20 Ma) AFT ages from directly below the depositional contacts with the VMA Great Unconformity (QFT 5, QFT 10), relative to their structurally equivalent counterparts below the Gold Butte Block and the western Colorado Plateau unconformities.

Our interpretation of the apparent southwestward younging of AFT ages, from 18.9 ± 4.1 Ma in Lime Kiln Canyon and 17.2 ± 2.3 Ma in Cabin Canyon to 14.7 ± 1.1 Ma in southwest Black Ridge, is that they may record the progressive exhumation of a semi-coherent VMA footwall block during top-to-the-southwest transport of hanging walls shallowly soutwest-dipping normal faults. In our interpretation, Black Ridge was still thermally insulated (i.e. buried beneath >3-4 kilometers of crust) while the Cabin Canyon and Lime Kiln Canyon crust was exhumed to shallower than 3-4 kilometer paleodepths. This interpretation assumes minimal movement on the Hen Spring Fault, which would greatly complicate the pre-extensional position of Black Ridge and Bunkerville Ridge relative to the Cabin Canyon segment of the VMA core. We recognize that this assumption is controversial (see Campagna and Aydin, 1994, Williams et al., 1997), and also recognize that these AFT sample distributions would be greatly complicated by basement-penetrating deformations.

The age-elevation traverse at Mount Bangs records no evidence suggestive of a crustal profile, indicating that either exhumation was too rapid to record paleodepths below the fossil partial annealing zone depth (i.e Gold Butte Block), and/or samples are from a similar crustal depth due to a "domed" crustal profile (Figure 3-5). Both scenarios are likely, given the rapid rate of regional extension (Brady et al., 2001) and the arched geometry of the Great Unconformity over the north-dipping Proterozoic core of the northern VMA, respectively. If a trend can be taken from the data, ages appear to "young" towards higher elevations, suggesting that the apatite PAZ may have been domed during or after cooling of these rocks through their closure temperatures (see Figure 3-5 and "Tectonic Interpretation" section).

The two oldest AFT ages (21.7 ± 2.3 Ma and 20.1 ± 2.5 Ma, Figure 3-5) come from 1 meter and 400 meters, respectively, below the Great Unconformity, which separates Proterozoic rocks from autochthonous (depositionally intact) Tapeats Sandstone. These ages are regionally important because they are significantly younger than AFT ages from just below the Great Unconformity in the western Grand Canyon (61-45 Ma; Naeser et al, 1989; Kelley et al, 2001) and the Gold Butte block (50-34 Ma; Fitzgerald et al., 1991; Reiners et al., 2000), but predate the onset of extension in the Lake Mead region (circa 18 Ma). Mean track lengths associated with these samples range from 13.4 μm to 12.8 μm (Naeser et al, 1989; Fitzgerald et al., 1991; Kelley et al, 2001; Table 3-1), notably shorter than track lengths associated with 17-14 Ma AFT ages (13.6 μm to 14.7 μm, Table 3-1, Fitzgerald et al., 1991). Coupled with large standard deviation track lengths (>2.5, Table 3-1), the short track lengths suggest protracted residence of 22-20 Ma samples within the AFT partial annealing zone (110°C - 70°C), probably beginning at 26 Ma (Kelley, person commun). The similarity in track length and standard deviation length in samples ranging from 61 Ma (Kelley et al., 2001) to 20 Ma suggests regional, long-lived, slow cooling over a 40 Ma time interval. This represents regionally persistent Paleocene to early Miocene erosion, consistent with sedimentological and tectonic studies (i.e. Beard, 1996). The onset of Miocene extension is marked by the abundance of 17-14 Ma AFT ages with long track lengths from the Gold Butte block and the VMA, which suggest rapid exhumation of these crystalline terrains during the middle Miocene, in agreement with dating of ashes in syntectonic sediments (Beard, 1996), and structural studies.

The relatively young 22-20 Ma VMA AFT ages beneath the VMA Great Unconformity, when compared to the 90-50 Ma ages of identical structural position in the Gold Butte block and the Grand Canyon, can be resolved when considered in the context of pre-extensional paleogeography (Figure 3-6). In the Eocene, erosional beveling of Phanerozoic strata from the northeast, where the VMA was overlain by >5 kilometers of Cambrian through Cretaceous strata, to the southwest, where the Gold Butte block was overlain by 2.5 kilometers of Cambrian through Permian strata, to the far southwest, where the Kingman uplift was aerially exposed (Young, 1979), reflected the gentle north-dip of the Great Unconformity and consequent northward deepening of the Proterozoic-Cambrian contact. Assuming a regionally consistent geotherm of 25°C / kilometer, the top 1.5 kilometers of the Gold Butte block resided in the AFT partial annealing zone during this time, confirmed by the 50 Ma to 34 Ma ages recorded at 0.1 to 1.2 kilometer paleodepths below the Great Unconformity (Fitzgerald et al., 1991). Conversely, the base of the AFT partial annealing zone was present *above* the Great Unconformity at the VMA, due to the increased thickness of Phanerozoic section. Proterozoic rocks exceeded temperatures of 110°C, and AFT ages below the Great Unconformity were zero due to full annealing of tracks. Steady erosion from the Paleocene to early Miocene eroded most of the Cretaceous section in the VMA, and began to expose Permian rocks in the North Virgin Mountains by circa 25 Ma (Beard, 1996). Preliminary AFT modeling (see Appendix B) suggests that QFT 5 may have entered the AFT partial annealing zone at this time. By 22-20 Ma, still prior to extension, rocks immediately beneath the Great Unconformity in the VMA were well within AFT partial annealing zone temperatures (110-70°C), due to erosion of overlying Mesozoic strata (Figure 3-7).

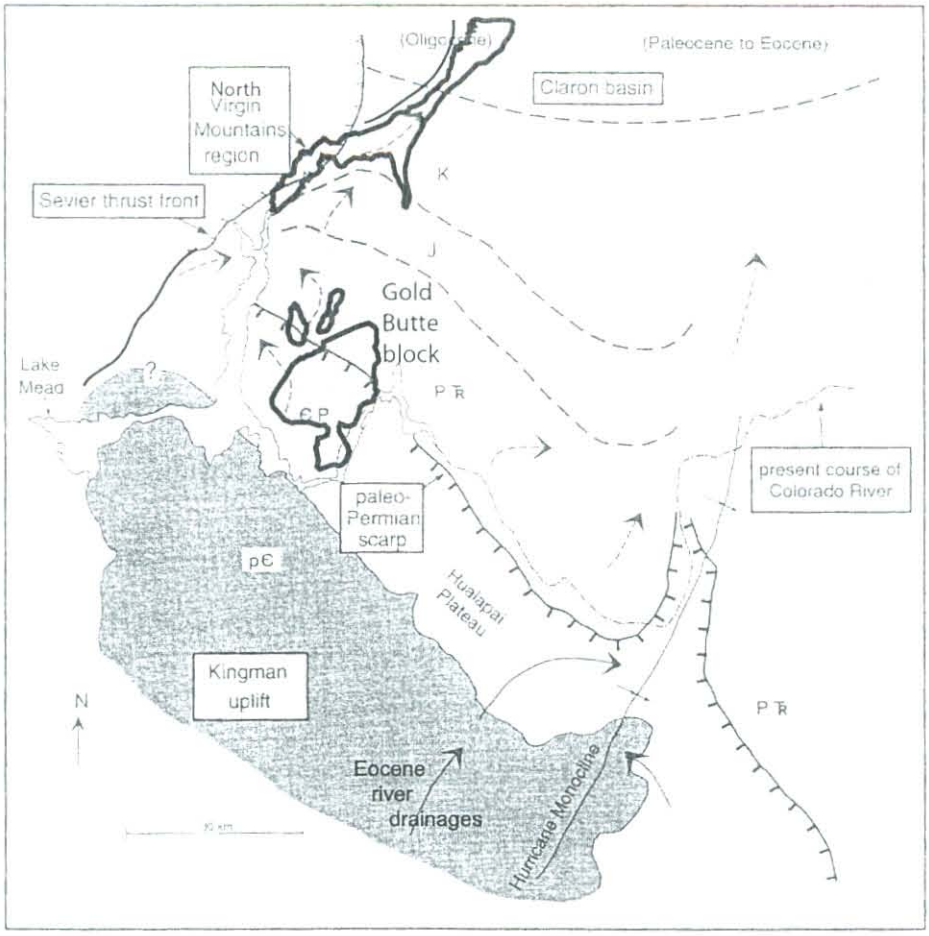

Figure 3-6: Simplified paleogeographic sketch map of southeastern Nevada and northwestern Arizona during the early Cenozoic, modified from Beard (1996) and references therein. Inferred location of the Kingman uplift from Young (1979) and Bohannon (1984). Erosional beveling of strata from NE to SW shown by inferred Eocene surface contacts between EP (Cambrian through Permian strata); PT (Permian to Triassic strata); J (Jurassic strata); and K (Cretaceous strata). Present positions of the Proterozoic core of the Gold Butte block and North Virgin Mountains (VMA) shown by heavy lines. During this time, prior to extensional unroofing, Proterozoic rocks of the Kingman uplift were exposed, those at Gold Butte were buried beneath 1-2 km of Paleozoic strata, and those at the North Virgin Mountains were buried beneath more than 4 km of Paleozoic through Cretaceous strata. The northward-thickening Phanerozoic section reflects the gentle north dip of the top-of-Proterozoic surface from the Kingman uplift to the North Virgin Mountains. See text for details.

Similar southward beveling on the Colorado Plateau probably accounts for the Eocene AFT ages in the western Grand Canyon, which lies 50-60 kilometers southeast of the VMA. AFT ages below the Great Unconformity should also decrease westward into the Basin and Range, with the increased depositional thickness of Paleozoic strata within the miogeocline, and increased structural thickness of the Phanerozoic section due to thin-skinned Sevier thrusting. Thus we expect pre-extensional Proterozoic crust in the VBDZ to have been hotter northward, parallel to the miogeoclinal edge and Sevier front, and hotter to the west, into the thrust terrain.

8. Tectonic evolution of the VMA and regional implications

We summarize our best hypothesis for the Late Mesozoic to recent tectonic evolution of the Virgin Mountain anticline as follows (see Figure 3-7);

1. In the late Cretaceous, thrusting within the eastern Sevier belt began to overlap spatially and temporally with development of basement-penetrating Laramide faults east of the Paleozoic miogeocline (i.e. Dorr et al., 1977), where contraction produced steep reverse faults and monoclinal drag-folds in Phanerozoic rocks in the Grand Canyon (i.e. Huntoon, 1990). Paired east and west-dipping monoclines developed in the foreland of the Sevier thrust belt, locally forming the west and east limbs of an anticline (the VMA), respectively (Figure 3-7A). The Proterozoic basement core in parts of this structure was vertically uplifted an estimated 3 kilometers, relative to strata to the east (Figure 3-7A), along a northeast-trending axis, the orientation of which was strongly controlled by basement foliations. Similar structures developed at systematic spacing intervals

Figure 3-7: Simplified cross-sectional reconstructions of the Virgin Mountain anticline, from east (right) to west (left), location shown on Figure 3-2. No vertical exaggeration. Difficulty in balancing cross-sections is a result of probable out-of-plane motion on Piedmont and Spoon faults, although unconstrained.

Circa 25 Ma cross-section, Figure 3-7A: Pre-extensional geometry of the Virgin Mountain anticline, bound by the North Monocline, an unnamed monocline to the east, and Spoon / Front reverse faults. The Proterozoic core of the VMA, although elevated, is overlain by > 4km of Paleozoic and Mesozoic strata, placing sub-unconformity Proterozoic basement at temperatures above the AFT partial annealing zone (see text). Thickness of the post-Laramide, pre-25 Ma Mesozoic section as shown by dashed line, inferred from regional thicknesses of the Moenkopi and Navajo Formations. Early Cretaceous section eroded from this area, as marked by deposition of Rainbow Gardens on Jurassic Navajo Sandstone, however Cretaceous strata lie beneath Rainbow Gardens conglomerate 5-10 kilometers to south (Bohannon, 1991; see Plate 1), suggesting pre-25 Ma undulating structural topography. Rainbow Gardens basal conglomerate is being actively deposited in the Tom and Cull Wash area, and contains large Permian clasts (Beard, 1996), derived from the hanging wall of the east monocline fault in our model.

Circa 18-16 Ma cross-section, Figure 3-7B: Early extensional geometry of the VMA, marked by the initiation of Miocene extension along steep, east-southeast dipping normal faults which sole into a subhorizontal detachment fault system within the Bright Angel Shale and at the Great Unconformity ("SE-side down movement on detachment faults", see Figure 3-4). The North Monocline fault reactivated in normal sense. Rainbow Gardens Member conglomerate is aerially exposed, suggested by absence of the overlying 18-14 Ma Thumb Member in the North Virgin Mountains (Beard, 1996). Thumb Member actively deposited to the south. Apatite fission-track sample QFT 10 shallower than 4 kilometers depth, suggested by the 20 Ma AFT age (see text), while other AFT sites within (17.1 Ma) or below (15.5) this depth during this initial extension (see text for details).

Present day cross-section, Figure 3-7C (modified from Bohannon and Lucchitta, 1991): Includes movement along west-dipping listric faults (West Branch, Grand Wash), minimal normal inversion of Spoon / Front and east monocline faults, and large scale normal offset along the Piedmont fault, sub-parallel to steeply west dipping Paleozoic strata. East strands of the Piedmont faults are projected to merge with the main Piedmont fault at depth, and crosscut the North Monocline fault, projected from the south (Figure 3-3). Projected ramp-flat geometry of VMA core "exhuming" faults as determined from field observations of numerous bedding parallel faults within the Paleozoic and Mesozoic section (this study; Beard, person. commun.; Bohannon, person. commun.). Location and depth of 20.1 Ma AFT age projected from QFT 10 (Figure 3-5) south of this section. Depth of basin fill deposits, and thickness of Mesozoic section in hanging wall of Piedmont fault interpreted from seismic imaging (Bohannon et al., 1993).

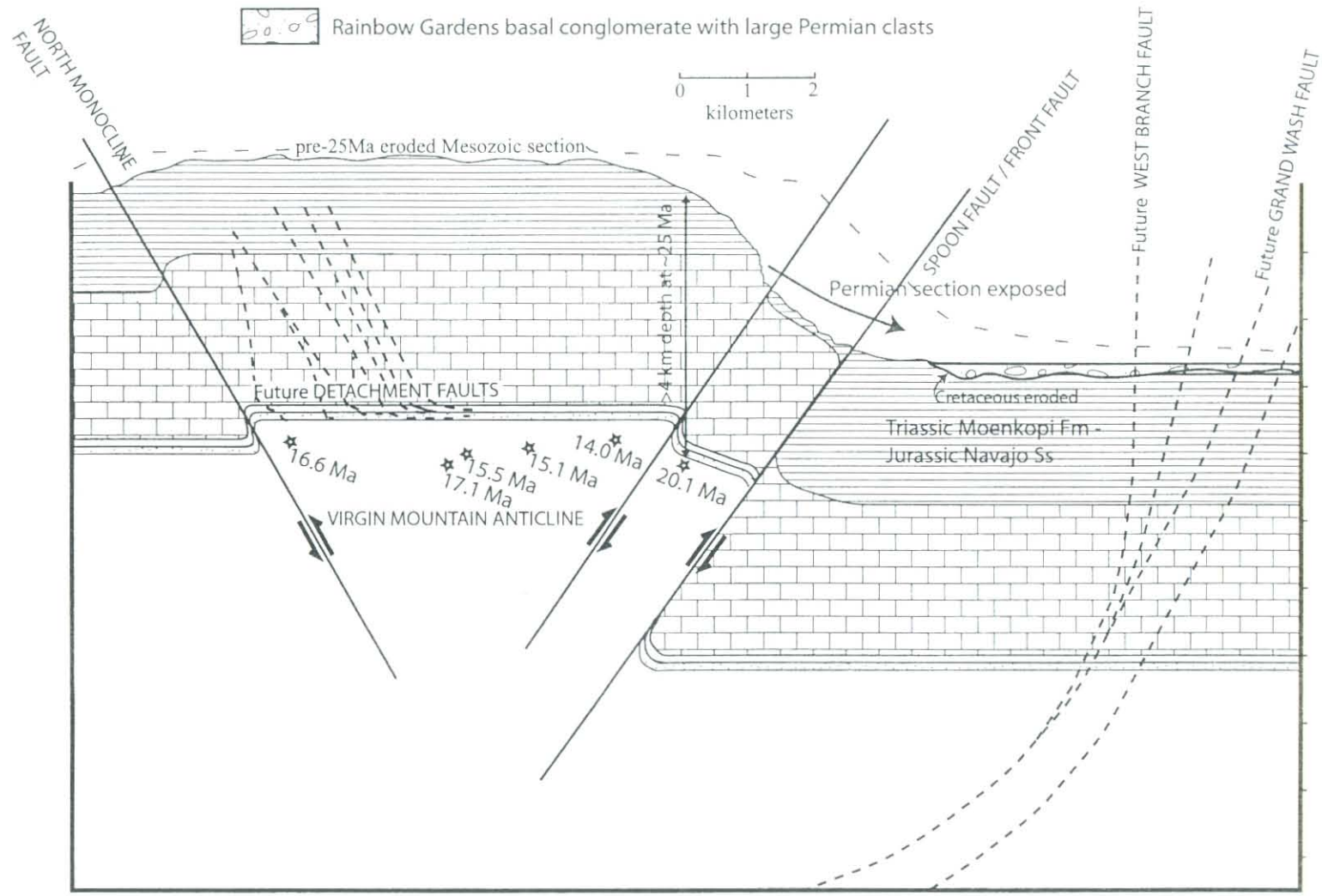

Figure 3-7A: Early Miocene pre-extension: circa 25 Ma

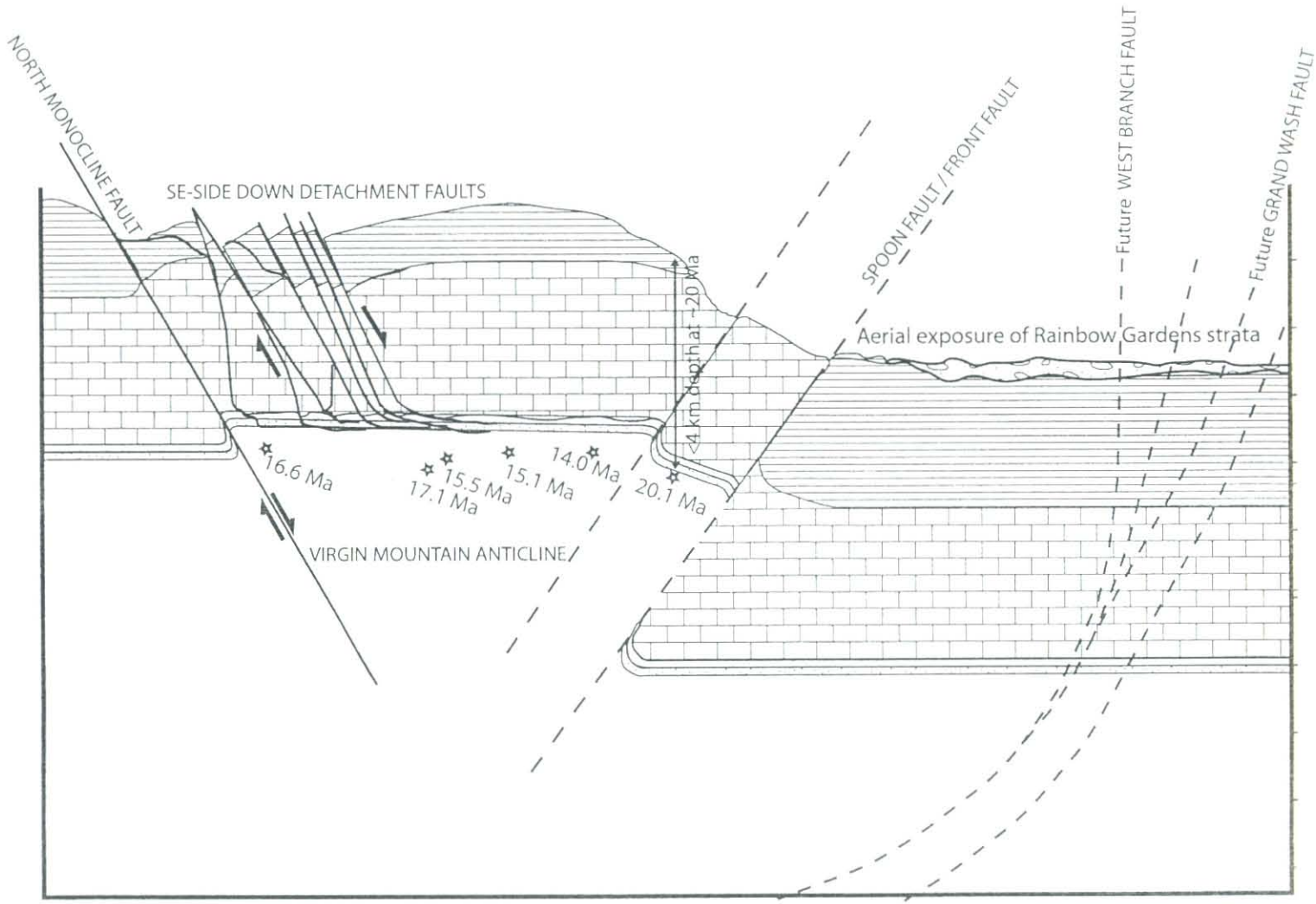

Figure 3-7B: Middle Miocene early extension: 18-16 Ma

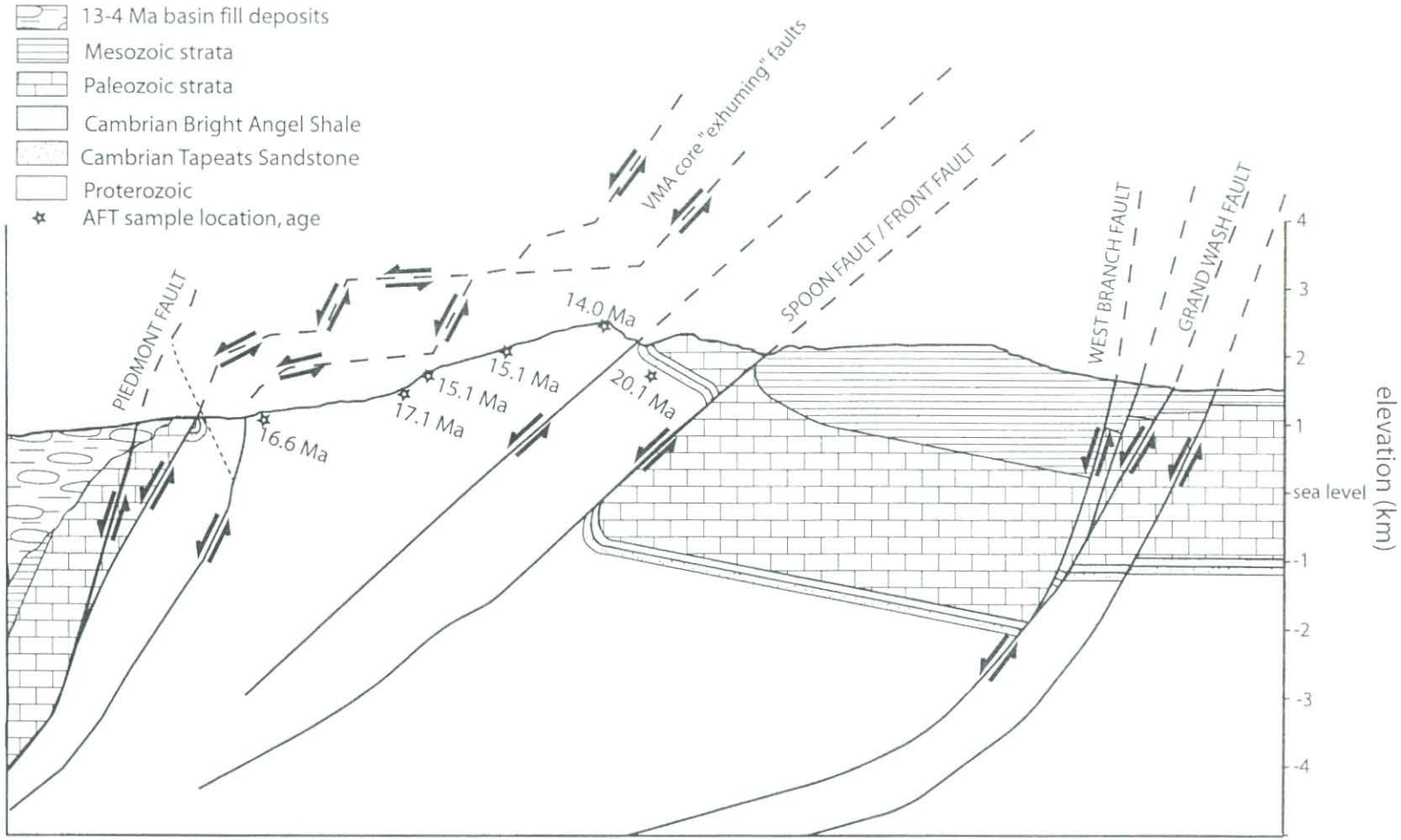

Figure 3-7C: Present structure

throughout the Colorado Plateau during the Laramide orogeny, and some Proterozoic rocks below the Great Unconformity cooled to below 50°C by 70 Ma (Kelley et al., 2001). A north-sloping, structurally controlled paleotopography developed, as the Kingman highlands to the south of the VMA formed during uplift (Figure 3-6). In the North Virgin Mountains, "draping" of Phanerozoic section over the basement uplift, and the local presence of Sevier thrusts, kept temperatures at the Great Unconformity above the partial annealing temperature of apatite (>110°C, Figures 3-5, 3-7A). Cretaceous sediments were likely shed from the Sevier highlands south and west of the VMA, and deposited east of the VMA, in the future Tom and Cull Wash area.

2. From the Paleogene to the early Miocene (Figure 3-7A), little or no tectonic activity is record in the Virgin Mountains area. Erosion of highlands to the south and west stripped Laramide uplifts of their cover rocks and deposited Eocene "rim gravels" onto the Colorado Plateau (Lucchitta, 1966). Erosion in the South Virgin Mountains beveled the Mesozoic and Paleozoic section down to the Cambrian section in the south, and the Permian section in the north (Lucchitta, 1966; Matthews, 1976; Bohannon, 1984; Lucchitta and Young, 1986), synchronous with progressive cooling of Proterozoic rocks below the Great Unconformity in the Gold Butte Block (Fitzgerald, 1991). In the VMA area, erosional beveling cut down only to Jurassic and Cretaceous strata (Figure 3-7A), despite downward cutting by northeast-directed drainage. In the early Miocene (~25 Ma), paleocurrent and lithologic relationships within the Rainbow Gardens Member basal conglomerate (Figure 3-7A) suggest pre-extensional deposition in overall NE-flowing braided streams, with localized SE-directed paleoflow off of an area of moderate to abrupt relief within the North Virgin Mountains (Beard, 1996). We interpret the local

shedding of coarse Permian clasts into the Rainbow Gardens conglomerate (Beard, 1996) as further evidence for pre-extensional uplift of the VMA, where Permian strata were exposed in the hanging wall of the east, VMA-bounding reverse fault and associated monocline (Figure 3-7A). We cannot dismiss the possibility that Permian section was also exposed in hanging walls of local Sevier thrusts, although geologic evidence of these thrusts is not present in the vicinity of this cross-section. Using a 25°C isotherm, the Great Unconformity was still at paleodepths of roughly 4 kilometers, equivalent to a Cambrian through Jurassic section, until 22-20 Ma, as determined from AFT data. Preliminary modeling (Appendix B) suggests that rocks directly below the Great Unconformity may have entered the AFT partial annealing zone (<110°C) by 26 Ma.

3. Although the timing of onset of Miocene extension is unconstrained, regional structural studies of Anderson (1987), recognition that deposition of the Thumb Member of the Horse Spring Formation (16-14 Ma) was strongly controlled by extensional deformation and that the Rainbow Gardens Member was pre-extensional (Beard, 1996), and clustered AFT ages from 17-14 Ma in the Gold Butte Block (Fitzgerald et al, 1991) and VMA (Table 3-1, Figure 3-5), suggest that peak extensional tectonism occurred from 16-14 Ma. We propose that early extension took place along linked normal and subhorizontal normal decollement faults, partially analogous to the ramp-flat geometry characteristic of thrust belts (Figure 3-4, 3-7B). Steep conjugate normal faults ("ramps") soled out into mechanically weak basal surfaces ("flats"), including the Moenkopi shale unit (Anderson and Barnhard, 1993) in the Mesozoic section, the Bright Angel shale and Tapeats sandstone in the Cambrian section, and the Great Unconformity, resulting in the dramatic tectonic thinning of these units (Figure 3-7B). Extensional allochtons of tilted

strata were translated above autochthonous basement rocks towards the adjacent, stable Colorado Plateau block in the VMA, and similar fault geometries are observed in the Gold Butte Block (Karlstrom et al, in prep). Basement-bounding normal faults within the VMA partially presumably reactivated Laramide reverse faults along the east (Spoon / Front fault, east monocline fault) and west (North Monocline fault) flanks (Figure 3-7B), although earlier reverse sense offsets were still preserved. As extension intensified (16-10 Ma, Figure 3-7C), deep-biting, west-dipping listric normal faults formed throughout the region, resulting in wholesale east tilting of semi-coherent crustal blocks (i.e. Gold Butte block, Brady et al., 2001), and shift of the net extension direction to the west-northwest (Brady et al., 2001). West-side-down displacement along large listric faults east of the VMA (i.e. Grand Wash fault, West Branch fault, Figure 3-7C) resulted in 15-60° east-tilting of Cambrian through early Miocene strata, and "doming" of the originally sub-horizontal detachment surface at the Great Unconformity. West-dipping, downward-steepening, ramp-flat normal faults began to form along the northwest flank of the VMA (i.e. Piedmont fault, Figure 3-7C), tectonically exhuming Proterozoic rocks, which cooled rapidly through AFT closure temperatures from 16-14 Ma. Kinematically linked normal and left-lateral faults formed throughout the Lake Mead area during this time (Beard, 1996; Duebendorfer et al, 1998).

4. Structural analysis of the Virgin River depression suggests that peak upper crustal extension occurred from 13-10 Ma, and may have exceeded 60% (Bohannon et al., 1993). Proterozoic rocks of the VMA were aerially exposed during this time, and deposited into the red sandstone unit (10-12 Ma) of the Horse Spring Formation (Bohannon et al., 1993; Figure 3-7C: "13-4 Ma basin fill deposits"). Northeast-striking,

basement-penetrating, probable left-lateral faults of unknown displacement were active shortly after deposition and consolidation of the red sandstone unit (Figure 3-8). The Overton pull apart basin, a result of left-lateral movement on the Hen Spring-Bitter Ridge fault (Campagna and Aydin, 1994) probably formed sometime around 10 Ma (Beard, 1996). We confirm that left lateral slip is probable (but unconstrained) along strands of the Hen Spring fault, as east-west striking red sandstone strata exposed on the north flank of Bunkerville Ridge (Bohannon and Beard, personal communication) are steeply dipping to overturned to the south and sub-parallel to the Hen Spring fault (Figure 3-8). Mapping of the red sandstone stratigraphy reveals an unroofing sequence, where basal units consist primarily of Paleozoic limestone clasts and grade upward (northward) into Cambrian-bearing units, and finally Proterozoic-bearing units, which contain locally derived granitic, amphibolitic, and metasedimentary clasts up to 1 meter in diameter (Figure 3-8). The presence of Proterozoic clasts in overturned red sandstone stratigraphy confirms that the basement core of the VMA was at least partially exhumed prior to this period of basement-penetrating left-lateral faulting.

5. Post 10 Ma, most fault activity had ceased and the Virgin River began to subside over a large area (Bohannon et al., 1993). Recurring movement on the Piedmont fault (Figure 3-7C) continued into the Quaternary, when fault scarps cut poorly consolidated Quaternary sediment on the west limb of the VMA. This movement continued to utilize Proterozoic foliations as zones of weakness.

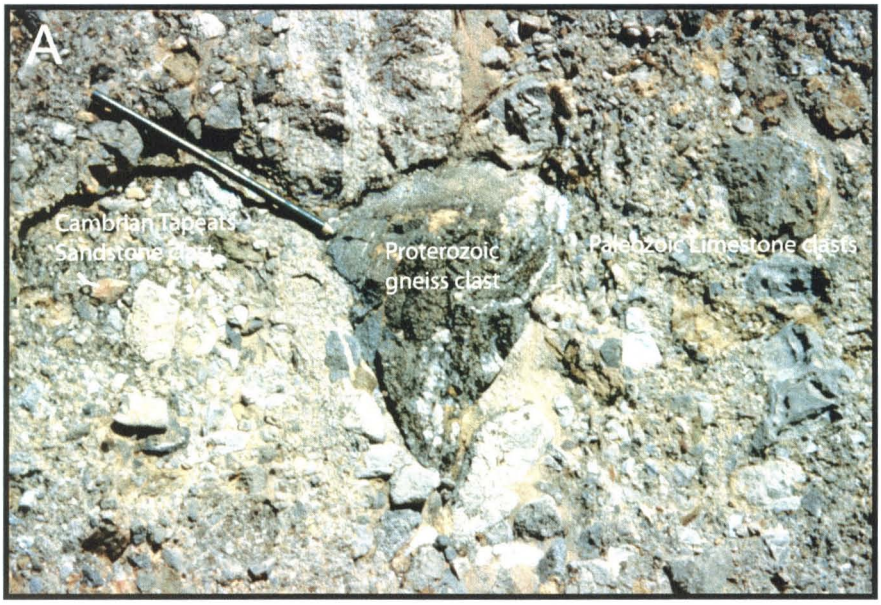

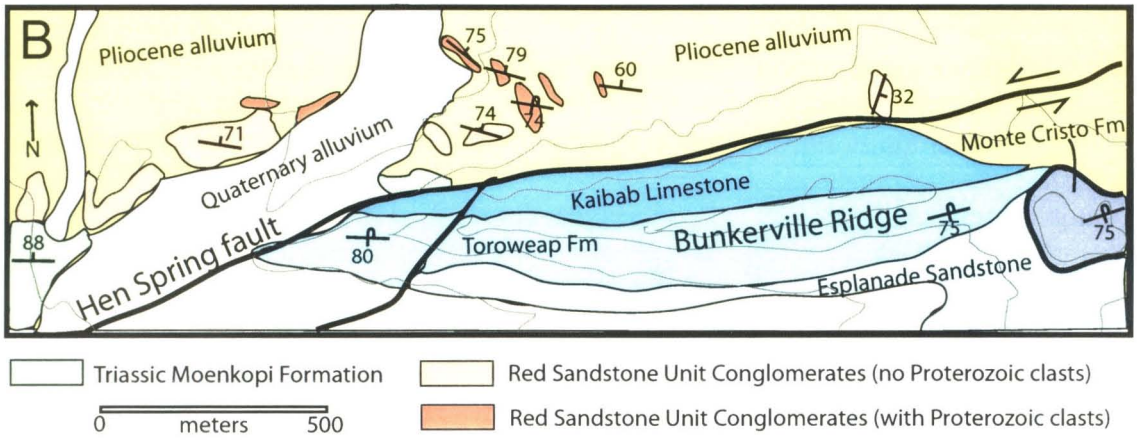

Figure 3-8: A) Large Proterozoic clast in vertically dipping conglomerates to the north of Bunkerville Ridge. Clasts of Proterozoic metasedimentary gneiss and schist, amphibolite, granite, and pegmatite are large and sub-angular, suggesting local derivation from the exposed VMA basement. At the base of the conglomeritic section, no Proterozoic rocks are present, however "up-section", the frequency of lower Cambrian and Proterozoic clasts within the conglomerate increases, to a maximum of 5-15 percent (B). This pattern of deposition is suggestive of an unroofing sequence. Structural overturning of these rocks, a probable product of left-lateral strike-slip faulting along the Hen Spring fault, therefore appears to post-date extensional unroofing of the Proterozoic core of the VMA. This conglomerate was assigned to the middle Miocene red sandstone unit (12-10 Ma) of Bohannon (1984), suggesting that a component of strike-slip faulting and structural overturning post-dates 12-10 Ma. A local map of conglomaritic outcrops appears in Figure 8B.

9. Conclusions

The Virgin Mountain anticline initially formed as a basement-cored uplift, flanked by outward-verging reverse faults and associated monoclinal drag-folds in Cambrian through Mesozoic strata during Laramide contraction (Figure 3-7A). Our evidence for this ancestry includes regional arguments (position of VMA between Sevier and Laramide orogens, systematic separation intervals of Laramide monoclines) and field arguments (Laramide monoclines mapped on east and west flanks of the VMA, large, proximal Permian clasts in pre-extensional Miocene conglomerate). The overall northeast-trending orientation of this uplift was strongly controlled by northeast-striking Proterozoic foliations, which helped "direct" early contractional strains and the consequent uplift of the VMA. The north plunge of the structure is not unlike the north plunge of the Kingman uplift to the south, suggesting that the complicated north-south variation in elevation of the top-of-Proterozoic surface in the region may represent an extension-enhanced relict of Laramide contraction. The presence of Sevier thrusts suggests that the leading edge of the Sevier belt may have reached this area, and preservation of upper Mesozoic and Cretaceous rocks around the VMA suggest that it was not an isolated, rapidly eroding highland such as the Kingman uplift to the south.

Slow regional cooling and erosion from the Eocene to the early Miocene beveled the Paleozoic and Mesozoic section overlying the Proterozoic rocks southward in the Lake Mead region (Bohannon, 1984), resulting in cooling below the Great Unconformity to temperatures below the partial annealing zone in AFT. While Proterozoic rocks in the western Grand Canyon and the Gold Butte Block were within 2-3 kilometers of the

earth's surface at 75-46 Ma, the VMA Proterozoic rocks remained deeply buried and thermally insulated beneath Cambrian to Cretaceous strata until the early Miocene, when rocks directly below autochthonous Cambrian section in the VMA cooled slowly through the apatite partial annealing zone during erosion.

Middle Miocene extension (18-16 Ma) was initiated along linked steep normal faults and subhorizontal normal faults with a cumulative geometry broadly analogous to a ramp-flat thrust belt. Detachment horizons in the Bright Angel Shale and at the Great Unconformity in the North Virgin Mountains allowed for southeast-directed transport and "domino block-style" tilting of Paleozoic and Mesozoic extensional allochtons. This was followed by pronounced roughly east-west extension along west-dipping listric normal faults, which tilted the crust, domed the Great Unconformity detachment surface, and locally enhanced basement topography. While these normal faults undoubtedly interacted with left-lateral strike-slip faults, the role of strike-slip faulting in generating the pronounced basement topography remains highly unconstrained. Similarly, the roles of isostatic uplift, north-south shortening, and lower / middle crustal flow in generating the VMA uplift remain unconstrained, and the importance of any of these processes is not testable by any of the structural (Figure 3-3, 3-4), sedimentological (Figure 3-6, 3-8), or AFT data we present (Figure 3-5). We do recognize the possibility that oblique or strike-slip movement on some basement penetrating faults (despite a lack of structural evidence for this) could further complicate the geometries of our cross-sectional reconstructions (Figure 3-7).

The Proterozoic core of the VMA was aerially exposed sometime during deposition of the red sandstone unit (13-10 Ma, Bohannon, 1984), noted by the presence

of coarse, locally derived Proterozoic clasts in exposed presumed red sandstone strata at the base of Bunkerville Ridge (Figure 3-8). These units appear to have been overturned during probably left-slip along the Hen Spring fault system, after the VMA was a mature, prominent structure.

Chapter 4:

Detailed structural and tectonic studies utilizing MASTER remote sensing imagery: A case study from the North Virgin Mountains, Southeast Nevada and Northwest Arizona

Mark C. Quigley and Karl E. Karlstrom, Department of Earth and Planetary Sciences, University of New Mexico

Simon J. Hook, Jet Propulsion Laboratory, NASA

1. Abstract

MODIS/ASTER Airborne Simulator (MASTER) data were acquired over the Lake Mead region, Nevada and Arizona, in order to evaluate the utility of the data for geological mapping in a structurally complex area. Flight lines included coverage of the North Virgin Mountains, a rugged mountain terrain straddling the Basin and Range – Colorado Plateau margin 2 km east of Mesquite, Nevada. This northeast-trending mountain uplift is an asymmetric anticline cored by polydeformed Proterozoic crystalline rocks and overlain by complexly faulted Phanerozoic sedimentary rocks to the north, east, and south, and unconsolidated sediment to the west. MASTER images were used in conjunction with aerial photographs, previous geologic mapping, and new geologic mapping and sampling transects to examine and refine seven 1:24,000 quadrangles in the North Virgin Mountains. Major advances included: 1) Recognition of regional tectonic thinning in the lower Cambrian Tapeats Sandstone and Bright Angel Shale due to detachment faulting, providing a basis for refined models of Miocene extension in this region; 2) Recognition of complex fold-interference patterns in extremely heterogeneous Proterozoic basement due to near orthogonal Paleoproterozoic contractional events; 3)

Recognition of compositional variations in Proterozoic granitoid plutons and supracrustal rocks that correlate with field observations, enabling accurate lithologic interpretations between mapped transects and in remote areas; 4) Remote mapping of Proterozoic shear zones due to their position between lithologies with distinct spectral characteristics; 5) Recognition of variations in alluvial fan composition, and fan inter-fingering that reflect the dominant source-rock types exposed in the adjacent mountain fronts; 6) Recognition of brittle faults in Proterozoic rocks where they offset lithological traces, and Quaternary fault scarps that offset alluvial fans. A primary benefit of the MASTER method is that it provides a scale of lithologic "lumping" that is appropriate for 1:24,000 scale geologic mapping. We conclude that the MASTER thermal infrared images dramatically increase the efficiency and quality of geologic mapping in areas of structurally complex crystalline and sedimentary rocks in areas with good exposure and limited vegetation cover, to the extent that they are an essential component of any present or future geologic mapping projects.

2. Introduction

The MODIS/ASTER Airborne Simulator (MASTER) is a 50 channel airborne imaging spectrometer developed to support the Moderate Resolution Imaging Spectroradiometer (MODIS) and Advanced Spaceborne Thermal Emission and Reflectance Radiometer (ASTER) science teams. ASTER and MODIS are two of five instruments included on the Terra spacecraft launched into Earth's orbit in December 1999. MASTER data were acquired over the north Virgin Mountains in October 1999 in

order to evaluate the usefulness of MASTER and ASTER-like data for geological mapping in structurally complex basement rocks. Previous studies had demonstrated that multispectral thermal infrared data acquired by instruments like the Thermal Infrared Multispectra Scanner (TIMS) were useful for geological mapping (Hook et al, 1994). MASTER is the replacement for the six channel TIMS and has a wider spectral and dynamic range (Hook et al. 2001). The MASTER data used in this study were acquired from an altitude of 8.3 kilometers and have a pixel size of approximately 17 meters.

3. Theoretical Framework

The reflectance and emissivity spectra of minerals exhibit diagnostic features at various wavelengths, providing a means for their remote discrimination and identification. Silicate minerals, which compose most crustal rocks, exhibit spectral features in the 8 to 12 μm wavelength range or thermal infrared. Framework silicates such as quartz and feldspar have spectral features at the shorter end of this wavelength range whereas sheet and chain silicates, and silicates containing isolated SiO_4 tetrahedra have features at progressively longer wavelengths (Hunt, 1980). This difference in the position of spectral features in silicate minerals allows the discrimination of felsic from mafic crystalline rocks, quartz-dominated from clay-dominated or carbonate-dominated sedimentary rocks, and quartz-rich from carbonate-rich sedimentary deposits (i.e. alluvial fans), with instruments that sample across the thermal infrared wavelength range such as MASTER.

4. Geologic Setting

The North Virgin Mountains (Figure 1-1, 4-1), located approximately 130 km northeast of Las Vegas, Nevada, consist of highly metamorphosed and deformed Proterozoic rocks, unmetamorphosed and variably deformed Paleozoic to middle Miocene sedimentary rocks, and generally undeformed late Miocene to Quaternary poorly consolidated sedimentary rocks and basalt. This northeast-trending mountain uplift straddles the Basin and Range - Colorado Plateau margin, with relatively flat-lying Phanerozoic rocks in the northeast, and complexly folded and faulted Phanerozoic rocks throughout the west and southeast segments. The complex geometry of the North Virgin Mountains is a product of dramatic Miocene extension and uplift superimposed on Laramide-Sevier contractional structures (Quigley et al, 2001), resulting in an east-tilted, basement-cored anticline (the *Virgin Mountain Anticline,* VMA). The east limb, although faulted, is mostly intact, consisting of moderately east-dipping Cambrian through early Miocene sedimentary rocks separated by erosional disconformities. The west limb is highly attenuated, and present only in the far northwest and mid-west segments of the VMA. Directly to the west of the VMA lies the Virgin River depression, which at 8 kilometers deep (Bohannon et al., 1993), is one of the deepest Neogene extensional basins in the Basin and Range. The dramatic vertical structural relief of the top-of-Proterozoic surface (up to 10 kilometers) occurs over a lateral distance of 10-15 kilometers, from the peak of Mount Bangs to the deepest part of the Virgin River depression (Figure 1-1). The nature and kinematic significance of the VMA has been the subject of much debate, and remains controversial and enigmatic (i.e. Beal, 1965; Moore,

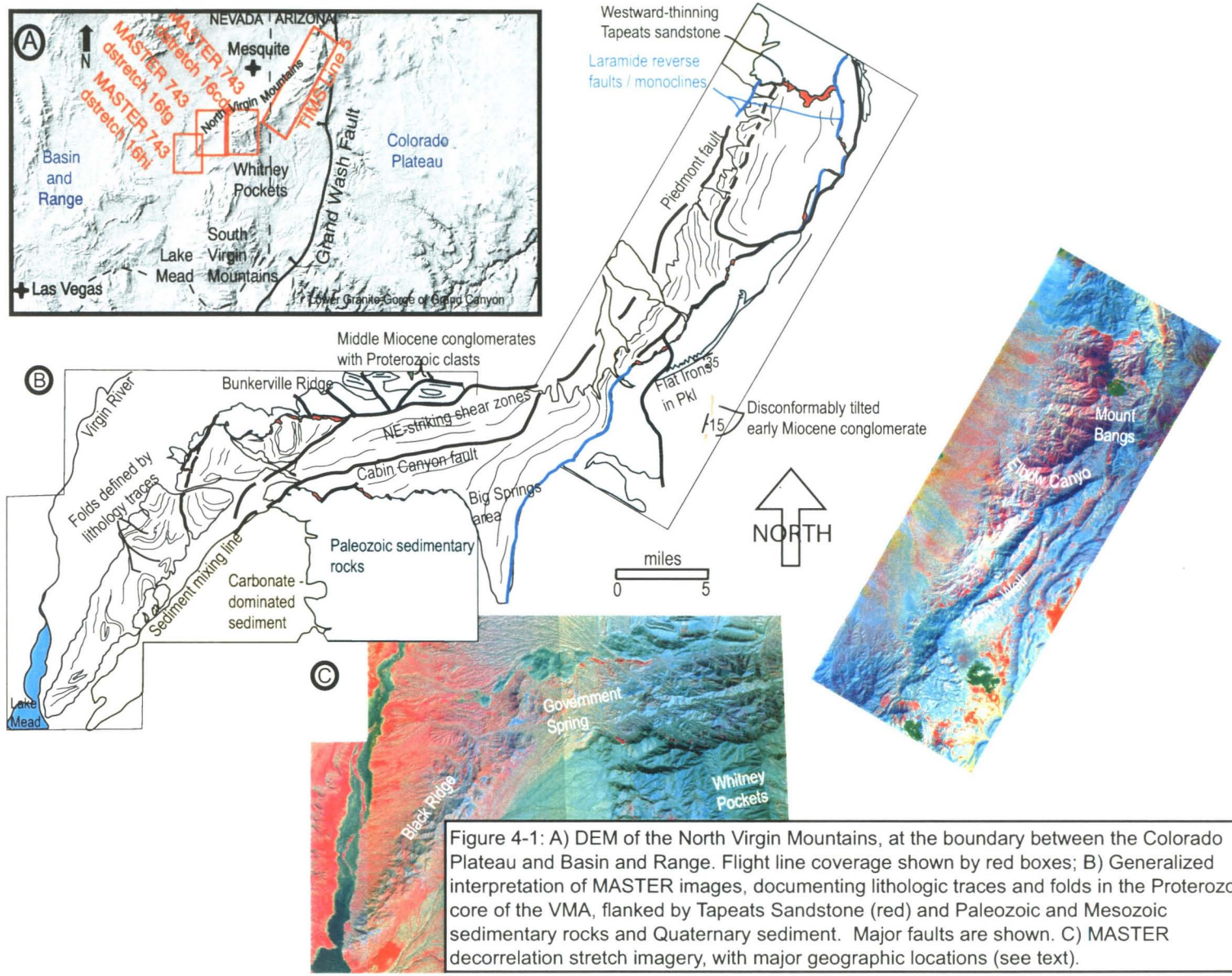

Figure 4-1: A) DEM of the North Virgin Mountains, at the boundary between the Colorado Plateau and Basin and Range. Flight line coverage shown by red boxes; B) Generalized interpretation of MASTER images, documenting lithologic traces and folds in the Proterozoic core of the VMA, flanked by Tapeats Sandstone (red) and Paleozoic and Mesozoic sedimentary rocks and Quaternary sediment. Major faults are shown. C) MASTER decorrelation stretch imagery, with major geographic locations (see text).

1976; Hintze, 1986; Wernicke and Axen, 1988; Anderson and Barnhard, 1993; Bohannon et al., 1993; Langenheim et al., 2001, Quigley et al., 2001).

Significant tectonic boundaries lie in the vicinity of the North Virgin Mountains, including the Proterozoic proposed Mojave –Yavapai Proterozoic province boundary to the east (Karlstrom and Bowring, 1988), the leading edge of low-angle Sevier thin-skinned thrusting to the west (Axen et al, 1990), and the western limit of Laramide high-angle reverse faulting typically found within in the Colorado Plateau (Huntoon, 1990), and the breakaway zone for the Basin and Range-Colorado Plateau transition (Wernicke et al., 1988). In spite of the tectonic significance of this region, many areas remain incompletely mapped, although recent efforts have been made (Beard, 1993, 1996; Billingsley, 1995: Billingsley and Bohannon, 1995; Bohannon, 1991; Bohannon and Lucchitta, 1991; Williams et al., 1997). The use of MASTER imagery is essential in completing geologic mapping and interpreting the variety of rock types and structures ranging from Paleoproterozoic to present.

5. Data Processing

MASTER data are provided as calibrated at-sensor radiance in Hierarchical Data Format (HDF). The radiance emitted from the surface and measured by MASTER is affected by transmission through the atmosphere. Since this study utilizes the ground radiance data, the atmospheric component was removed using the approach described by Hook et al. (1992). After removal of the atmospheric component, the ground radiance values are a function of the surface temperature and emissivity.

The temperature component is highly correlated between channels and dominates the ground radiance. Since this study is primarily interested in variations in emissivity, which relate to differences in composition, the emissivity component of the ground radiance was enhanced using the decorrelation stretch (Gillespie et al., 1986). The decorrelation stretch enhances emissivity variations while maintaining temperature differences. In a decorrelation stretch image (Figure 4-1, 4-2), emissivity variation is displayed as color differences and temperature variations are displayed as differences in brightness. Thus, at higher elevations, correspondingly cooler temperatures and increased vegetation cover decrease image brightness and geologic interpretation becomes more difficult. In Figure 4-2, lower elevation exposures are bright and easily interpreted whereas higher elevations (Mount Bangs, Figure 4-3) are difficult to interpret.

The decorrelation stretch images are registered to existing maps using tie points and printed at a scale of 1:24,000. These data are taken into the field and used in conjunction with topographic maps, previous 1:24,000 USGS geologic maps, USGS 1:24,000 7.5 minute orthophotoquads, and USGS 1:24,000 HAP80 orthophotos for new geologic mapping. They are also used to target "key areas" for more detailed (1:12,000, 1:6,000) examination. Mapping and sampling transects are conducted at regular intervals throughout the area, and geologic data "extrapolated" between transects through use of the MASTER imagery. Sampling of distinct lithologies on the decorrelation stretch imagery is also conducted for further geologic correlation (Table 4-1). Despite the ease with which lithologically distinct units are picked out, units containing similar compositions, despite different origins, (e.g. psammite vs granodiorite, see Figure 4-3) are essentially indistinguishable. In this case, field traverses, previous mapping, and

Table 4-1. Mineralogy and color on MASTER images of the rock units within the North Virgin Mountains		
Rock Unit	Mineralogy	Color on MASTER decorrelation stretch
Proterozoic rocks		
Amphibolite gneiss	50-70% hornblende, 20-40% plagioclase, 0-10% clinopyroxene, 0-20% biotite, 1-3% potassium feldspar, quartz, garnet, sphene,	Bright to pale blue
Pelitic and semi-pelitic gneiss and schist	20-35% quartz, 20-30% biotite, 10-30% muscovite, 10-30% sillimanite 0-15% potassium feldspar, 0-10% plagioclase, 0-10% garnet	Purple
Psammitic gniess and orthogneiss	30-40% quartz, 30% plagioclase, 10-15% potassium feldspar, 5-15% biotite, hornblende, 1-5% garnet, sillimanite	Redish purple
Granodiorite gneiss	25-45% quartz, 30-40% plagioclase, 5-10% biotite, potassium feldspar, muscovite, chlorite	Pale to bright red
Monzogranite gneiss	25-35% quartz, 35-40% potassium feldspar, 30% plagioclase, 1-5% hornblende, biotite, epidote, muscovite, garnet, chlorite	Red
Leucopegmatite dikes	Variable, 30-40% quartz, 30-40% plagioclase, 30-40% potassium feldspar, 1-10% muscovite, biotite, garnet, magnetite, tourmaline	Red
Ultramafic rocks	Variable, 50-95% hornblende, 2-20% clinopyroxene, 0-10% orthopyroxene, 5-50% plagioclase, 0-10% quartz, biotite, quartz	Bright blue
Quartzite	95-98% quartz, 0-5% biotite, hornblende, plagioclase	Bright red
Melange rocks	Variable, contain clinoyroxene-, calcite-, quartz, hornblende-domainted layers, 5-10% garnet, biotite, muscovite	Variable, pale blue to pale green
Phanerozoic rocks		
Sandstones (i.e. Tapeats, Esplande, Navajo)	Quartz-dominated	Bright red
Shales (i.e. Bright Angel)	Variable, clay minerals + quartz, feldspar, calcite, dolomite	Dark purple to green
Limestones (I.e. Muav, Monte Cristo)	Calcite or dolomite - dominated	Green

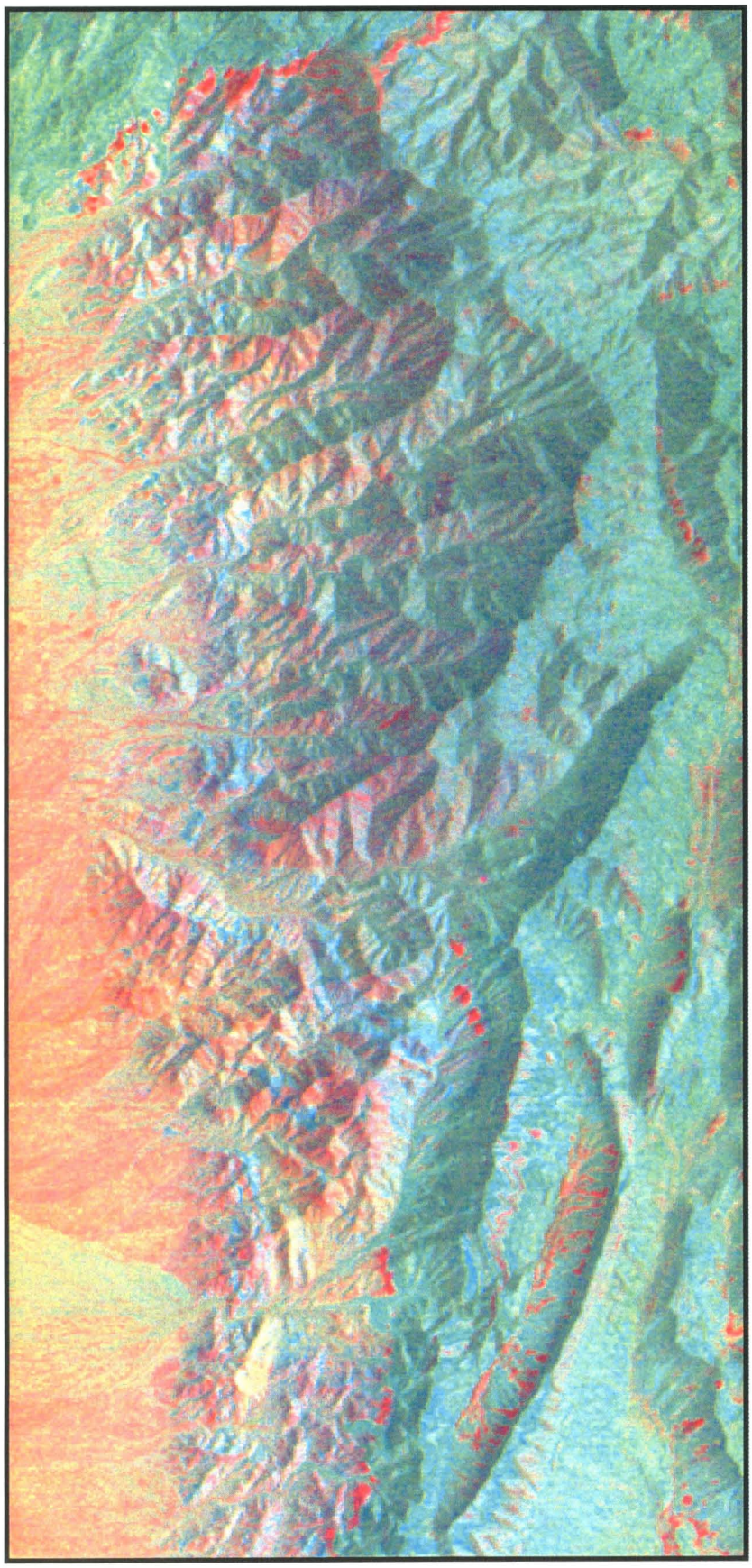

Figure 4-2: MASTER decorrelation stretch image of parts of the Mount Bangs, Elbow, and Jacob's Well areas. See Figure 4-3 for geologic interpretation.

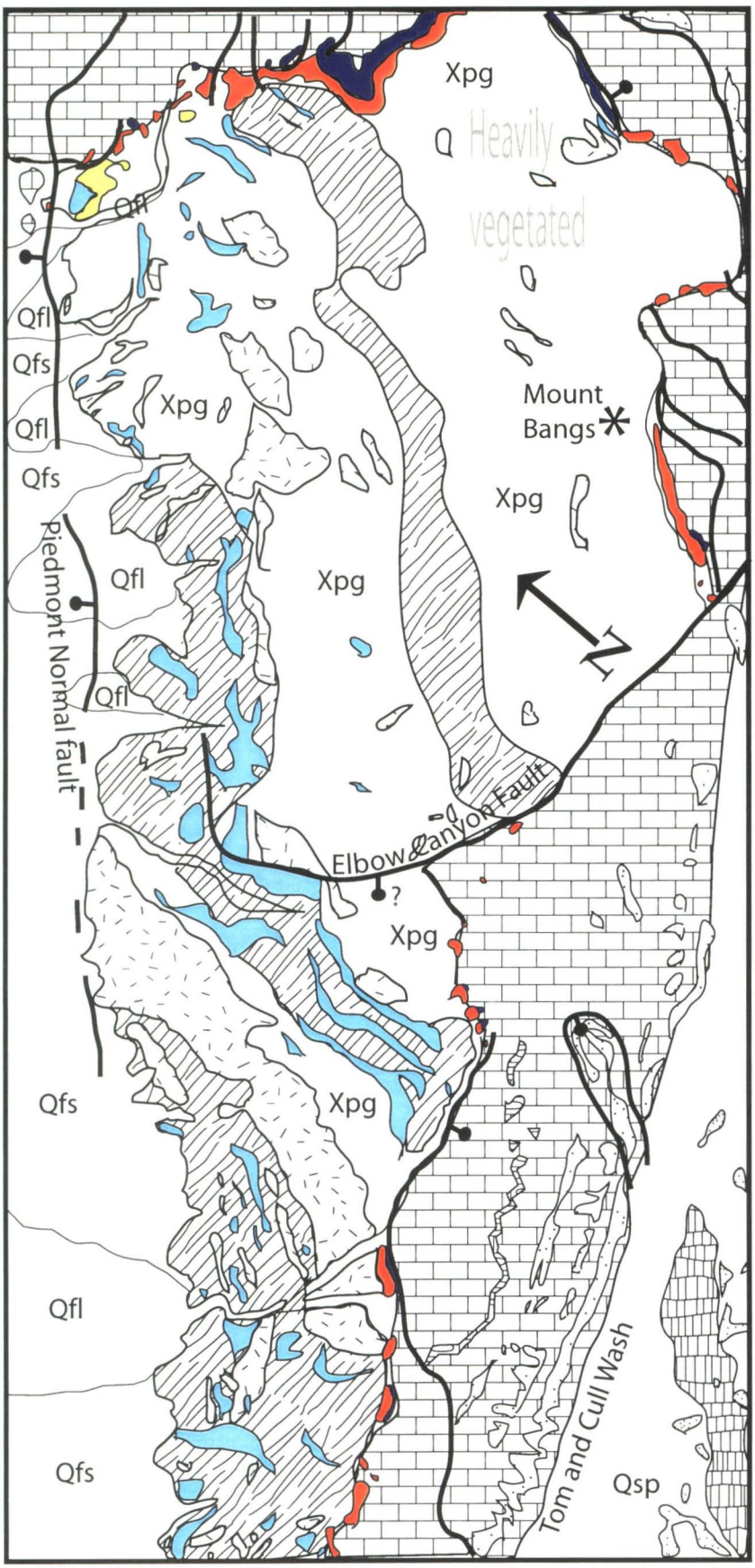

Legend

- Qsp — Quaternary pediment deposits
- Qfs — Quaternary fan deposit, Proterozoic clast dominated
- Qfl — Quaternary fan deposit, carbonate dominated
- Basalt flows (Pleistocene to Miocene?)
- Navajo Sandstone (Jurassic)
- Esplande and Coconino sandstone (Permian)
- Monte Cristo chert member (Mississippian)
- Paleozoic Limestone (undivided)
- Bright Angel Shale (Cambrian)
- Tapeats sandstone (Cambrian)
- Monzogranite gniess and pegmatite (Proterozoic)
- Amphibolite gneiss (Proterozoic)
- Pelitic gneiss and schist (Proterozoic)
- Xpg — Psammitic gneiss (Proterozoic)
- Quartzite (Proterozoic)

0 metres 2000

Figure 4-3: Geologic interpretation of the area covered by Figure 4-2. Major lithologic contacts, faults, and alluvial fan compositions were easily identified based on MASTER image interpretation

foliation trends determined from the airphotos are necessary to map these units separately.

Using the procedure outlined above the first author mapped an area of approximately 50 km^2 at a scale of 1:24,000, and conducted detailed mapping in key regions.

6. Data Interpretation

MASTER data acquired over the North Virgin Mountains were first correlated with existing geologic maps of the region to calibrate image characteristics (color, texture) with known rock units. This was particularly useful within the Proterozoic core of the VMA, where the structural and lithologic complexities revealed by geological mapping (i.e. Beal, 1965) were mimicked by MASTER imagery. Once a MASTER-geology template was established, MASTER data interpretation was broadened to cover large (>50 km^2) areas of unmapped Proterozoic rocks within the Elbow Canyon, Mount Bangs, Hen Spring, Virgin Peak, Black Ridge, and Jacob's Well 1:24,000 quadrangles. MASTER data led to new structural interpretations within the Cambrian section, and mapping of Quaternary fans in the Black Ridge, Elbow Canyon, and Mount Bangs quadrangles. Data interpretation is herein arranged into Proterozoic, Phanerozoic, and Quaternary sections, summarizing advances in lithologic and structural interpretations made from the data, and tectonic significance of these interpretations.

Proterozoic Geology

Lithologies

The crystalline core of the VMA is composed of Paleoproterozoic metasedimentary gneiss and schist (60%), granodiorite gneiss (13%), amphibolite gneiss (9%), monzogranite gneiss (8%), leucopegmatite dikes (6%), ultramafic rocks (2%), and tectonic mélange (2%), the latter of which is an intimate mixture of ultramafic boudins, diopside-marble, chert, and calc-amphibolite gneiss. Geologic observations and preliminary geochronologic data are strongly correlative with those from the Cerbat Mountains in NW Arizona (Dubendorfer et al, 2001) and the Granite Gorges of the Grand Canyon (Ilg et al, 1996). The VMA rocks are thus placed within the Mojave province, a Paleoproterozoic terrain characterized by upper-amphibolite to granulite facies metamorphism, isotopically enriched Pb and Nd signatures (Bennett and DePaolo, 1987; Wooden and Dewitt, 1991), and "old" detrital zircon ages (Wooden and Miller, 1990).

The complex folding and interfingering characteristic of the Paleoproterozoic rocks, from millimeter scale to map scale, dissuaded complete, detailed mapping of the core of the VMA until this study. After the work of Beal (1965), 50% of the Proterozoic core of the VMA remained unmapped until the present, and the tectonic history unstudied.

The pelitic and semi-pelitic gneisses and schists appear purple in the MASTER images (Figure 4-1, 4-2). The composition and texture of this unit are quite variable on the outcrop scale, consisting of garnet-biotite, garnet-biotite-muscovite-sillimanite,

hornblende-biotite-garnet, and cordierite-muscovite-biotite-fibrolite-dominated schists with schistose to gneissic and migmatitic textures. The semi-pelitic lithologies have a lighter purple tinge, due to the increased abundance of quartz in the assemblage, with chemical analyses yielding 54.77 % SiO_2 (Beal, 1965). These rocks commonly grade into psammitic gneiss, which appears reddish-purple in the MASTER images and is dominated by a quartz-feldspar-hornblende-biotite assemblage. Chemical analyses yield 70.89% SiO_2. Although the difference in SiO_2 between the pelitic and psammitic units is reflected in the spectral data, and consequently the MASTER images, the grading of these units into one another allows for some uncertainty in placement of geologic contacts using the images. This problem is lessened in that, at the 17 meter pixel size, the MASTER images provide an average bulk composition. These two units are delineated on the geologic interpretation map (Figure 4-3), with gradations between them resolvable by detailed field examination, and contain spectacular records of the polyphase Paleoproterozoic deformation that affected the North Virgin Mountains.

The amphibolitic units are dominated by varying amounts of hornblende, clinopyroxene, plagioclase, garnet, and biotite, and contain metabasalt, gabbro, amphibolite gneiss, and hornblendite dikes. These units appear as bright to pale blue bands in the images, with increasing brightness a function of increasingly mafic composition. Ultramafic boundins, where large enough to either affect the bulk pixel signature (roughly 5 meters) or span an entire pixel (17 meters), are similarly characterized by a bright blue color. It is thus difficult to distinguish these clinopyroxene + hornblende ± orthopyroxene ultramafic units from the more mafic amphibolitic units without field checking. Additional techniques are being developed which will allow a

quantitative determination of the weight percent silica of the rock from the imagery and should help distinguish these units. The tectonic mélange unit, which contains intensely interlayered amphibolite, marble, ultramafic rocks, and cherts, is not easily characterized on the images due to its compositionally anisotropic nature, although dominant foliation patterns and the larger tectonic slivers are evident.

The granodiorite gneiss is composed dominantly of feldspar and quartz, with varying amounts of hornblende, biotite, and garnet. This unit is perhaps the most variable in composition, ranging from a mafic composition similar to the amphibolite gneiss to that of a monzogranite, and thus appears as very pale to bright red on the images. Mingling textures between the granodiorite and amphibolitic units are observed, suggesting that the abundant granodioritic composition may represent an end-member to a differentiating arc-magmatic system.

The monzogranite gneiss appears bright red in the MASTER images, due to high SiO_2 values, particularly in a sample analyzed by Beal (77.75% SiO_2, 1965). Multiple phases of granitic intrusions include quartz phyric, K-feldspar porphyritic, aplitic, and 2 phases of pegmatitic intrusions, the latter of which are the youngest of the Proterozoic rock units within the VMA. Intrusions contain varying amounts of muscovite, sericite, biotite, and epidote. Overall, distinguishing multiphase granitoids and pegmatites from one another was only moderately successful.

In the farthest north section of Figure 4-2, scattered bright red outcrops within the Proterozoic rocks were field mapped as Proterozoic quartzites (Figure 4-3). Although essentially indistinguishable from the Tapeats sandstone on the MASTER images (see below), the presence of these bodies within the Proterozoic rocks of the NVM are

important because quartzites have not been mapped within the Grand Canyon to the immediate east, but are present farther west within the Mojave crustal province.

Structures

Macroscopic to outcrop scale structures were mapped utilizing the lithologic interpretations described above, and complex geometries were targeted for detailed structural studies. The remarkable compositional heterogeneity of the rock types and intensity of deformation allows for a correlation between lithologic trace and foliation trace, thus structural domains became evident from lithologic trace interpretation of the images. The following major structures were identified:

1) The dominant regional foliation, as determined from the images, is northeast-striking in southwest Black Ridge, north- and northwest-striking in north Black Ridge and Government Spring, northeast-trending south of Government Spring, northeast-striking in Jacob's Well, northeast and north-striking in Elbow Canyon, and north-northeast striking in Mount Bangs. Northwest and north–striking contacts appear to wrap into northeast-striking orientations in southwest Black Ridge, and throughout the central axis of the VMA. This regional northeast strike is S_2 regionally and in the Grand Canyon (Ilg et al, 1996).

2) Large north-northwest-trending folds were mapped in the Black Ridge area, easily visible due to the involvement of bright blue colored amphibolitic rocks and bright red monzogranites. The north fold plunges vertically and shows a mushroom-shaped outcrop pattern suggestive of a Ramsay type-2 refolded fold (Figure 4-1). To the south of this fold, a similar scale, similar style fold appears to have been rotated into a northeast-trending orientation.

3) Amphibolite layers are strongly attenuated and boudinaged throughout the VMA

4) Monzogranite dikes and plutons are most commonly concordant with other lithologic contacts, and dominantly strike north to northeast.

Summary

The following tectonic interpretation stems from integrating MASTER data with geochronologic, structural, and metamorphic studies of the Proterozoic basement. The northwest-striking fabric mapped from MASTER imagery and ground data is associated with strains developed during northeast-southwest contraction, and is folded and overprinted by the north-trending sub-vertical fabric readily visible on MASTER imagery. This northwest fabric (S_1), where mapped within the pelitic schist unit south of Big Springs Canyon, is at a high angle to compositional layering (S_o). In Whitney Pockets, however, lithologic contacts strike northwest and contain a bedding parallel S_1 foliation. Based on regional studies (i.e. Duebendorfer et al., 2001; Ilg et al., 1996), D_1 is typified by bedding-subparallel thrusting and development of recumbent nappe folds. The Big Springs area provides a rare glimpse into the hinge region of one of these nappe structures, where the F_1 axial plane (S_1) is orthogonal to bedding.

Elsewhere, record of this event has been completely obliterated by the intense layer-parallel, north and northeast-trending fabric (S_2). The north-trending fabric appears to represent an intermediate finite strain state between the northwest-trending S_1 fabric and the northeast-trending S_2 fabric. This is visible on the images where north-trending lithologic contacts bend into northeast-trending orientations in Black Ridge and to the north and south of Elbow Canyon. Close examination of monzogranite plutons and dikes, easily observable on MASTER images, suggests syn-kinematic emplacement of

these bodies during D_2 deformation. For this reason, monzogranite units are observed to trend north and northeast on MASTER images, but rarely northwest. Kinematic analysis of the Virgin Mountain shear zone (Quigley et al, 2001) suggests synchronous northwest-side-up thrusting accompanying this upper amphibolite-facies, northwest-southeast directed contractional event.

Further structural studies of the monzogranite intrusions reveal that they have been almost ubiquitously mylonitized during a lower-temperature deformational event, creating a foliation parallel, strongly fissile fabric (S_3). This is due likely to their quartzofeldspathic composition, which would be rheologically weak relative to more mafic units under upper-greenschist facies conditions. The position and orientation of monzogranite bodies on the MASTER images thus correlates well with the location of these shear zones, which are part of a dextral-transpressive partitioned deformation zone preliminarily dated at circa 1670-1650 Ma (Quigley et al, 2001).

Finally, basement-penetrating brittle faults are recognized where lithologic trends are sharply disrupted or are at high angles to lithologic trends across a linear structure. Perhaps the best example of this appears in the center of Figure 4-2, where the Elbow Canyon fault separates north- from northeast-striking lithologic domains (Figure 4-3). Many brittle structures in the North Virgin Mountains, however, have reactivated foliation planes and lithologic boundaries, and are thus difficult to map using MASTER images.

Phanerozoic Geology

Lithologies

Most of the Phanerozoic rocks of the VMA have been recently remapped at 1:24,000 scale (Beard, 1993, 1996; Billingsley, 1995; Billingsley and Bohannon, 1995; Bohannon, 1991; Bohannon and Lucchitta, 1991; Williams et al., 1997). MASTER images are thus excellent for refining geologic contacts on these published maps, and targeting areas of structural complexity that may have gone previously unnoticed. Most mapped stratigraphic contacts correlated well with the images. However, one unrecognized complexity was the thinning and/or structural removal of the lower Cambrian section. The main focus of this study was to utilize MASTER imagery to examine the apparent thinning of the Cambrian Tapeats sandstone and the Bright Angel shale at the Proterozoic – Phanerozoic interface, and to note the presence of Cambrian rocks at the northwest end of the VMA, which appeared in MASTER images but were not noted on recent geologic maps (Billingsley and Bohannon, 1995).

The Tapeats sandstone appears bright red on the images (Figure 4-1, 4-2), and is noted by rounded, discontinuous outcrops that often trace the Paleoproterozoic – Cambrian contact throughout the VMA (the "Great Unconformity", Powell, 1875). The overlying Bright Angel shale is rarely visible on the MASTER images, as it is extremely incompetent, and often occurs as a slope dominated by Paleozoic limestone clasts and sediment eroded from above. Small, purple-colored outcrops of the Bright Angel shale are visible in the northern section of Figure 4-2. The Esplande and Navajo sandstones, and the Monte Cristo member of the Redwall Formation are also present as bright red units in Figure 4-2. It is important to remember that the MASTER imagery maps mineralogy, not differences in structure, and since these are all sandstones they appear similar in the images. The remainder of the Phanerozoic section is dominated by calcitic

and dolomitic limestones, which appear green on the MASTER images. The images used in this study measure the radiation from the surface in the thermal infared part of the spectrum (8-12 um) and do not have sufficient spectral resolution to enable the limestones to be distinguished from the dolomites. Limestone and dolomite also exhibit spectral features at shorter wavelengths in the short wave infrared (SWIR - 2-2.5 um). Given data with sufficient spectral detail in either of these wavelength ranges it would be possible to distinguish the limestone from dolomite. The MASTER instrument does have sufficient spectral resolution in the SWIR and MASTER data have been used in the area to the south to distinguish these units (Hook et al., in prep.)

Structures

The discontinuous outcrop patterns of the Tapeats sandstone and the Bright Angel shale, as observed in MASTER images, can be explained by one of three possibilities; 1) burial of section by landslides of overlying sedimentary rocks, thus obscuring surficial expressions, 2) omission of section due to normal or reverse faulting, and 3) thinning of section due to basal faulting and associated glide along bedding planes. All three processes have occurred within the North Virgin Mountains, and thus distinguishing between processes requires careful MASTER interpretation coupled with field checks.

In Figure 4-2, all processes can be seen. In the south part of the image, scattered outcrops of bright red Tapeats sandstone trace the east end of the Proterozoic exposures, and appear to be segmented by valleys and landslides of green Paleozoic limestones coming off the high ridges to the immediate east. This is interpreted as a continuous north-trending section of Tapeats that appears discontinuous due to burial by surficial processes (type 1). In the central part of the image, these outcrops continue until they

come against the Elbow Canyon fault (Figure 4-3), where they curve to the northeast and disappear from the image. The juxtaposition of Paleozoic limestones against the Proterozoic rocks across this structure, the curving and disappearance of Tapeats outcrops, and the deflection of Paleoproterozoic lithologic traces along this curved lineament to the west, suggest that this is a normal fault with sufficient displacement to omit the Tapeats section (type 2). In the north part of the image, where the Great Unconformity trends east-west, bright red Tapeats outcrops gradually become thinner from east to west, before disappearing completely. When ground examined, numerous faults were observed to sole into the Bright Angel shale and Tapeats sandstone in this area, resulting in pronounced basal thinning of these units (type 3). When this area was explored further, a sub-horizontal normal fault was found along the Great Unconformity, with thinned, domino-style allochthonous fault blocks of Tapeats sandstone overlying fault gouge and Proterozoic basement.

A very thin, north-south trending section of Tapeats is visible to the east of two small ridges of Paleozoic limetone in the farthest northwest exposures of Proterozoic rocks. These ridges were previously mapped as Proterozoic rocks. Utilization of MASTER imagery resulted in a re-interpretation of these units, and targeted the thinned Tapeats sandstone unit for ground study. When examined, it was found that the Tapeats sandstone was basally thinned, overturned to the east, and in fault contact with Proterozoic basement. The similarly thinned Bright Angel shale ranged from overturned, to vertical, to moderately west-dipping. The ridges were composed of moderately west dipping Muav limestone. This structure mimics those found within the Laramide monoclines of the Grand Canyon, suggesting that the VMA had a Laramide component

of uplift. Furthermore, the presence of Cambrian section arching over the VMA helps define the overall structure as an anticline.

Summary

The following conclusions regarding the nature of Laramide contraction and Miocene extension were drawn, based on integrating MASTER image interpretation with structural field data:

1. Monoclinal geometries in the Cambrian section along the northwest limb of the VMA, as noted from MASTER imagery and structural study, suggest that Laramide contraction did occur here, and that some component of the VMA uplift is due to Late Cretaceous contractional deformation;

2. Proterozoic basement was structurally decoupled from the Phanerozoic section during Miocene extension, through soling of normal faults within the Bright Angel shale, Tapeats sandstone, and the Great Unconformity;

3. Steep, basement-penetrating normal faults omitted large amounts of Phanerozoic section, and were easily mapped in basement rocks where the fault trace offset to Proterozoic lithological traces

Quaternary Geology

Alluvial fan composition and mixing

Some of the most dramatic features visible on the MASTER images are the spectacular alluvial fans cascading to the west and east off of the VMA uplift. Bulk alluvial fan compositions are easily determined from the MASTER images, and where distinct fan compositions are in contact, intermingling and mixing signatures (lobate-cuspate contacts and intermediate "mixed" MASTER colors, respectively) are present.

Bright-red colored fans are SiO_2 rich, owing to derivation from a quartz-rich source region such as granitic bedrock (southwest Black Ridge) or Phanerozoic sandstones (east of Elbow Canyon and Mount Bangs). Fans are observed to redden-downward (away from source region), a likely proxy for sediment maturation. Bright-red beach and eolian deposits are also visible on the images, present near the shores of Lake Mead.

Reddish-purple and redish-blue colored fans suggest intermediate SiO_2 compositions and are derived from Proterozoic source regions with varying proportions of metasedimentary gneiss and schist, amphibolite, and granite. On the northwest flank of the VMA, fans derived from the immediate range front are blue colored, due to the abundance of mafic rocks there. Fans that are source canyons penetrating deeper into the Proterozoic rocks are reddish purple, due to the increasing abundance of psammitic and granitic gneisses eastward of the range front.

Green-colored fans are derived from carbonate and dolomite sedimentary rocks, which dominate the Paleozoic and Mesozoic sequence. The most dramatic carbonate fan sources the Paleozoic section in the Whitney Pockets area. This fan comes in abrupt contact with the purple-red fans derived from Black Ridge, suggesting a remarkable compositional variance due to quite distinct source regions. The sharp contacts where fans merge indicate immiscibility, reminiscent of merging rivers with different water density.

Structures

Quaternary fault scarps are visible as linear features cutting the alluvial fans west of Elbow Canyon and Mount Bangs. The most dramatic of these is visible three kilometers north-northwest of Elbow Canyon, where the steeply west-dipping Piedmont

normal fault cuts Quaternary fans draining from the west range front. Upon field examination, this fault was observed to have reactivated highly fissile mylonitic foliation surfaces in the Proterozoic rocks, evidence that Proterozoic foliation traces have continued to influence the geometry of brittle deformation from the Cretaceous through to the Quaternary.

7. Conclusions

Utilizing new MASTER thermal infared imagery in conjunction with detailed structural, metamorphic, and geochronologic studies resulted in the production of seven quadrangles of geologic mapping by one M.S. student. These maps were fundamental in developing a tectonic model for the long-lived geologic history of the North Virgin Mountains. Detailed new and refined geologic maps were produced for the North Virgin Mountains, and three generations of Paleoproterozoic fabrics, a Laramide monocline, Miocene detachment and steeply-dipping brittle faults, and Quaternary fault scarps were delineated and targeted for further research, based on interpretation of the MASTER thermal infared imagery. These results signify the importance of using multispectral thermal infrared data in geologic studies of Proterozoic through Quaternary lithologies, and interpretation of complex macroscopic brittle and ductile structures, where exposure warrants this technique. MASTER thermal infrared imagery is an essential part of efficient field mapping in the Mojave province and other regions of the world with minimal vegetation cover.

Appendixes

Appendix A: $^{39}Ar/^{40}Ar$ thermochronology

In this study, we take advantage of the variable argon retentivities and corresponding closure temperatures of hornblende (500-550°C), biotite (300-350°C) and K-feldspar (150-250°C), to examine the Proterozoic mid-crustal thermal evolution of the NVM crustal terrain.

Appendix Table 1. Argon isotopic results for micas and amphiboles.

ID	Temp (°C)	$^{40}Ar/^{39}Ar$	$^{37}Ar/^{39}Ar$	$^{36}Ar/^{39}Ar$ ($\times 10^{-3}$)	$^{39}Ar_K$ ($\times 10^{-15}$ mol)	K/Ca	$^{40}Ar^*$ (%)	^{39}Ar (%)	Age (Ma)	±1σ (Ma)
Q119, Biotite, wt. = 1.23 mg, J=0.015681, NM-134, Lab#=52047-01										
A	650	32.99	0.0860	8.060	51.8	5.9	92.8	17.1	707.1	1.3
B	750	39.67	0.0792	5.843	75.3	6.4	95.7	41.8	841.9	1.4
C	850	39.09	0.1358	5.804	40.0	3.8	95.6	55.0	831.9	1.6
D	920	47.90	0.2248	8.106	13.5	2.3	95.0	59.5	971.6	1.6
E	1000	45.32	0.1577	6.361	34.6	3.2	95.9	70.9	937.2	1.5
F	1075	41.11	0.1506	5.651	72.4	3.4	96.0	94.7	868.4	1.5
G	1100	41.14	0.2016	5.168	13.6	2.5	96.3	99.2	871.6	1.4
H	1180	49.08	1.878	7.577	2.45	0.27	95.7	100.0	996.7	2.9
total gas age			n=8		303.8	4.5			843.1	1.4
no plateau										
Q-60B Biotite, wt. = 0.36 mg, J=0.015648, NM-134, Lab#=52031-01										
A	650	22.02	0.1771	14.72	8.03	2.9	80.3	8.8	440.2	1.7
B	750	59.44	0.0710	4.658	7.08	7.2	97.7	16.6	1165.9	2.2
C	850	73.04	0.0836	2.026	9.12	6.1	99.2	26.6	1366.9	1.8
D	920	70.13	0.0836	2.532	11.4	6.1	98.9	39.1	1326.0	2.0
E	1000	71.60	0.1196	2.549	8.46	4.3	99.0	48.4	1345.8	2.0
F	1075	73.48	0.1752	2.590	12.9	2.9	99.0	62.6	1370.7	1.8
G	1110	74.95	0.2173	1.774	8.84	2.3	99.3	72.3	1393.2	2.4
H	1180	76.04	0.1313	1.036	14.7	3.9	99.7	88.4	1410.4	2.0
I	1210	77.10	0.2398	0.8056	7.10	2.1	99.7	96.2	1424.8	2.2
J	1250	76.27	0.2585	1.181	3.42	2.0	99.6	100.0	1412.7	2.5
total gas age			n=10		91.0	4.1			1278.8	1.8
plateau		MSWD=13**	n=3	steps H-J	25.2	3.1		27.7	1416	14*
Q-90A Biotite, wt = 0.74 mg, J=0.015743, NM-134, Lab#=52040-01										
A	550	53.26	0.5867	99.77	0.431	0.87	44.8	0.2	575	18
B	650	49.69	4.272	24.60	0.430	0.12	86.1	0.4	931	12
C	750	76.88	0.8475	9.390	1.45	0.60	96.5	1.0	1396.1	4.6
D	820	81.57	0.0230	4.365	6.49	22.2	98.4	3.8	1473.8	2.1
E	900	83.95	0.0094	1.391	20.8	54.3	99.5	12.7	1514.2	2.0
F	975	84.07	0.0074	0.4944	25.3	69.3	99.8	23.5	1518.9	1.9
G	1010	84.06	0.0098	0.1674	16.2	52.2	99.9	30.5	1519.9	2.2
H	1080	83.34	0.0151	0.4706	33.6	33.8	99.8	44.9	1510.0	2.0
I	1110	83.39	0.0230	0.4348	21.3	22.1	99.8	54.0	1510.8	2.4
J	1150	83.24	0.0104	0.4467	21.0	49.2	99.9	63.0	1509.1	1.8
K	1200	83.83	0.0090	0.2811	35.6	56.9	99.9	78.2	1516.8	2.4
L	1300	84.19	0.0209	0.2238	49.5	24.5	99.9	99.4	1521.4	2.1
M	1650	83.85	0.0551	7.469	1.29	9.3	97.4	100.0	1490.8	4.8
total gas age			n=13		233.4	41.8			1510.8	1.9
plateau		MSWD=7.8**	n=9	steps E-M	224.6	42.8		96.2	1514	9*

Appendix Table 1. Argon isotopic results for micas and amphiboles.

ID	Temp (°C)	$^{40}Ar/^{39}Ar$	$^{37}Ar/^{39}Ar$	$^{36}Ar/^{39}Ar$ ($\times 10^{-3}$)	$^{39}Ar_K$ ($\times 10^{-15}$ mol)	K/Ca	$^{40}Ar^*$ (%)	^{39}Ar (%)	Age (Ma)	±1σ (Ma)
Q81 Muscovite wt. = 0.58 mg, J=0.015495, NM-134, Lab#=52023-01										
A	600	47.34	0.0307	31.48	1.61	16.6	80.4	0.7	835.5	4.2
B	650	56.61	0.0084	3.082	1.86	60.7	98.4	1.5	1122.2	3.3
C	700	62.16	0.0071	2.315	2.90	71.4	98.9	2.8	1206.9	2.5
D	775	68.88	0.0064	1.358	7.58	79.6	99.4	6.1	1304.5	1.8
E	825	72.46	0.0033	0.6963	12.3	155.8	99.7	11.5	1355.0	1.8
F	875	73.63	0.0026	0.5763	20.9	196.4	99.8	20.6	1370.8	1.6
G	900	73.99	0.0018	0.2256	20.4	280.9	99.9	29.5	1376.8	1.6
H	925	73.85	0.0014	0.3967	18.6	362.8	99.8	37.6	1374.4	1.7
I	975	73.83	0.0011	0.3329	32.2	445.0	99.9	51.6	1374.3	2.1
J	1010	74.14	0.0014	0.4425	24.6	372.8	99.8	62.4	1378.0	1.7
K	1050	74.40	0.0012	0.3834	25.1	436.6	99.8	73.3	1381.5	1.7
L	1110	74.14	0.0007	0.3103	31.5	770.8	99.9	87.0	1378.5	2.3
M	1200	73.63	0.0014	1.240	9.79	352.7	99.5	91.3	1368.2	1.9
N	1300	71.69	0.0027	0.9907	4.11	192.3	99.6	93.1	1343.5	2.5
O	1650	74.51	0.0001	0.7799	15.8	######	99.7	100.0	1381.5	1.7
total gas age			n=15		229.2	706.3			1364.4	1.6
plateau		MSWD=25**	n=9	steps G-O	182.0	851.0		79.4	1375	15*
Q81 Hornblende, wt. = 1.40 mg, J=0.015479, NM-134, Lab#=52024-01										
A	800	12064	2.849	279.9	0.199	0.18	99.3	2.0	9436	117
D	1020	862.0	4.983	5.486	0.693	0.10	99.9	9.0	4808	41
E	1080	102.9	11.15	5.195	3.75	0.046	99.4	46.6	1720.1	3.1
F	1120	95.67	10.87	4.688	3.71	0.047	99.5	83.9	1641.3	2.9
G	1160	130.5	9.868	86.54	0.084	0.052	81.0	84.7	1756	66
H	1200	101.2	11.84	15.21	0.154	0.043	96.5	86.3	1671	27
I	1300	94.58	11.28	8.150	0.980	0.045	98.4	96.1	1617.9	5.1
K	1650	103.4	11.44	18.83	0.387	0.045	95.5	100.0	1682	13
total gas age			n=8		9.96	0.053			2048.0	9.2
plateau		MSWD=8.3**	n=5	steps F-K	5.31	0.046		53.4	1638	17*
Q60B Hornblende, wt. = 2.03 mg, J=0.0155000, NM-134, Lab#=52025-01										
A	800	136.1	4.539	36.72	1.97	0.11	92.3	4.9	1952.2	4.8
B	850	102.8	1.349	10.10	0.845	0.38	97.2	7.0	1687.7	6.9
C	950	46.02	1.947	3.144	3.32	0.26	98.3	15.3	958.7	2.3
D	1020	81.58	5.333	3.587	4.22	0.096	99.2	25.8	1469.5	2.4
E	1080	94.22	8.285	2.871	16.4	0.062	99.8	66.5	1627.3	1.9
F	1120	77.81	6.308	4.011	1.70	0.081	99.1	70.7	1422.0	4.1
G	1160	89.22	7.796	13.88	0.848	0.065	96.1	72.8	1529.6	6.9
H	1200	98.18	9.220	3.783	4.36	0.055	99.6	83.7	1670.5	2.6
I	1300	97.96	8.921	4.319	5.74	0.057	99.4	98.0	1665.8	2.5
J	1400	92.39	8.577	7.699	0.467	0.059	98.3	99.1	1590.3	8.9
K	1650	90.02	8.273	26.12	0.355	0.062	92.2	100.0	1497	12
total gas age			n=11		40.2	0.090			1570.7	2.5
plateau		MSWD=1.7	n=2	steps H-I	10.1	0.056		25.1	1668	5*

Appendix Table 1. Argon isotopic results for micas and amphiboles.

ID	Temp (°C)	$^{40}Ar/^{39}Ar$	$^{37}Ar/^{39}Ar$	$^{36}Ar/^{39}Ar$ (x 10^{-3})	$^{39}Ar_K$ (x 10^{-15} mol)	K/Ca	$^{40}Ar^*$ (%)	^{39}Ar (%)	Age (Ma)	±1σ (Ma)
Q12 Hornblende, wt. = 2.61 mg, J=0.0155135, NM-134, Lab#=52026-01										
A	800	140.1	9.932	103.8	0.445	0.051	78.7	1.2	1807	13
C	950	53.57	6.358	14.38	0.678	0.080	93.0	3.0	1036.3	7.0
D	1020	80.63	11.01	15.35	0.527	0.046	95.5	4.4	1424.9	9.3
E	1080	96.00	11.47	3.829	19.9	0.044	99.8	56.9	1651.3	1.8
F	1120	93.96	11.25	4.023	11.1	0.045	99.7	86.1	1627.1	2.7
G	1160	94.32	11.75	31.34	0.320	0.043	91.2	86.9	1537	15
H	1200	95.10	12.18	5.110	1.33	0.042	99.4	90.4	1638.0	4.3
I	1300	93.87	12.15	4.520	2.93	0.042	99.6	98.2	1625.8	3.1
J	1400	96.83	12.45	4.882	0.278	0.041	99.5	98.9	1659	14
K	1650	95.98	11.23	16.97	0.413	0.045	95.7	100.0	1606	12
total gas age			n=10		37.9	0.045			1628.1	2.7
plateau		MSWD=23**	n=7	steps E-K	36.2	0.044		95.6	1639	20*
Q90A Hornblende, wt. = 1.93 mg, J=0.015585, NM-134, Lab#=52028-01										
A	800	133.3	5.030	140.6	0.320	0.10	69.1	0.9	1610	19
B	850	119.3	1.510	23.76	0.146	0.34	94.2	1.3	1827	29
C	950	89.28	1.840	8.904	0.684	0.28	97.2	3.1	1544.5	7.0
D	1020	77.14	2.626	4.145	0.958	0.19	98.7	5.7	1412.7	5.0
E	1080	106.0	7.983	4.385	2.35	0.064	99.4	12.1	1758.2	3.3
F	1120	95.77	10.87	3.510	16.8	0.047	99.8	57.8	1653.7	2.0
G	1160	93.58	10.02	4.186	7.38	0.051	99.5	77.9	1625.1	2.5
H	1200	93.05	9.741	4.085	3.69	0.052	99.5	88.0	1618.7	2.6
I	1300	91.17	7.351	6.438	2.18	0.069	98.6	93.9	1584.8	3.2
J	1400	95.45	11.62	5.826	1.23	0.044	99.2	97.3	1643.5	4.7
K	1650	95.74	11.80	8.673	0.996	0.043	98.3	100.0	1637.6	6.0
total gas age			n=11		36.7	0.060			1638.2	2.7
plateau		MSWD=74**	n=6	steps F-K	32.2	0.050		87.9	1630	35*
Q108 Hornblende, wt. = 2.55 mg, J=0.015718, NM-134, Lab#=52045-01										
A	800	177.8	11.46	68.18	1.43	0.045	89.2	1.7	2266.6	6.7
B	850	58.23	3.944	16.09	0.426	0.13	92.4	2.2	1107	11
C	950	63.97	4.366	10.32	0.870	0.12	95.8	3.2	1219.2	5.6
DD	1020	90.28	5.443	3.671	7.54	0.094	99.3	12.0	1589.7	2.3
E	1080	87.15	5.433	2.001	49.5	0.094	99.8	69.9	1558.3	2.0
F	1120	82.80	4.750	2.677	4.85	0.11	99.5	75.5	1501.7	2.6
G	1160	80.77	4.806	11.10	1.22	0.11	96.4	76.9	1445.1	4.4
H	1200	85.43	5.686	3.424	5.18	0.090	99.3	83.0	1532.9	2.8
I	1300	83.94	6.526	2.826	13.2	0.078	99.6	98.4	1518.3	2.2
J	1400	74.06	7.553	15.52	0.509	0.068	94.6	99.0	1344.5	8.9
K	1650	91.47	18.87	19.11	0.854	0.027	95.5	100.0	1572.5	6.9
total gas age			n=11		85.6	0.091			1553.5	2.2
plateau		MSWD=192**	n=7	steps E-K	75.4	0.091		88.0	1524	52*

Appendix Table 1. Argon isotopic results for micas and amphiboles.

ID	Temp (°C)	$^{40}Ar/^{39}Ar$	$^{37}Ar/^{39}Ar$	$^{36}Ar/^{39}Ar$ (x 10^{-3})	$^{39}Ar_K$ (x 10^{-15} mol)	K/Ca	$^{40}Ar^*$ (%)	^{39}Ar (%)	Age (Ma)	±1σ (Ma)
Qft-18 Altered biotite, wt. = 0.70 mg, J=0.015342, NM-140, Lab#=52508-01										
A	585	14.67	0.3296	23.74	18.6	1.5	52.3	28.8	200.5	1.2
B	685	22.19	1.013	19.32	8.38	0.50	74.6	41.8	408.3	1.7
C	785	23.58	1.001	11.45	8.11	0.51	86.0	54.3	488.5	1.5
D	855	27.55	0.3254	16.35	6.66	1.6	82.5	64.6	539.7	1.7
E	935	30.77	0.8381	19.49	6.81	0.61	81.5	75.1	587.2	2.0
F	1010	38.12	1.194	14.01	5.61	0.43	89.4	83.8	758.9	1.8
G	1045	44.27	1.767	5.386	1.63	0.29	97.2	86.3	915.4	3.7
H	1115	47.45	2.987	2.623	3.55	0.17	98.9	91.8	979.8	2.2
I	1145	52.16	0.9140	0.4314	2.82	0.56	99.9	96.1	1060.0	2.4
J	1185	56.96	0.6166	0.2902	1.98	0.83	99.9	99.2	1132.6	2.6
K	1235	57.25	0.8912	1.472	0.517	0.57	99.4	100.0	1132.1	7.7
total gas age			n=11		64.7	0.91			521.7	1.7
no plateau										
Qft-20 Biotite, wt. = 0.61 mg, J=0.0151200, NM-140, Lab#=52509-01										
A	585	53.90	0.0328	12.90	15.7	15.5	92.9	8.0	1016.9	1.8
B	685	72.15	0.0070	1.865	40.9	72.8	99.2	29.0	1323.2	2.3
C	785	73.19	0.0116	1.572	23.3	44.0	99.4	40.9	1337.9	1.9
D	855	72.13	0.0213	1.704	9.64	23.9	99.3	45.8	1323.7	2.0
E	935	72.94	0.0165	1.857	22.2	30.9	99.3	57.2	1333.7	2.0
F	1010	70.89	0.0144	1.873	39.0	35.4	99.2	77.2	1306.7	2.0
G	1045	73.34	0.0106	1.627	21.4	48.3	99.4	88.2	1340.0	2.0
H	1115	75.60	0.0115	0.8677	23.1	44.3	99.7	100.0	1371.7	1.8
total gas age			n=8		195.2	44.1			1305.9	1.8
plateau		MSWD=115**	n=7	steps B-H	179.6	46.6		92.0	1336	33*
Qft-21 Biotite, wt. = 1.03 mg, J=0.0149108, NM-140, Lab#=52465-02										
A	585	54.57	0.0100	9.881	34.3	51.1	94.7	8.2	1029.9	2.2
B	685	73.20	0.0043	0.9994	89.3	117.8	99.6	29.6	1327.1	2.3
C	785	76.13	0.0057	0.7670	68.7	89.2	99.7	46.1	1365.4	2.1
D	855	71.50	0.0096	1.263	38.1	53.4	99.5	55.2	1304.1	2.1
E	935	72.50	0.0053	0.9466	74.5	96.4	99.6	73.0	1318.2	1.9
F	1010	75.55	0.0044	0.6123	61.9	116.3	99.8	87.8	1358.6	2.4
G	1045	76.38	0.0049	1.082	20.7	103.2	99.6	92.8	1367.4	2.2
H	1115	78.42	0.0048	0.4762	25.2	107.3	99.8	98.8	1395.1	2.2
I	1145	78.97	0.0031	1.179	4.89	167.0	99.6	100.0	1399.4	2.8
total gas age			n=9		417.6	96.9			1316.9	2.0
plateau		MSWD=244**	n=8	steps B-I	383.3	101.0		91.8	1351	49*

Appendix Table 1. Argon isotopic results for micas and amphiboles.

ID	Temp (°C)	$^{40}Ar/^{39}Ar$	$^{37}Ar/^{39}Ar$	$^{36}Ar/^{39}Ar$ (x 10^{-3})	$^{39}Ar_K$ (x 10^{-15} mol)	K/Ca	$^{40}Ar^*$ (%)	^{39}Ar (%)	Age (Ma)	±1σ (Ma)
Qft-14 Biotite, wt. = 1.04 mg, J=0.0149592, NM-140, Lab#=52466-01										
A	585	64.83	0.0046	7.823	22.5	110.4	96.4	5.8	1190.8	1.9
B	685	76.44	0.0017	0.6964	99.5	306.6	99.7	31.4	1372.6	2.7
C	785	75.50	0.0023	0.3495	63.0	224.5	99.9	47.6	1362.1	2.5
D	855	75.44	0.0070	0.7526	23.8	73.2	99.7	53.8	1359.7	2.1
E	935	76.83	0.0039	0.5403	46.2	131.5	99.8	65.6	1378.1	2.1
F	1010	76.59	0.0040	0.5075	57.3	126.2	99.8	80.4	1375.3	2.1
G	1045	76.71	0.0042	0.7875	24.2	120.5	99.7	86.6	1375.7	1.9
H	1115	76.08	0.0067	0.5471	26.6	76.4	99.8	93.5	1368.7	2.1
I	1145	74.71	0.0037	0.2943	17.2	138.6	99.9	97.9	1352.2	1.9
J	1185	73.86	0.0031	0.4003	8.19	164.6	99.8	100.0	1341.0	2.4
total gas age			n=10		388.4	182.4			1359.0	2.1
plateau		MSWD=32**	n=9	steps B-J	365.9	186.9		94.2	1365	18*
Qft-24b Biotite, wt. = 0.94, J=0.0151612, NM-140, Lab#=52479-01										
A	585	56.77	0.0066	3.690	13.5	76.9	98.1	3.9	1103.9	1.8
B	685	78.27	0.0013	0.2976	58.6	401.5	99.9	21.0	1410.1	2.0
C	785	78.89	0.0009	0.2234	71.6	598.7	99.9	41.9	1418.1	2.5
D	855	78.91	0.0021	0.2158	28.4	242.7	99.9	50.2	1418.4	1.9
E	935	80.05	0.0016	0.1798	52.4	313.5	99.9	65.5	1432.7	2.3
F	1010	79.35	0.0009	0.1293	72.5	587.3	100.0	86.6	1424.1	2.6
G	1045	78.82	0.0012	0.4959	19.0	421.9	99.8	92.2	1416.2	1.9
H	1115	78.73	0.0017	0.1860	20.4	294.9	99.9	98.1	1416.3	2.1
I	1145	79.10	0.0029	1.021	6.39	178.9	99.6	100.0	1417.8	2.5
total gas age			n=9		342.7	433.3			1407.7	2.0
plateau		MSWD=9.8**	n=8	steps B-I	329.2	447.9		96.1	1419	10*

Isotopic ratios corrected for blank, radioactive decay, and mass discrimination, not corrected for interferring rec
Individual analyses show analytical error only; mean age errors also include error in J and irradiation parameters.
Analyses in italics are excluded from plateau age calculations.

* 2 σ error

** MSWD outside of 95% confidence window, plateau errors multiplied by square root of MSWD.

Summary of 40Ar/39Ar mica and hornblende ages.

Sample	Min	% K_2O[1]	WMA[2] (Ma)	± WMA (2σ)	MSWD	Steps	%^{39}Ar	TGA[3] (Ma)	±TGA[4] (2σ)
Q119	B	6.2						843.1	2.8
Q60B	B	6.4	1416	14	13	H-J	27.7	1279	3.6
Q90A	B	8.0	1514	9	7.8	E-M	96.2	1511	3.8
Qft-14	B	9.8	1365	18	32	B-J	94.2	1359.0	4.1
Qft-18	B	2.3						521.7	3.4
Qft-20	B	8.1	1336	33	115	B-H	92.0	1306	3.6
Qft-21	B	10.3	1351	49	244	B-I	91.8	1317	4.0
Qft-24b	B	9.2	1419	10	9.8	B-I	96.1	1408	4.0
Q81	M	10	1375	15	25	G-O	79.4	1364	3.2
Q81	H	0.18	1638	17	8.3	F-K	53.4	2048	18
Q60B	H	0.50	1668	5	1.7	H-I	25.1	1571	5.0
Q12	H	0.37	1639	20	23	E-K	95.6	1628	5.4
Q90A	H	0.48	1630	35	74	F-K	87.9	1638	5.4
Q108	H	0.85	1524	52	192	E-K	88.0	1554	4.4

[1] K_2O calculated from sample weight and ^{39}Ar concentration assuming Q81 muscovite contians 10.0 weight percent K_2O.

[2] WMA - weighted mean age calculated by weighting each step by the inverse of its variance. Error calculated by Taylor (1982) method.

[3] TGA - total gas age calculated by weighting each step by its ^{39}Ar concentration.

[4] TGA - total gas age error calculated by weighting each step error by its ^{39}Ar concentration.

Min = Mineral dated. B=Biotite, M=Muscovite, H=Hornblende

Appendix Table 2. Virgin Mountains K-feldspar argon data.

ID	Temp (°C)	$^{40}Ar/^{39}Ar$	$^{37}Ar/^{39}Ar$	$^{36}Ar/^{39}Ar$ (x 10^{-3})	$^{39}Ar_K$ (x 10^{-15} mol)	K/Ca	$^{40}Ar^*$ (%)	^{39}Ar (%)	Age (Ma)	±1σ (Ma)	Time (min)
Qft-10 K-feldspar, wt. = 2.05 mg, J=0.0149454, NM-140, Lab#=52459-01											
A	450	792.7	0.0117	53.65	1.49	43.8	98.0	0.1	4572.5	8.4	10.4
B	450	46.12	0.0055	7.177	0.720	92.7	95.4	0.2	911.4	6.7	20.8
C	450	29.54	0.0160	5.116	0.573	31.9	94.9	0.2	630.9	8.5	29.1
D	500	34.93	0.0146	1.293	1.05	34.9	98.9	0.3	750.7	4.9	9.9
E	500	23.32	0.0210	1.636	1.28	24.3	97.9	0.4	529.4	4.1	20.7
F	500	24.07	0.0267	0.1913	1.18	19.1	99.8	0.5	552.9	4.3	29.0
G	550	50.56	0.0221	1.871	2.34	23.1	98.9	0.7	1006.6	3.1	11.0
H	550	24.85	0.0126	-0.7240	2.46	40.4	100.9	1.0	573.5	2.6	21.3
I	550	25.35	0.0103	0.3576	2.28	49.6	99.6	1.2	577.1	2.6	29.2
J	600	40.91	0.0124	0.7252	3.76	41.2	99.5	1.5	856.9	2.1	10.8
K	600	31.25	0.0071	1.664	3.79	71.5	98.4	1.8	681.9	2.2	21.2
L	600	46.06	0.0121	39.90	3.42	42.3	74.4	2.1	745.7	3.0	29.2
M	650	46.64	0.0122	0.3498	4.65	41.9	99.8	2.5	952.2	2.0	10.9
N	650	41.69	0.0113	0.1133	4.71	45.1	99.9	2.9	872.8	1.8	20.7
O	650	43.93	0.0144	0.1857	4.08	35.3	99.9	3.3	909.4	2.4	29.3
P	700	50.94	0.0139	1.824	5.53	36.8	98.9	3.7	1012.7	1.9	10.2
Q	700	46.10	0.0073	0.3478	5.28	69.9	99.8	4.2	943.6	1.8	20.5
R	700	47.96	0.0081	0.5702	4.54	63.1	99.7	4.6	972.0	2.2	29.0
S	750	53.81	0.0081	0.3835	5.47	62.9	99.8	5.1	1062.7	2.3	11.3
T	750	52.71	0.0096	0.2150	5.75	53.4	99.9	5.6	1046.9	2.2	21.2
U	750	54.77	0.0085	0.2791	4.77	60.1	99.9	6.0	1077.4	2.3	29.7
V	800	61.37	0.0078	0.3282	5.28	65.8	99.8	6.4	1172.5	2.2	11.1
W	800	61.37	0.0078	0.0288	6.01	65.4	100.0	6.9	1173.8	2.2	21.1
X	850	69.06	0.0083	0.4695	8.58	61.7	99.8	7.7	1277.1	2.2	11.2
Y	850	70.92	0.0057	0.2758	9.26	90.1	99.9	8.5	1302.4	2.0	21.4
Z	900	78.08	0.0062	0.4144	11.1	82.4	99.8	9.4	1393.3	2.0	11.3
ZA	900	78.31	0.0042	0.1663	13.6	122.0	99.9	10.6	1397.1	2.0	21.3
ZB	950	82.36	0.0046	0.3659	16.1	110.0	99.9	12.0	1446.1	2.0	11.5
ZC	950	78.98	0.0025	0.2172	18.9	208.1	99.9	13.6	1405.2	2.4	21.5
ZD	1000	80.24	0.0048	0.3096	23.4	106.6	99.9	15.7	1420.5	1.9	11.4
ZE	1000	75.45	0.0036	0.2836	30.2	143.4	99.9	18.3	1360.8	1.8	21.5
ZF	1050	77.34	0.0047	0.4146	38.7	107.8	99.8	21.6	1384.1	2.0	10.3
ZG	1050	73.52	0.0038	0.2784	44.9	132.5	99.9	25.5	1336.1	2.0	20.2
ZH	1100	80.88	0.0057	0.6183	55.9	90.3	99.8	30.3	1427.1	2.5	10.0
ZI	1100	77.38	0.0052	0.2334	63.4	97.7	99.9	35.8	1385.3	2.3	19.9
ZJ	1100	76.76	0.0050	0.2611	106.8	101.3	99.9	45.0	1377.4	3.3	53.4
ZK	1100	76.76	0.0042	0.2662	130.1	122.8	99.9	56.3	1377.4	2.0	114.1
ZL	1100	77.40	0.0034	0.4034	121.6	149.6	99.8	66.8	1384.9	2.8	234.1
ZM	1200	86.90	0.0035	0.4776	76.4	146.2	99.8	73.4	1499.7	3.2	5.7
ZN	1300	77.53	0.0025	0.3341	234.0	205.9	99.9	93.6	1386.8	3.3	6.8
ZO	1400	72.77	0.0028	0.3045	28.1	182.0	99.9	96.0	1326.4	2.1	7.2
ZP	1685	74.45	0.0031	0.4944	46.2	163.6	99.8	100.0	1347.3	2.4	6.8
total gas age			n=42		1157.5	137.3			1362.2	2.5	

Appendix Table 2. Virgin Mountains K-feldspar argon data.

ID	Temp (°C)	$^{40}Ar/^{39}Ar$	$^{37}Ar/^{39}Ar$	$^{36}Ar/^{39}Ar$ (x 10^{-3})	$^{39}Ar_K$ (x 10^{-15} mol)	K/Ca	$^{40}Ar^*$ (%)	^{39}Ar (%)	Age (Ma)	±1σ (Ma)	Time (min)
Qft-14 K-feldspar, wt. = 2.26 mg, J=0.0148870, NM-140, Lab#=52460-01											
A	450	252.9	0.0279	53.98	0.940	18.3	93.7	0.1	2724.2	9.8	9.7
B	450	46.59	0.0126	8.984	0.426	40.7	94.3	0.1	907.6	9.2	20.3
C	450	40.24	0.0487	16.24	0.394	10.5	88.1	0.2	764.1	10.4	28.7
D	500	26.11	0.0249	3.573	0.754	20.5	96.0	0.2	571.4	6.2	10.1
E	500	20.06	0.0170	4.437	1.07	30.1	93.5	0.3	443.7	3.9	20.3
F	500	18.54	0.0144	4.089	1.21	35.5	93.5	0.4	413.7	3.6	28.8
G	550	27.61	0.0090	1.716	2.71	56.5	98.2	0.6	611.2	1.8	11.0
H	550	17.36	0.0074	1.301	3.46	69.4	97.8	0.9	406.1	1.6	20.8
I	550	18.93	0.0075	1.322	3.51	68.3	97.9	1.2	439.3	1.6	29.6
J	600	28.10	0.0076	0.5549	5.06	67.0	99.4	1.7	627.0	1.6	10.4
K	600	24.21	0.0063	0.3414	5.36	81.0	99.6	2.1	552.8	1.4	20.9
L	600	25.87	0.0057	1.408	4.39	89.3	98.4	2.5	579.3	1.6	28.8
M	650	30.33	0.0118	0.6437	5.27	43.3	99.4	3.0	668.3	1.5	10.4
N	650	27.30	0.0109	0.5936	4.86	46.8	99.4	3.4	611.5	1.4	20.2
O	650	30.69	0.0121	1.047	4.03	42.2	99.0	3.7	672.9	1.7	29.2
P	700	33.20	0.0230	0.4840	3.43	22.2	99.6	4.0	721.6	1.9	10.4
Q	700	29.47	0.0191	0.7344	3.34	26.7	99.3	4.3	651.8	1.9	20.5
R	700	30.40	0.0264	2.059	2.60	19.4	98.0	4.5	661.8	2.4	28.0
S	750	39.29	0.0290	1.015	2.39	17.6	99.2	4.7	825.4	2.5	10.8
T	750	33.67	0.0385	0.9571	2.49	13.2	99.2	4.9	727.7	2.4	20.6
U	750	35.64	0.0427	2.566	2.20	11.9	97.9	5.1	754.2	2.6	29.5
V	800	42.68	0.0523	1.019	2.01	9.8	99.3	5.3	882.2	2.8	10.2
W	800	40.40	0.0503	1.142	2.62	10.1	99.2	5.5	843.6	2.2	21.1
X	850	47.80	0.0439	1.180	3.30	11.6	99.3	5.8	963.9	2.3	11.1
Y	850	45.96	0.0439	1.212	4.10	11.6	99.2	6.1	934.4	2.1	20.9
Z	900	53.58	0.0317	0.8045	4.93	16.1	99.6	6.6	1054.3	2.0	11.1
ZA	900	51.68	0.0194	0.9540	6.84	26.4	99.5	7.1	1024.8	1.7	21.0
ZB	950	59.32	0.0146	0.7221	8.08	35.0	99.6	7.8	1138.6	2.1	11.3
ZC	950	57.30	0.0106	0.5336	10.9	48.0	99.7	8.8	1110.2	1.8	21.5
ZD	1000	63.28	0.0082	0.4829	12.3	62.3	99.8	9.8	1195.1	2.2	11.3
ZE	1000	63.15	0.0073	0.5130	16.1	69.8	99.8	11.2	1193.2	1.8	21.2
ZF	1050	67.30	0.0080	0.7023	16.9	63.6	99.7	12.6	1249.1	2.2	9.8
ZG	1050	66.02	0.0063	0.4324	25.4	80.8	99.8	14.8	1232.9	1.7	20.1
ZH	1100	67.35	0.0078	0.7375	20.3	65.1	99.7	16.5	1249.7	1.9	9.1
ZI	1100	66.89	0.0063	0.3216	33.5	80.4	99.9	19.4	1245.1	2.3	19.9
ZJ	1100	67.00	0.0055	0.2648	73.4	93.3	99.9	25.7	1246.8	2.4	67.0
ZK	1100	68.03	0.0042	0.3839	81.6	121.6	99.8	32.6	1260.1	2.1	124.5
ZL	1100	68.72	0.0035	0.5350	89.7	147.0	99.8	40.3	1268.7	2.3	232.5
ZM	1200	67.67	0.0040	0.1649	48.9	128.5	99.9	44.5	1256.2	1.9	5.7
ZN	1300	71.06	0.0021	0.0974	215.2	245.3	100.0	62.8	1301.2	3.0	6.6
ZO	1400	69.48	0.0021	0.1523	131.0	238.4	99.9	74.0	1280.4	2.7	7.1
ZP	1685	71.73	0.0021	0.0825	304.1	240.0	100.0	100.0	1310.1	2.8	6.7
total gas age			n=42		1171.1	176.2			1240.4	2.4	

Appendix Table 2. Virgin Mountains K-feldspar argon data.

ID	Temp (°C)	$^{40}Ar/^{39}Ar$	$^{37}Ar/^{39}Ar$	$^{36}Ar/^{39}Ar$ ($\times 10^{-3}$)	$^{39}Ar_K$ ($\times 10^{-15}$ mol)	K/Ca	$^{40}Ar^*$ (%)	^{39}Ar (%)	Age (Ma)	$\pm 1\sigma$ (Ma)	Time (min)
Qft-18 K-feldspar, wt. =1.90 mg, J=0.0147412, NM-140, Lab#=52461-01											
A	450	669.9	0.0321	80.55	1.30	15.9	96.5	0.1	4246	14	9.7
B	450	42.25	-0.0161	17.29	0.570	-	87.9	0.2	787	13	20.8
C	450	24.84	0.0037	4.635	0.499	137.0	94.5	0.2	536	14	28.7
D	500	18.76	-0.0022	1.144	0.969	-	98.2	0.3	432.9	7.1	9.6
E	500	16.37	0.0104	1.799	1.33	49.2	96.8	0.5	378.1	5.1	20.4
F	500	11.44	0.0040	1.320	1.29	126.3	96.6	0.6	271.9	5.2	28.4
G	550	34.68	0.0047	1.654	2.72	108.8	98.6	0.9	736.0	3.1	11.0
H	550	11.44	0.0087	-0.0224	2.75	58.8	100.1	1.1	280.9	2.5	21.1
I	550	11.24	0.0036	-0.2786	2.43	141.8	100.7	1.4	278.1	2.9	29.5
J	600	46.84	0.0085	1.664	4.61	60.0	99.0	1.8	939.1	2.7	10.1
K	600	14.91	0.0082	-0.4658	3.85	62.2	100.9	2.2	360.9	1.9	20.6
L	600	15.82	0.0085	-0.5015	3.01	59.8	100.9	2.5	380.8	2.4	28.8
M	650	29.47	0.0117	0.3872	4.06	43.6	99.6	2.9	648.4	2.2	10.7
N	650	21.78	0.0100	0.3774	3.64	51.2	99.5	3.3	499.8	2.3	20.4
O	650	22.02	0.0088	0.5952	2.80	58.0	99.2	3.6	503.2	2.9	29.0
P	700	33.99	0.0139	-0.3506	3.40	36.8	100.3	3.9	734.2	2.7	9.4
Q	700	26.40	0.0083	-0.4162	3.39	61.2	100.5	4.2	595.0	2.5	20.4
R	700	26.89	0.0125	-0.6958	2.68	40.9	100.8	4.5	605.9	3.0	28.4
S	750	36.34	0.0125	-0.7462	2.97	40.8	100.6	4.8	777.4	2.8	11.0
T	750	31.08	0.0100	-0.9239	2.87	50.8	100.9	5.1	685.2	2.7	20.8
U	750	32.67	0.0103	-1.0461	2.50	49.6	100.9	5.3	714.3	3.3	29.1
V	800	38.94	0.0125	0.0095	2.63	40.9	100.0	5.6	818.0	3.7	10.6
W	800	40.45	0.0133	-0.2010	3.30	38.3	100.2	5.9	844.4	2.8	20.6
X	850	45.57	0.0132	0.9416	4.76	38.6	99.4	6.4	922.3	2.4	11.1
Y	850	48.31	0.0124	0.2018	5.51	41.1	99.9	6.9	968.9	2.3	21.2
Z	900	54.39	0.0107	0.4462	6.56	47.6	99.8	7.6	1060.0	2.2	11.2
ZA	900	58.39	0.0077	-0.0527	7.58	66.6	100.0	8.3	1120.2	2.1	21.0
ZB	950	63.26	0.0085	0.1245	8.95	60.0	99.9	9.2	1187.8	2.4	11.3
ZC	950	63.80	0.0069	0.1301	10.9	74.0	99.9	10.3	1195.2	2.2	21.4
ZD	1000	66.45	0.0089	0.3890	13.3	57.4	99.8	11.6	1230.2	2.0	11.2
ZE	1000	65.71	0.0068	0.1993	16.3	74.6	99.9	13.3	1221.0	1.8	21.3
ZF	1050	66.97	0.0090	0.2956	17.6	57.0	99.9	15.0	1237.5	1.9	9.8
ZG	1050	65.89	0.0070	0.2207	21.6	72.5	99.9	17.2	1223.3	1.8	19.4
ZH	1100	65.88	0.0106	0.8965	23.7	48.1	99.6	19.5	1220.4	2.1	9.6
ZI	1100	65.68	0.0107	0.3824	27.2	47.5	99.8	22.2	1219.8	2.3	19.2
ZJ	1100	66.69	0.0094	0.6133	50.9	54.0	99.7	27.3	1232.5	2.7	65.6
ZK	1100	68.56	0.0094	0.8471	50.4	54.1	99.6	32.3	1256.5	1.8	122.1
ZL	1100	69.14	0.0100	1.134	55.3	51.3	99.5	37.8	1263.1	1.8	233.9
ZM	1200	67.37	0.0027	0.1492	60.3	188.5	99.9	43.8	1243.4	1.9	5.8
ZN	1300	68.74	0.0025	0.2421	453.4	205.0	99.9	88.8	1261.2	4.2	6.7
ZO	1400	66.14	0.0025	0.4663	45.9	205.1	99.8	93.4	1225.6	1.8	7.1
ZP	1685	68.37	0.0028	0.3505	66.8	183.8	99.8	100.0	1255.9	2.2	6.7
total gas age			n=42		1006.6	146.6			1211.2	2.9	

Appendix Table 2. Virgin Mountains K-feldspar argon data.

ID	Temp (°C)	$^{40}Ar/^{39}Ar$	$^{37}Ar/^{39}Ar$	$^{36}Ar/^{39}Ar$ ($\times 10^{-3}$)	$^{39}Ar_K$ ($\times 10^{-15}$ mol)	K/Ca	$^{40}Ar^*$ (%)	^{39}Ar (%)	Age (Ma)	±1σ (Ma)	Time (min)
Qft-20 K-feldspar, wt. = 1.87 mg, J=0.0146928, NM-140, Lab#=52462-01											
A	450	705.2	0.0118	80.62	1.41	43.2	96.6	0.1	4327.9	7.0	9.4
B	450	66.25	0.0257	15.40	0.688	19.9	93.1	0.2	1164.0	5.6	19.3
C	450	61.45	0.0004	19.84	0.590	1286.8	90.5	0.3	1076.8	5.8	28.4
D	500	53.90	0.0065	9.153	1.09	78.2	95.0	0.4	1011.6	4.1	9.3
E	500	26.38	-0.0010	6.829	1.28	-	92.3	0.5	551.6	3.3	19.7
F	500	22.98	0.0069	3.055	1.22	74.5	96.1	0.6	506.4	3.3	28.3
G	550	44.99	0.0074	2.690	2.41	68.6	98.2	0.9	902.3	2.9	10.3
H	550	19.66	0.0087	1.900	2.78	58.6	97.1	1.2	445.8	1.7	20.7
I	550	20.21	0.0090	3.823	2.67	56.8	94.4	1.5	445.5	2.0	29.1
J	600	33.95	0.0069	1.223	4.69	73.4	98.9	1.9	723.4	1.9	10.4
K	600	16.35	0.0086	1.393	5.26	59.2	97.5	2.5	379.1	1.3	20.4
L	600	18.13	0.0066	0.6277	5.01	77.8	99.0	3.0	421.7	1.4	28.7
M	650	24.19	0.0061	0.5322	6.81	83.2	99.4	3.7	545.2	2.0	9.5
N	650	21.84	0.0079	0.4450	8.54	64.7	99.4	4.6	499.1	1.1	20.2
O	650	24.18	0.0087	0.8083	8.00	58.8	99.0	5.4	543.5	1.1	28.5
P	700	34.60	0.0095	0.5190	8.72	53.5	99.6	6.3	738.5	1.4	8.7
Q	700	30.06	0.0094	0.3144	10.9	54.4	99.7	7.5	657.8	1.2	20.0
R	700	32.80	0.0092	0.4808	9.41	55.3	99.6	8.4	706.7	1.5	27.9
S	750	45.47	0.0109	0.5052	10.2	46.7	99.7	9.5	920.4	1.5	11.1
T	750	40.38	0.0105	0.2203	10.5	48.7	99.8	10.6	838.9	1.6	20.8
U	750	44.28	0.0103	0.6017	9.09	49.3	99.6	11.5	900.9	1.4	29.1
V	800	57.73	0.0100	0.1666	8.88	50.8	99.9	12.4	1107.1	1.9	10.2
W	800	54.01	0.0108	0.3530	9.85	47.1	99.8	13.5	1052.1	2.0	20.8
X	850	68.27	0.0121	0.4972	12.0	42.3	99.8	14.7	1251.1	2.0	11.1
Y	850	64.92	0.0097	0.3941	12.4	52.5	99.8	16.0	1206.5	1.8	21.0
Z	900	83.21	0.0075	0.6346	14.6	68.3	99.8	17.5	1438.5	2.2	10.9
ZA	900	76.33	0.0045	0.6594	15.3	112.7	99.7	19.1	1354.2	2.0	21.0
ZB	950	94.71	0.0053	0.9279	20.1	96.8	99.7	21.2	1569.8	2.4	11.3
ZC	950	83.92	0.0037	0.5928	20.5	136.6	99.8	23.3	1447.0	1.8	21.3
ZD	1000	94.76	0.0046	1.056	31.5	110.8	99.7	26.6	1569.9	2.6	11.0
ZE	1000	84.44	0.0040	0.5987	29.5	129.1	99.8	29.6	1453.2	2.3	21.1
ZF	1050	95.51	0.0043	1.012	44.9	119.0	99.7	34.3	1578.3	2.8	9.8
ZG	1050	83.89	0.0042	0.5427	40.8	120.1	99.8	38.5	1446.8	2.4	19.6
ZH	1100	93.59	0.0044	0.8364	43.7	116.1	99.7	43.0	1557.6	2.1	7.6
ZI	1100	82.81	0.0039	0.4094	39.5	130.9	99.9	47.1	1434.4	2.1	16.2
ZJ	1100	82.22	0.0032	0.4397	73.5	158.0	99.8	54.7	1427.2	2.6	69.6
ZK	1100	82.73	0.0026	0.5157	58.8	196.7	99.8	60.8	1433.1	2.3	125.4
ZL	1100	85.49	0.0019	0.8127	49.8	272.2	99.7	66.0	1464.8	2.4	242.8
ZM	1200	96.53	0.0026	0.5672	29.7	197.7	99.8	69.0	1591.0	2.5	5.8
ZN	1300	85.03	0.0018	0.4482	245.7	282.2	99.8	94.5	1460.7	4.1	6.7
ZO	1400	76.02	0.0032	0.4698	29.0	158.5	99.8	97.5	1351.0	2.3	7.1
ZP	1685	76.42	0.0030	0.7854	24.4	170.9	99.7	100.0	1354.8	1.8	6.7
total gas age			n=42		965.8	171.3			1368.5	2.5	

Appendix Table 2. Virgin Mountains K-feldspar argon data.

ID	Temp (°C)	$^{40}Ar/^{39}Ar$	$^{37}Ar/^{39}Ar$	$^{36}Ar/^{39}Ar$ (x 10^{-3})	$^{39}Ar_K$ (x 10^{-15} mol)	K/Ca	$^{40}Ar^*$ (%)	^{39}Ar (%)	Age (Ma)	±1σ (Ma)	Time (min)
Qff-21 K-feldspar, wt. =1.88 mg, J=0.0147066, NM-140, Lab#=52463-01											
A	450	151.1	0.0627	53.80	1.95	8.1	89.5	0.3	1974.9	6.4	10.0
B	450	15.21	0.0246	11.13	0.899	20.7	78.4	0.4	291.0	5.6	20.8
C	450	12.51	0.0292	8.323	0.726	17.5	80.3	0.5	248.3	7.1	28.9
D	500	14.23	0.0316	3.752	1.25	16.2	92.2	0.6	317.9	4.3	10.2
E	500	8.839	0.0270	3.841	1.40	18.9	87.2	0.8	193.2	3.9	20.2
F	500	8.107	0.0318	5.475	1.29	16.0	80.0	1.0	164.0	4.2	28.6
G	550	18.05	0.0373	2.045	2.39	13.7	96.7	1.3	411.6	2.2	11.0
H	550	7.585	0.0322	1.927	2.42	15.8	92.5	1.6	176.7	2.2	20.9
I	550	7.440	0.0296	2.228	2.22	17.2	91.2	1.9	171.1	2.3	28.6
J	600	17.45	0.0399	2.564	3.77	12.8	95.7	2.4	395.7	1.6	10.3
K	600	9.437	0.0334	1.022	4.01	15.3	96.8	2.9	227.0	1.4	20.3
L	600	11.27	0.0314	2.230	3.61	16.2	94.2	3.4	261.1	1.6	28.7
M	650	16.65	0.0406	1.102	4.37	12.6	98.1	4.0	387.8	1.5	9.4
N	650	14.86	0.0434	0.8385	5.14	11.8	98.4	4.6	350.9	1.3	20.2
O	650	17.45	0.0459	0.8654	4.22	11.1	98.6	5.2	406.4	1.7	28.3
P	700	22.03	0.0607	1.106	4.46	8.4	98.5	5.8	499.5	1.6	9.8
Q	700	23.16	0.0641	0.8125	4.75	8.0	99.0	6.4	523.8	1.6	19.3
R	700	26.90	0.0703	1.329	3.70	7.3	98.6	6.9	593.7	2.1	28.3
S	750	31.40	0.0773	2.726	3.83	6.6	97.5	7.4	670.0	2.2	10.5
T	750	33.45	0.0884	0.9855	3.90	5.8	99.2	7.9	716.4	2.6	20.2
U	750	38.69	0.1030	1.965	3.68	5.0	98.5	8.3	802.6	2.2	28.9
V	800	44.31	0.1168	0.5268	3.44	4.4	99.7	8.8	902.6	2.2	10.5
W	800	47.56	0.1031	1.137	4.19	4.9	99.3	9.3	951.3	2.2	20.8
X	850	52.77	0.1105	2.001	5.00	4.6	98.9	10.0	1027.2	2.1	10.9
Y	850	55.43	0.0870	1.206	5.57	5.9	99.4	10.7	1070.3	2.0	21.1
Z	900	58.48	0.0785	0.9289	6.34	6.5	99.5	11.5	1115.5	2.2	10.9
ZA	900	60.36	0.0577	0.8540	8.04	8.8	99.6	12.6	1142.5	1.9	20.8
ZB	950	62.64	0.0440	0.9257	8.80	11.6	99.6	13.7	1174.0	1.9	11.3
ZC	950	64.45	0.0316	0.9158	10.4	16.2	99.6	15.1	1198.9	1.8	21.3
ZD	1000	67.34	0.0331	1.009	11.0	15.4	99.6	16.5	1237.5	2.4	11.0
ZE	1000	68.57	0.0238	0.9168	12.9	21.4	99.6	18.2	1254.2	1.9	21.2
ZF	1050	71.13	0.0350	1.040	13.2	14.6	99.6	19.9	1287.4	2.2	9.0
ZG	1050	72.04	0.0284	0.8368	18.5	18.0	99.7	22.3	1299.9	1.9	18.5
ZH	1100	74.71	0.0318	1.640	18.5	16.0	99.4	24.7	1331.1	1.9	8.3
ZI	1100	75.18	0.0303	0.7123	26.9	16.8	99.7	28.2	1340.5	2.0	18.8
ZJ	1100	75.79	0.0319	0.7022	51.3	16.0	99.7	34.9	1348.2	2.0	56.4
ZK	1100	76.43	0.0328	0.7297	60.3	15.6	99.7	42.8	1356.2	1.9	123.8
ZL	1100	74.91	0.0253	0.6924	75.1	20.2	99.7	52.6	1337.2	2.2	232.8
ZM	1200	75.31	0.0171	0.5028	45.7	29.9	99.8	58.5	1342.9	2.4	5.8
ZN	1300	75.06	0.0085	0.3553	190.1	59.7	99.9	83.3	1340.3	4.1	6.7
ZO	1400	73.78	0.0228	0.5401	41.0	22.4	99.8	88.6	1323.4	2.1	7.1
ZP	1685	73.54	0.0066	0.5531	87.4	77.0	99.8	100.0	1320.3	3.6	6.7
total gas age			n=42		767.6	34.6			1246.2	2.6	

Appendix Table 2. Virgin Mountains K-feldspar argon data.

ID	Temp (°C)	$^{40}Ar/^{39}Ar$	$^{37}Ar/^{39}Ar$	$^{36}Ar/^{39}Ar$ (x 10^{-3})	$^{39}Ar_K$ (x 10^{-15} mol)	K/Ca	$^{40}Ar^*$ (%)	^{39}Ar (%)	Age (Ma)	±1σ (Ma)	Time (min)
Qff-24b K-feldspar, wt. =1.94 mg, J=0.0147650, NM-140, Lab#=52464-01											
A	450	1137.0	0.0230	139.3	1.02	22.2	96.4	0.1	5130	12	9.8
B	450	42.47	0.0373	20.75	0.428	13.7	85.6	0.1	775	12	20.5
C	450	35.52	-0.0104	19.83	0.402	-	83.5	0.2	655	13	29.0
D	500	44.76	0.0066	8.356	0.719	77.6	94.5	0.2	875.0	7.4	9.2
E	500	18.91	0.0228	2.593	0.854	22.4	96.0	0.3	427.8	5.8	19.5
F	500	21.10	0.0205	6.339	0.903	24.9	91.1	0.4	450.5	5.5	28.6
G	550	31.42	0.0186	1.883	1.83	27.4	98.2	0.6	677.0	3.0	10.4
H	550	25.70	0.0275	1.287	2.45	18.5	98.5	0.8	572.7	2.5	21.0
I	550	27.91	0.0120	1.492	2.49	42.6	98.4	1.1	613.8	2.4	28.7
J	600	36.47	0.0133	1.459	4.31	38.4	98.8	1.5	769.4	2.2	9.7
K	600	35.78	0.0127	0.7392	5.35	40.1	99.4	2.0	761.1	1.6	20.4
L	600	37.93	0.0094	1.084	4.74	54.4	99.2	2.5	796.4	2.9	28.5
M	650	49.78	0.0121	3.682	6.69	42.2	97.8	3.1	977.0	1.8	9.8
N	650	44.16	0.0103	0.9687	5.35	49.6	99.4	3.6	900.7	2.3	20.5
O	650	52.04	0.0234	4.156	4.84	21.9	97.6	4.1	1009.6	2.1	28.5
P	700	53.93	0.0224	5.238	5.22	22.8	97.1	4.6	1033.4	2.5	10.0
Q	700	49.15	0.0128	1.627	3.47	39.9	99.0	5.0	976.7	2.4	19.7
R	700	49.69	0.0067	1.972	2.63	76.3	98.8	5.2	983.4	2.9	28.1
S	750	55.96	0.0086	4.231	3.12	59.4	97.8	5.5	1067.8	3.1	10.3
T	750	52.04	0.0112	2.673	2.80	45.6	98.5	5.8	1016.2	3.3	20.8
U	750	52.30	0.0150	2.319	2.43	33.9	98.7	6.0	1021.7	3.0	28.9
V	800	57.39	0.0177	3.059	2.96	28.9	98.4	6.3	1094.0	2.7	10.4
W	800	55.04	0.0079	1.587	3.11	64.2	99.1	6.6	1065.9	2.9	20.7
X	850	58.77	0.0188	2.324	4.50	27.2	98.8	7.0	1116.9	2.4	10.9
Y	850	56.28	0.0078	0.9511	4.59	65.6	99.5	7.5	1086.8	2.1	20.9
Z	900	60.02	0.0189	2.958	7.07	27.0	98.5	8.2	1132.2	2.1	10.8
ZA	900	57.57	0.0060	0.9078	6.88	85.0	99.5	8.8	1105.7	2.2	21.0
ZB	950	60.40	0.0154	2.348	12.2	33.0	98.9	10.0	1140.2	1.8	11.2
ZC	950	57.78	0.0051	1.801	12.0	99.6	99.1	11.2	1104.9	2.8	21.2
ZD	1000	59.37	0.0117	2.048	22.0	43.5	99.0	13.3	1126.7	1.6	11.2
ZE	1000	58.48	0.0050	1.184	20.3	101.2	99.4	15.3	1117.6	1.6	21.1
ZF	1050	57.97	0.0076	1.601	36.0	67.5	99.2	18.8	1108.6	1.8	8.0
ZG	1050	57.95	0.0052	0.9483	36.1	97.9	99.5	22.3	1111.0	1.8	18.3
ZH	1100	59.34	0.0056	1.492	22.4	91.2	99.3	24.5	1128.6	1.6	39.3
ZI	1100	58.22	0.0060	1.327	68.9	85.5	99.3	31.2	1113.2	2.0	5.3
ZJ	1100	60.15	0.0044	0.9788	152.5	116.1	99.5	45.9	1142.3	2.3	65.4
ZK	1100	60.42	0.0036	0.9162	103.9	142.4	99.6	56.0	1146.3	3.3	119.1
ZL	1100	61.12	0.0033	1.139	60.1	154.7	99.4	61.9	1155.2	1.9	124.7
ZM	1100	61.69	0.0032	1.336	34.9	160.0	99.4	65.2	1162.5	1.9	116.6
ZN	1200	59.87	0.0034	1.220	119.8	148.0	99.4	76.9	1137.3	2.1	6.7
ZO	1300	58.75	0.0032	1.117	173.2	161.8	99.4	93.7	1121.7	2.8	7.1
ZP	1400	56.99	0.0031	1.152	31.5	162.5	99.4	96.7	1096.3	1.9	7.1
ZQ	1685	59.97	0.0030	1.524	32.7	171.2	99.2	99.9	1137.5	2.1	6.7
ZR	1685	68.22	0.0130	19.02	0.941	39.3	91.8	100.0	1180.6	9.0	6.7
total gas age			n=44		1030.6	122.7			1120.1	2.2	

Appendix Table 2. Virgin Mountains K-feldspar argon data.

ID	Temp (°C)	$^{40}Ar/^{39}Ar$	$^{37}Ar/^{39}Ar$	$^{36}Ar/^{39}Ar$ ($\times 10^{-3}$)	$^{39}Ar_k$ ($\times 10^{-15}$ mol)	K/Ca	$^{40}Ar^*$ (%)	^{39}Ar (%)	Age (Ma)	±1σ (Ma)	Time (min)
Q45 K-feldspar, wt. 1.93 mg, J=0.0156761, Lab#=52044-01											
A	450	1139.1	0.0113	31.60	1.67	45.3	99.2	0.2	5284.2	7.4	11.3
B	450	51.26	0.0009	5.792	0.766	569.2	96.6	0.3	1036.5	7.4	21.4
C	450	44.04	0.0283	11.55	0.635	18.0	92.2	0.3	888.7	8.4	29.7
D	500	62.55	0.0034	4.511	1.18	149.3	97.8	0.5	1213.3	5.1	11.2
E	500	25.57	0.0051	2.014	1.23	99.1	97.6	0.6	595.5	4.2	21.3
F	500	21.56	0.0000	3.416	1.06	-	95.2	0.7	503.3	5.1	29.6
G	550	79.94	0.0085	3.252	2.32	60.0	98.8	1.0	1453.2	3.3	11.5
H	550	26.34	0.0050	1.913	2.16	101.3	97.8	1.2	611.8	2.8	21.7
I	550	28.33	0.0092	2.685	1.93	55.7	97.1	1.4	646.9	3.1	29.9
J	600	51.75	0.0055	2.111	3.19	92.2	98.7	1.8	1061.5	3.0	11.5
K	600	31.77	0.0025	2.047	3.39	206.0	98.0	2.1	717.2	2.1	21.6
L	600	31.60	0.0000	1.224	3.13	24283	98.8	2.5	718.5	2.2	29.9
M	650	50.11	0.0060	1.715	4.65	84.6	98.9	3.0	1037.5	2.1	11.3
N	650	35.46	0.0000	0.8769	4.65	-	99.2	3.5	792.3	1.9	21.5
O	650	38.04	0.0005	0.6906	4.12	1115.9	99.4	4.0	839.7	2.2	29.8
P	700	44.94	0.0025	0.5907	4.94	200.4	99.6	4.5	958.8	2.0	11.3
Q	700	39.11	0.0002	0.6749	5.06	2138.6	99.4	5.1	858.7	2.3	21.3
R	700	41.59	0.0032	1.112	4.65	158.6	99.2	5.6	899.5	2.2	29.7
S	750	46.13	0.0004	0.9460	5.20	1411.8	99.3	6.1	976.7	1.9	11.6
T	750	42.12	0.0019	0.5379	5.66	267.1	99.6	6.8	911.5	1.8	21.6
U	800	47.99	0.0065	0.8388	7.42	78.6	99.4	7.6	1007.6	2.0	11.5
V	800	44.71	0.0007	0.5684	7.76	684.9	99.6	8.4	955.0	1.6	21.5
W	850	50.74	0.0015	0.4651	9.09	348.9	99.7	9.4	1053.3	1.9	11.7
X	850	51.03	0.0009	0.4065	9.78	571.2	99.7	10.5	1058.1	1.6	21.7
Y	900	59.84	0.0025	0.3965	10.8	205.8	99.8	11.7	1191.6	1.9	11.6
Z	900	58.79	0.0014	0.5482	12.6	372.4	99.7	13.1	1175.6	1.8	21.6
ZA	950	68.76	0.0053	0.6619	14.7	95.9	99.7	14.7	1316.4	2.3	11.8
ZB	950	66.81	0.0010	0.4151	16.8	523.8	99.8	16.6	1290.7	2.1	21.8
ZC	1000	76.06	0.0069	0.6481	21.7	73.5	99.7	18.9	1413.3	2.0	11.7
ZD	1000	71.84	0.0021	0.5369	23.8	242.2	99.7	21.6	1358.5	1.8	21.7
ZE	1050	78.00	0.0043	0.5590	31.1	118.0	99.8	25.0	1438.6	2.3	10.8
ZF	1050	74.92	0.0029	0.4465	25.1	174.9	99.8	27.7	1399.3	2.1	15.9
ZG	1100	83.03	0.0035	0.7171	39.7	147.4	99.7	32.1	1501.0	2.2	10.7
ZH	1100	77.40	0.0029	0.5085	42.2	176.6	99.8	36.7	1431.1	2.3	25.7
ZI	1100	78.43	0.0026	0.5962	54.0	193.2	99.7	42.7	1443.8	2.2	64.0
ZJ	1100	80.51	0.0023	0.8193	63.7	220.2	99.7	49.7	1469.3	2.3	130.2
ZK	1100	82.57	0.0017	0.9944	76.2	306.8	99.6	58.0	1494.3	3.0	251.1
ZL	1200	88.32	0.0016	0.5790	82.3	318.2	99.8	67.1	1565.4	2.4	4.4
ZM	1250	85.67	0.0011	0.5144	214.5	463.2	99.8	90.7	1533.9	3.5	5.0
ZN	1300	72.84	0.0028	0.4793	45.6	185.3	99.8	95.7	1372.0	2.3	4.9
ZO	1400	75.83	0.0088	0.8155	15.9	58.1	99.6	97.4	1409.7	2.1	5.2
ZP	1700	77.08	0.0048	2.557	23.4	107.3	99.0	100.0	1419.3	1.9	4.9
total gas age			n=42		909.8	387.3			1418.2	2.4	

Appendix Table 2. Virgin Mountains K-feldspar argon data.

ID	Temp (°C)	$^{40}Ar/^{39}Ar$	$^{37}Ar/^{39}Ar$	$^{36}Ar/^{39}Ar$ (x 10^{-3})	$^{39}Ar_K$ (x 10^{-15} mol)	K/Ca	$^{40}Ar^*$ (%)	^{39}Ar (%)	Age (Ma)	±1σ (Ma)	Time (min)
Q95 K-feldspar, wt. =1.88 mg, J=0.01571948, NM-134, Lab#=52046-01											
A	450	611.2	0.0000	48.59	0.474	-	97.6	0.4	4222	21	11.4
B	450	26.64	0.0000	11.57	0.184	-	87.1	0.6	561	30	21.4
C	450	27.83	0.0000	22.84	0.120	-	75.7	0.7	516	51	29.8
D	500	50.59	0.0000	6.217	0.300	-	96.3	1.0	1026	20	11.3
E	500	16.28	0.0000	1.551	0.229	-	97.0	1.2	400	24	21.2
F	500	19.28	0.0000	-1.2766	0.197	-	101.8	1.4	485	27	29.7
G	550	96.92	0.0145	2.587	0.792	35.3	99.2	2.1	1661.1	8.5	11.6
H	550	23.77	0.0050	-1.9786	0.398	102.9	102.4	2.5	584	14	21.6
I	550	21.24	0.0000	5.487	0.322	-	92.2	2.8	484	18	30.0
J	600	39.62	0.0024	0.5584	0.663	208.9	99.5	3.4	870.2	8.9	11.5
K	600	20.62	0.0056	0.9678	0.547	91.1	98.5	3.9	500	10	21.5
L	600	22.44	0.0000	0.1837	0.429	-	99.6	4.3	543	13	29.9
M	650	31.61	0.0259	-0.2946	0.627	19.7	100.2	4.8	729.0	9.1	11.4
N	650	24.33	0.0170	0.0681	0.638	30.0	99.8	5.4	583.4	8.3	21.5
O	650	23.71	0.0000	-2.4967	0.579	-	103.0	6.0	586.3	9.7	29.7
P	700	33.74	0.0114	-2.5572	0.848	44.7	102.2	6.7	781.1	6.9	11.2
Q	700	25.28	0.0269	-0.0104	0.781	19.0	99.9	7.5	603.3	7.2	21.4
R	700	27.06	0.0000	-0.9997	0.635	-	101.0	8.0	644.9	8.5	29.7
S	750	29.14	0.0000	-3.2267	0.654	-	103.2	8.6	698.4	8.7	11.5
T	750	28.70	0.0293	-1.0726	0.693	17.4	101.0	9.3	677.6	8.1	21.6
U	800	29.78	0.0323	-1.4366	0.762	15.8	101.4	10.0	700.5	7.0	11.5
V	800	31.13	0.0397	0.4699	0.736	12.9	99.5	10.7	715.6	7.4	21.5
W	850	34.49	0.0489	-0.7445	0.793	10.4	100.6	11.4	785.1	7.1	11.7
X	850	35.53	0.0083	0.8216	0.804	61.4	99.2	12.1	795.7	6.9	21.7
Y	900	37.82	0.0459	0.2742	0.965	11.1	99.7	13.0	839.9	6.5	11.6
Z	900	39.99	0.0251	-0.9785	1.01	20.3	100.7	13.9	884.6	5.7	21.6
ZA	950	42.53	0.0248	-1.0049	1.28	20.6	100.6	15.1	928.2	5.0	11.8
ZB	950	42.62	0.0085	-0.2358	1.45	59.8	100.1	16.4	925.9	4.6	21.8
ZC	1000	45.51	0.0203	0.1700	2.16	25.2	99.8	18.4	972.4	3.5	11.6
ZD	1000	46.15	0.0130	0.3249	2.53	39.3	99.7	20.7	982.2	3.0	21.7
ZE	1050	49.34	0.0194	-0.0741	3.68	26.3	100.0	24.1	1035.8	2.6	10.9
ZF	1050	48.43	0.0158	0.8135	3.19	32.3	99.5	27.1	1016.9	2.8	15.8
ZG	1100	52.88	0.0151	0.9403	5.12	33.8	99.4	31.7	1086.7	1.9	10.8
ZH	1100	52.18	0.0155	0.8076	4.87	32.9	99.5	36.2	1076.5	2.1	25.8
ZI	1100	54.95	0.0105	1.560	6.50	48.4	99.1	42.2	1115.9	2.2	64.3
ZJ	1100	58.75	0.0106	3.096	7.42	48.0	98.4	49.0	1166.3	2.2	130.0
ZK	1100	61.48	0.0059	4.481	8.76	87.0	97.8	57.0	1200.4	2.2	251.4
ZL	1200	63.45	0.0032	0.3980	11.2	160.0	99.8	67.3	1246.1	2.1	4.3
ZM	1250	60.85	0.0026	0.3731	26.7	198.1	99.8	91.8	1208.9	1.7	5.0
ZN	1300	61.01	0.0000	0.5620	3.50	-	99.7	95.0	1210.3	2.6	5.0
ZO	1400	64.29	0.0207	1.017	3.87	24.6	99.5	98.6	1255.4	2.8	5.5
ZP	1700	176.3	0.0984	26.43	1.56	5.2	95.6	100.0	2335.3	6.6	5.2
total gas age			n=42		109.0	94.2			1133.2	3.2	

Appendix Table 2. Virgin Mountains K-feldspar argon data.

ID	Temp (°C)	$^{40}Ar/^{39}Ar$	$^{37}Ar/^{39}Ar$	$^{36}Ar/^{39}Ar$ (x 10^{-3})	$^{39}Ar_K$ (x 10^{-15} mol)	K/Ca	$^{40}Ar^*$ (%)	^{39}Ar (%)	Age (Ma)	±1σ (Ma)	Time (min)
Q119 K-feldspar, wt. = 1.89 mg, J=0.0155686, NM-134, Lab#=52027-01											
A	450	453.7	0.0252	10.44	1.78	20.2	99.3	0.2	3755.0	5.9	11.6
B	450	45.83	0.0369	12.88	0.674	13.8	91.7	0.3	908.6	6.2	21.4
C	450	31.23	0.0288	18.40	0.637	17.7	82.5	0.3	608.6	6.8	29.8
D	500	32.52	0.0206	6.245	1.26	24.7	94.3	0.5	703.9	3.6	11.3
E	500	12.79	0.0184	8.073	1.52	27.7	81.2	0.6	270.3	3.1	21.3
F	500	10.84	0.0059	11.70	1.52	86.4	67.9	0.8	195.7	3.7	29.6
G	550	29.45	0.0120	4.518	3.05	42.6	95.4	1.1	654.4	2.2	11.6
H	550	6.772	0.0098	5.302	3.12	52.0	76.5	1.4	140.0	1.7	21.6
I	550	6.781	0.0083	7.117	3.03	61.5	68.6	1.7	126.2	2.0	30.0
J	600	23.13	0.0077	3.145	5.32	66.4	95.9	2.3	535.1	1.3	11.5
K	600	7.026	0.0035	3.980	5.33	146.8	82.9	2.8	156.63	0.98	21.6
L	600	8.173	0.0077	5.430	4.76	66.2	80.1	3.3	175.0	1.5	29.9
M	650	16.32	0.0051	2.882	6.47	99.8	94.6	4.0	388.8	1.1	11.4
N	650	10.99	0.0019	3.565	6.71	268.8	90.2	4.7	259.0	1.0	21.4
O	650	12.98	0.0044	5.220	6.00	116.2	87.9	5.3	295.0	1.2	29.8
P	700	16.41	0.0038	2.228	6.82	132.7	95.8	6.0	395.0	1.0	11.3
Q	700	16.31	0.0037	3.608	7.75	139.5	93.3	6.9	383.7	1.1	21.4
R	700	18.54	0.0026	5.576	6.65	199.4	91.0	7.5	420.6	1.3	29.7
S	750	24.41	0.0010	2.956	7.36	524.5	96.3	8.3	562.8	1.5	11.6
T	750	21.30	0.0028	0.4796	7.86	182.5	99.2	9.1	513.1	1.2	21.8
U	800	23.98	0.0047	0.5986	9.41	109.5	99.2	10.1	568.1	1.0	11.4
V	800	24.79	0.0024	0.4531	9.92	215.5	99.4	11.1	585.6	1.2	21.6
W	850	28.68	0.0016	0.2720	10.9	315.4	99.6	12.3	664.0	1.1	11.7
X	850	30.31	0.0016	0.4466	11.1	317.1	99.5	13.4	694.3	1.2	21.7
Y	900	34.45	0.0035	0.3302	11.5	143.8	99.6	14.6	772.5	1.3	11.7
Z	900	35.18	0.0031	0.5414	12.9	165.7	99.5	16.0	784.7	1.3	21.7
ZA	950	40.17	0.0045	0.5173	14.7	112.6	99.6	17.5	873.3	1.2	11.8
ZB	950	39.26	0.0022	0.5701	17.6	227.1	99.5	19.3	857.2	1.3	21.8
ZC	1000	43.01	0.0031	0.4425	22.6	162.5	99.6	21.7	922.2	1.4	11.7
ZD	1000	41.26	0.0024	0.4806	26.3	211.6	99.6	24.4	892.3	1.4	21.7
ZE	1050	41.53	0.0031	0.3932	36.6	165.8	99.7	28.2	897.3	1.5	10.9
ZF	1050	40.80	0.0027	0.4007	28.6	187.6	99.6	31.2	884.7	1.9	15.9
ZG	1100	40.11	0.0033	0.3556	48.3	152.5	99.7	36.3	873.0	1.6	10.7
ZH	1100	40.84	0.0029	0.3021	58.1	173.2	99.7	42.3	886.0	1.3	25.8
ZI	1100	43.31	0.0029	0.3021	76.8	173.3	99.7	50.3	927.8	1.8	67.6
ZJ	1100	44.65	0.0026	0.3803	97.8	197.6	99.7	60.5	949.9	1.7	129.6
ZK	1100	46.64	0.0025	0.5038	115.4	206.9	99.6	72.5	982.0	2.3	246.7
ZL	1200	52.67	0.0023	0.2820	49.6	223.6	99.8	77.7	1078.7	2.0	4.4
ZM	1250	51.23	0.0020	0.1699	131.0	252.5	99.9	91.3	1056.9	2.3	5.3
ZN	1300	49.46	0.0027	0.3004	40.4	188.2	99.8	95.5	1028.4	1.7	5.0
ZO	1400	48.26	0.0078	0.9765	10.7	65.0	99.4	96.7	1006.0	1.8	5.2
ZP	1700	47.66	0.0030	2.776	32.1	170.6	98.2	100.0	987.7	1.8	4.9
total gas age			n=42		959.9	193.8			897.8	1.7	

Appendix B: Apatite fission-track thermochronology

Uranium atoms decay by two different mechanisms; decay by α and β emmision to isotopes of Pb, and by the spontaneous nuclear fission of primarily ^{238}U, which produces two roughly equal and highly charged parts (Spear, 1993). When these two ionized fragments move rapidly away from another under their mutual repulsion, they create a damaged region in the host crystal over a distance of 10-15 μm. At high temperatures (>110°C for apatite), this region quickly anneals by diffusion, and any evidence for this transfer of energy from the particles to the atoms of the crystal is effectively lost. At temperatures below the host mineral's closure temperature (< 80°C for apatite) the annealing process shuts off, and the damaged regions, or "fission tracks" accumulate at a rate proportional to the amount of uranium in the sample and the uranium decay constant. At temperatures within the host mineral's "partial annealing zone" (80-110°C for apatite), AFT ages and track lengths are reduced compared to the original AFT ages and lengths. Mean track lengths within the PAZ are typically 8-13 μm (Kelley et al, 2001). The number of tracks present is proportional to the time passed since the rock passed through the closure temperature for the mineral of interest; when the mineral is etched in acid, these tracks become more easily visible under a microscope, and can thus be counted. Fission-track length is a function of the cooling rate and can thus be used to give an estimate of the rate at which these blocks were exhumed.

Methods

Apatite fission tracks are separated using standard magnetic and heavy liquid techniques, and dated using the external detector method, as outlined below:

1) Mount apatite grain in epoxy, polish and etch for 25 seconds in 5 M HNO_3 to reveal fission tracks
2) Place a muscovite detector on the age mount and send sample to Texas A&M Nuclear Science Center for irradiation. Calibrate neutron fluence using CN-6 glass and Durango apatite, fluence determined using zeta of 4771 and track counts in CN-6 glass muscovite detector
3) Count the fission tracks in the age mount and muscovite detector at 1000x power. Determine ages using the formula X of Fleisher and Walker, 1975. Measure track lengths following the method outlined in Kelley et al, 1992.
4) Preliminary AFT modeling was done using the fission-track length program of Ketcham et al, in review. While results have yet to be quantified, preliminary models of QFT 5 were run, the results of which appear in the text.

Appendix C: Structural data from the North Virgin Mountains

The following tables include foliation, lineation, bedding, and fault measurements taken at stations throughout the North Virgin Mountains.

Appendix Table 3: Structural data from the North Virgin Mountains

Station No.	S1	S1 dip	S2 fol	S2 dip	S2 fol/S2 AP	S2 dip
001	000	000	72	61	92	50
002	000	000	0	0	0	0
003	000	000	0	0	0	0
004	000	000	158	49	0	0
005	000	000	244	54	0	0
006	000	000	34	15	0	0
007	000	000	225	57	0	0
008	000	000	273	27	268	38
009	000	000	300	62	268	54
010	000	000	258	54	308	62
011	000	000	371	36	0	0
012	000	000	310	89	0	0
013	000	000	258	32	0	0
014	000	000	268	41	250	16
015	000	000	270	51	0	0
016	000	000	252	41	0	0
017	000	000	272	43	310	54
018	000	000	262	65	92	90
019	000	000	71	74	0	0
020	000	000	90	60	0	0
021	000	000	92	61	40	60
022	000	000	000	000	0	0
023	000	000	78	32	0	0
024	000	000	82	60	0	0
025	000	000	85	60	0	0
026	000	000	58	62	0	0
027	000	000	122	38	0	0
028	000	000	58	67	0	0
029	000	000	43	65	0	0
030	000	000	51	85	0	0
031	000	000	251	54	0	0
032	000	000	264	39	0	0
033	000	000	262	34	0	0
034	000	000	290	38	0	0
035	000	000	278	30	0	0
036	000	000	256	52	0	0
037	000	000	282	80	21	66
038	000	000	256	65	163	18
039	000	000	198	45	0	0
040	000	000	262	46	0	0
041	000	000	242	43	0	0
042	000	000	38	62	0	0
043	000	000	22	63	31	59
044	000	000	*61*	*51*	78	64
045	000	000	89	53	0	0
046	000	000	59	28	0	0
047	000	000	2	42	0	0
048	000	000	12	69	0	0
049	000	000	22	59	0	0

Appendix Table 3: Structural data from the North Virgin Mountains

050	000	000	6	63	0	0
051	000	000	103	61	0	0
052	000	000			0	0
053	000	000	6	25	0	0
054	000	000	21	44	334	10
055	000	000	50	55	0	0
056	000	000	65	90	0	0
057	000	000	74	74	0	0
058	000	000	210	88	0	0
059	000	000	220	90	0	0
060	000	000	64	62	0	0
061	000	000	70	59	0	0
062	000	000	68	56	55	61
063	000	000	91	37	0	0
064	000	000	125	15	0	0
065	000	000	75	63	0	0
066	000	000	40	17	0	0
067	000	000	68	83	75	90
068	000	000	244	88	245	53
069	000	000	278	83	228	78
69	000	000	75	90	55	90
70	000	000	245	85	0	0
071	000	000	48	80	231	71
072	000	000	262	80	262	80
073	000	000	10	51	0	0
074	000	000	25	70	0	0
075	000	000	50	76	235	78
076	000	000	230	85	0	0
077	000	000	39	74	0	0
078	000	000	244	63	0	0
079	000	000	0	0	0	0
080	000	000	76	57	252	45
081	000	000	8	90	11	82
082	000	000	48	61	0	0
083	000	000	45	73	55	76
084	000	000	15	90	0	0
085	000	000	4	81	355	78
086	000	000	0	0	0	0
087	000	000	31	47	0	0
088	000	000	6	77	0	0
089	000	000	64	84	75	76
090	000	000	0	0	0	0
091	000	000	225	25	0	0
092	000	000	264	16	0	0
093	000	000	265	61	0	0
094	000	000	245	54	305	82
095	000	000	85	82	0	0
096	000	000	75	71	0	0
097	000	000	51	66	0	0
098	000	000	5	55	0	0

Appendix Table 3: Structural data from the North Virgin Mountains

099	000	000	70	70	0	0
100	000	000	34	59	0	0
101	000	000	64	74	0	0
102	000	000	345	57	0	0
103	000	000	60	65	0	0
104	000	000	90	81	0	0
105	000	000	74	64	0	0
106	000	000	54	38	0	0
107	000	000	283	66	0	0
108	000	000	81	49	0	0
109	000	000	79	51	85	51
110	000	000	52	39	178	36
111	000	000	355	25	0	0
112	000	000	78	39	0	0
113	000	000	63	58	0	0
114	000	000	212	79	0	0
115	000	000	215	75	0	0
116	000	000	61	61	0	0
117	000	000	25	56	0	0
118	000	000	258	88	87	70
119	000	000	42	91	0	0
120	000	000	91	36	0	0
121	000	000	68	68	90	83
122	000	000	64	63	0	0
123	000	000	236	47	0	0
124	000	000	260	80	0	0
125	000	000	72	84	76	89
126	000	000	232	31	0	0
127	000	000	71	81	0	0
128	000	000	49	87	0	0
129	000	000	61	62	72	64
130	000	000	84	63	29	62
131	000	000	94	61	0	0
132	000	000	58	61	0	0
133	000	000	105	69	0	0
134	000	000	90	41	0	0
135	000	000	284	34	340	23
136	000	000	221	76	179	59
137	000	000	214	67	0	0
138	000	000	221	46	225	59
139	000	000	160	66	125	68
140	000	000	221	54	355	60
141	000	000	155	75	0	0
142	000	000	195	73	200	54
143	000	000	25	73	0	0
144	000	000	10	76	0	0
145	000	000	63	74	0	0
146	000	000	251	37	0	0
147	000	000	0	0	0	0
148	000	000	203	21	0	0

Appendix Table 3: Structural data from the North Virgin Mountains

149	000	000	229	69	0	0
200	000	000	0	0	0	0
201	000	000	0	0	0	0
202	000	000	245	41	0	0
203	000	000	76	66	0	0
205	000	000	175	51	0	0
206	000	000	98	66	0	0
207	000	000	210	56	350	88
208	000	000	51	70	0	0
209	000	000	270	89	0	0
210	000	000	0	0	0	0
211	000	000	0	0	0	0
213	000	000	215	68	0	0
213	000	000	246	81	0	0
214	000	000	259	59	0	0
215	000	000	254	86	205	78
216	000	000	29	41	196	72
217	000	000	345	45	0	0
220	000	000	175	81	0	0
221	000	000	75	80	0	0
222	000	000	0	0	0	0
223	000	000	251	51	218	48
234	000	000	45	80	0	0
235	000	000	260	40	0	0
236	000	000	210	64	0	0
237	000	000	155	28	0	0
238	000	000	259	41	0	0
239	000	000	0	0	0	0
240	000	000	0	0	0	0
241	000	000	0	0	0	0
242	000	000	231	71	0	0
243	000	000	170	63	0	0
244	000	000	5	38	0	0
245	000	000	0	0	0	0
J1	000	000	76	89	0	0
J2	000	000	75	89	0	0
J3	000	000	70	89	0	0
J4	000	000	65	88	0	0
J6	000	000	66	83	0	0
J8	000	000	75	88	0	0
J10	000	000	68	75	0	0
J11	000	000	253	78	0	0
J12	000	000	61	71	0	0
J13	000	000	65	85	0	0
J14	000	000	241	88	0	0
J15	000	000	62	89	0	0
J16	000	000	55	72	0	0
J17	000	000	70	89	0	0
J19	000	000	230	70	0	0
J21	000	000	85	89	0	0

Appendix Table 3: Structural data from the North Virgin Mountains

J22	000	000	265	66	0	0
J23	000	000	79	86	0	0
J24	000	000	245	64	0	0
J25	000	000	65	47	0	0
300	000	000	46	59	0	0
300	000	000	15	42	0	0
301	000	000	313	51	0	0
302	000	000	155	36	0	0
303	000	000	141	26	0	0
304	000	000	310	69	0	0
305	000	000	308	41	150	61
306	000	000	0	0	0	0
307	000	000	0	0	0	0
308	000	000	70	83	0	0
308	000	000	61	80	0	0
308	000	000	258	45	0	0
308	000	000	74	88	0	0
309	000	000	58	79	0	0
309	000	000	230	88	0	0
310	000	000	240	88	0	0
311	000	000	255	86	0	0
311	000	000	54	57	0	0
312	000	000	0	0	0	0
313	330	43	14	76	14	71
313	0	0	11	75	0	0
313	306	41	37	86	0	0
314	0	0	29	44	0	0
314	345	44	20	72	27	65
315	70	48	33	81	0	0
315	36	41	55	88	270	69
316	0	0	274	41	0	0
317	0	0	355	54	0	0
318	0	0	344	44	0	0
319	94	30	136	71	0	0
320	000	000	215	66	0	0
320	000	000	205	58	0	0
320	000	000	240	62	0	0
321	000	000	234	39	0	0
321	000	000	220	60	0	0
322	000	000	202	53	0	0
323	000	000	20	67	0	0
324	000	000	61	65	0	0
325	000	000	204	38	0	0
326	000	000	46	31	0	0
327	000	000	6	51	0	0
328	000	000	234	86	0	0
329	000	000	16	79	0	0
330	000	000	310	38	0	0
331	000	000	8	88	0	0
332	000	000	255	86	0	0

Appendix Table 3: Structural data from the North Virgin Mountains

333	000	000	102	45	0	0
400	000	000	25	54	0	0
401	000	000	30	61	30	52
402	000	000	31	56	0	0
403	000	000	6	36	0	0
404	000	000	340	45	0	0
405	000	000	5	49	0	0
406	000	000	35	47	0	0
406	000	000	351	46	0	0
406	000	000	9	47	0	0
406	000	000	265	51	0	0
406	000	000	266	76	0	0
406	000	000	330	54	0	0
407	000	000	40	45	0	0
408	000	000	0	0	0	0
409	000	000	210	64	0	0
410	000	000	170	42	0	0
411	000	000	0	0	0	0
412	000	000	248	84	0	0
413	000	000	0	0	0	0
414	000	000	0	0	0	0

Appendix Table 3: Structural data from the North Virgin Mountains

Station No.	Lin unknown	Trend	L-tectonite	trend	F2 FA	trend
001	60	175	0	0	0	0
002	0	0	0	0	0	0
003	0	0	0	0	0	0
004	36	335	0	0	0	0
005	23	328	1	290	0	0
006	12	145	0	0	0	0
007	0	0	0	0	0	0
008	26	38	0	0	0	0
009	42	308	0	0	62	84
010	0	0	0	0	0	0
011	0	0	0	0	0	0
012	0	0	0	0	0	0
013	32	330	0	0	0	0
014	0	0	0	0	0	0
015	0	0	0	0	0	0
016	0	0	0	0	0	0
017	0	0	0	0	0	0
018	0	0	0	0	0	0
019	0	0	0	0	0	0
020	31	120	0	0	0	0
021	0	0	0	0	0	0
022	0	0	0	0	140	89
023	0	0	0	0	0	0
024	0	0	0	0	0	0
025	0	0	0	0	0	0
026	0	0	0	0	0	0
027	0	0	0	0	0	0
028	11	56	0	0	0	0
029	0	0	0	0	0	0
030	0	0	0	0	0	0
031	0	0	0	0	0	0
032	0	0	0	0	0	0
033	31	352	0	0	0	0
034	12	308	0	0	0	0
035	20	89	0	0	0	0
036	0	0	0	0	0	0
037	0	0	0	0	16	98
038	0	0	0	0	0	0
039	0	0	64	364	0	0
040	0	0	0	0	0	0
041	0	0	0	0	0	0
042	61	101	0	0	0	0
043	0	0	0	0	36	44
044	20	89	0	0	39	121
045	18	116	8	122	0	0
046	0	0	0	0	0	0
047	40	102	0	0	0	0
048	0	0	77	162	0	0
049	50	70	0	0	0	0

Appendix Table 3: Structural data from the North Virgin Mountains

050	63	94	47	122	0	0
051	0	0	0	0	0	0
052	0	0	0	0	0	0
053	0	0	17	12	0	0
054	11	70	0	0	0	0
055	0	0	0	0	0	0
056	0	0	0	0	0	0
057	9	249	0	0	0	0
058	0	0	0	0	0	0
059	0	0	0	0	0	0
060	0	0	0	0	44	185
061	0	0	0	0	0	0
062	0	0	0	0	0	0
063	25	113	0	0	0	0
064	0	0	0	0	0	0
065	0	0	0	0	0	0
066	15	270	0	0	0	0
067	0	0	0	0	0	0
068	22	38	0	0	0	0
069	0	0	0	0	78	355
69	15	251	0	0	0	0
70	22	55	0	0	0	0
071	0	0	0	0	0	0
072	0	0	0	0	34	264
073	0	0	0	0	0	0
074	0	0	30	41	0	0
075	0	0	0	0	25	54
076	0	0	0	0	0	0
077	48	78	0	0	0	0
078	0	0	0	0	0	0
079	0	0	0	0	0	0
080	30	41	0	0	0	0
081	22	17	0	0	0	0
082	0	0	0	0	0	0
083	47	83	0	0	0	0
084	0	0	0	0	0	0
085	31	11	0	0	0	0
086	0	0	0	0	0	0
087	0	0	0	0	0	0
088	0	0	0	0	0	0
089	75	150	0	0	40	78
090			0	0	0	0
091	21	345	0	0	0	0
092			0	0	0	0
093	39	304	0	0	0	0
094	46	310	0	0	0	0
095			0	0	0	0
096			0	0	0	0
097	54	155	0	0	0	0
098	39	135	0	0	0	0

Appendix Table 3: Structural data from the North Virgin Mountains

099	32	82	0	0	0	0
100	57	155	0	0	0	0
101	73	116	0	0	0	0
102	57	75	0	0	0	0
103	0	0	0	0	0	0
104	62	131	0	0	0	0
105	7	76	0	0	0	0
106	0	0	0	0	0	0
107	0	0	0	0	0	0
108	11	254	0	0	0	0
109	0	0	0	0	48	200
110	0	0	0	0	0	0
111	0	0	0	0	0	0
112	0	0	0	0	0	0
113	0	0	11	64	0	0
114	0	0	0	0	0	0
115	0	0	0	0	0	0
116	0	0	0	0	0	0
117	0	0	0	0	0	0
118	0	0	0	0	0	0
119	0	0	0	0	0	0
120	0	0	0	0	0	0
121	31	82	0	0	0	0
122	0	0	0	0	0	0
123	71	39	0	0	0	0
124	11	75	0	0	0	0
125	24	92	0	0	0	0
126	28	315	0	0	0	0
127	0	0	0	0	0	0
128	0	0	0	0	0	0
129	21	89	0	0	0	0
130	21	54	0	0	0	0
131	0	0	0	0	0	0
132	39	103	0	0	0	0
133	0	0	0	0	0	0
134	0	0	0	0	0	0
135	0	0	0	0	0	0
136	51	251	0	0	0	0
137	0	0	70	295	0	0
138	0	0	48	320	16	253
139	61	303	0	0	0	0
140	0	0	0	0	71	360
141	0	0	0	0	0	0
142	0	0	0	0	0	0
143	68	58	0	0	0	0
144	71	59	0	0	0	0
145	0	0	0	0	0	0
146	26	345	0	0	0	0
147	0	0	0	0	0	0
148	19	325	0	0	0	0

Appendix Table 3: Structural data from the North Virgin Mountains

149	67	305	0	0	0	0
200	0	0	0	0	0	0
201	0	0	0	0	0	0
202	0	0	0	0	0	0
203	0	0	0	0	0	0
205	46	228	0	0	0	0
206	41	240	0	0	0	0
207	53	205	34	181	0	0
208	0	0	0	0	0	0
209	0	0	0	0	0	0
210	0	0	0	0	0	0
211	0	0	0	0	0	0
213	44	245	0	0	0	0
213	64	278	0	0	0	0
214	48	310	0	0	0	0
215	86	326	0	0	0	0
216	67	355	90	304	0	0
217	0	0	0	0	0	0
220	35	350	0	0	0	0
221	0	0	0	0	0	0
222	0	0	28	290	0	0
223	0	0	0	0	0	0
234	0	0	0	0	0	0
235	0	0	0	0	0	0
236	62	308	0	0	0	0
237	0	0	0	0	0	0
238	0	0	31	321	0	0
239	0	0	0	0	0	0
240	0	0	0	0	0	0
241	0	0	0	0	0	0
242	42	34	0	0	0	0
243	61	305	0	0	0	0
244	31	59	0	0	0	0
245	0	0	0	0	0	0
J1	0	0	0	0	0	0
J2	0	0	0	0	0	0
J3	0	0	0	0	0	0
J4	0	0	0	0	0	0
J6	0	0	0	0	0	0
J8	0	0	0	0	0	0
J10	0	0	0	0	0	0
J11	0	0	0	0	0	0
J12	0	0	0	0	0	0
J13	0	0	0	0	0	0
J14	0	0	0	0	0	0
J15	0	0	0	0	0	0
J16	0	0	0	0	0	0
J17	0	0	0	0	0	0
J19	0	0	0	0	0	0
J21	0	0	0	0	0	0

Appendix Table 3: Structural data from the North Virgin Mountains

J22	0	0	0	0	0	0
J23	0	0	0	0	0	0
J24	0	0	0	0	0	0
J25	0	0	0	0	0	0
300	31	85	0	0	0	0
300	40	92	0	0	0	0
301	24	333	0	0	0	0
302	0	0	0	0	0	0
303	0	0	0	0	0	0
304	0	0	0	0	0	0
305	19	296	0	0	0	0
306	0	0	0	0	0	0
307	0	0	0	0	0	0
308	65	194	0	0	0	0
308	25	230	0	0	0	0
308	24	64	0	0	0	0
308	59	76	0	0	0	0
309	77	164	0	0	0	0
309	82	327	0	0	0	0
310	37	250	0	0	0	0
311	55	280	0	0	0	0
311	5	66	0	0	0	0
312	0	0	0	0	0	0
313	0	0	0	0	33	75
313	0	0	0	0	0	0
313	0	0	0	0	24	42
314	0	0	0	0	0	0
314	0	0	0	0	53	161
315	0	0	0	0	0	0
315	51	49	0	0	0	0
316	0	0	0	0	0	0
317	0	0	0	0	0	0
318	0	0	0	0	0	0
319	12	152	0	0	0	0
320	64	293	0	0	0	0
320	58	299	0	0	0	0
320	49	308	0	0	0	0
321	36	331	0	0	0	0
321	59	305	0	0	0	0
322	51	272	0	0	0	0
323	60	140	0	0	0	0
324	55	176	0	0	0	0
325	37	315	0	0	0	0
326	26	135	0	0	0	0
327	0	0	0	0	0	0
328	59	250	0	0	0	0
329	2	190	0	0	0	0
330	35	81	0	0	0	0
331	0	0	0	0	0	0
332	83	55	0	0	0	0

Appendix Table 3: Structural data from the North Virgin Mountains

333	39	243	0	0	0	0
400	0	0	0	0	0	0
401	38	80	0	0	46	89
402	53	115	0	0	0	0
403	34	75	0	0	0	0
404	38	90	0	0	0	0
405	0	0	0	0	0	0
406	43	83	0	0	0	0
406	43	76	0	0	0	0
406	46	61	0	0	0	0
406	28	75	0	0	0	0
406	34	66	0	0	0	0
406	50	71	0	0	0	0
407	39	110	0	0	0	0
408	0	0	0	0	0	0
409	0	0	0	0	0	0
410	29	310	0	0	0	0
411	0	0	0	0	0	0
412	0	0	0	0	0	0
413	0	0	0	0	0	0
414	0	0	0	0	0	0

Appendix Table 3: Structural data from the North Virgin Mountains

Station No.	F3 AP	dip	F3 FA	trend	F4 AP	dip	F4 FA	trend
001	0	0	0	0	0	0	0	0
002	0	0	0	0	0	0	0	0
003	0	0	0	0	0	0	0	0
004	245	54	48	265	0	0	0	0
005	0	0	0	0	0	0	0	0
006	0	0	0	0	0	0	0	0
007	282	45	14	304	0	0	0	0
008	0	0	0	0	0	0	0	0
009	0	0	0	0	0	0	0	0
010	0	0	0	0	0	0	0	0
011	0	0	0	0	0	0	0	0
012	162	68	0	0	0	0	0	0
013	324	72	40	332	0	0	0	0
014	0	0	0	0	0	0	0	0
015	0	0	0	0	0	0	0	0
016	0	0	0	0	0	0	0	0
017	245	52	0	0	0	0	0	0
018	0	0	0	0	0	0	0	0
019	0	0	0	0	0	0	0	0
020	0	0	0	0	0	0	0	0
021	0	0	0	0	0	0	0	0
022	86	144	0	0	0	0	0	0
023	20	68	41	22	0	0	0	0
024	0	0	0	0	0	0	0	0
025	0	0	0	0	0	0	0	0
026	0	0	0	0	0	0	0	0
027	0	0	0	0	0	0	0	0
028	0	0	0	0	0	0	0	0
029	0	0	0	0	0	0	0	0
030	0	0	0	0	0	0	0	0
031	0	0	0	0	0	0	0	0
032	0	0	0	0	0	0	0	0
033	0	0	0	0	0	0	0	0
034	0	0	0	0	0	0	0	0
035	0	0	0	0	0	0	0	0
036	0	0	0	0	0	0	0	0
037	84	89	31	220	0	0	0	0
038	0	0	0	0	0	0	0	0
039	0	0	0	0	0	0	0	0
040	40	70	39	252	0	0	0	0
041	174	68	67	250	0	0	0	0
042	0	0	0	0	0	0	0	0
043	0	0	0	0	0	0	0	0
044	0	0	0	0	0	0	0	0
045	0	0	0	0	0	0	0	0
046	0	0	0	0	0	0	0	0
047	0	0	0	0	0	0	0	0
048	0	0	0	0	0	0	0	0
049	0	0	0	0	0	0	0	0

Appendix Table 3: Structural data from the North Virgin Mountains

050	148	80	64	152	18	63	60	12
051	0	0	0	0	0	0	0	0
052	0	0	0	0	0	0	0	0
053	0	0	0	0	0	0	0	0
054	0	0	0	0	0	0	0	0
055	0	0	0	0	0	0	0	0
056	0	0	0	0	0	0	0	0
057	0	0	0	0	0	0	0	0
058	0	0	0	0	0	0	0	0
059	0	0	0	0	0	0	0	0
060	0	0	0	0	0	0	0	0
061	0	0	0	0	0	0	0	0
062	355	43	38	100	0	0	0	0
063	343	28	0	0	0	0	0	0
064	0	0	0	0	0	0	0	0
065	0	0	0	0	0	0	0	0
066	325	14	13	108	0	0	0	0
067	*100*	*88*	*86*	*112*	105	81	70	225
068	295	41	39	118	85	81	62	55
069	0	0	0	0	0	0	0	0
69	0	0	0	0	0	0	0	0
70	0	0	0	0	0	0	0	0
071	0	0	0	0	0	0	0	0
072	0	0	0	0	0	0	0	0
073	312	74	60	66	60	48	43	160
074	0	0	0	0	0	0	0	0
075	10	40	31	59	0	0	0	0
076	0	0	0	0	0	0	0	0
077	0	0	0	0	0	0	0	0
078	332	60	46	63	0	0	0	0
079	0	0	0	0	0	0	0	0
080	0	0	0	0	0	0	0	0
081	245	81	65	45	20	86	28	39
082	0	0	0	0	0	0	0	0
083	278	65	40	74	0	0	0	0
084	0	0	0	0	0	0	0	0
085	265	59	70	344	0	0	0	0
086	0	0	0	0	0	0	0	0
087	0	0	0	0	0	0	0	0
088	0	0	0	0	0	0	0	0
089	0	0	0	0	0	0	0	0
090	285	68	53	85	0	0	0	0
091	0	0	0	0	0	0	0	0
092	0	0	0	0	0	0	0	0
093	0	0	0	0	0	0	0	0
094	0	0	0	0	0	0	0	0
095	0	0	0	0	0	0	0	0
096	0	0	0	0	45	74	21	225
097	0	0	0	0	0	0	0	0
098	0	0	0	0	0	0	0	0

Appendix Table 3: Structural data from the North Virgin Mountains

099	0	0	0	0	0	0	0	0
100	0	0	0	0	0	0	0	0
101	0	0	0	0	0	0	0	0
102	0	0	0	0	0	0	0	0
103	0	0	0	0	0	0	0	0
104	0	0	0	0	0	0	0	0
105	0	0	0	0	0	0	0	0
106	0	0	0	0	0	0	0	0
107	0	0	0	0	0	0	0	0
108	0	0	0	0	0	0	0	0
109	360	50	0	0	0	0	0	0
110	0	0	0	0	0	0	0	0
111	53	30	6	215	0	0	0	0
112	0	0	0	0	0	0	0	0
113	0	0	0	0	0	0	0	0
114	0	0	0	0	0	0	0	0
115	0	0	0	0	0	0	0	0
116	0	0	0	0	0	0	0	0
117	0	0	0	0	0	0	0	0
118	0	0	0	0	0	0	0	0
119	0	0	0	0	0	0	0	0
120	0	0	0	0	0	0	0	0
121	0	0	0	0	0	0	0	0
122	0	0	0	0	0	0	0	0
123	0	0	0	0	0	0	0	0
124	0	0	0	0	0	0	0	0
125	0	0	0	0	0	0	0	0
126	0	0	0	0	0	0	0	0
127	0	0	0	0	0	0	0	0
128	0	0	0	0	0	0	0	0
129	0	0	0	0	0	0	0	0
130	0	0	0	0	0	0	0	0
131	0	0	0	0	0	0	0	0
132	0	0	0	0	0	0	0	0
133	0	0	0	0	0	0	0	0
134	0	0	0	0	0	0	0	0
135	0	0	0	0	0	0	0	0
136	0	0	0	0	0	0	0	0
137	0	0	0	0	0	0	0	0
138	169	42	41	239	0	0	0	0
139	0	0	0	0	0	0	0	0
140	0	0	0	0	0	0	0	0
141	0	0	0	0	0	0	0	0
142	0	0	0	0	0	0	0	0
143	0	0	0	0	0	0	0	0
144	0	0	0	0	0	0	0	0
145	0	0	0	0	0	0	0	0
146	0	0	0	0	0	0	0	0
147	0	0	0	0	0	0	0	0
148	0	0	0	0	0	0	0	0

Appendix Table 3: Structural data from the North Virgin Mountains

149	0	0	0	0	0	0	0	0
200	0	0	0	0	0	0	0	0
201	0	0	0	0	0	0	0	0
202	125	63	34	295	0	0	0	0
203	0	0	0	0	0	0	0	0
205	0	0	0	0	0	0	0	0
206	0	0	0	0	0	0	0	0
207	0	0	0	0	0	0	0	0
208	0	0	0	0	0	0	0	0
209	10	75	75	105	0	0	0	0
210	0	0	0	0	0	0	0	0
211	0	0	0	0	0	0	0	0
213	0	0	0	0	0	0	0	0
213	0	0	0	0	0	0	0	0
214	270	78	59	271	0	0	0	0
215	0	0	0	0	0	0	0	0
216	29	29	27	91	0	0	0	0
217	320	74	73	86	0	0	0	0
220	0	0	0	0	0	0	0	0
221	0	0	0	0	0	0	0	0
222	0	0	0	0	0	0	0	0
223	0	0	0	0	0	0	0	0
234	0	0	0	0	0	0	0	0
235	230	19	11	262	0	0	0	0
236	0	0	0	0	0	0	0	0
237	0	0	0	0	0	0	0	0
238	0	0	0	0	0	0	0	0
239	0	0	0	0	0	0	0	0
240	0	0	0	0	0	0	0	0
241	0	0	0	0	0	0	0	0
242	0	0	0	0	0	0	0	0
243	0	0	0	0	0	0	0	0
244	0	0	0	0	0	0	0	0
245	0	0	0	0	0	0	0	0
J1	0	0	0	0	0	0	0	0
J2	0	0	0	0	0	0	0	0
J3	0	0	0	0	0	0	0	0
J4	0	0	0	0	0	0	0	0
J6	0	0	0	0	0	0	0	0
J8	0	0	0	0	0	0	0	0
J10	0	0	0	0	0	0	0	0
J11	0	0	0	0	0	0	0	0
J12	0	0	0	0	0	0	0	0
J13	0	0	0	0	0	0	0	0
J14	0	0	0	0	0	0	0	0
J15	0	0	0	0	0	0	0	0
J16	0	0	0	0	0	0	0	0
J17	0	0	0	0	0	0	0	0
J19	0	0	0	0	0	0	0	0
J21	0	0	0	0	0	0	0	0

Appendix Table 3: Structural data from the North Virgin Mountains

J22	0	0	0	0	0	0	0	0
J23	0	0	0	0	0	0	0	0
J24	0	0	0	0	0	0	0	0
J25	0	0	0	0	0	0	0	0
300	0	0	0	0	0	0	0	0
300	0	0	0	0	0	0	0	0
301	0	0	0	0	0	0	0	0
302	0	0	0	0	0	0	0	0
303	270	62	11	275	0	0	0	0
304	128	52	16	289	0	0	0	0
305	0	0	0	0	0	0	0	0
306	0	0	0	0	0	0	0	0
307	0	0	0	0	0	0	0	0
308	0	0	0	0	0	0	0	0
308	0	0	0	0	0	0	0	0
308	0	0	0	0	0	0	0	0
308	0	0	0	0	0	0	0	0
309	0	0	0	0	0	0	0	0
309	251	81	76	53	0	0	0	0
310	0	0	0	0	0	0	0	0
311	0	0	0	0	0	0	0	0
311	0	0	0	0	0	0	0	0
312	0	0	0	0	0	0	0	0
313	0	0	0	0	0	0	0	0
313	0	0	0	0	0	0	0	0
313	0	0	0	0	0	0	0	0
314	276	29	25	67	0	0	0	0
314	275	51	41	61	0	0	0	0
315	0	0	0	0	0	0	0	0
315	0	0	0	0	0	0	0	0
316	11	75		35	0	0	0	0
317	239	81	86	1	0	0	0	0
318	0	0	0	0	0	0	0	0
319	0	0	0	0	0	0	0	0
320	0	0	0	0	0	0	0	0
320	0	0	0	0	0	0	0	0
320	0	0	0	0	0	0	0	0
321	0	0	0	0	0	0	0	0
321	0	0	0	0	0	0	0	0
322	0	0	0	0	0	0	0	0
323	0	0	0	0	0	0	0	0
324	0	0	0	0	0	0	0	0
325	0	0	0	0	0	0	0	0
326	0	0	0	0	0	0	0	0
327	69	56	51	115	0	0	0	0
328	0	0	0	0	0	0	0	0
329	0	0	0	0	0	0	0	0
330	0	0	0	0	0	0	0	0
331	0	0	0	0	0	0	0	0
332	0	0	0	0	0	0	0	0

Appendix Table 3: Structural data from the North Virgin Mountains

333	0	0	18	121	0	0	0	0
400	20	58	0	0	0	0	0	0
401	0	0	0	0	0	0	0	0
402	0	0	0	0	0	0	0	0
403	0	0	0	0	0	0	0	0
404	0	0	0	0	0	0	0	0
405	46	81	42	56	0	0	0	0
406	0	0	0	0	0	0	0	0
406	0	0	0	0	0	0	0	0
406	0	0	0	0	0	0	0	0
406	0	0	0	0	0	0	0	0
406	0	0	0	0	0	0	0	0
406	0	0	0	0	0	0	0	0
407	0	0	0	0	0	0	0	0
408	0	0	0	0	0	0	0	0
409	0	0	0	0	0	0	0	0
410	0	0	0	0	0	0	0	0
411	0	0	0	0	0	0	0	0
412	0	0	0	0	0	0	0	0
413	0	0	0	0	0	0	0	0
414	0	0	0	0	0	0	0	0

Appendix Table 3: Structural data from the North Virgin Mountains

Station No.	Sed Bed	Comments		
001				
002	233/63			
003	206/15			
004	254/58			
005				
006				
007				
008				
009				
010				
011				
012				
013				
014				
015				
016				
017				
018				
019				
020				
021				
022				
023				
024		Fault - 228/67, 18/052		
025				
026				
027				
028				
029				
030				
031				
032		Fault 322/68		
033				
034				
035				
036				
037				
038				
039				
040				
041				
042				
043				
044		Add s2= 110/90		
045				
046				
047				
048				
049				

Appendix Table 3: Structural data from the North Virgin Mountains

050		
051		
052		
053		
054		
055		
056		
057		
058		
059		
060		Fault slick - 21/206, 70/010
061		
062		
063		
064		
065		
066		
067		fault 295/81,49/300, *could be F4*
068		S2 273/51,48/031,
069		Folds may be shear related, not S2
69		fault 222/89,24/044
70		
071		S2,2 wk fabric in granite
072		
073		
074		
075		
076	0	
077	0	
078		
079	205/47	
080		more s2 = 268/64, 355/44
081	212/42	
082		
083		
084		
085		
086	040/48	beds overturn 236/86, 180/80, 040/48
087		
088		
089		
090		
091		
092		
093		
094		
095		
096		
097		
098		

Appendix Table 3: Structural data from the North Virgin Mountains

099				
100				
101				
102				
103				
104				
105				
106				
107				
108				
109				
110		hinge 254/04, 030/69		
111				
112				
113				
114				
115				
116				
117				
118				
119				
120				
121				
122				
123				
124				
125				
126				
127				
128				
129				
130				
131				
132				
133				
134				
135				
136				
137				
138		more folds 220/50,49/295 see notes		
139		see notes		
140				
141				
142				
143				
144				
145				
146				
147	057/22	F5?in limestone 356/72, 51/360		
148				

Appendix Table 3: Structural data from the North Virgin Mountains

149				
200	265/26			
201	020/60			
202				
203				
205				
206				
207				
208				
209				
210	057/45	faults see notes		
211	085/35			
213				
213				
214				
215		see notes - s1 in amph?		
216		see notes		
217				
220				
221		faults see notes		
222				
223				
234				
235				
236				
237				
238	270/82			
239	see notes			
240	see notes			
241	062/51			
242	see notes			
243	see notes			
244				
245	see map			
J1				
J2				
J3				
J4				
J6				
J8				
J10				
J11				
J12				
J13				
J14				
J15				
J16				
J17				
J19				
J21				

Appendix Table 3: Structural data from the North Virgin Mountains

J22				
J23				
J24				
J25				
300				
300				
301				
302				
303				
304				
305				
306	020/32			
307				
308				
308				
308				
308				
309				
309				
310				
311				
311				
312				
313				
313				
313				
314				
314				
315				
315				
316				
317				
318				
319				
320				
320				
320				
321				
321				
322				
323				
324				
325				
326				
327				
328				
329				
330				
331				
332				

Appendix Table 3: Structural data from the North Virgin Mountains

333				
400				
401				
402				
403				
404				
405				
406				
406				
406				
406				
406				
406				
406				
407				
408				
409				
410				
411				
412				
413				
414				

REFERENCES CITED

Albin, A., and Karlstrom, K.E., 1991, Orthogonal Proterozoic fabrics in northwestern Arizona: Multiple orogenic events or progressive deformation during continental assembly, in Karlstrom, K.E., ed., Proterozoic geology and ore deposits of Arizona: Arizona Geological Society Digest v.19, p. 67-84.

Anderson, E.M., 1942, The Dynamics of Faulting and Dyke Formation with Application to Britain: Edinburgh, Oliver and Boyd, 191 p.

Anderson, R.E., 1971, Thin skinned distension in Tertiary rocks of southeastern Nevada: Geological Society of America Bulletin, v. 82, p. 42-58.

Anderson, R.E., 1973, Large-magnitude late Tertiary strike-slip faulting north of Lake Mead, Nevada: U.S. Geological Survey Professional Paper 794, 18 p.

Anderson, R.E. and Barnhard, T.P., Aspects of three-dimensional strain at the margin of the extensional orogen, Virgin River depression area, Nevada, Utah, and Arizona: GSA Bulletin, v.105, p.1019-1052, 1993.

Anderson, R.E., Barnhard, T.P., Snee, L.W., 1994, Roles of plutonism, midcrustal flow, tectonic rafting, and horizontal collapse in shaping the Miocene strain field of the Lake Mead area, Nevada and Arizona: Tectonics, v. 13, no. 6, p. 1,381-1,410.

Axen, G.J., and Wernicke, B.P., 1987, Magnitude and style of Miocene upper-crustal extension in the southern Nevada area: Geological Society of America, Abstracts with Programs, v. 19, p. 576.

Axen, G.J., and Wernicke, B.P., 1989, Reply to Comment on "On the role of isostasy in the evolution of normal fault systems" by D.G. Carpenter and others: Geology, v. 17, p. 775-776.

Axen, G.J., Wernicke, B.P., Taylor, W.J., and Skelly, M.F. , 1990, Mesozoic and Cenozoic tectonics of the Sevier thrust belt in the Virgin River Valley area, southern Nevada: in Wernicke. B.P., ed., Basin and Range extension near the latitude of Las Vegas, Nevada: Geological Society of America Memoir, v. 176, p. 123-154.

Beal, L.H., 1965, Geology and mineral deposits of the Bunkerville mining district, Clark County, Nevada: Bulletin of the Nevada Bureau of Mines, v 63.

Beard, L.S., 1993, Geologic map of the Whitney Pocket 7.5-minute quadrangle, Clark County, Nevada: U.S. Geological Survey Open-File Report 93-716, 15 p., scale 1:24,000

Beard, L.S., 1996, Paleogeography of the Horse Spring Formation in relation to the Lake Mead fault system: in Beratan, K.K., ed., Reconstructing the history of Basin and Range extension using sedimentology and stratigraphy: Geological Society of America Special Paper 303, p. 27-60.

Bell, T., 1981, Foliation development: the contribution, geometry and significance of progressive bulk inhomogeneous shortening: Tectonophysics, v. 75, p. 273-296.

Bennett, V.C., and DePaolo, D.J., 1987, Proterozoic crustal history of the western United States as determined by neodymium isotopic mapping: Geological Society of America Bulletin, v. 99, p. 674-685.

Berk, A., Bernstein, L.S., and Robertson, D.C., 1989. MODTRAN: A Moderate Resolution Model for LOWTRAN 7. Tech. Rep. GL-TR-89-0122, Geophys. Lab., Bedford, Mass.

Betts, P. and Giles, D., 2000, 1.8 Ga to 1.1 Ga evolution of the Australian continent: a northern, central, and eastern Australian perspective: Geol. Soc. Austral., 15th Geological Convention, 59: 34.

Billingsley, G. H., 1995, Geologic map of the Littlefield quadrangle, northern Mohave County, Arizona: U.S. Geological Survey Open-File Report 95-559, 15 p., scale 1:24,000

Billingsley, G. H., and Bohannon, R. C., 1995, Geologic map of the Elbow Canyon quadrangle, northern Mohave County, Arizona: U.S. Geological Survey Open-File Report 95-560, 16 p., scale 1:24,000

Bohannon, R.G., 1979, Strike-slip faults of the Lake Mead region of southern Nevada, *in* Armentrout, J.M., Cole, M.R., and Terbest, H., eds., Cenozoic paleogeography of the Western United States - Pacific Coast Paleogeography Symposium 3: Los Angeles, Pacific Section, Society of Economic Paleontologists and Mineralogists, p. 129-139.

Bohannon, R.G., 1983, Mesozoic and Cenozoic tectonic development of the Muddy, North Muddy, and northern Black Mountains, Clark County, Nevada, *in* Miller, D.M., Todd, R., and K.A. Howard, eds., Tectonic and stratigraphic studies in the eastern Great Basin, Geological Society of America Memoir, 157, p. 125-148.

Bohannon, R.G., 1984, Nonmarine sedimentary rocks of Tertiary age in the Lake Mead region, southeastern Nevada and northwestern Arizona: U.S. Geological Survey Professional Paper 1259, 72 p.

Bohannon, R.G., 1991, Geologic map of the Jacobs Well and southern part of the Elbow Canyon quadrangles, Mohave County, Arizona: U.S. Geological Survey Miscellaneous Investigations Series Map I-2167, scale 1:24,000

Bohannon, R.G., and Lucchitta, I., 1991, Geologic map of the Mount Bangs Quadrangle, Mohave County, Arizona: U.S. Geological Survey Miscellaneous Investigations Series Map I-2166, scale 1:24,000

Bohannon, R.G., Grow, J.A., Miller, J.J., and Blank, R.H., Jr., 1993, Seismic stratigraphy and tectonic development of Virgin River depression and associated basin, southeastern Nevada and northwestern Arizona: Geological Society of America Bulletin, v. 105, p. 501-520.

Brady, R.J., 1998, The geology of the Gold Butte breakaway zone and the mechanical evolution of normal fault systems: California Institute of Technology, Ph.D. thesis, 189 p.

Brady, R.A., Wernicke, B.P., and Fryxell, J.E., 2000, Kinematic evolution of a large-offset continental normal fault system, South Virgin Mountains, Nevada: Geological Society of America Bulletin, v. 111.

Campagna, D.J., and Aydin, A., 1994, Basin genesis associated with strike-slip faulting in the Basin and Range, southeastern Nevada: Tectonics, v. 13, p. 327-341.

Cavosie, A., 2001, Chemical and tectonic evolution of a Proterozoic ophiolite fragment in the northern Colorado Front Range, and analysis of the kinematic history of the associated Buckhorn Creek shear zone: unpublished M.S. thesis, University of New Mexico

Cavosie, A. and Selverstone, J., in review, Early Proterozoic oceanic crust in the northern Colorado Front Range: Implications for crustal growth and initiation of basement faults: Tectonics.

Chamberlain, K.R. and Bowring, S.A., 2001, Apatite-feldspar U-Pb thermochronometer; a reliable, mid-range (approximately 450 degrees C), diffusion-controlled system; *in* What are we dating? Understanding the crystallogenesis of U-Pb geochronometers: Geological Society of America annual meeting, Chemical Geology v.172, no. 1-2, p.173-200

Chamberlain, K.R. and Bowring, S.A., 1990, Proterozoic geochronologic and isotopic boundary in NW Arizona: Journal of Geology v.98, no. 3, p.399-416

Condie, Kent C., 1983, Precambrian history of the Rocky Mountain region: in Proceedings of the Denver Region Exploration Geologists Society symposium; the genesis of Rocky Mountain ore deposits; changes with time and tectonics v.11-12

Crowley, J. K. and S. J. Hook, 1996, Thermal Infrared Multispectral Scanner (TIMS) Study of Playa Evaporite Minerals in Death Valley, California: Journal of Geophysical Research, v. 101 pp. 643-660.

Deer, W., Howie, R., Zussman, J., 1992, An introduction to the rock forming minerals, 2nd Edition, Addision Wesley Longman Limited, 696 p.

Dorr, J. A., Jr., Spearing, D. R., Steidtmann, J. R., 1977, Deformation and deposition between a foreland uplift and an impinging thrust belt; Hoback Basin, Wyoming: Geological Society of America Special Paper no. 177, 82 p.

Dubendorfer, E.M., Beard, L.S., Smith E.I., 1998, Restoration of Tertiary deformation in the Lake Mead region, southern Nevada: The role of strike-slip transfer faults, in Faulds, J.E., and Stewart J.H., eds., Accommodation Zones and Transfer Zones: The Regional Segmentation of the Basin and Range Province: Boulder, Colorado, Geological Society of America Paper 323.

Duebendorfer, E.M., and Sharp, W.D., 1998, Variation in displacement along strike of the South Virgin - White Hills detachment fault: Perspective from the northern White Hills, northwestern Arizona: Geological Society of America Bulletin, v. 110, p. 1574-1589.

Duebendorfer, E.M., Chamberlain, K.R., and Jones, C.S., 2001, Paleoproterozoic tectonic history of the Cerbat Mountains, northwest Arizona: Implications for crustal assembly in the southwestern United States: Geological Society of America Bulletin, v. 113, p. 575-590.

Fitzgerald, P.G., Fryxell, J.E., and Wernicke, B.P., 1991, Miocene crustal extension and uplift in southeastern Nevada: Constraints from fission-track analysis: Geology, v. 19, p. 1013-1016.

Fryxell, J.E., Salton, G.G., Selverstone, J., and Wernicke, B.P., 1992, Gold Butte crustal section, south Virgin Mountains, Nevada: Tectonics, v. 11, p. 1099-1120.

Gillespie, A.R., Kahle, A.B. and Walker, R.E., 1986, Color Enhancement of Highly Correlated Images. I. Decorrelation and HSI Contrast Stretches: Remote Sensing of Environment, vol. 20, pp. 209-235.

Harland, W.B., 1971, Tectonic transpression in Caledonian Spitzbergen: Geological Magazine, v.108, pp. 27-42.

Hirth, G. and Tullis, J., 1992, Dislocation creep regimes in quartz aggregates: Journal of Structural Geology v.14, no. 2, p.145-159

Hoffman, P.F., 1988. United Plates of America, the birth of a craton: Early Proterozoic assembly and growth of Laurentia: Annual Review of Earth and Planetary Science Letters, v. 16, pp. 543–603.

Hook, S. J., Gabell, A. R., Green, A. A., and P. S. Kealy, 1992, A Comparison of Techniques for Extracting Emissivity Information from Thermal Infrared Data for Geologic Studies: Remote Sensing of Environment, vol. 42, pp.123-135.

Hook, S. J., Karlstrom, K. E., Miller, C. F., and K. J. W. McCaffrey 1994, Mapping the Piute Mountains, CA with Thermal Infrared Multispectral Scanner (TIMS) Data: Journal of Geophysical Research, vol. 99 pp. 15,605-15.622.

Hook, S. J., Myers, J. J., Thome, K. J., Fitzgerald, M. and A. B. Kahle, 2001, The MODIS/ASTER Airborne Simulator (MASTER) – A New Instrument for Earth Science Studies: Remote Sensing of Environment, vol. 76, pp. 93-102.

Hudleston, P., 1999, Strain compatibility and shear zones: is there a problem?: Journal Struct Geo 21, 923-932.

Hunt, G. R., 1980. Electromagnetic radiation: The communication link in remote sensing: in Remote Sensing in Geology, edited by B. S. Siegal and A. R. Gillespie, pp. 5-45, John Wiley, New York.

Huntoon, P.W., 1990, Phanerozoic structural geology of the Grand Canyon: Grand Canyon Geology, p.261-309.

Ilg, B., Karlstrom, K.E., Hawkins, D., and Williams, M.L. 1996, Tectonic evolution of paleoproterozoic rocks in the Grand Canyon, Insights into middle crustal processes: Geological Society of America Bulletin, v. 108, p. 1149- 1166.

Jessup, M., Karlstrom, K.E., Livaccari, R., Connelly, J., Tyson, A., Rogers, S.A., Complex Proterozoic crustal assembly of southwestern North America involving northeast, then northwest, directed convergence in an arcuate subduction system: The Black Canyon of the Gunnison, southwestern Colorado: In press AGU monograph, 2003

Jones, R., Holdsworth, R.E., and Bailey, W., 1997, Lateral extrusion in transpression zones: the importance of boundary conditions: Journal of Structural Geology, v 19, pp. 1201-1217.

Jones, R.R., and Tanner, P.W.G, 1995, Strain partitioning in transpression zones: Journal of Structural Geology, v. 17, p. 793-802

Jones, C., Deubendorfer, E.M., Orr, T., Hanlon, J., and Chamberlain, K., 1996, Polyphase deformation of Proterozoic rocks in the Cerbat Mountains, Arizona: Implications

for crustal assembly in the southwestern U.S.: Geological Society of America Abstracts with Programs, v. 28, p. 315

Karlstrom, K.E., 1998. Introduction to special issues: Lithospheric structure and evolution of the Rocky Mountains: Rocky Mountain Geology, v. 33, no.2, p. 157-160.

Karlstrom, K.E., and Bowring, S.A., 1988, Early Proterozoic assembly of tectonostratigraphic terrains in southwestern North America: Journal of Geology, v. 96, p. 561-576.

Karlstrom, K.E., Harlan, S.S., Williams, M.L., McLelland, J., Geissman, J.W., and Ahall, K-I., 2001, Long-lived (1.8-0.8 Ga) Cordilleran type orogen in southern Laurentia, its extensions to Australia and Baltica, and implications for refining Rodinia: Precambrian Research, v. 111, p. 5-30.

Karlstrom, K.E., and Bowring, S.A., 1993, Proterozoic orogenic history in Arizona: in Van Schmus, W.R., Bickford, M.E., Anderson, J.L., Bender, E.E., Anderson, R.R., Bauer, P.W., Robertson, J.M., Bowring, S.A., Condie, K.C., Denison, R.E., Gilbert, M.C., Grambling, J.A., Mawer, C.K., Shearer, C.K., Hinze, W.J., Karlstrom, K.E., Kisvarsanyi, E.B., Lidiak, E.G., Reed, J.C., Jr., Sims, P.K., Tweto, O., Silver, L.T., Treves, S.B., Williams, M.L., Wooden, J.L., Transcontinental Proterozoic provinces, in Reed, J.C., Jr., Bickford, M.E., Houston, R.S., Link, P.K., Rankin, D.W., Sims, P.K., and Van Schmus, W.R., eds., Precambrian: Conterminous U.S.: Boulder, Colorado, Geological Society of America, The Geology of North America, v. C-2.

Karlstrom, K.E., Quigley, M.C., Bowring, S.A., Hook, S., Heizler, M., in prep, Low angle detachment along the Great Unconformity near the Colorado Plateau- Basin and Range breakaway: arguments against a tipped crustal section in the Gold Butte area, southern Nevada.

Karlstrom, K.E., Ilg, B.R., Williams, M.L., Hawkins, D.P., Bowring, S.A., and Seaman, S.J., Paleoproterozoic rocks of the Granite Gorges: in Beus, S.S. and Morales, M., eds., Grand Canyon Geology: Oxford University Press, second edition, in press.

Karlstrom, K.E., and Humphreys, G., 1998, Influence of Proterozoic accretionary boundaries in the tectonic evolution of western North America: Interaction of cratonic grain and mantle modification events: Rocky Mountain Geology, v. 33, no.2, p. 161-179

Karlstrom, K.E., and Seaman, S., 2001, Collaborative Research: Relationship between ultramafic rocks and crustal sutures in the North American Southwest, unpublished National Science Foundation Research Proposal

Karlstrom, K.E., Harlan, S.S., Williams, M.L., McLelland, J., Geissman, J.W. and Åhäll. K.-I., 1999, Refining Rodinia: Geologic Evidence for the Australian-Western U.S. connection in the Proterozoic: GSA Today, v 9: p 1–7.

Karlstrom, K.E., and Williams, M.L., in press, Nature of the middle crust-heterogeneity of structure and process due to pluton-enhanced tectonism: an example from Proterozoic rocks of the North American Southwest: in Brown, Micheal, and Rushmer, Tracy, eds., Evolution and Differentiation of the Continental Crust: Cambridge University Press, (expected 2002).

Kruse, S., M. McNutt, J. Phipps-Morgan, and L. Royden, 1991, Lithospheric extension near Lake Mead, Nevada: A model for ductile flow in the lower crust: Journal of Geophysical Research, v. 96, p. 4435-4456.

Langenheim, V.E., Bohannon, R.G., Glen, J.M., Jachens, R.C., Grow, J.A., Miller, J.J., Dixon, G.L., and Katzer, T.C., 2001, Basin configuration of the Virgin River Depression, Nevada, Utah, and Arizona: A geophysical view of deformation along the Colorado Plateau – Basin and Range transition: Utah Geological Association Publication 30, The Mackin Volume, p. 205-226.

Li, Z-X., Zhang, L. and Powell, C.M., 1995. South China in Rodinia: Part of the missing link between Australia-East Antarctica and Laurentia. Geology, 23: 407–410.

Longwell, C.R., 1928, Geology of the Muddy Mountains, Nevada, with a section through the Virgin Range to the Grand Wash Cliffs, Arizona: U.S. Geological Survey Bulletin 798, 152 p.

Longwell, C.R., 1936, Geology of the Boulder Reservoir floor, Arizona-Nevada: Geological Society of America Bulletin, v. 47, p. 1393-1476.

Longwell, C. R., Pampeyan, E. H. Bowyer, B. and R. J. Roberts, 1965. Geology and Mineral Deposits of Clark County, Nevada. Nevada Bureau of Mines Bulletin, vol. 62, pp 126-133.

Marshak, S., Karlstrom, K.E., Timmons, M.J., 2000, Inversion of Proterozoic extensional faults: an explanation for the patterns of Laramide and Ancestral Rockies intracratonic deformation, USA: Geology, v. 28, p. 735-738.

McCoy. A., 2001, The Proterozoic Ancestry of the Colorado Mineral Belt: ca. 1.4. Ga shear zone in central Colorado, unpublished M.S. thesis, University of New Mexico, 159 p.

McDougall, I., and Harrison, T.M., 1999, Geochronology and Thermochronology by the $^{39}Ar/^{40}Ar$ Method: Oxford, Oxford University Press, 212 p.

Moore, R.T., 1972, Geology of the Virgin and Beaverdam Mountains, Arizona: Arizona Bureau of Mines Bulletin 186, 65 p.

Moores, E.M., 1991, Southwest U.S.-East Antarctic (SWEAT) connection; a hypothesis: Geology, 19: 425–428.

Naeser, C.W., 1979, Fission-track dating and geologic annealing of fission tracks: in Lectures in Isotope Geology, edited by E. Jager and J.C. Hunziker, New York, Springer Verlag, p. 154-169.

Naeser, C. W., Duddy, I. R., Elston, D. P., Dumitru, T. A., and Green, P. F., 1989, Chapter 17: Fission track dating: Ages for Cambrian strata and Laramide and post-middle Eocene cooling events from the Grand Canyon, Arizona: in Elston, D.P., Billingsley, G.H., and Young, R.A., eds., Geology of the Grand Canyon, Northern Arizona (with Colorado River Guides), American Geophysical Union, p. 139-144.

Nyman, M.W., Karlstrom, K.E., Kirby, E., Graubard, R.D., 1994 Mesoproterozoic contractional orogeny in western North America: Evidence from ca. 1.4Ga plutons: Geology, v.22, p. 901-904.

Powell, J.W., 1875, Exploration of the Colorado River of the west and its tributaries: Washington, Government Printing Office, 291 p.

Quigley, M.C., Karlstrom, K.E., Kelley, S., and Heizler, M., 2001, Tectonic Inheritence at the Colorado Plateau-Basin and Range margin: Miocene uplift of the Virgin Mountain anticline influenced by reactivation of Laramide and Proterozoic structures: Utah Geological Association Publication 30, p. 427

Quigley, M.C., Karlstrom, K.E., and Hook, S., Detailed structural and tectonic studies utilizing MASTER remote sensing imagery: A case study from the North Virgin Mountains, Southeast Nevada and Northwest Arizona, in prep.

Quigley, M.C., Karlstrom, K.E., and Kelley, S.A., Influence of Proterozoic and Laramide structures on Miocene genesis of the Virgin Mountain anticline, southeast Nevada and northwest Arizona: Constraints from structural and apatite fission-track analysis, in prep.

Ramsay, J.G., and Huber, M.I., 1983, The Techniques of Modern Structural Geology: Academic Press, 307 p.

Robin, P.-Y. F, and Cruden, A.R., Strain and vorticity patterns in ideally ductile transpression zones: Journal of Structural Geology v 16, p 447-466.

Sanderson, D.J., and Marchini, W.R.D., 1984, Transpression: Journal of Structural Geology, v. 6, p. 449-458.

Sears, J.W. and Price, R.A., 2000, New look at the Siberian connection: No SWEAT: Geology, v. 28, p. 423–426.

Selverstone, J., Aleinikoff, J., Hodgins, M., and Fanning, C.M., 2000, Mesoproterozoic reactivation of a Paleoproterozoic transcurrent boundary in the Colorado Front Range: Implications for ca. 1.7 and 1.4 Ga tectonism. Rocky Mtn. Geology v. 35, p. 136-162.

Shaw, C.A., 2001, Genesis and evolution of Proterozoic crustal boundaries in the southern Rocky Mountains, PhD thesis, University of New Mexico, 361 p.

Shaw, C.A., and Karlstrom, K.E., 1999, The Yavapai-Mazatzal crustal boundary in the southern Rocky Mountains: Rocky Mountain Geology, v. 34, no.1, p. 37-52.

Shaw, C.A., Karlstrom, K.E., Williams, M.L., Jercinovic, M.J., and McCoy, A.M., 2001, Electron-microprobe monazite dating of ca. 1.71-1.63 Ga and ca. 1.45-1.38 Ga deformation in the Homestake shear zone, Colorado: Origin and early evolution of a persistent intracontinental tectonic zone: Geology, v. 29, p. 739-742.

Stewart, M.E., and Taylor, W.J., 1996, Structural analysis and fault segment boundary identification along the Hurricane fault in southwestern Utah: Journal of Structural Geology v. 18, p.1017-1029

Tikoff, B., and Greene, D., 1997, Stretching lineations in transpressional shear zones: an example from the Sierra Nevada Batholith, California: Journal of Structural Geology, v. 19, p. 29-39.

Timmons, M.J., Karlstrom, K.E., Dehler, C.M., Geissman, J.W., and Heizler, M.T., 2001, Proterozoic multistage (~1.1 and ~0.8 Ga) extension in the Grand Canyon Supergroup and establishment of northwest and north-south tectonic grains in the southwestern United States: Geological Society of America Bulletin, v. 113, p. 163-180.

Thomas, W.M., Clark, S.H., Young, E.D., Orrell, S.E., and Anderson, J.L., 1988, Proterozoic high-grade metamorphism in the Colorado River region, Nevada, Arizona and California: in Ernst, W.G., ed., Metamorphism and Crustal Evolution of the Western United States, Rubey Volume VII, Prentice Hall, Englewood Cliffs, N.J.

Tyson, A.R., Karlstrom, K.E., Chamberlain, K.R., Morozova, E.A., Smithson, S.B., Dueker, K., and Foster, C.T., 2002, Proterozoic Farwell Mountain -- Lester Mountain suture zone, northern Colorado: Subduction flip and progressive assembly of arcs: Geology, in press.

Spear, F.S., 1993, Metamorphic phase equilibria and pressure-temperature-time paths: Mineralogical Society of America Monograph, Washington D.C., 799p.

Volborth, A., 1962, Rapakivi-type granites in the Precambrian complex of Gold Butte, Clark County, Nevada: Geological Society of America Bulletin, v. 73, p. 813-832

Wernicke, B.P., Axen, G.J., and Snow, J.K., 1988, Basin and Range extensional tectonics at the latitude of Las Vegas, Nevada: Geological Society of America Bulletin, v. 100, p. 1738-1757.

Wernicke, B.P., and Axen, G.J., 1988, On the role of isostasy in the evolution of normal fault systems: Geology, v. 16, p. 848-851

Williams, M.L., 1991, Overview of Early Proterozoic Metamorphism in Arizona. In Karlstrom, K.E. (ed.), Proterozoic Geology and Ore Deposits of Arizona: Arizona Geological Society Digest 19, p.11-26.

Williams, M.L., Jercinovic, M.J., Terry, M.P, 1999, Age Mapping and Chemical Dating of Monazite Using the Electron Microprobe: Deconvoluting Multistage Tectonic Histories: Geology. v.27, p. 1023-1026.

Williams, V.S., Bohannon, R.G., and Hoover, D.L., 1997, Geologic map of the Riverside quadrangle, Clark County, Nevada: U.S. Geological Survey Geologic Map GQ-1770, scale 1:24,000.

Wooden, J.L., and Dewitt, E.D., 1991, Pb isotopic evidence for the boundary between the Early Proterozoic Mojave and central Arizona crustal provinces in western Arizona: in Karlstrom, K.E., ed., Proterozoic geology and ore deposits of Arizona, Arizona Geological Society Digest v. 19, p27-50.

Wooden, J.L., and Miller, D.M., 1990, Chronologic and isotopic framework for early Proterozoic crustal evolution in the eastern Mojave desert region, SE California: Journal of Geophysical Research, V.95, p. 20133-20146.

Wooden J.L., and Dewitt, E., 1991, Pb isotopic evidence for a major early Proterozoic crustal boundary in western Arizona: in Karlstrom, K.E., ed., Proterozoic geology and ore deposits of Arizona: Arizona Geological Society Digest v.19, p. 277-280.

Wooden, J. L.; Miller, D. M.; Howard, K. A, 1988, Early Proterozoic chronology of the eastern Mojave Desert: Abstracts with Programs - Geological Society of America v.20, no. 3, p.243

Wooden J.L., and Miller, D.M., 1990, Chronologic and isotopic framework for Early Proterozoic crustal evolution in the eastern Mojave Desert, California: Journal of Geophysical Research, v.95, p.20133-20146.

Yamaguchi, Y., Kahle, A. B., Tsu, H., Kawakami, T. and M. Pniel, 1998, Overview of Advanced Spaceborne Thermal Emission Reflectance Radiometer: IEEE Transactions Geoscience and Remote Sensing, vol. 36 pp. 1062-1071.

Young, R.A., 1979, Laramide deformation, erosion and plutonism along the southwestern margin of the Colorado Plateau: Tectonophysics, v. 61, p. 25-47.